

*Iowa Department of Transportation
Research Project TPF-5(193) Supplement #101*

DEVELOPMENT OF IOWA DOT COMBINATION BRIDGE SEPARATION BARRIER WITH BICYCLE RAILING - PHASE I

Submitted by

Chaz M. Ginger, M.S.M.E
Former Graduate Research Assistant

John D. Reid, Ph.D.
Professor

Robert W. Bielenberg, M.S.M.E., E.I.T.
Research Engineer

Ronald K. Faller, Ph.D., P.E.
Research Professor & MwRSF Director

Scott K. Rosenbaugh, M.S.C.E., E.I.T.
Research Engineer

Cody S. Stolle, Ph.D., E.I.T.
Research Assistant Professor

MIDWEST ROADSIDE SAFETY FACILITY

Nebraska Transportation Center
University of Nebraska-Lincoln

Main Office

Prem S. Paul Research Center at Whittier School
Room 130, 2200 Vine Street
Lincoln, Nebraska 68583-0853
(402) 472-0965

Outdoor Test Site

4630 N.W. 36th Street
Lincoln, Nebraska 68524

Submitted to

Iowa Department of Transportation

800 Lincoln Way
Ames, IA 50010

MwRSF Research Report No. TRP-03-397-19

August 16, 2019

TECHNICAL REPORT DOCUMENTATION PAGE

1. Report No. TRP-03-397-19	2.	3. Recipient's Accession No.	
4. Title and Subtitle Development of Iowa DOT Combination Bridge Separation Barrier with Bicycle Railing – Phase I		5. Report Date August 16, 2019	
		6.	
7. Author(s) Ginger, C.G., Reid, J.D., Bielenberg, R.W., Faller, R.K., Rosenbaugh, S.K., and Stolle, C.S.		8. Performing Organization Report No. TRP-03-397-19	
9. Performing Organization Name and Address Midwest Roadside Safety Facility (MwRSF) Nebraska Transportation Center University of Nebraska-Lincoln Main Office: Prem S. Paul Research Center at Whittier School Room 130, 2200 Vine Street Lincoln, Nebraska 68583-0853		10. Project/Task/Work Unit No.	
		11. Contract © or Grant (G) No. TPF-5(193) Supplement #101	
12. Sponsoring Organization Name and Address Iowa Department of Transportation 800 Lincoln Way Ames, IA 50010		13. Type of Report and Period Covered Final Report: 2016 – 2019	
		14. Sponsoring Agency Code	
15. Supplementary Notes Prepared in cooperation with the Iowa Department of Transportation.			
16. Abstract <p>Iowa Department of Transportation (Iowa DOT) typically builds separation barriers between vehicle and pedestrian/bicycle facilities when sidewalks or trails are present on vehicular bridges. Currently, Iowa DOT employs a combination bridge rail that utilizes a concrete parapet that had previously been successfully evaluated to National Cooperative Highway Research Program (NCHRP) Report No. 350 Test Level 4 (TL-4) criteria for these situations. While the parapet had been successfully evaluated, the combination bridge rail system as a whole had not been evaluated to any crash test standards. Iowa DOT desired that researchers at Midwest Roadside Safety Facility (MwRSF) design and test a combination bridge separation barrier to current <i>Manual for Assessing Safety Hardware, Second Edition</i> (MASH 2016) TL-2 standards to use in place of their current, untested system.</p> <p>During this effort, previous combination rails, low-height vertical parapets, and zone of intrusion (ZOI) studies were reviewed to provide guidance on system design. A simulation effort was also performed to aid in height selection of the parapet, as well as placement of the attached bicycle rail to reduce the amount of negative vehicle-to-rail interaction with the system. Using the gathered data, a full system design was produced. It was then recommended that the proposed system be evaluated to MASH 2016 test designation no. 2-11 in order to assess the system's performance during a vehicle impact scenario.</p>			
17. Document Analysis/Descriptors Highway Safety, Roadside Appurtenances, MASH 2016, Simulation, LS-DYNA, LRFD, Bicycle Rail, TL-2		18. Availability Statement No restrictions. Document available from: National Technical Information Services, Springfield, Virginia 22161	
19. Security Class (this report) Unclassified	20. Security Class (this page) Unclassified	21. No. of Pages 162	22. Price

DISCLAIMER STATEMENT

This report was completed with funding from the Federal Highway Administration, U.S. Department of Transportation and the Iowa Department of Transportation. The contents of this report reflect the views and opinions of the authors who are responsible for the facts and the accuracy of the data presented herein. The contents do not necessarily reflect the official views or policies of the Iowa Department of Transportation nor the Federal Highway Administration, U.S. Department of Transportation. This report does not constitute a standard, specification, regulation, product endorsement, or an endorsement of manufacturers.

ACKNOWLEDGEMENTS

The authors wish to acknowledge the Iowa Department of Transportation for their contribution to this project. Acknowledgement is also given to the following individuals who made a contribution to the completion of this research project.

Midwest Roadside Safety Facility

J.C. Holloway, M.S.C.E., E.I.T., Research Engineer & Assistant Director – Physical Testing Division
K.A. Lechtenberg, M.S.M.E., E.I.T., Research Engineer
J.D. Schmidt, Ph.D., P.E., Research Assistant Professor
A.T. Russell, B.S.B.A., Testing and Maintenance Technician II
E.W. Krier, B.S., Construction and Testing Technician II
S.M. Tighe, Construction and Testing Technician I
D.S. Charroin, Construction and Testing Technician I
R.M. Novak, Construction and Testing Technician I
T.C. Donahoo, Construction and Testing Technician I
J.T. Jones, Construction and Testing Technician I
C.I. Sims, Construction and Testing Technician I
J.E. Kohtz, B.S.M.E., CAD Technician
E.L. Urbank, B.A., Research Communication Specialist
Undergraduate and Graduate Research Assistants

Iowa Department of Transportation

Chris Poole, P.E., Roadside Safety Engineer
Brian Smith, P.E., Methods Engineer
Daniel Harness, Transportation Engineer Specialist

TABLE OF CONTENTS

TECHNICAL REPORT DOCUMENTATION PAGE	i
DISCLAIMER STATEMENT	ii
ACKNOWLEDGEMENTS	ii
1 INTRODUCTION	1
1.1 Background and Problem Statement.....	1
1.2 Objective	4
1.3 Scope.....	4
2 LITERATURE REVIEW	5
2.1 Pedestrian/Bicycle Railings	5
2.2 Vertical/Low-Height Parapets	13
2.3 Vehicle Intrusion.....	13
3 LS-DYNA MODEL CALIBRATION.....	18
3.1 Introduction.....	18
3.2 Validation Effort	18
3.2.1 Introduction.....	18
3.2.2 Background	18
3.2.3 Vehicle Models	18
3.3 Baseline Models.....	19
3.3.1 Results of Unmodified, Silverado V3r (NCAC-Unmodified) Simulations..	19
3.3.2 Refined Tire Model (UNL) Simulation	22
3.3.3 Increased Steering Stiffness (UNL10x) Simulation	22
3.3.4 Initial Modeling Conclusion	28
3.4 Tire-Ground and Vehicle-Barrier Friction.....	28
3.5 Elastic Barrier	38
3.6 Conclusion	41
4 VEHICLE DIMENSION EVALUATION	43
4.1 Investigation of 2270P LS-DYNA Model and Test Vehicle Parameters	43
4.2 NCHRP 350 TL-2 Systems vs. 2270p	43
4.2.1 Purpose.....	43
4.2.2 NCHRP 350 vs MASH	45
4.2.3 Test Selection and Process.....	45
4.2.4 Results.....	48
4.2.5 Conclusion	48
5 INVESTIGATION OF BARRIER HEIGHT	51
5.1 Simulation Methods.....	51
5.2 Simulated Evaluation of Minimum Barrier Height	51
5.2.1 24-in. (610-mm) Barrier Height Simulation	51
5.2.2 25-in. (635 mm) Barrier Height Simulation	54

5.2.3 26-in. (660-mm) Barrier Height Simulation	57
5.2.4 27-in. (686-mm) Barrier Height Simulation	60
5.3 Height Simulations Comparison	63
5.4 Conclusion	65
6 PEDESTRIAN/BICYCLE RAIL DESIGN	66
6.1 Iowa DOT Requirements	66
6.2 LRFD Pedestrian/Bicycle Railing Design Loading	66
6.3 Rail and Post Design Concepts	67
6.4 Rail and Post Connection Concepts	69
6.5 Concept Selection	71
6.6 Post and Rail Calculations	71
6.6.1 Longitudinal Rail Element	71
6.6.2 Vertical Post Element	76
6.7 Baseplate Calculations	77
6.7.1 Loading	78
6.7.2 Required Thickness	78
6.7.3 Post Offset	82
6.8 Post-Rail and Post-Baseplate Connection Calculations	82
6.8.1 Post-Baseplate Loading	82
6.8.2 Weld Calculations	85
6.9 Anchor Rod Calculations	86
6.10 Splice Tube	89
6.11 Parapet Details	92
6.12 Preliminary Design Details for Full System Simulation Effort	93
7 MASH 2270P PICKUP TRUCK SIMULATION OF FULL SYSTEM	94
7.1 Introduction	94
7.2 System Model	94
7.3 Simulation Results	99
7.4 CIP Determination	114
7.4.1 Post Deformation	114
7.4.2 Vehicle Velocity Change	116
7.4.3 Lateral Vehicle Overlap	117
7.4.4 CIP Determination Conclusion	118
7.5 Additional Simulation Analysis	118
7.5.1 Anchor Rod Forces	119
7.5.2 Splice Tube Capacity	120
7.5.3 Splice Tube Bolt Forces	120
7.6 Conclusions	121
8 MASH 1100C SMALL CAR SIMULATION OF FULL SYSTEM	122
8.1 1100C Simulation	122
8.1.1 Simulation Details	122
8.1.2 Results	122
8.1.3 Vehicle-To-Rail Interaction	122
8.1.1 1100C Simulation Conclusion	125

8.2 Conclusion 125

9 COMBINATION TRAFFIC/BICYCLE RAIL DESIGN DETAILS 126

10 SUMMARY AND RECOMMENDATIONS..... 141

 10.1 Summary 141

 10.2 Recommendations..... 143

11 REFERENCES 144

12 APPENDICES 149

 Appendix A. Rail Design Calculations 150

LIST OF FIGURES

Figure 1. Iowa DOT Standard Separation Barrier (in service)	1
Figure 2. Iowa DOT Alternate Separation Barrier (in service)	2
Figure 3. C411 Combination Rail [5-6].....	5
Figure 4. BR27D Bridge Railing on Bridge Deck [8]	8
Figure 5. BR27C Bridge Railing on Bridge Deck [9]	9
Figure 6. Illinois 2399-1 with Added Pedestrian/Bicycle Railing [12]	9
Figure 7. Type 80 SW Bridge Railing [13].....	10
Figure 8. Minnesota Combination Traffic/Bicycle Rail [14].....	10
Figure 9. Missouri Combination Rail with Four Rail Elements [15]	11
Figure 10. 732SW Bridge Rail [16].....	12
Figure 11. Intrusion Zones for Tall TL-2 Barriers ≥ 27 in. (686 mm) and for Short TL-2 Barriers < 27 in. (686 mm) [32].....	17
Figure 12. Downstream Sequential Views, NCAC Model and Test No. 490024-2-1	20
Figure 13. Downstream Sequential Views, NCAC Model and Test No. 490024-2-1	21
Figure 14. Downstream Sequential Views, UNL Model and Test No. 490024-2-1	23
Figure 15. Downstream Sequential Views, UNL Model and Test No. 490024-2-1	24
Figure 16. Downstream Sequential Views, UNL 10x Model and Test No. 490024-2-1	25
Figure 17. Downstream Sequential Views, UNL 10x Model and Test No. 490024-2-1	26
Figure 18. Roll Comparison for Modified Friction Models	27
Figure 19. Pitch Comparison for Modified Friction Models	27
Figure 20. Yaw Comparison for Modified Friction Models	28
Figure 21. Downstream Sequential Views, UNL10xR2 Model and Test No. 490024-2-1	30
Figure 22. Downstream Sequential Views, UNL10xR2 Model and Test No. 490024-2-1	31
Figure 23. Downstream Sequential Views, UNL10xR3 Model and Test No. 490024-2-1	32
Figure 24. Downstream Sequential Views, UNL10xR3 Model and Test No. 490024-2-1	33
Figure 25. Downstream Sequential Views, UNL 10xr4 Model and Test No. 490024-2-1	34
Figure 26. Downstream Sequential Views, UNL 10xr4 Model and Test No. 490024-2-1	35
Figure 27. Longitudinal Change in Velocity Comparison for Modified Friction Simulations	36
Figure 28. Roll Comparison for Modified Friction Models	36
Figure 29. Pitch Comparison for Modified Friction Models	37
Figure 30. Yaw Comparison for Modified Friction Models	37
Figure 31. Roll Comparison for Elastic Barrier Models	39
Figure 32. Pitch Comparisons for Elastic Barrier Models	40
Figure 33. Yaw Comparison for Elastic Barrier Models	40
Figure 34. Elastic Barrier Simulations-Impact Forces Comparison	41
Figure 35. RSMG-1 Vehicle Dimension Comparison	49
Figure 36. RSMG-2 Vehicle Dimension Comparison	49
Figure 37. LPBR-1 Vehicle Dimension Comparison	50
Figure 38. Downstream Sequential View, 24-in. (610-mm) Tall Barrier Simulation	52
Figure 39. 24-in. (610-mm) Barrier Height Simulation ZOI Envelope	53
Figure 40. Downstream Sequential View, 25-in. (635 mm) Tall Barrier Simulation	55
Figure 41. 25-in. (635 mm) Barrier Height Simulation ZOI Envelope	56
Figure 42. Downstream Sequential View, 26-in. (660-mm) Tall Barrier Simulation	58
Figure 43. 26-in. (660-mm) Barrier Height Simulation ZOI Envelope	59
Figure 44. Downstream Sequential View, 27-in. (686 mm) Tall Barrier Simulation	61

Figure 45. 27-in. (686 mm) Barrier Height Simulation ZOI Envelope	62
Figure 46. Height Simulation Vehicle Dynamics Comparison	64
Figure 47. ZOI Comparison for Height Study Simulations, Front (Left) and Rear of Vehicle (Right)	65
Figure 48. AASHTO LRFD Pedestrian/Bicycle Rail Loading [1]	67
Figure 49. Rail Design Concepts	68
Figure 50. Fully-Bolted Connection Concept	70
Figure 51. Fully-Welded Connection Concept	70
Figure 52. Combination Connection Concept (Iowa DOT-Preferred Concept)	70
Figure 53. Example of Pedestrian/Bicycle Rail with Vertical Concentrated Load	72
Figure 54. Rail Force Diagram to Maximize Bending	72
Figure 55. Rail Force Diagram to Maximize Shear	73
Figure 56. Post Force Diagram	76
Figure 57. AISC <i>Steel Design Guide 1</i> Column Baseplate Loading General Case [47]	80
Figure 58. Baseplate Simplified Traffic Impact (Top) and Pedestrian/Bicycle Loading (Bottom)	81
Figure 59. Post Vehicle Impact Loading	83
Figure 60. Post-Baseplate Front-Flange Weld Tension Diagram	84
Figure 61. Rail-Post Rear-Flange Weld Tension	85
Figure 62. Concrete Area of Influence for Two Adjacent Anchors on Concrete Parapet [49]	87
Figure 63. Comparison of ACI 318-14 Concrete Breakout and Hybrid Failure Assumptions [49]	89
Figure 64. Typical Splice Tube Detail	90
Figure 65. Standard Built-up Section Cross Section	92
Figure 66. Splice Tube Parallel Plates Configuration for Section Modulus Calculation	92
Figure 67. Splice Tube Perpendicular Plates Configuration for Section Modulus Calculation	92
Figure 68. ASTM A572 Model Stress-Strain Curve Comparison	95
Figure 69. Post-Baseplate and Anchor Rod Connection	96
Figure 70. Splice Tube Bolt Model	97
Figure 71. Splice Tube Bolt Assembly with No Preload (Left) and with Preload (Right)	97
Figure 72. Combination Rail Model	98
Figure 73. Combination Rail Close-Up	98
Figure 74. Combination Rail Front-View	98
Figure 75. Full Impact Model Top-View	99
Figure 76. Downstream Sequential Views, Impact 4.3 ft (1.3 m) US from Post No. 7 Simulation	100
Figure 77. Post Snag Sequential Views, Impact 4.3 ft (1.3 m) US from Post No. 7 Simulation	101
Figure 78. Downstream Sequential Views, Impact 3.3 ft (1 m) US from Post No. 7 Simulation	102
Figure 79. Post Snag Sequential Views, Impact 3.3 ft (1 m) US from Post No. 7 Simulation	103
Figure 80. Downstream Sequential Views, Impact 1.7 ft (0.5 m) US from Post No. 7 Simulation	105
Figure 81. Post Snag Sequential Views, Impact 1.7 ft (0.5 m) US from Post No. 7 Simulation	106
Figure 82. Downstream Sequential Views, Impact 2.6 ft (0.8 m) US from Splice Simulation	107

Figure 83. Downstream Sequential Views, Impact 2.6 ft (0.8 m) US from Splice Reversed Simulation	108
Figure 84. Post Snag Sequential Views, Impact 2.6 ft (0.8 m) US from Splice Reversed Simulation	109
Figure 85. Downstream Sequential Views, Impact 3.8 ft (1.2 m) US from Splice Simulation...	111
Figure 86. Downstream Sequential Views, Impact 3.3 ft (1 m) US from Splice Simulation	112
Figure 87. Post Snag Sequential Views, Impact 3.8 ft (1.2 m) US from Splice Simulation	113
Figure 88. 4.3 ft (1.3 m) US Post No. 7 Fender Damage	115
Figure 89. 3.3 ft (1 m) US Post No. 7 Fender Damage.....	115
Figure 90. 1.7 ft (0.5 m) US Post No. 7 Fender Damage	115
Figure 91. 3.8 ft (1.2 m) US Post No. 7 Fender Damage	115
Figure 92. 2.6 ft (0.8 m) US Splice Reversed. Fender Damage	115
Figure 94. Longitudinal and Lateral Vehicle Change in Velocity Comparison	117
Figure 95. Longitudinal and Lateral Resultant Vehicle Change in Velocity Comparison	117
Figure 96. Downstream Sequential Views, 1100C Simulation	123
Figure 97. Post Snag Sequential Views, 1100C Simulation	124
Figure 98. Iowa Bicycle Rail – System Layout	127
Figure 99. Iowa Bicycle Rail – System Cross Section	128
Figure 100. Iowa Bicycle Rail – Rail and Concrete Parapet Details	129
Figure 101. Iowa Bicycle Rail – Rail and Concrete Parapet Details	130
Figure 102. Iowa Bicycle Rail – Splice Plate Assembly	131
Figure 103. Iowa Bicycle Rail – Splice Plate Component Details	132
Figure 104. Iowa Bicycle Rail – Rail and Post Assembly	133
Figure 105. Iowa Bicycle Rail – Rail Details	134
Figure 106. Iowa Bicycle Rail – System Post and Base Plate Details.....	135
Figure 107. Iowa Bicycle Rail – Concrete Parapet Assembly Details	136
Figure 108. Iowa Bicycle Rail – Concrete Parapet Assembly Details	137
Figure 109. Iowa Bicycle Rail – Concrete Parapet Reinforcement	138
Figure 110. Iowa Bicycle Rail – Hardware	139
Figure 111. Iowa Bicycle Rail – Bill of Materials.....	140
Figure A-1. Baseplate Additional Calculations	156
Figure A-2. Tensile Adhesive Anchorage Calculations	159
Figure A-3. Shear Adhesive Anchorage Calculations	160
Figure A-4. Built-Up Splice Tube Section Moduli Calculations.....	161

LIST OF TABLES

Table 1. Previously-Tested Combination Rails	6
Table 2. Previously-Tested Combination Rails (cont'd)	7
Table 3. Vertical/Low-Height Parapet Review Relevant System Details	14
Table 4. Vertical/Low-Height Parapet Review Relevant System Details (cont'd)	15
Table 5. Guidelines for Attachments-Relevant Systems [32].....	16
Table 6. Summary of Variational Analysis: Tire-Ground and Vehicle-Barrier Friction.....	29
Table 7. Summary of Elastic Barrier Model Simulations.....	38
Table 8. 2270P vs. Silverado Model Dimensions.....	44
Table 9. 2270P vs. 2000P Details	46
Table 10. 2270P Test Vehicle Dimensions.....	47
Table 11. ZOI Values for MASH 2-11 Simulation: 24-in. (610-mm) Tall, Rigid Vertical Parapet.....	51
Table 12. ZOI Values for MASH 2-11 Simulation: 25-in. (635-mm) Tall, Rigid Vertical Parapet.....	54
Table 13. ZOI Values for MASH 2-11 Simulation: 26-in. (660-mm) Tall, Rigid Vertical Parapet.....	57
Table 14. ZOI Values for MASH 2-11 Simulation: 26-in. (660-mm) Tall, Rigid Vertical Parapet.....	60
Table 15. Post Lateral and Longitudinal Deflections	116
Table 16. Vehicle Post Overlap	118
Table 17. US and DS Anchor Rod Forces	119
Table 18. 3.8 ft (1.2 m) US from Post No. 7, Splice Bolt Shear Forces.....	120
Table A-1. Rail and Post - Shear and bending Moment Values	151
Table A-2. Rail Section Details	152
Table A-3. Post Section Details	152
Table A-4. Rail and Post - Load vs. Resistance Comparisons.....	153
Table A-5. Rail and Post - Load and Capacity Calculations	154
Table A-6. AISC Baseplate Design Guide Calculations	155
Table A-7. Weld - Load and Capacity Calculations	157
Table A-8. Weld Connection Load vs. Resistance Comparisons	158

1 INTRODUCTION

1.1 Background and Problem Statement

The Iowa Department of Transportation (Iowa DOT) typically builds separation barriers between vehicle and pedestrian/bicycle facilities when sidewalks or trails are present on vehicular bridges. In order to meet American Association of State Highway and Transportation Officials (AASHTO) specifications [1], steel railings are often attached to crashworthy traffic barriers to achieve a minimum total system height above the trail surface of 42 in. (1,067 mm) for bicyclists. Public demand has encouraged Iowa DOT to also install railing separators when only a pedestrian sidewalk is present. Recently constructed separation barriers have included the bicycle railing hardware since it is assumed that bicyclists will use sidewalks that do not meet minimum criteria required in the design of “official” bike facilities.

Separation barrier used by Iowa DOT historically consisted of a 34-in. (864-mm) tall safety shape concrete barrier with a steel railing attached to its top surface, as shown in Figure 1. However, a literature review of published full-scale crash testing and simulation results did not produce evidence that this combination rail had previously demonstrated crashworthy performance according to guidelines presented in National Cooperative Highway Research Program (NCHRP) Report No. 350 or the *Manual for Assessing Safety Hardware* (MASH) [2-4], nor did the system appear in NCHRP Report No. 350 collection of crashworthy barriers.

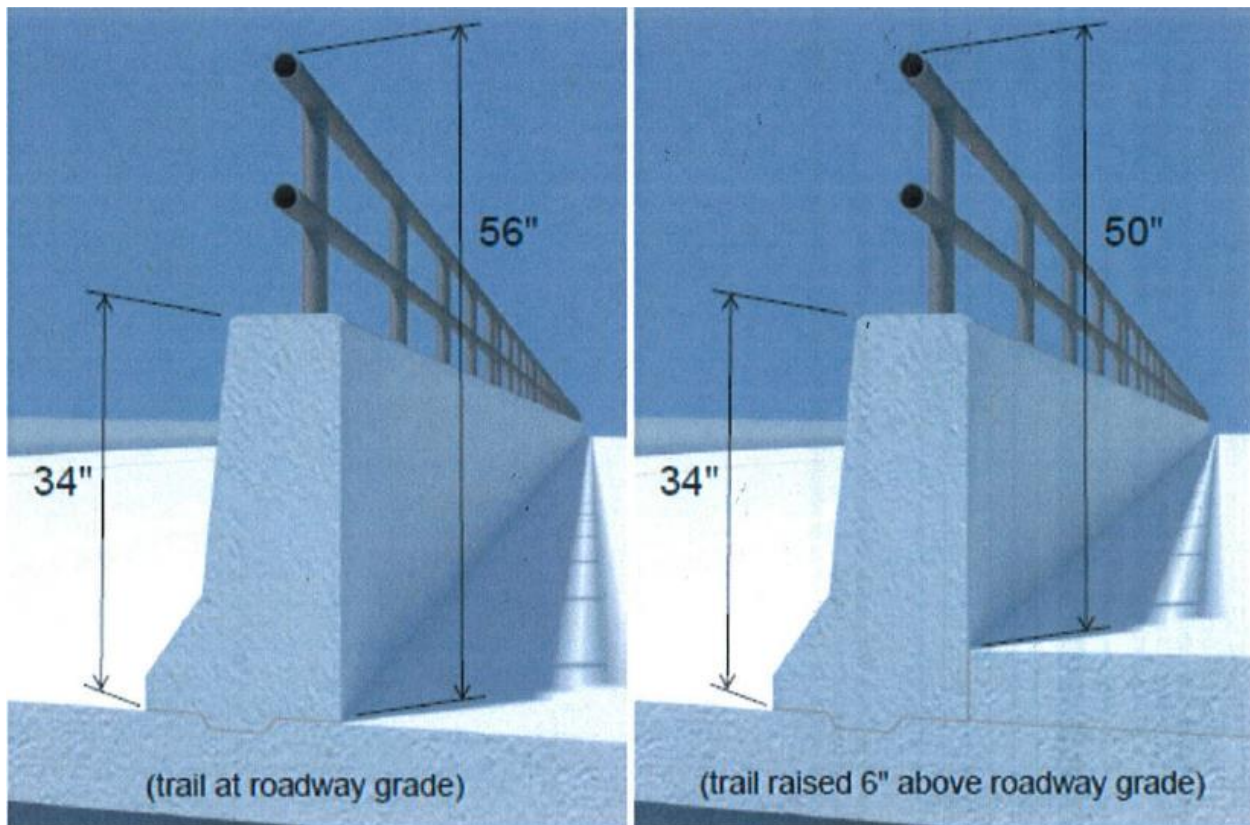


Figure 1. Iowa DOT Standard Separation Barrier (in service)

Since 1999, Iowa DOT has preferred the use of vertical-face concrete barriers for low-speed (45 mph or less) roadway bridges as separation barriers between vehicles and pedestrian facilities. The 34-in. (864-mm) tall, 10-in. (254-mm) wide vertical-face concrete barrier shape used on these projects, as shown in Figure 2, is based on a 32-in. (813 mm) tall barrier approved under NCHRP Report No. 350 for Test Level 4 (TL-4) conditions. The extra 2 in. (51 mm) of height are included to accommodate potential future bridge roadway grade raise. Vertical-face barriers are often used by transportation agencies when the total system height is 32 in. (813 mm) or less because of performance benefits like decreased vehicle rollover and reduced vehicle climbing potential. However, vertical-face barriers above 32 inches in height raise concerns over head ejection, the potential for vehicle occupant head contact with barrier components during vehicle contact with the barrier. Additionally, in urban areas, separation barriers frequently become obstructions to sight distance, which encourages designers to seek shorter height barriers for these cases.

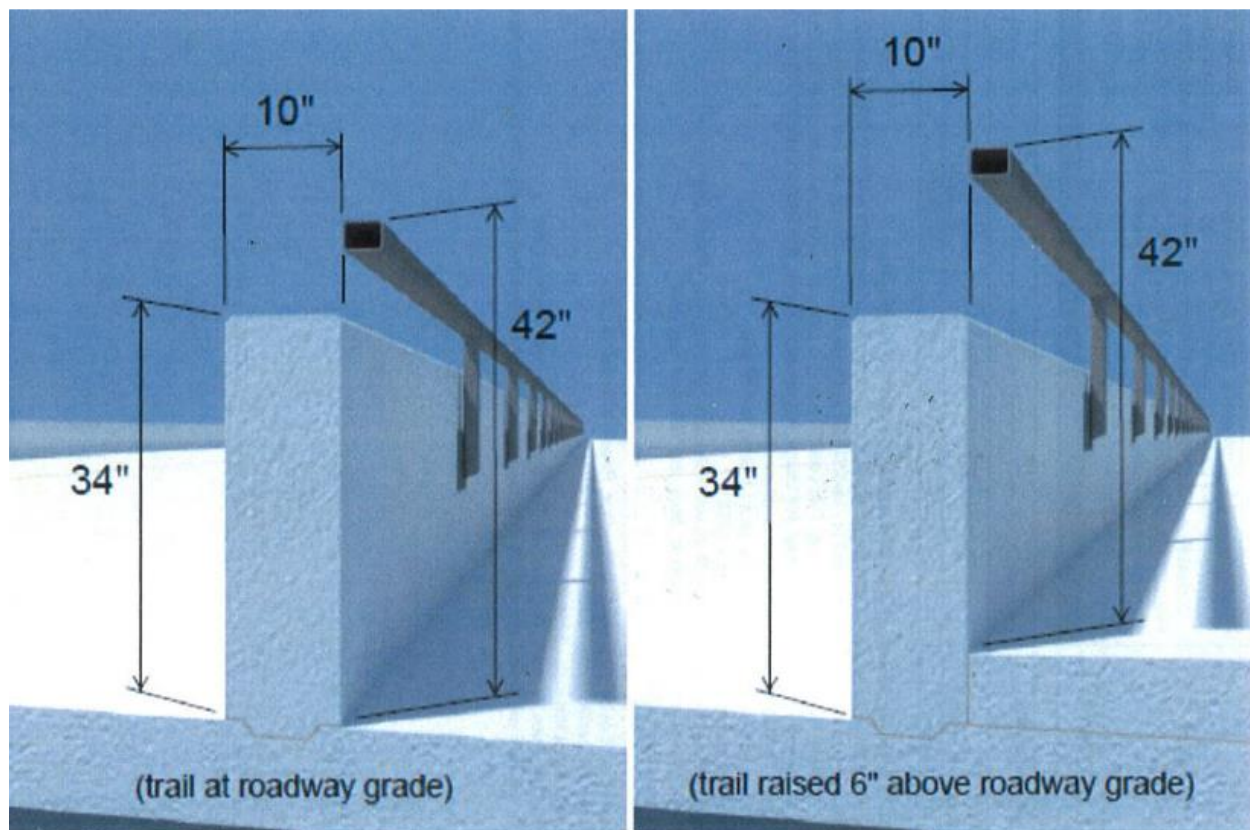


Figure 2. Iowa DOT Alternate Separation Barrier (in service)

The minimum safe height for vertical parapets under MASH 2016 criteria have not been fully evaluated and defined. Previous testing of TL-2, low-height, vertical barriers under NCHRP Report No. 350 indicated that vertical parapets as low as 20 in. (508 mm) have been acceptable. However, the increased center of gravity (CG) height of the 2270P vehicle makes the parapet height unlikely to perform as well under MASH 2016 criteria. Thus, heights greater than 20 in. (508 mm) may be necessary to meet the MASH 2016 TL-2 impact safety standards. Verification of a TL-2, low-height, vertical-face, traffic barrier with an attached bicycle railing would provide

a barrier option for projects where only a pedestrian railing is necessary and could help alleviate sight distance concerns in urban areas.

In order to meet AASHTO bicycle safety specifications, pedestrian railings must be attached to crashworthy traffic barriers and must have a minimum total height of 42 in. (1,067 mm) above the pedestrian walkway for bicyclists [1]. Because it is assumed that bicyclists will use sidewalks that do not meet minimum design criteria required for “official” bike facilities, recently-constructed roadside barriers adjacent to pedestrian walkways have had bicycle-compliant combination railings attached to them to meet the pedestrian/bicycle facility requirements without requiring excessively tall parapets.

Current Iowa DOT policy for bicycle rail attachments is based on the 1989 AASHTO *Guide Specifications for Bridge Railings* [7]. In section G2.7.1.2.2, the guide states,

“When a traffic railing is located between the roadway and a sidewalk or bikeway, the minimum height of the railing above the surface of the sidewalk or bikeway should be 24 inches and the railing should have a smooth surface to avoid snag points for pedestrians and cyclists.”

Thus, the separation bridge rail must have a minimum height of 24 in. (610 mm) relative to the sidewalk or bikeway. In addition, recent guidance from the 2014 AASHTO *LRFD Bridge Design Specifications*, 7th Edition, states that any additional pedestrian or bike combination railing mounted on the bridge rail must have a minimum height of 42 in. (1,067 mm) relative to the surface of the sidewalk or bikeway. The AASHTO specifications also provide structural loading requirements and define that the maximum allowable clear opening size for these types of railings must be small enough to prevent pass through of a 6-in. (152 mm) diameter sphere below 27 in. (686 mm) and small enough to prevent pass through of an 8-in. diameter sphere above 27 in. (686 mm). However, the opening size recommendations for bike railings are only specified for railings on the outer edge of a bikeway when highway traffic is separated from the bikeway by a traffic railing. For the project described herein, Iowa DOT is concerned with the bike railing on the separator barrier only. Thus, the combination bicycle railing would not be subject to the pass through specifications, but it would need to meet the 42 in. (1,067 mm) height relative to the surface of the sidewalk or bikeway and the structural loading requirement.

The location and design of the combination railing attachments play a crucial role in the safety performance of the total barrier system. Poorly placed and/or designed railing attachments could lead to vehicle snag, which could lead to excessive vehicle roll or occupant risk. Additionally, railings placed incorrectly could lead to an occurrence of head slap. While crashworthy traffic barriers are being used, Iowa DOT currently has no complete vehicle/pedestrian separation barrier system that is documented as fully crashworthy in accordance with NCHRP Report No. 350 [2] or AASHTO’s MASH 2016 [4]. Note that there is no difference between MASH 2009 [3] and MASH 2016 [4] criteria for longitudinal barriers such as the systems described in this project, except that additional occupant compartment deformation measurements are required by MASH 2016 when conducting full-scale crash testing.

1.2 Objective

The objective of the research project was to develop a MASH 2016 [4] TL-2 crashworthy, low-height, vertical-face, traffic barrier with an attached crashworthy bicycle railing. It was desired that the barrier be usable in standard applications as well as allow for the crashworthy bicycle railing to be added as needed. The design was to minimize the height of the concrete barrier portion of the system while providing improved visibility and sightlines. In addition, the new railing system was to comply with current AASHTO LRFD guidance for bicycle railings with respect to the parapet and combination railing [1].

1.3 Scope

The research objective was achieved by performing several tasks. First, a literature review was conducted on previous crash tests involving bicycle/pedestrian rails, systems utilizing a vertical-face and/or low-height barrier, and Zone of Intrusion (ZOI) studies. All the systems were reviewed and details were compiled to help aid in the design process. Next, a simulation and analysis effort was performed to determine the minimum parapet height that could be used in order to safely redirect the impacting vehicle, with 24 in. (610 mm) being the minimum acceptable height. Once the minimum height was determined, rail concept designs were generated and evaluated. Simulations of the preferred parapet height with the added bicycle rails were performed in order to help determine which design would provide the minimum amount of negative vehicle interaction, such as vehicle snagging and head slap, while still being cost effective. A final design was chosen and recommended for full-scale crash testing according to MASH 2016 test designation no. 2-11, which involves a 5,000-lb (2,270-kg) pickup truck impacting the combination rail at 44 mph (70 km/h) and with a 25-degree impact angle.

2 LITERATURE REVIEW

2.1 Pedestrian/Bicycle Railings

Historically, limited research has been performed on the development and crash testing of pedestrian/bicycle railings. Specifically, eight pedestrian/bicycle railings have been evaluated through full-scale crash testing and are listed in Tables 1 and 2.

The first of the previously-tested pedestrian/bicycle railings was the C411 bridge rail, as shown in Figure 3. The C411 barrier was a 42-in. (1,067-mm) tall by 12-in. (305-mm) thick reinforced concrete barrier with 6-in. (152-mm) wide by 28-in. (711-mm) high openings at 18-in. (457-mm) center-to-center longitudinal spacing [5-6]. After two full-scale crash tests, the system was determined to be acceptable according to the Performance Level 1 (PL-1) criteria established in the 1989 AASHTO *Guide Specifications for Bridge Railings* [7]. A couple of items should be noted relative to this system. First, while the height of this system meets the 42-in. (1,067-mm) minimum height for pedestrians noted in the 1989 AASHTO *Guide Specifications for Bridge Railings*, it does not have a railing attachment which could be easily grasped by an out-of-control cyclist as noted elsewhere in the guide commentary. Additionally, the 42-in. (1,067-mm) vertical height would have increased potential for occupant head slap due to its vertical face.

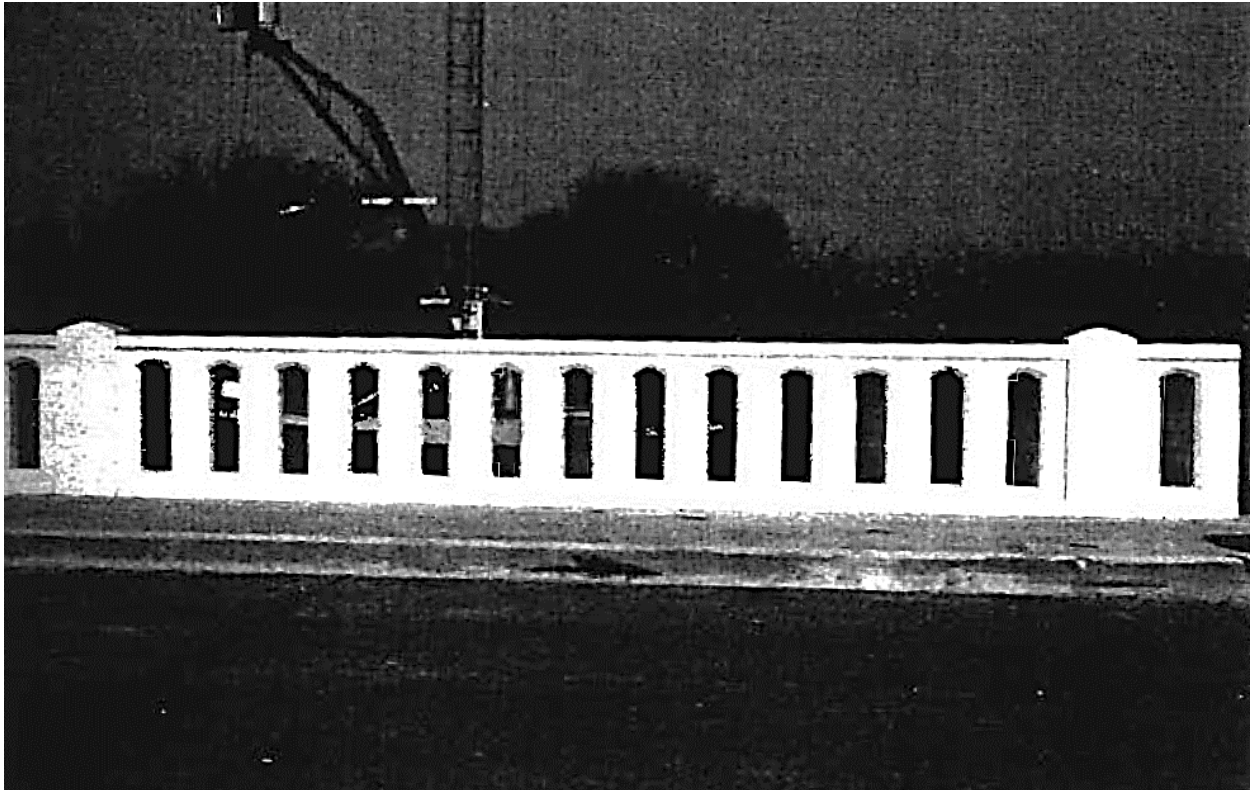


Figure 3. C411 Combination Rail [5-6]

Table 1. Previously-Tested Combination Rails

System [ref #]	Test No.	Vehicle	Test Level	Parapet Details			Railing Details		Pass/ Fail	Failure Mechanism
				Shape	Height	Width	Post	Rail		
C411 [5-6]	1185-5	Small Car	AASHTO PL-1	Vertical Aesthetic	42 in.	12 in.	None	None	Pass	None
	1185-6	Sedan							Pass	
BR27D [8-10]	7069-22	Small Car	AASHTO PL-1	Vertical mounted on sidewalk	18 in.	10 in.	4" x 4" x 3/16" A500 Grade B	4" x 4" x 1/4" A500 Grade B, 42" overall height, Two elements	Pass	None
	7069-23	Pickup		Vertical on bridge deck					Pass	
	7069-30	Small Car							Pass	
	7069-31	Pickup							Pass	
BR27C [9,11]	7069-24	Small Car	AASHTO PL-2	Vertical mounted on sidewalk	24 in.	10 in.	4" x 4" x 3/16" A500 Grade B	4" x 4" x 1/4" A500 Grade B, 42" overall height, One element	Pass	None
	7069-25	Pickup		Vertical on bridge deck					Pass	
	7069-26	SUT							Pass	
	7069-32	Small Car							Pass	
	7069-33	Pickup							Pass	
	7069-34	SUT							Pass	
Illinois 2399-1 [12]	472070-5	Small Car	AASHTO PL-1	Tubular Steel on 6" curb	25 in.	10.375 in.	2" x 3" x 3/16" Tubular steel	2" x 3" x 3/16" Tubular steel, Two elements, 54" overall height	Pass	None

Table 2. Previously-Tested Combination Rails (cont'd)

System [ref #]	Test No.	Vehicle	Test Level	Parapet Details			Railing Details		Pass/ Fail	Failure Mechanism
				Shape	Height	Width	Post	Rail		
Type 80SW [13]	541	Small Car	NCHRP 350 TL-4	Beam and Post on sidewalk	32 in.	20.7 in. @ base, 11.8 in. @ top	Tubular steel rail, 42" overall height		Pass	None
	542	Pickup							Pass	
	543	SUT							Pass	
MnDOT Combination Bridge Rail [14]	MNPD-1	Pickup	NCHRP 350 TL-4	New Jersey	32 in.	18 in. @ base, 9 in. @ top	4" x 2" x 1/8" A500 Grade B, 120" post spacing	3" x 2" x 1/8" A500 Grade B, Two elements, 54" overall height	Pass	None
	MNPD-2	SUT							Pass	
MoDOT Combination Bridge Rail [15]	MOBR-1	Pickup	NCHRP 350 TL-4	Single Slope	32 in.	Standard Single Slope	4" x 2" x 1/4" A500 Grade B, 120" post spacing	3" x 2" x 1/4" A500 Grade B, Three elements, 54" overall height	Fail	Vehicle snagged rail causing vehicle rollover
	MOBR-2	Pickup						3" x 2" x 1/4" A500 Grade B, Four elements, 54" overall height	Fail	
732SW [16]	130MAS H3P13- 01	Pickup	MASH 2009 [3] TL-3	Vertical	32 in.	9 in. @ base, 12 in. @ top	Tubular steel pedestrian handrail, 43" overall height above bridge deck		Pass	None
	130MAS H3C13- 02	Small Car							Fail	Occupant risk values exceeded limits
	110MAS H2C14- 01	Small Car	MASH 2009 [3] TL-2						Pass	None

The second system, the BR27D, as shown in Figure 4, consisted of two horizontal, tubular steel rails supported by vertical, tubular steel posts attached to a rectangular concrete barrier [8-10]. The BR27D employed an 18-in. (457-mm) tall, vertical-faced concrete parapet with an attached steel railing creating an overall height of 42 in. (1,067 mm). The system was constructed in two configurations, one with a raised concrete sidewalk and one without. Two full-scale crash tests were utilized to evaluate each configuration. The system was deemed acceptable according to AASHTO PL-1 criteria [7].

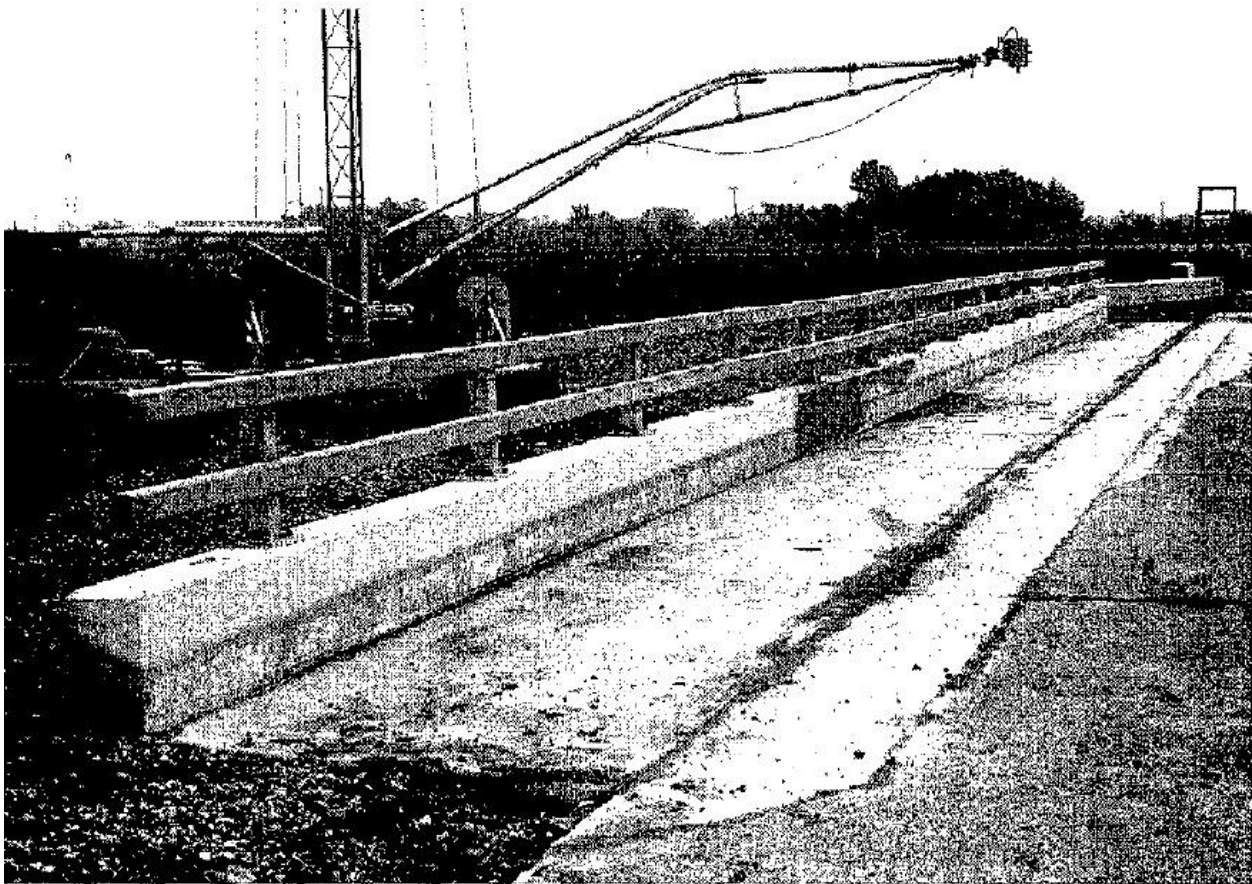


Figure 4. BR27D Bridge Railing on Bridge Deck [8]

The third pedestrian/bicycle railing, the BR27C, as shown in Figure 5, consisted of a single horizontal, tubular steel rail supported by vertical, tubular steel posts and was attached to a 24-in. (610-mm) tall rectangular concrete barrier [9,11]. The system was also constructed with and without a raised sidewalk. The BR27C was determined to be acceptable according to the AASHTO PL-2 criteria based on a total of six full-scale tests, three for each configuration [7].

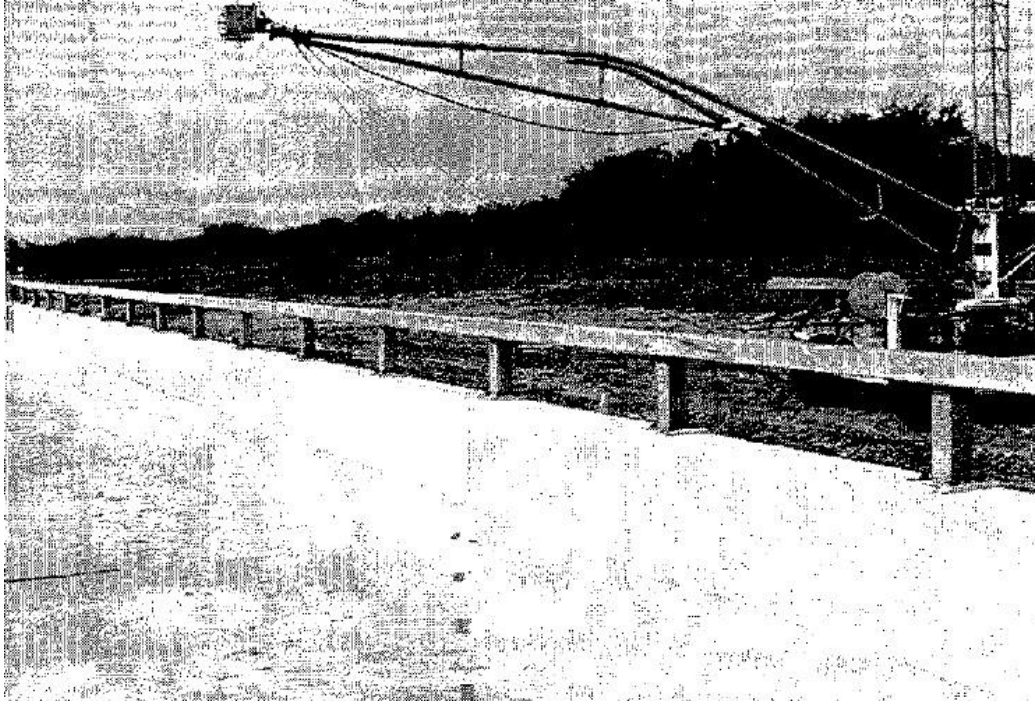


Figure 5. BR27C Bridge Railing on Bridge Deck [9]

The fourth design, as shown in Figure 6, consisted of two horizontal, tubular steel rails and vertical tubular steel posts attached to the Illinois 2399-1 traffic railing system [12]. The system was determined to be acceptable according to AASHTO PL-1 criteria based on one full-scale crash test [7].

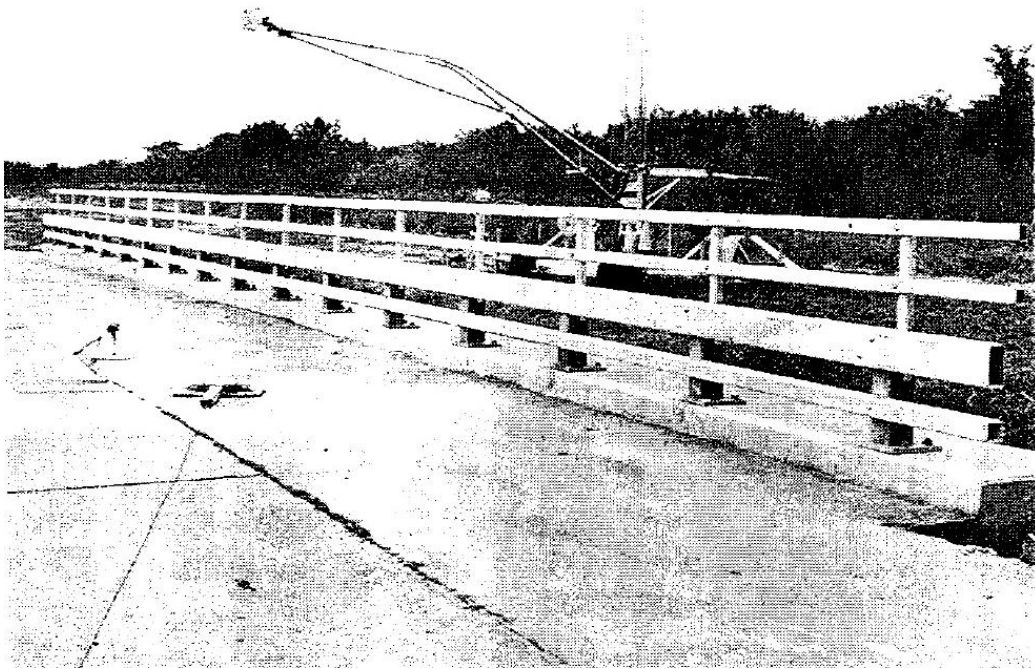


Figure 6. Illinois 2399-1 with Added Pedestrian/Bicycle Railing [12]

The fifth system, the Type 80SW, as shown in Figure 7, consisted of a single tubular pedestrian handrail mounted atop an aesthetic, open concrete bridge rail with a 8.9-in. (225-mm) tall by 59.1-in. (1,500-mm) wide sidewalk [13]. A total of four crash tests were performed on this system under NCHRP 350 TL-4 criteria, two with a small car, one with a pickup truck, and one with a single-unit truck. After testing, the system was recommended for TL-2 use due to the railing being a snagging hazard at higher speeds as well as to provide better protection for pedestrians.



Figure 7. Type 80 SW Bridge Railing [13]

The sixth pedestrian/bicycle railing, the Minnesota Combination Traffic/Bicycle Rail, as shown in Figure 8, was designed for use with the standard New Jersey safety shape bridge rail [14]. The system utilized two longitudinal, tubular steel rails with tubular, breakaway steel posts as vertical supports. One wire rope cable was strung through each longitudinal tube to prevent the railing from falling below the concrete barrier after impact. In addition, solid vertical spindles ran between the upper and lower longitudinal rails. The system successfully met the NCHRP 350 TL-4 criteria by passing full-scale crash tests with both a pickup truck and a single-unit truck.



Figure 8. Minnesota Combination Traffic/Bicycle Rail [14]

The seventh system, the Missouri Combination Rail, as shown in Figure 9, was designed to be used on a single slope concrete barrier [15]. Originally, the system consisted of a top mounted pedestrian rail that utilized three longitudinal members. This system was tested under NCHRP 350 TL-4 criteria, but did not pass as the vehicle did not remain upright during the test. The vehicle's hood engaged the horizontal members of the rail, restricting vehicle climb, and causing the vehicle to pivot around the horizontal rails. The climb restriction caused the vehicle to encounter significant roll as it exited the system, and the vehicle subsequently rolled over. The system was redesigned with a fourth longitudinal member and retested. During testing, the impacting vehicle experienced snagging, and the vehicle rolled once again.



Figure 9. Missouri Combination Rail with Four Rail Elements [15]

The eighth and final traffic/pedestrian railing, the 732SW, as shown in Figure 10, consisted of a 32-in. (813-mm) tall vertical, concrete barrier with a top-mounted pedestrian handrail and an 8-in. (203-mm) tall by 98-in. (2,489-mm) wide sidewalk [16]. After a total of three crash tests, two at TL-3 and one at TL-2, the system was determined to be acceptable for TL-2 conditions under MASH 2009 [3]. Although the 8-in. tall curb with approximately 4:1 front batter did not constitute a low-height parapet, it was believed that the curb would contribute to low-angle vehicle redirection at shallow encroachment angles.

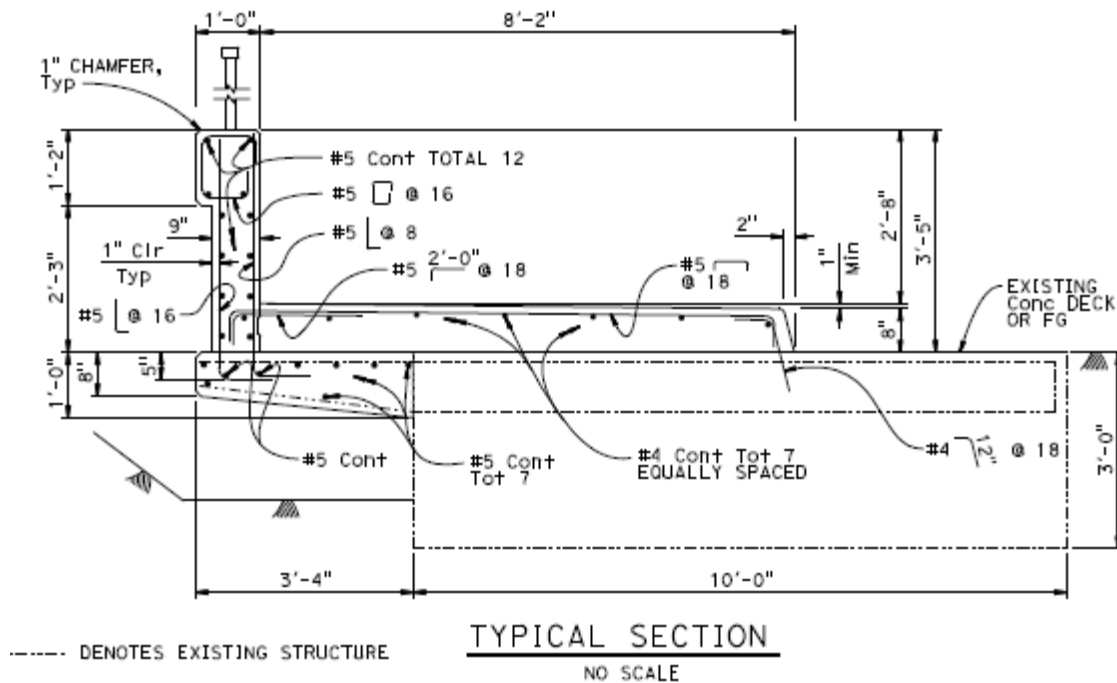


Figure 10. 732SW Bridge Rail [16]

For the reviewed systems, only the 732SW, designed by CALTRANS, was tested to MASH 2009 TL-2 criteria. The systems that were considered to be the most relevant to this project were the BR27C and BR27D as they both used low-height, vertical parapets. However, these systems are outdated as they were tested to PL-1 and PL-2 test criteria. Based on the literature review, limited guidance was gained as none of the systems closely matched the desired system.

2.2 Vertical/Low-Height Parapets

There existed a desire to determine the minimum parapet height greater than or equal to 24 in. (610 mm) that was capable of meeting the MASH 2016 TL-2 criteria. Thus, it was deemed necessary to also review the results from previously crash-tested systems that utilize vertical parapets. Systems utilizing a height lower than the standard 32 in. (813 mm) were given special attention. This review was performed to aid in determining parapet geometries that would contain the vehicle without causing rollover or override of the barrier, while producing an acceptable level of occupant risk.

Unlike safety shape barriers, which more easily allow for impacting vehicles to climb up the face of the parapet, vertical parapets do not allow for the same degree of vehicle climb. Reduced vehicle climb can result in larger vehicle deformations, higher lateral vehicle accelerations, and increased occupant risk under the same impact conditions. When using a low-height, vertical parapet, the propensity for the vehicle to roll toward the barrier increases as height decreases due to difference between the CG of the vehicle and the barrier top height. For some impacts, a CG height above the top surface of the barrier could result in excessive roll angles, complete rollover of the impacting vehicle, or vaulting over the barrier.

From the 94 full-scale crash tests found and reviewed, a total of 14 systems utilized a vertical-faced parapet with an overall height lower than 32 in. (813 mm). From these systems, none were tested according to MASH 2009 or MASH 2016 TL-2 criteria, and only seven were successfully evaluated at comparable test levels (NCHRP 350 TL-2, AASHTO PL-1). All 14 systems were able to contain and redirect impacting vehicles without exceeding roll limit or occupant risk criteria, except for the T202 barrier, which had some failures in certain test configurations. These 14 systems are summarized in Tables 3 and 4.

The number of successfully-tested, low-height systems suggests that a parapet height between 24 in. (610 mm) and 32 in. (813 mm) could provide adequate results. Further analysis was needed to select an appropriate barrier height.

2.3 Vehicle Intrusion

Previous crash tests of concrete barriers revealed a potential for pickup trucks to extend over the top of the parapet and contact structures above or behind the barrier; this lateral and vertical encroachment of the vehicle behind the top front edge of the barrier is referred to as the “Zone of Intrusion” (ZOI). Previously-tested systems and ZOI studies were reviewed to provide guidance on the proper set back of pedestrian/bicycle rails to reduce chances of negative interaction between the vehicle and railing.

Starting in 1999, researchers at MwRSF performed a comprehensive review of numerous systems to establish guidelines for placing attachments on bridge rails and median barriers [32]. It was desired to determine the ZOI of impacting vehicles on different parapet geometries so that an attachment could be placed either outside of the ZOI envelope or placed such that the negative interaction between the vehicle and attachment could be reduced to a minimum.

Table 3. Vertical/Low-Height Parapet Review Relevant System Details

System [ref. #]	Test No.	Vehicle	Test Level	Impact Conditions		Pass/ Fail	Height (in.)	Failure Mechanism	Dynamic Deflection (in.)
				Speed (mph)	Angle (deg.)				
T202 [17-19]	1179-3	Sedan	NCHRP 230	59.2	26	Pass	27	None	N/A
	418048-4	Small Car	NCHRP 350 TL-3	62.6	20.3	Fail		Occupant Compartment Crush	0
	418048-5	Small Car		62.2	20.6	Pass		None	0
	418048-6	Pickup		61.8	25.3	Pass		None	0
	441382-1	Pickup		62.8	26.1	Fail		Vehicle Rollover	0
	441382-2	Pickup		62.6	25	Pass	30	None	0
Stone Masonry Guardwall [20]	1818-5-3-87	Small Car	NCHRP 230	61.2	20.2	Pass	27	None	N/A
	1818-5-4-87	Sedan		60.8	25.3	Pass		None	N/A
	1818-5-88	Sedan		61	24	Pass		None	N/A
Modified Kansas Corral [21]	KM-1	Small Car	AASHTO PL-1	51.0	20.5	Pass	27	None	0
	KM-2	Pickup		46.6	20.0				0
Artificial Stone Concrete Median Barrier [20]	1818-7-88	Small Car	NCHRP 230	61.3	21.0	Pass	27	None	N/A
	1818-12-88	Sedan		61.5	25.0				3
Iowa Steel Temporary Barrier Rail [22]	I5-1	Pickup	AASHTO PL-2	60.6	22.5	Pass	29	None	17.6

Table 4. Vertical/Low-Height Parapet Review Relevant System Details (cont'd)

System [ref. #]	Test No.	Vehicle	Test Level	Impact Conditions		Pass/ Fail	Height (in.)	Failure Mechanism	Dynamic Deflection (in.)
				Speed (mph)	Angle (deg.)				
Nebraska Open Concrete Bridge Rail [23-25]	NEOCR-1	Pickup	AASHTO PL-1	47.7	20	Pass	29	None	0
	NEOCR-2	Pickup		45.9	20				0
	NEOCR-3	SUT	AASHTO PL-2	48.5	17.1				0.4
	NEOCR-4	SUT		51.9	16.8				1.1
	NEOCR-5	Pickup		59.8	21.7				0
	NEOCR-6	Pickup		61	20				0
	NIT-1	Pickup	NCHRP 350 TL-4	62	26.6				1
TTI Low-Profile PCB [26]	9901F-1	Pickup	NCHRP 230	44.4	26.1	Pass	20	None	5
	9901F-2	Small Car		45.7	21.3				0
BR27D [8]	7069-30	Small Car	AASHTO PL-1	51.2	20.5	Pass	18	None	0
	7069-31	Pickup		45.6	18.8				0.5
BR27C [11]	7069-32	Small Car	AASHTO PL-2	60.3	19.8	Pass	24	None	0
	7069-33	Pickup		55.3	19.6				0
Tennessee Post and Beam [27]	71991-1	Small Car	NCHRP 230	61.1	21.3	Pass	27	None	N/A
	7199-4	Pickup		61.9	25.6				N/A
Masonry wall [19]	405181-1	Pickup	NCHRP 350 TL-3	61.6	24.9	Pass	27	None	0.6
Low-Profile Concrete Bridge Rail [28]	LPBR-1	Pickup	NCHRP 350 TL-2	43.5	27.1	Pass	20	None	N/A
FDOT Low Profile TCB [29]	26-6094-001	Pickup	NCHRP 350 TL-2	42.3	25	Pass	18	None	7.5
	26-6094-002	Small Car		44	20				2.5
Rough Stone Masonry Guardwall [30-31]	RSMG-1	Pickup	NCHRP 350 TL-2	44.4	24.2	Pass	22	None	0.25
	RSMG-2	Pickup		44.4	24.2		20		4.4

From the systems reviewed by MwRSF researchers, six systems were determined to be relevant to this review. These systems all used a parapet height lower than the standard of 32 in. (813 mm) and were tested at TL-2 or higher tests levels. Details such as barrier height and maximum significant intrusion for each system are listed in Table 5. Values of vehicle intrusion were found using a combination of film and photographic analysis.

Table 5. Guidelines for Attachments-Relevant Systems [32]

Barrier Class	Barrier Name	Barrier Height (in.)	Test Level Equivalence	Vehicle	Max Significant Intrusion (in.)	Vehicle Component
Concrete with Sloped Face	Low Profile Portable Concrete Barrier	20	TL-2	small car	12	hood/fender
				pickup	28	hood/fender
	Federal Lands Modified Kansas Corral Bridge Rail	27	TL-2	small car	2	car side
				pickup	5	hood/fender
Concrete with Vertical Face	Nebraska Open Concrete Bridge Railing	29	TL-4	pickup	16	leading box corner
				pickup	14	fender/leading box corner
	Nebraska Open Concrete Bridge Rail	29	TL-2	pickup	12	hood/fender
				pickup	12	hood/fender
Concrete/Steel Combination Bridge Rails	BR27C Bridge Railing on Deck	42	TL-4	small car	0	none
				pickup	10	hood
	BR27D Bridge Railing on Deck	42	TL-2	small car	0	none
				pickup	7	hood

For these systems, the Low-Profile, Portable Concrete Barrier had the highest intrusion at a value of 28 in. (711 mm) for the pickup truck at a barrier height of 20 in. (508 mm). This barrier also had significant lateral deflections, thus the results may not directly reflect the intrusion for a rigid barrier of the same height. The Federal Lands Modified Kansas Corral Bridge Rail provided the lowest intrusion with a railing height of 27 in. (686 mm). The two combination rails, BR27C and BR27D, provided a maximum significant intrusion of 10 in. (254 mm) and 7 in. (178 mm), respectively. These two systems have an attached pedestrian/bicycle rail, so the intrusion could have been limited by that interaction, and both provided successful results with no snagging of the vehicle on the pedestrian/bicycle rail.

After reviewing all of the systems, MwRSF provided general guidelines for attachments for each test level [32]. MwRSF showed that the intrusion zone extended 12 in. (305 mm) behind the front face of the barrier and a total of 78 in. (1981 mm) above the ground line for TL-2 barriers with a height greater than 26 in. (660 mm), as shown in Figure 11. Similarly, for TL-2 barriers that

had a height lower than 27 in. (686 mm), the intrusion zone extended a total of 28 in. (711 mm) behind the front face and 78 in. (1,981 mm) above the ground line. Due to the lack of systems, the intrusion zone for the lower-height TL-2 barriers was generated from the review of the Low-Profile, Portable Concrete Barrier, which had much lower height than 27 in. (686 mm) at an overall railing height of 20 in. (508 mm).

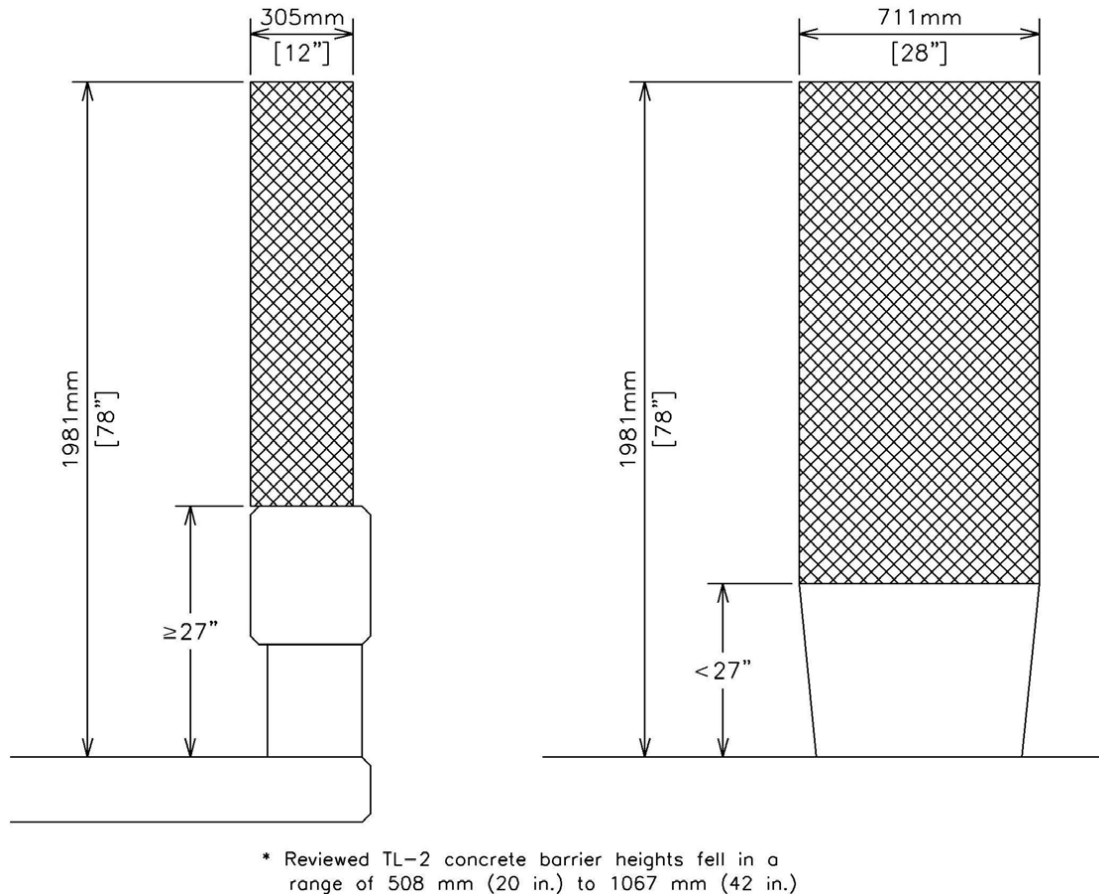


Figure 11. Intrusion Zones for Tall TL-2 Barriers ≥ 27 in. (686 mm) and for Short TL-2 Barriers < 27 in. (686 mm) [32]

Due to the lack of ZOI data for low-height systems, an appropriate rail setback could not be established without further investigation. The guidelines provided by MwRSF for systems with top parapet heights of 27 in. (686 mm) or less would require an unreasonably large rail setback if no vehicle-rail interaction was desired.

Review of previous combination rails and the ZOI guidelines provided by MwRSF suggested that vehicle interaction with the combination bicycle railing would be difficult eliminate for the low-height parapet envisioned in this research. The two reviewed combination rails experienced some interaction with the rail but did not act as a snagging hazard or become a debris hazard to the impacting vehicle or others. Therefore, a successful bicycle railing design for Iowa DOT would likewise require that the upper railing withstand vehicle contact without becoming a hazard to occupants or nearby pedestrians and bicyclists.

3 LS-DYNA MODEL CALIBRATION

3.1 Introduction

A study was performed using nonlinear, finite element analysis (FEA) to help determine a recommended height for the vertical parapet as well as help determine the extent to which the vehicle extended over the front face of the barrier to help aid in bicycle/pedestrian rail placement and design. LS-DYNA was the software used for the simulation effort [33].

3.2 Validation Effort

3.2.1 Introduction

No previously-performed simulation efforts were found of vertical-faced parapets using MASH 2009 or MASH 2016 criteria. Thus, it was determined that a validation effort was necessary in order to build confidence in any conclusions or recommendations that would be made using the results from the FEA study.

3.2.2 Background

To validate the model that was used for this research project, a TL-3 vertical-face parapet was simulated using full-scale crash test no. 490024-2-1 [34]. The system, referred to as the T222 bridge rail, was developed by researchers at Texas A&M Transportation Institute (TTI). The system utilized a 32-in. (813-mm) tall parapet that was attached to the roadway using steel anchor plates, which produced an overall system height of 32¾ in. (832 mm). The T222 system was considered the most relevant system for the validation effort on the grounds that it employed a vertical-faced parapet, was tested under MASH 2009 criteria, and used the 2270P vehicle.

During test no. 490024-2-1, the truck impacted the T222 barrier and was redirected safely. No wheel or suspension disengagement occurred, and all four tires remained inflated during the test. The barrier had a dynamic deflection of 2.1 in. (53 mm) during the test, but fully restored with no permanent set. Damage to barrier was minor and consisted of spalling, contact marks, and minor cracking.

3.2.3 Vehicle Models

The vehicle model used for the simulation effort was based off the National Crash Analysis Center (NCAC) 2270P Chevy Silverado model that had been previously modified by MwRSF personnel for roadside safety applications. The model used for this effort was the Version 3 – Reduced Silverado model (V3r). During the validation process, vehicle-to-barrier friction, steering damping, barrier properties, and vehicle tire models were all varied in order to create a model that would accurately recreate what was observed in physical testing.

- The first simulation series utilized an unmodified (default) version of the Silverado V3r model. This model is referred to as the NCAC-Unmodified model. The tire model used within the NCAC model is considered a stable option but provides less accuracy as the tire model is stiffer than measured real-world tire properties [35-36]. The vehicle model approximated wheel steering effects by modeling rotational

joints at the spindle and tie rods to allow the tire to turn and applying a damping function to movements of the steering rack and tie rods.

- The second model of the Silverado utilized a modified version of the refined tire model previously developed at UNL's MwRSF [35] with simplified geometry, and was denoted as the UNL tire model. The UNL tire model is less stiff than the default NCAC-Unmodified tire, which better-reproduces large dynamic tire deflections during impacts with curbs and bumps but has also shown some instabilities during impacts with stiff objects including guardrail posts. No changes were made to the steering system or damping function.
- The third model was a modification of the UNL model. The default steering damping function was multiplied by a scale factor of 10. The third model was denoted as UNL10x.

3.3 Baseline Models

A total of three models with varying parameters were produced for the initial modeling of test no. 490024-2-1 of the T222 bridge rail. The crash event that was simulated corresponded to the 3-11 test condition found in MASH 2016, which involves a 5,000-lb (2270-kg) pickup truck impacting at 62 mph (100 km/h) and 25 degrees. Rigid, fixed shell elements were used to model the 32-in. (813-mm) tall T222 bridge rail.

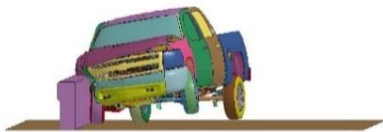
The data and results from the simulations of each of the three models were compared with physical testing based on video comparison and transducer data. The models were also compared with respect to one another in order to choose the most accurate model.

3.3.1 Results of Unmodified, Silverado V3r (NCAC-Unmodified) Simulations

The initial simulation of the low-height concrete parapet test conducted at TTI Analysis of the simulation for the T222 impacted by the NCAC-Unmodified vehicle model. Researchers determined that the unmodified version of the V3r did not adequately reproduce the redirection behavior of the vehicle during test no. 490024-2-1, as shown in Figures 12 and 13. The model exhibited large resultant pitch and roll angular displacements compared to the full-scale crash test. Yaw motions following tail slap of the barrier also diverged from the physical testing. Additionally, the front wheels of the NCAC-Unmodified model tended to steer toward the barrier, while the front wheels in test no. 490024-2-1 did not steer with respect to the vehicle.



Time = 0.000 sec



Time = 0.100 sec



Time = 0.200 sec



Time = 0.300 sec

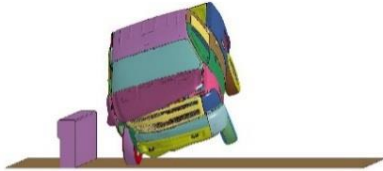
Figure 12. Downstream Sequential Views, NCAC Model and Test No. 490024-2-1



Time = 0.400 sec



Time = 0.500 sec



Time = 0.600 sec



Time = 0.700 sec

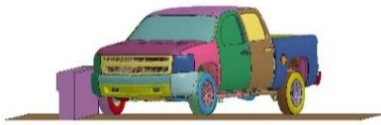
Figure 13. Downstream Sequential Views, NCAC Model and Test No. 490024-2-1

3.3.2 Refined Tire Model (UNL) Simulation

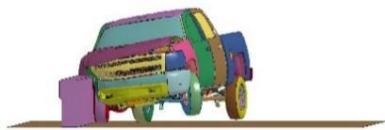
A simulation using the UNL vehicle with the refined UNL tire model was performed and analyzed. The UNL model provided a marginally better roll and pitch comparison to the full-scale test no. 490024-2-1 as compared with the NCAC-Unmodified model. Unfortunately, the yaw behavior during the simulation was still inconsistent with the test. Sequential images of the UNL simulation and full-scale test are shown in Figures 14 and 15.

3.3.3 Increased Steering Stiffness (UNL10x) Simulation

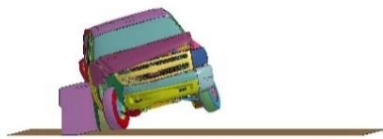
Another model using the UNL10x vehicle, which included the refined UNL tire model and increased damping on the steering system, was also performed. Analysis showed that the pitch and yaw were improved compared to the NCAC-Unmodified and UNL simulations. However, the roll observed during the UNL10x simulation was slightly worse when compared to the UNL model. Sequential images of the simulation and test no. 490024-2-1 are shown in Figures 16 and 17. The roll, pitch, and yaw comparison between the NCAC, UNL, and UNL 10x models can be seen in Figures 18 through 20.



Time = 0.000 sec



Time = 0.100 sec



Time = 0.200 sec



Time = 0.300 sec



Figure 14. Downstream Sequential Views, UNL Model and Test No. 490024-2-1



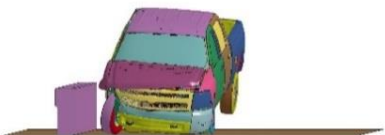
Time = 0.400 sec



Time = 0.500 sec



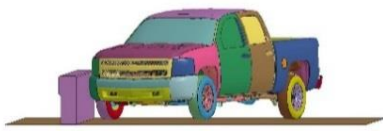
Time = 0.600 sec



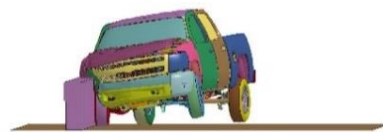
Time = 0.700 sec



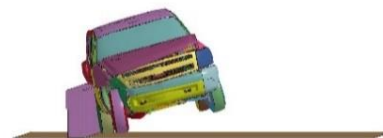
Figure 15. Downstream Sequential Views, UNL Model and Test No. 490024-2-1



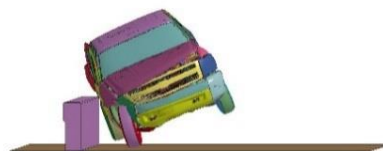
Time = 0.000 sec



Time = 0.100 sec



Time = 0.200 sec



Time = 0.300 sec

Figure 16. Downstream Sequential Views, UNL 10x Model and Test No. 490024-2-1



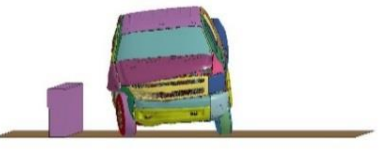
Time = 0.400 sec



Time = 0.500 sec



Time = 0.600 sec



Time = 0.700 sec



Figure 17. Downstream Sequential Views, UNL 10x Model and Test No. 490024-2-1

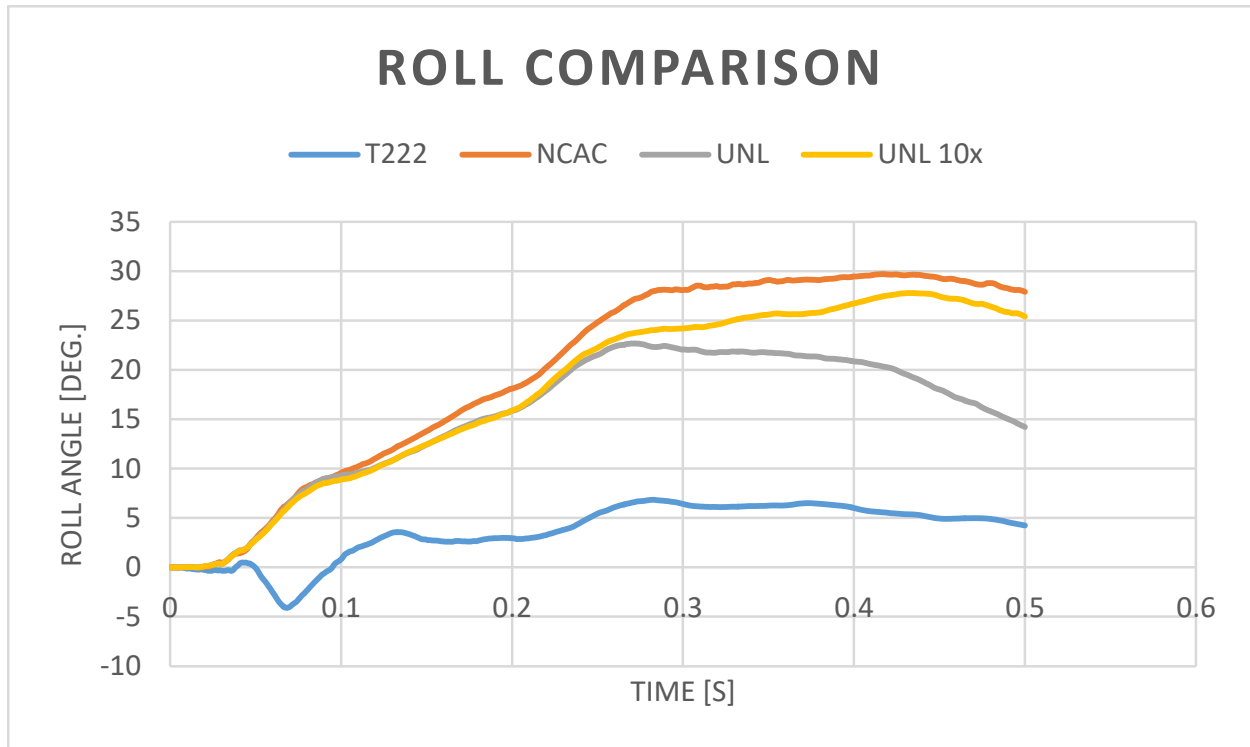


Figure 18. Roll Comparison for Modified Friction Models

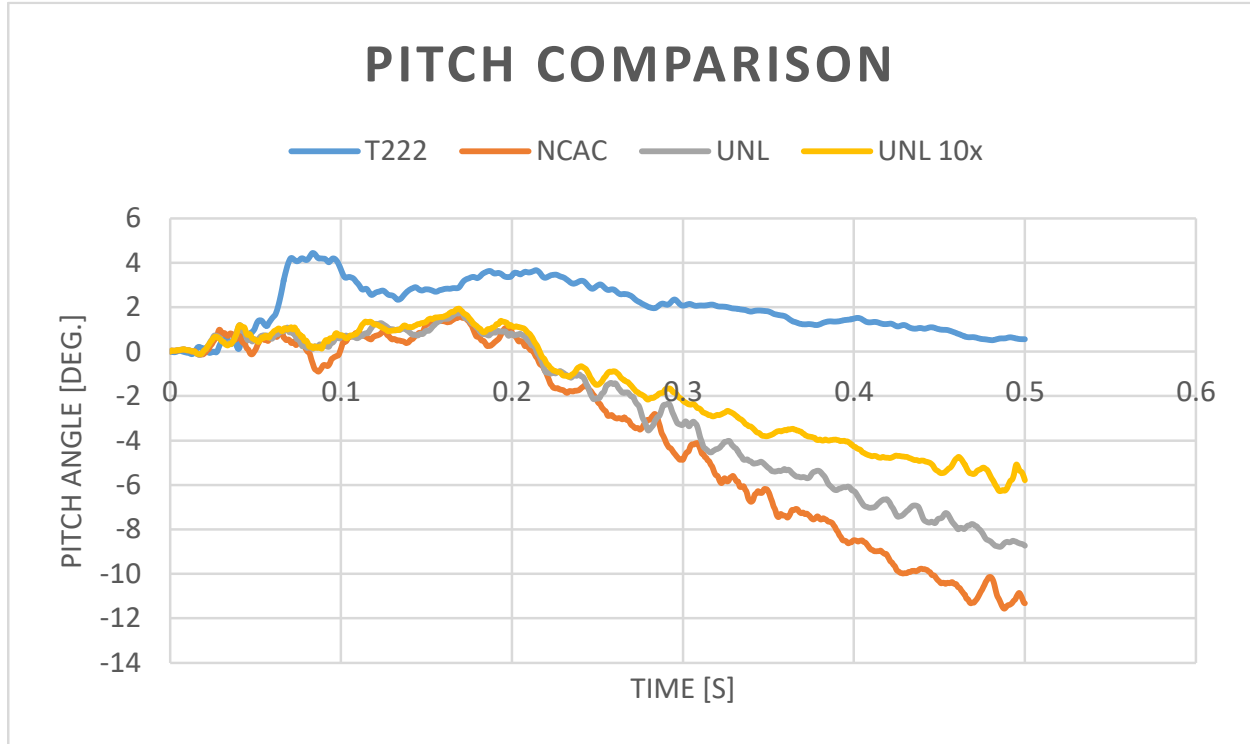


Figure 19. Pitch Comparison for Modified Friction Models

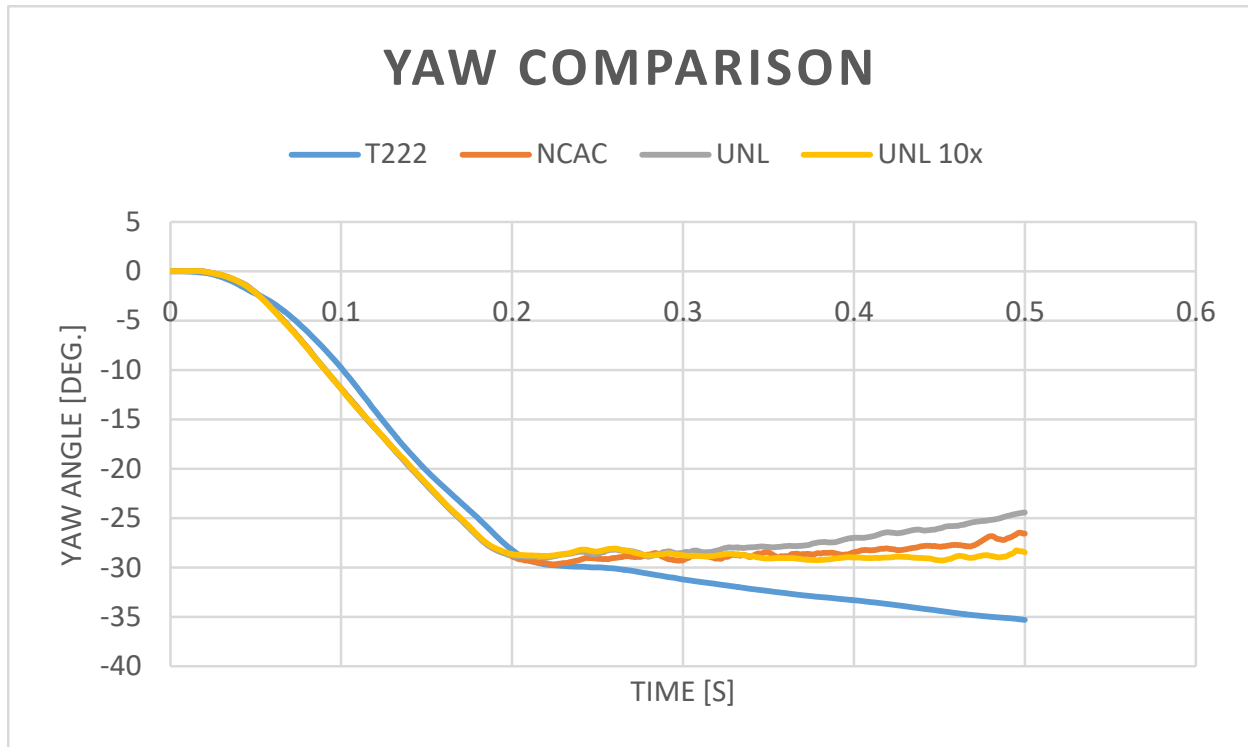


Figure 20. Yaw Comparison for Modified Friction Models

3.3.4 Initial Modeling Conclusion

The critical verification parameters used to evaluate the model were roll, pitch, and yaw angular displacements. The closest model to test results was the refined V3r model with increased steer damping (UNL10x), with the best overall pitch and yaw comparison. The refined V3r model (UNL) had improved roll behavior compared to the UNL10x, but did not match the yaw or pitch behavior as well. The unmodified V3r model (NCAC-Unmodified) had the poorest overall correlation. Therefore, researchers recommended further refinements using the UNL10x model.

3.4 Tire-Ground and Vehicle-Barrier Friction

To increase the accuracy of the simulations and improve confidence in computer simulation models, further refinements were evaluated using the UNL10x vehicle model. Three variations were explored: tire-ground friction only; vehicle-barrier friction only; and combined changes to tire-ground friction and vehicle-barrier friction. Model variations are summarized in Table 6.

A previous effort performed by MwRSF researchers showed that decreasing the tire-ground friction to a nominal value of 0.4 decreased roll and pitch angular displacements [37]. Review of the baseline models demonstrated that for all vehicle models, high tire-ground friction resulted in unexpected behaviors, including wheel hop, unusual wheel rotations, and unexpected vibrations of suspension components. Therefore, researchers reduced tire-pavement friction values from 0.9 to 0.4 to evaluate changes in vehicle reactions. The revised model was deemed UNL10xR2.

Table 6. Summary of Variational Analysis: Tire-Ground and Vehicle-Barrier Friction

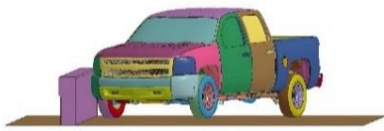
Model Name	Parameter Adjustment		Comparison to Baseline Model Results	Recommendation
	Original	Revised		
UNL10x	None (baseline)		N/A (baseline)	Use UNL10xR4 model for further analysis
UNL10xR2	Tire-Ground Friction = 0.9	Tire-Ground Friction = 0.4	Reduced unexpected vibrations in suspension & tires	
UNL10xR3	Vehicle-Barrier Friction = 0.1	Vehicle-Barrier Friction = 0.4	Improved longitudinal ΔV , slightly improved angular displacements	
UNL10xR4	Tire-Ground Friction: 0.9 Vehicle-Barrier Friction = 0.1	Tire-Ground Friction: 0.4 Vehicle-Barrier Friction = 0.4	Improved longitudinal ΔV , slightly improved angular displacements	

The reduced tire-ground friction decreased the unexpected tire and suspension deflections and vibrations. However, roll and pitch response were virtually unchanged by varying the tire-ground friction. A comparison of test no. 490024-2-1 and the UNL10xR2 simulation is shown in Figures 21 and 22.

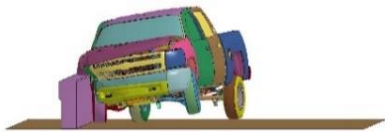
Vehicle to barrier friction was also studied in order to get a better understanding of how friction would affect the model. Previous studies had shown that modifying the vehicle to barrier friction provided significant changes to vehicle dynamics [37, 38], although no standardized values were recommended for general vehicle-barrier impact simulations. For this study, the vehicle to barrier friction was increased to 0.4 from 0.1, and the model was deemed UNL10xR3.

The UNL10xR3 simulation provided a slightly-improved roll and yaw behavior compared to the UNL10x and UNL10xR2 models, but the pitch behavior diverged from the test results. A comparison of the UNL10xR3 model and test no. 490024-2-1 is shown in Figures 23 and 24. In addition, the increase in vehicle-to-barrier friction resulted in a somewhat counterintuitive reduction in longitudinal vehicle delta-V compared to the baseline model, as shown in Figure 27.

Finally, a model that used decreased vehicle to ground friction coupled with increased vehicle to barrier friction was simulated. Analysis of the combined modified friction model, deemed UNL10xR4, had the best comparison with test data and was the preferred model. A comparison of the UNL10xR4 model and test no. 490024-2-1 is shown in Figures 25 and 26. Plots of angular displacement and longitudinal change in vehicle velocity (ΔV) are shown in Figures 27 through 30. It was determined that the UNL10xR4 simulation provided the best overall results and was chosen for further refinement.



Time = 0.000 sec



Time = 0.100 sec



Time = 0.200 sec



Time = 0.300 sec

Figure 21. Downstream Sequential Views, UNL10xR2 Model and Test No. 490024-2-1



Time = 0.400 sec



Time = 0.500 sec

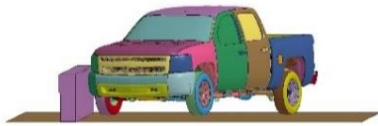


Time = 0.600 sec

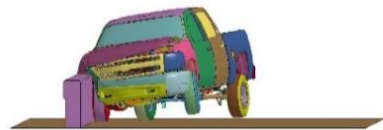


Time = 0.700 sec

Figure 22. Downstream Sequential Views, UNL10xR2 Model and Test No. 490024-2-1



Time = 0.000 sec



Time = 0.100 sec



Time = 0.200 sec

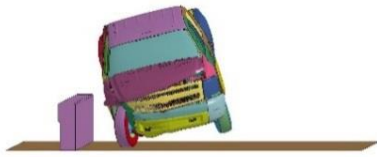


Time = 0.300 sec

Figure 23. Downstream Sequential Views, UNL10xR3 Model and Test No. 490024-2-1



Time = 0.400 sec



Time = 0.500 sec



Time = 0.600 sec

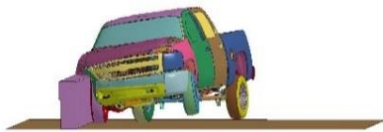


Time = 0.700 sec

Figure 24. Downstream Sequential Views, UNL10xR3 Model and Test No. 490024-2-1



Time = 0.000 sec



Time = 0.100 sec



Time = 0.200 sec



Time = 0.300 sec

Figure 25. Downstream Sequential Views, UNL 10xr4 Model and Test No. 490024-2-1



Time = 0.400 sec



Time = 0.500 sec



Time = 0.600 sec



Time = 0.700 sec

Figure 26. Downstream Sequential Views, UNL 10xr4 Model and Test No. 490024-2-1

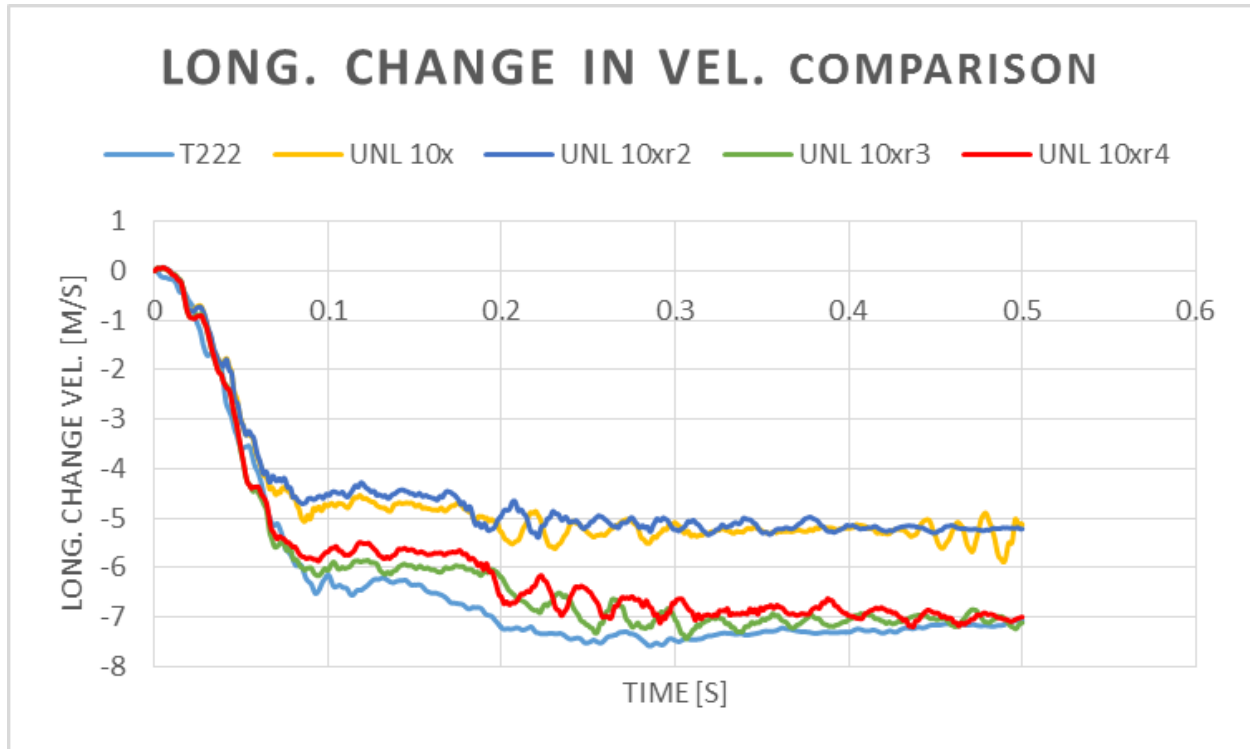


Figure 27. Longitudinal Change in Velocity Comparison for Modified Friction Simulations

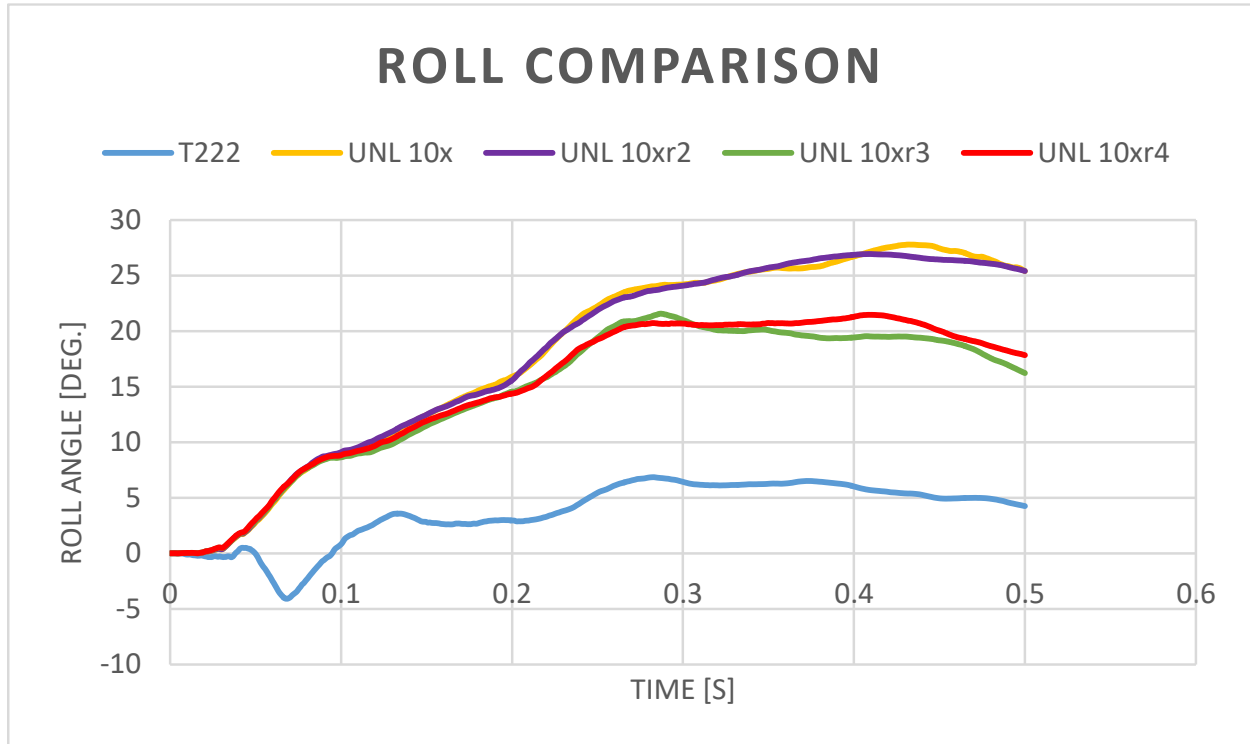


Figure 28. Roll Comparison for Modified Friction Models

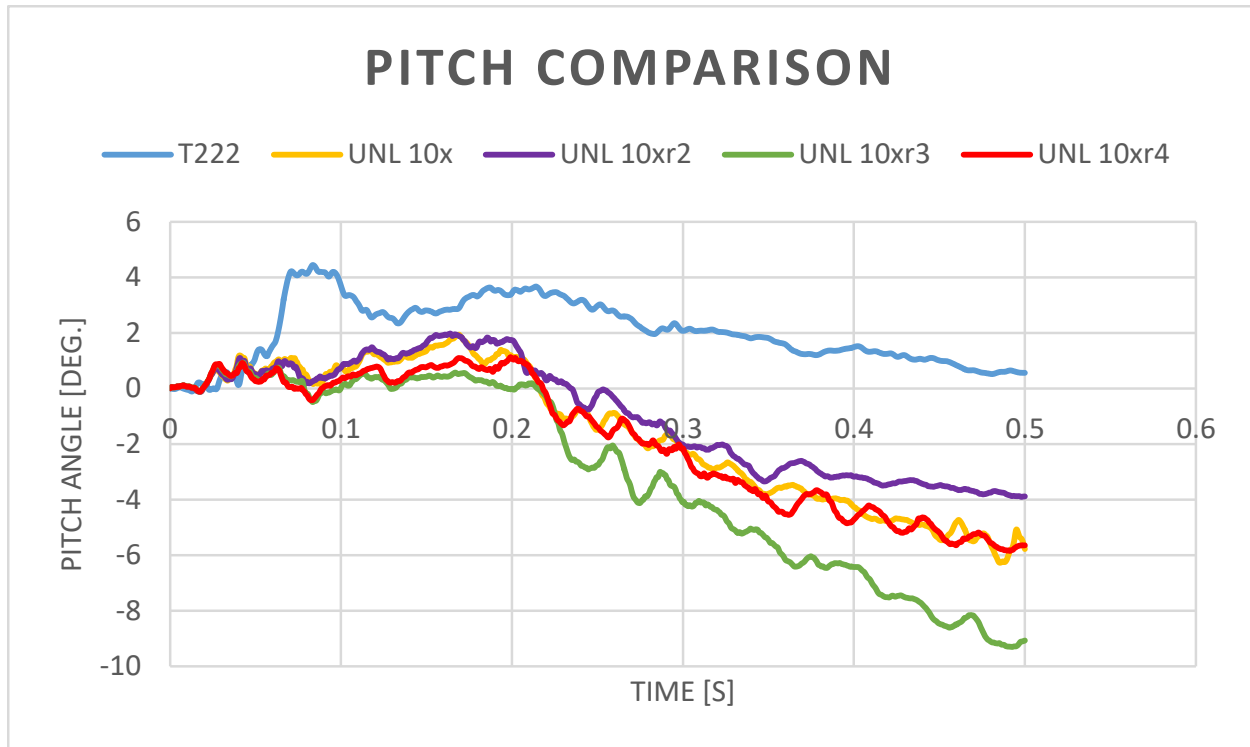


Figure 29. Pitch Comparison for Modified Friction Models

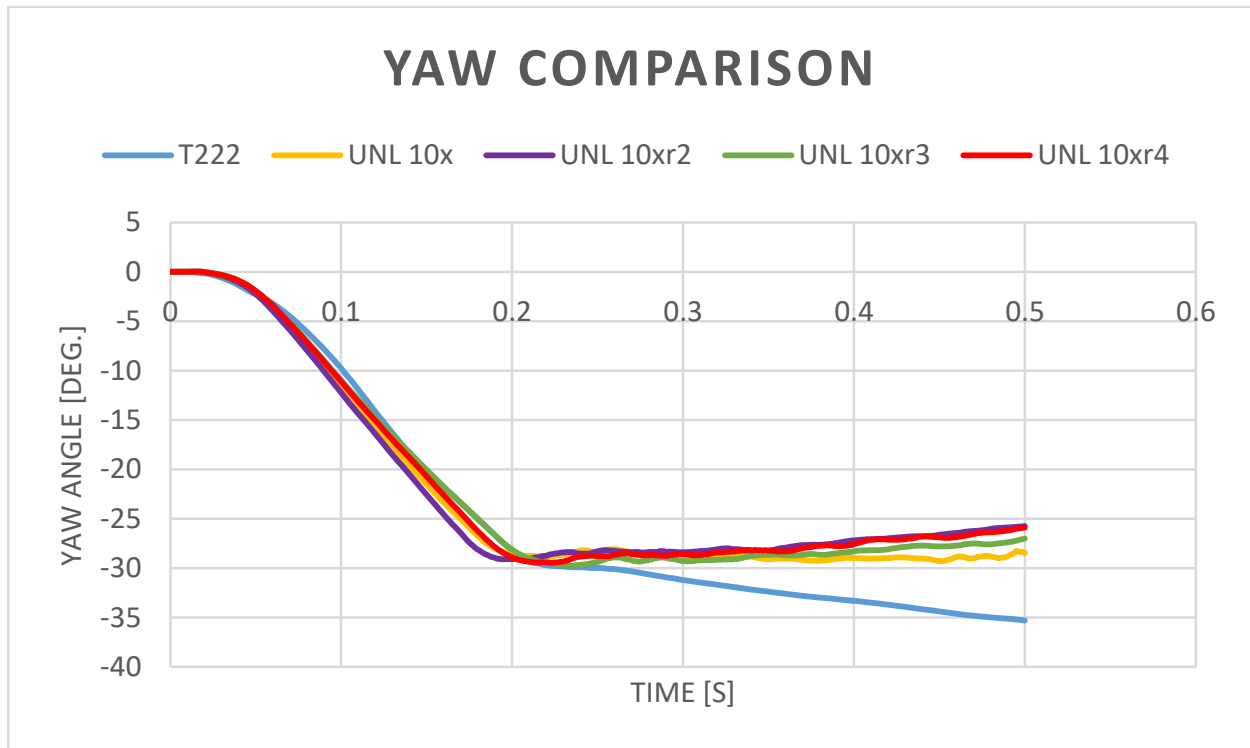


Figure 30. Yaw Comparison for Modified Friction Models

3.5 Elastic Barrier

Further exploration was conducted to determine if additional revisions could improve model behavior compared to the UNL10xR4 model. For test no. 490024-2-1, the barrier displaced laterally during impact, but all baseline simulation models utilized a rigid, immovable barrier for the analysis. Researchers attempted to model the barrier deflection by modeling the barrier as an elastic cantilever. Furthermore, because the truck model utilized rigid wheel rims and hubs, wheel-to-barrier interactions produced locally high forces and likely contributed to excessive pitch and roll behaviors. By modeling the barrier with an elastic, deformable material, rigid-rigid contact instabilities could be avoided without substantially changing vehicle model or behavior.

To model the barrier as elastic, the elements of the barrier were changed from shells to solids, and the material of the barrier was changed from MAT_RIGID to MAT_ELASTIC. Since the barrier in test no. 490024-2-1 was placed on anchor plates, which allowed the barrier to translate laterally before allowing it to flex, the exact material parameters that were needed to cause the desired deflection were unknown. Consequently, in order to replicate the dynamic deflection of the barrier, the concrete model's Young's modulus was incrementally decreased from a peak value of 29007.5 ksi (200 GPa) until the barrier deflection matched test results. An additional "soft" model was also studied to observe the effect on vehicle dynamics.

Table 7. Summary of Elastic Barrier Model Simulations

Model Name	Young's Modulus of Concrete	Barrier Dynamic Deflection
UNL10xR4	Rigid (baseline model)	0 (baseline model)
UNL10xR6	29.7 Mpsi (200 GPa)	0.005 in. (0.1 mm)
UNL10xR7	72.5 ksi (0.5 GPa)	1.1 in. (27 mm)
UNL10xR8	7.3 ksi (0.05 GPa)	7.7 in. (196 mm)
UNL10xR9	29.0 ksi (0.2 GPa)	2.3 in. (59 mm)
490024-2-1 [34]	N/A (Full-scale test)	2.13 in. (54 mm)

The UNL 10xR6 model utilized the UNL10xR4 baseline model, and modeled the concrete barrier using an elastic modulus of 29 Mpsi (200 GPa). This elastic modulus is similar to many steels. As expected, the stiff barrier experienced only small deflections and there were minimal differences to vehicle dynamics compared to the UNL10xR4 baseline model. The maximum dynamic deflection of the barrier was 0.005 in. (0.1 mm), more than 2 in. (51 mm) less than what was observed in test no. 490024-2-1.

For model UNL10xR7, the modulus of elasticity was decreased to 72.5 ksi (0.5 GPa). Decreasing the modulus of elasticity resulted in increased vehicle roll toward the barrier, while the vehicle pitch and yaw remained similar to that seen in the UNL 10xr4 baseline model. The maximum dynamic deflection of the barrier in model UNL10xR7 was 1.1 in. (27 mm), which occurred during tail slap; the maximum dynamic deflection during the initial impact was 0.7 in. (19 mm). Despite increased barrier deflection, vehicle angular displacements did not significantly improve using the softer concrete model, compared to the UNL10xR4 baseline model.

For model UNL10xR8, the modulus of elasticity was decreased to 7.3 ksi (0.05 GPa). Roll displacements significantly increased with the softer concrete model and dynamic deflections

increased to 7.7 in. (196 mm) during the initial impact, and 5.6 in. (142 mm) during tail slap. Dynamic deflection of the barrier in the UNL 10xr8 model exceeded the dynamic deflection produced during physical testing by more than 5 in. (127 mm). Overall, the softer barrier model diverged from test results and provided a poorer comparison with test data than the baseline UNL10xr4 model.

The final barrier stiffness revision was deemed UNL10xr9, and utilized a modulus of elasticity of 29.0 ksi (0.2 GPa). While the vehicle dynamics showed improvement over the UNL 10xr8 model, the model did not show an improvement over the UNL 10xr4 model. The dynamic deflection, however, compared well with the physical testing. During simulation, initial impact generated 1.8 in. (45 mm) of initial dynamic deflection followed by a 2.3 in. (59 mm) deflection during tail slap.

Results of the elastic barrier analysis are shown in Figures 31 through 33. Analysis of results showed that the increased flexure of the barrier caused divergent response. As the modulus of elasticity was decreased, an increase in vehicle roll toward the barrier was produced, as shown in Figure 31. The pitch of the vehicle was not affected to the same degree as the roll; the pitch remained relatively the same throughout the modeling, as shown in Figure 32. However, the pitch in the UNL10xr8 model showed a much larger deviation from the test data after tail slap occurred when compared to previous models, such as the UNL10xr4 model. Yaw angular displacement, as shown in Figure 33, showed little change with changing barrier stiffness.

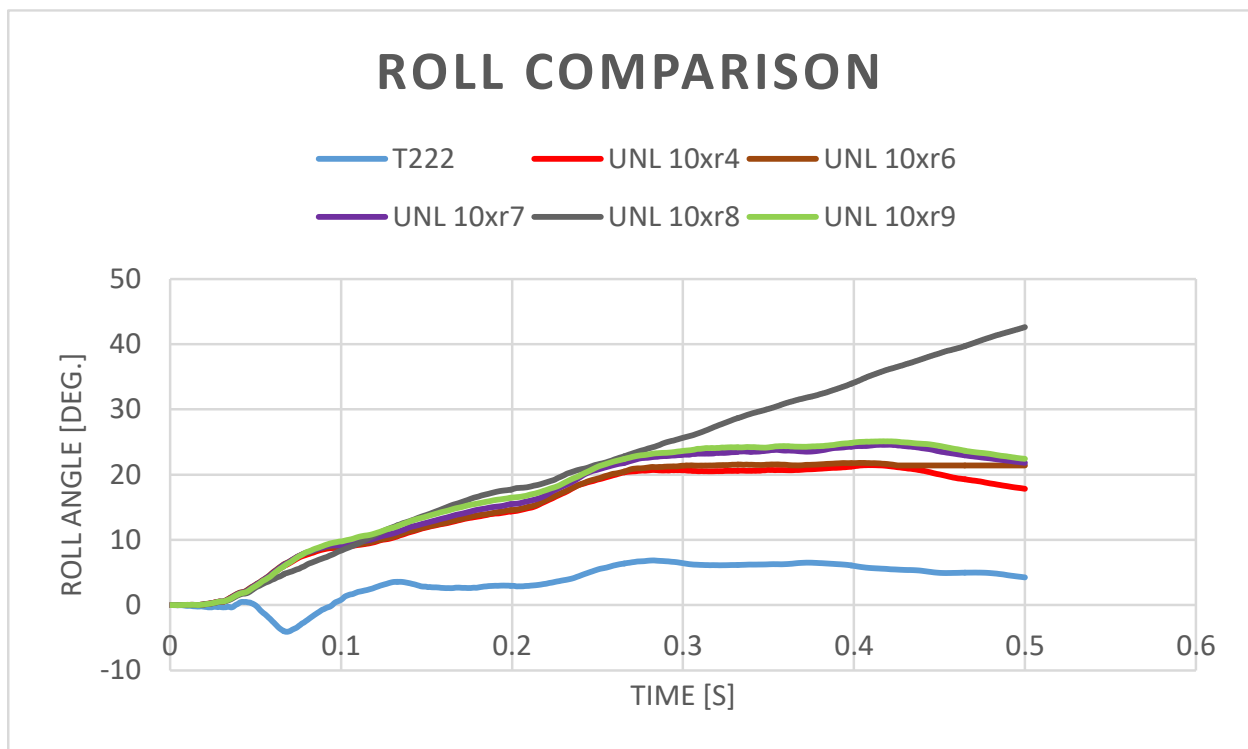


Figure 31. Roll Comparison for Elastic Barrier Models

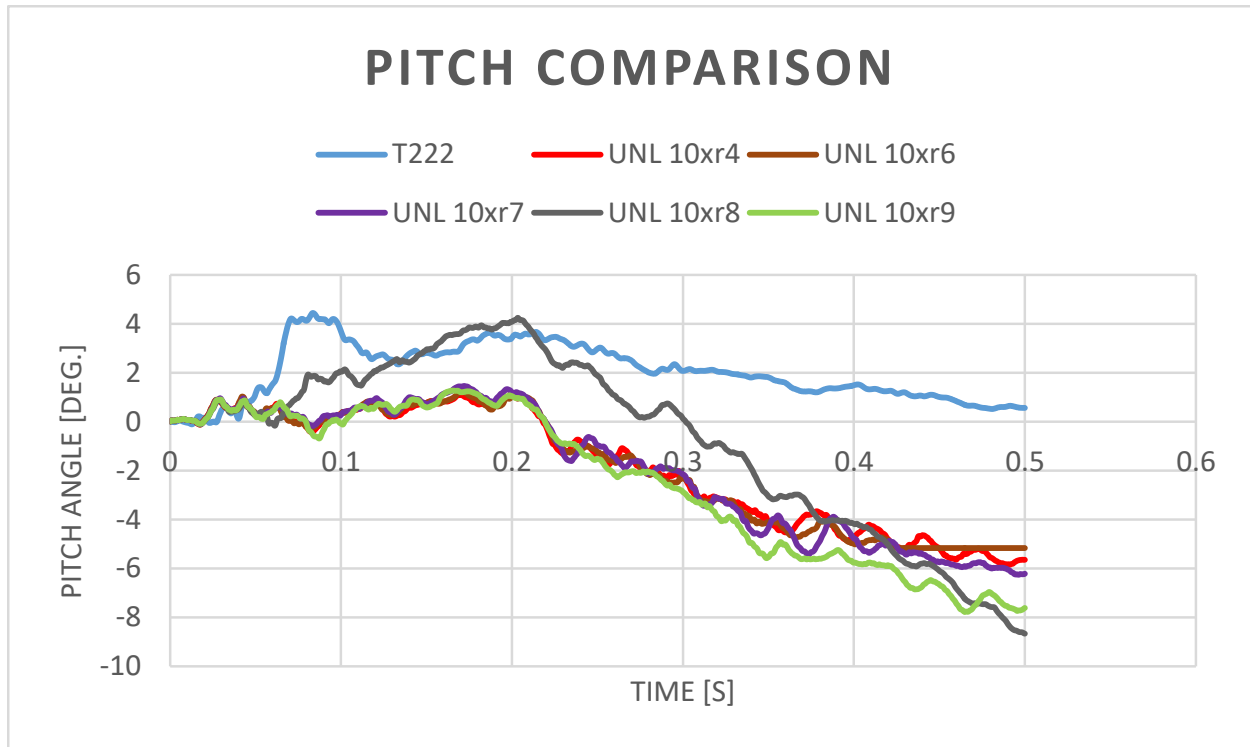


Figure 32. Pitch Comparisons for Elastic Barrier Models

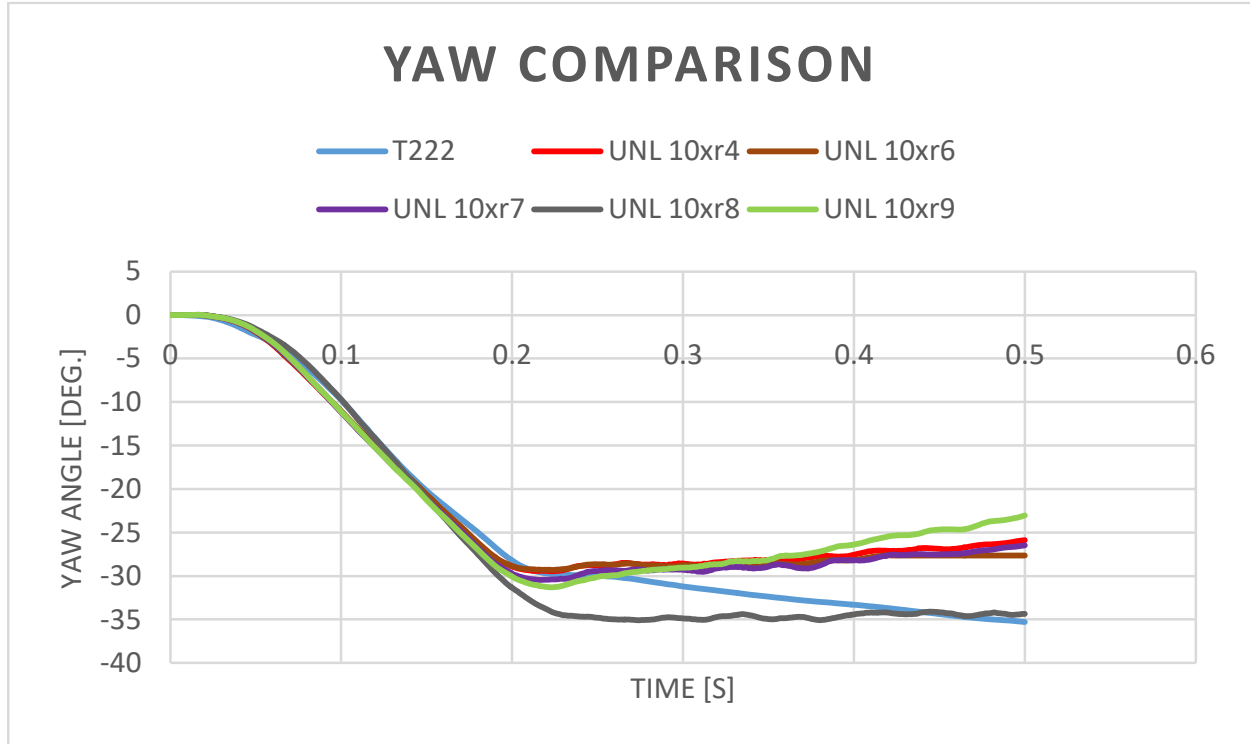


Figure 33. Yaw Comparison for Elastic Barrier Models

Another important result was the dynamic deflection increased the perpendicular wall force decreased, but were still much larger than measured values during full-scale testing. Most 2270P vehicles tested at TL-3 conditions experience an initial wall force peak ranging from 70 to 90 kips (311 to 400 kN). During test no. 490024-2-1, the wall force during initial impact reached a maximum value of 78.9 kips (351.0 kN) and produced a value of 31.4 kips (140.0 kN) during tail slap. However, every simulation experienced a wall force greater than 100 kips (444.8 kN), as shown in Figure 34. Peak dynamic deflection greater than what was experienced in the test nonetheless did not replicate measured wall forces, and tail slap was observed to be particularly high-force events in simulation and much lower-severity during testing.

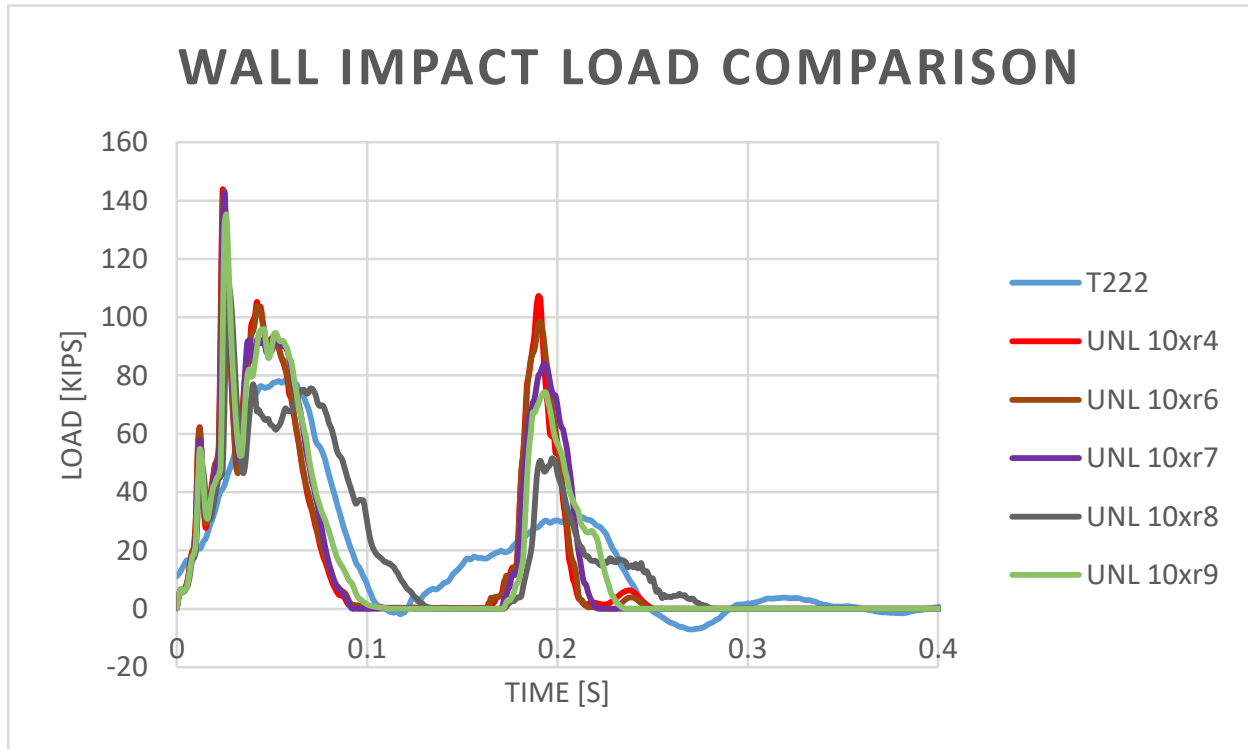


Figure 34. Elastic Barrier Simulations-Impact Forces Comparison

3.6 Conclusion

Three types of modifications were made to validate computer simulation models: changes in vehicle tire and steering stiffness; changes in tire-ground and vehicle-barrier friction; and changes in barrier elasticity. Efforts were conducted in sequence and built off of recommendations of previous steps.

It was determined that the modified V3r truck model with increased steer damping, reduced tire-ground friction (0.4), and increased vehicle-barrier friction (0.4), produced the best overall result. Elastic barrier deflections did not result in improved vehicle dynamics, but did greatly increase complexity, model run time, and computational cost compared to the UNL10xR4 model. Therefore, the UNL10xR4 model was considered validated and recommended for further exploratory simulations.

Other model refinements, which were not considered in this study but which could improve the accuracy of the simulation study, were primarily focused on improvements to the vehicle model. The truck rear axle consisted of a prismatic, solid-element, reduced-stiffness, cylindrical member connected to rigid joints at the wheel, rigid wheel hubs, and a rigid differential. This configuration likely produces rapid, stiff force transfer through the box of the vehicle and likely exacerbated roll and pitch behaviors. Other refinements to the frame, chassis, and box connections could also improve vehicle dynamics results. However, such revisions were beyond the scope of this study and would need to be validated with additional physical testing.

4 VEHICLE DIMENSION EVALUATION

4.1 Investigation of 2270P LS-DYNA Model and Test Vehicle Parameters

Simulated roll, pitch, yaw, tail slap, and longitudinal change in velocity could not be validated to the desired extent during baseline model calibration. It was determined that differences between the make, model, stiffness, and structure of the crash test vehicle and simulated vehicle model could be significant and strongly contribute to the deviations between simulation model and test results. Thus, increased roll and pitch observed during simulation may be attributed to vehicle differences rather than problems with the barrier model or impact simulation itself. Therefore, a brief investigation of the differences between the Dodge Ram 1500 Quad Cab test vehicle in test no. 490024-2-1, and the 2007 Chevrolet Silverado quad cab pickup truck vehicle was conducted.

A comparison of the dimensions measured on the Silverado model (referenced from a static equilibrium height) and the 2270P vehicle used in test no. 490024-2-1 is shown in Table 8. In general, the Silverado model is longer and wider vehicle than the truck used in testing. The CG height of the Silverado model was also 0.99 in. (25 mm) lower than the CG of the Dodge truck, and the wheel base of the Silverado model was 3 in. (76 mm) longer than the test vehicle.

Reference data was used to estimate the inertial differences between simulation and full-scale test vehicles as well [39, 40]. The pitch, roll, and yaw inertias of the Chevrolet Silverado vehicle model were higher than the Dodge Ram 1500 using the formula estimates; unfortunately, only actual inertial reference measurements were available for the Silverado and were much higher on average than the formula estimates. It is unclear what the actual inertial measurements of the test vehicle are; however, based on a comparison of estimated values from derived formulas, the Silverado vehicle model appeared to have 10% larger pitch, roll, and yaw moments of inertia than the test vehicle.

4.2 NCHRP 350 TL-2 Systems vs. 2270p

4.2.1 Purpose

While the initial simulation effort was being performed, a comparison between the NCHRP 350 2000P vehicle and MASH 2016 2270P vehicle was being performed in parallel. Due to the lack of low-height, vertical-face barriers that were crash tested to MASH 2016 TL-2 conditions, it was determined necessary to compare the 2000P and the 2270P vehicles in order to gain a better understanding of how the 2270P vehicle might perform on these particular systems. Since there were successfully-tested NCHRP 350 TL-2 systems that utilized a low-height vertical parapet, the comparison of the two vehicles was made in order to make the results of the NCHRP 350 tests more relevant for this project. The comparison was also used to create confidence in the simulation effort as well as serve as a replacement in the event the simulations did not provide reasonable results.

Table 8. 2270P vs. Silverado Model Dimensions

Vehicle Measurements	Dodge Ram 1500 from Test No. 490024-2-1 ⁽¹⁾	2007 Chevrolet Silverado LS- DYNA Model ⁽²⁾	Difference (in.)
<i>Overall Geometry (in.)</i>			
CG Height	28.5	28.64	-0.99
Length from Front Drive Wheels to CG	62.3		
Overall Length, Bumper to Bumper	223.75	230.12	6.37
Roof/Overall height	75	75.48	0.48
Height of Front of Hood	46	45.63	-0.37
Front of Hood to Front of Bumper	2.88	3.08	0.20
Bottom of Door Height	14	15.14	1.14
<i>Bumper Geometry (in.)</i>			
Bottom of Front Bumper Height	15	12.70	-2.30
Top of Front Bumper Height	26.5	30.61	4.11
Front Bumper Width	78.25	72.34	-5.91
Bottom of Rear Bumper Height	20.5	20.15	-0.35
Top of Rear Bumper Height	29	30.32	1.32
Rear Bumper Width	77.5	67.78	-9.72
<i>Wheels & Suspensions (in.)</i>			
Wheelbase	140.5	143.50	3.00
Front Bumper to Center of Front Wheel	36	39.55	3.55
Rear Bumper to Center of Rear Wheel	47.25	47.02	-0.23
Front Track Width	68.5	71.60	3.10
Rear Track Width	68	69.69	1.69
Tire Diameter	30.5	30.45	-0.05
Wheel Diameter	16	18.13	2.13
<i>Inertial Measurements (lb ft s²)</i>			
Yaw Moment of Inertia	3,595 formula Not measured	3,953 formula 4,787 experimental	10% (est)
Roll Moment of Inertia	820 formula Not measured	896 formula 774 experimental	9% (est)
Pitch Moment of Inertia	3,712 formula Not measured	4,102 formula 4,446 experimental	10% (est)

- (1) Measurements taken from References 34 and 39. Roll, pitch, and yaw inertias were calculated using formulas first derived in May/June 1989 Accident Reconstruction Journal, Vol 1 No. 3.
- (2) Measurements taken from Reference 40 and geometrical measurements of FEA model. Roll, pitch, and yaw inertias were calculated using formulas first derived in May/June 1989 Accident Reconstruction Journal, Vol 1 No. 3, and were also measured using laboratory experiments.

4.2.2 NCHRP 350 vs MASH

With the introduction of MASH 2009 came changes to the test vehicles. Specifically, the pickup truck designation was changed from 2000P to 2270P, and was associated with an increase in mass of 591 lb (270 kg). The overall length of the vehicle was increased by a total of 26 in. (660 mm) and the wheelbase was increased by 16 in. (406 mm). The CG height for the 2270P vehicle was increased by a total of 0.45 in. (11 mm) over the 2000P vehicle. Differences between the 2270P and 2000P vehicles are compiled in Table 9.

The increased mass of the 2270P vehicle implies increased impact severity when compared to the 2000P vehicle. The increased CG height suggests increased propensity for vehicle roll. However, the wider track width of the 2270P would provide the opposite result, as a wider vehicle generally provides more roll stability. Based on the overall comparison, it would be expected that the 2270P vehicle would show increased vehicle roll when compared to the 2000P vehicle, while the increased wheel base and overall length would provide the 2270P vehicle with increased pitch and possibly yaw stability.

Once the nominal dimensions of the NCHRP 350 2000P and MASH 2016 2270P vehicles were compared, a list of dimensions of 2270P vehicles from recent crash tests was compiled in order to provide a representation of the general dimensions of recently-tested vehicles. These dimensions, which are shown in Table 10, were then used to compare to vehicles and barriers used in previous NCHRP 350 tests in order to provide guidance as to how the 2270P vehicle would behave during testing of low-height parapets.

4.2.3 Test Selection and Process

During the literature search, a total of three systems were found that were considered relevant for the comparison between the 2000P and 2270P vehicles. The tests that were chosen were the first test of the Rough Stone Masonry Guardwall (RSMG-1), the second test of the Rough Stone Masonry Guardwall (RSMG-2), and testing of the Low-Profile Bridge Rail (LPBR-1) [28, 30-31]. These systems were designed and tested at MwRSF under NCHRP 350 TL-2 criteria. These three tests were chosen for the comparison due to the use of low-height, vertical-faced, barriers that were determined to be acceptable according to NCHRP 350 TL-2 conditions. Specifically, the system tested during test no. RSMG-1 had an overall height of 22 in. (559 mm), while the systems tested during test nos. RSMG-2 and LPBR-1 were 20 in. (508 mm) tall.

Once the tests were chosen, the relevant vertical dimensions of the test vehicle used for the specific test, the average of the relevant dimensions of the 2270P vehicle compiled previously, as well as the barrier dimensions were all plotted together within Microsoft Excel. Plotting these values allowed for a visual representation of the heights of the vehicles compared to the barriers to help assist in estimating how the 2270P would react to these low-height barriers.

The main goal of this process was to see which components of the 2000P vehicle were captured by a given barrier height and then compare those heights with the same components on the 2270P vehicle. If the heights were similar or the same components would be captured within the barrier height, then the likelihood of the 2270P vehicle being captured by that barrier height would be considered higher. If the components of the 2270P vehicle were not captured within the barrier height, then the chance of the vehicle being captured would be considered lower.

Table 9. 2270P vs. 2000P Details

Property	2000P	2270P	Nominal Difference	
			lb	kg
MASS, lb (kg)				
Test Inertial	4409 ± 99 (2000 ± 45)	5000 ± 110 (2270 ± 50)	+ 591	+ 270
Dummy	---	Optional		
Max. Ballast	440 (200)	440 (200)	0	0
Gross Static	4409 ± 99 (2000 ± 45)	5000 ± 110 (2270 ± 50)	+ 591	+ 270
DIMENSIONS, in. (mm)			in.	mm
Wheelbase	132 ± 10 (3350 ± 250)	148 ± 12 (3760 ± 300)	+ 16	+ 410
Front Overhang	31 ± 4 (800 ± 100)	39 ± 3 (1000 ± 75)	+ 8	+ 200
Overall Length	211 ± 10 (5350 ± 250)	237 ± 13 (6020 ± 325)	+ 26	+ 670
Overall Width	---	78 ± 2 (1950 ± 50)	---	
Hood Height	---	43 ± 4 (1100 ± 75)	---	
Track Width	65 ± 6 (1650 ± 150)	67 ± 1.5 (1700 ± 38)	+ 2	+ 50
CENTER OF MASS LOCATION, in. (mm)			in.	mm
Aft of Front Axle	55 ± 6 (1400 ± 150)	63 ± 4 (1575 ± 100)	+ 8	+ 175
Above Ground (minimum)	27.55 (700)	28.0 (710)	+ 0.45	+ 10
LOCATION OF ENGINE	Front	Front		
LOCATION OF DRIVE AXLE	Rear	Rear		
TYPE OF TRANSMISSION	Manual or Automatic	Manual or Automatic		
OTHER				
	Regular Cab	Quad Cab		
	2wd	2wd		
	Conventional Bed	Conventional Bed		
	½ Ton (1500) or ¾ Ton (2500)	½ Ton (1500)		

Table 10. 2270P Test Vehicle Dimensions

Property	ILT-1 (in.) [41]	MGSL-1 (in.) [42]	MGSL-2 (in.) [42]	34AGT-1 (in.) [43]	MSPBN-1 (in.) [44]	Average (in.)
Front Bumper Width	76.5	78.0	78.0	77.6	79.1	77.9
Roof/Overall height	74.6	75.5	76.0	73.3	74.4	74.7
Overall Length, Bumper to Bumper	229.3	228.0	227.4	229.3	229.3	228.6
Rear Bumper to Center of Rear wheel	48.9	47.0	48.1	48.7	48.1	48.2
Wheel Center to Center Length	139.9	140.4	140.2	140.2	140.2	140.2
Front Bumper to Center of Front Wheel	39.4	40.6	39.0	40.1	41.3	40.1
Bottom of Front Bumper Height	9.1	14.0	13.0	6.4	8.6	10.2
Top of Front Bumper Height	28.0	27.5	29.1	29.3	27.1	28.2
Bottom of Rear Bumper Height	20.0	21.3	21.4	20.4	19.5	20.5
Top of Rear Bumper Height	30.2	29.6	30.2	30.0	29.0	29.8
Front Track Width	69.1	68.1	68.1	68.3	67.0	68.1
Rear Track Width	68.3	68.0	68.1	67.8	67.8	68.0
Height of Front of Hood	46.7	45.5	47.1	44.5	46.1	46.0
Front of Hood to Front of Bumper	4.5	4.0	3.3	4.5	4.8	4.2
Tire Diameter	33.0	32.2	32.2	31.3	31.7	32.1
Wheel Diameter	21.6	18.5	21.5	18.5	18.5	19.7
Bottom of Door Height	14.4	16.3	16.5	13.5	14.0	14.9
Rear Bumper Width	77.2	75.2	75.4	77.0	80.5	77.1
CG Height	28.4	28.7	29.7	28.0	28.4	28.6

4.2.4 Results

During analysis of the three test comparisons, all three NCHRP 350 TL-2 tests were able to capture the center of the wheels, the bottom of the door, and bottom of the bumper within the barrier height, as shown in Figures 35 through 37. When looking at those same components on the 2270P vehicle, it was clear that the same components were also captured within the heights of the barriers. Results also found that the bottom of bumper and bottom of door height of the 2270P vehicle were not only captured, but were captured at a lower height than the 2000P vehicle. Since the bottom of the bumper is lower than that of the bumper on the 2000P vehicle, this result simply means that a greater portion of the bumper was captured by the barrier. The same can be applied to the bottom of the door. Since the bottom of door height is lower on the 2270P vehicle, more of the vehicle will be captured by the barrier. Capturing more of the vehicle and at lower heights than the 2000P vehicle creates confidence that a test using the 2270P vehicle would be successful purely based on these dimensions. When looking at the center of wheel height, 2270P vehicles show a maximum difference in height of 2 in. (51 mm) above the 2000P vehicle. The center of the wheel was captured within the barrier height, but the increased height suggests a less stable response from the 2270P vehicle.

It was observed that the CG height was higher for the 2270P vehicle than it was for 2000P vehicle in all the chosen tests. In general, this result was expected as MASH 2016 criteria for the 2270P vehicle sets the nominal CG height higher than that used for the NCHRP 350 2000P vehicle. Due to the 2270P vehicle's increased CG height, it would be expected that the 2270P vehicle would show a higher tendency to roll as it impacted the barrier.

4.2.5 Conclusion

Based on the comparison between the 2200P and 2270P vehicles, it was determined there was a high probability of the 2270P vehicle being captured by low-height parapets. The only result that would negatively affect the parapet's ability to capture the vehicle was that the CG height of the 2270P vehicle was higher than that of the 2000P, though only by 0.5 in. (13 mm). The fact that the same components captured on the 2000P vehicle were also captured on the 2270P vehicle provides confidence that the 2270P vehicle would likely be captured. While the results of this comparison provided promising results, it is important to note that this comparison did not take into account the difference between the vehicles' masses. The effect of the additional mass of the 2270P vehicle was not quantified.

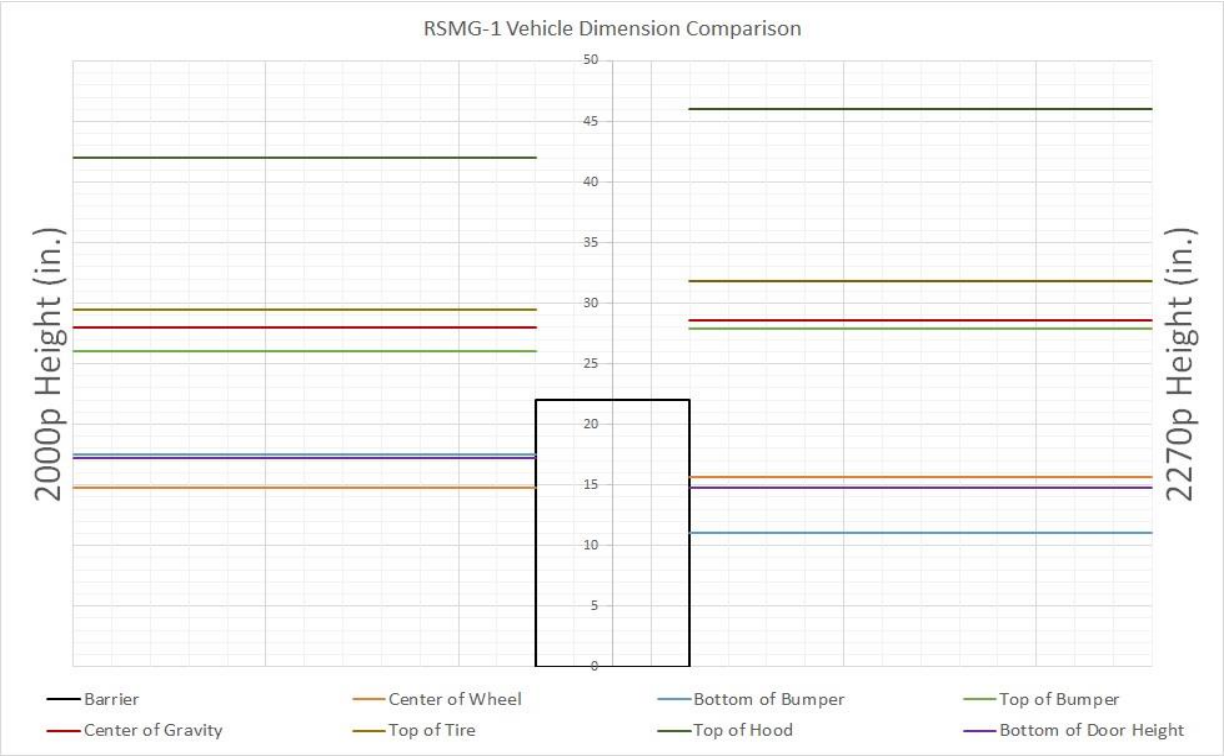


Figure 35. RSMG-1 Vehicle Dimension Comparison

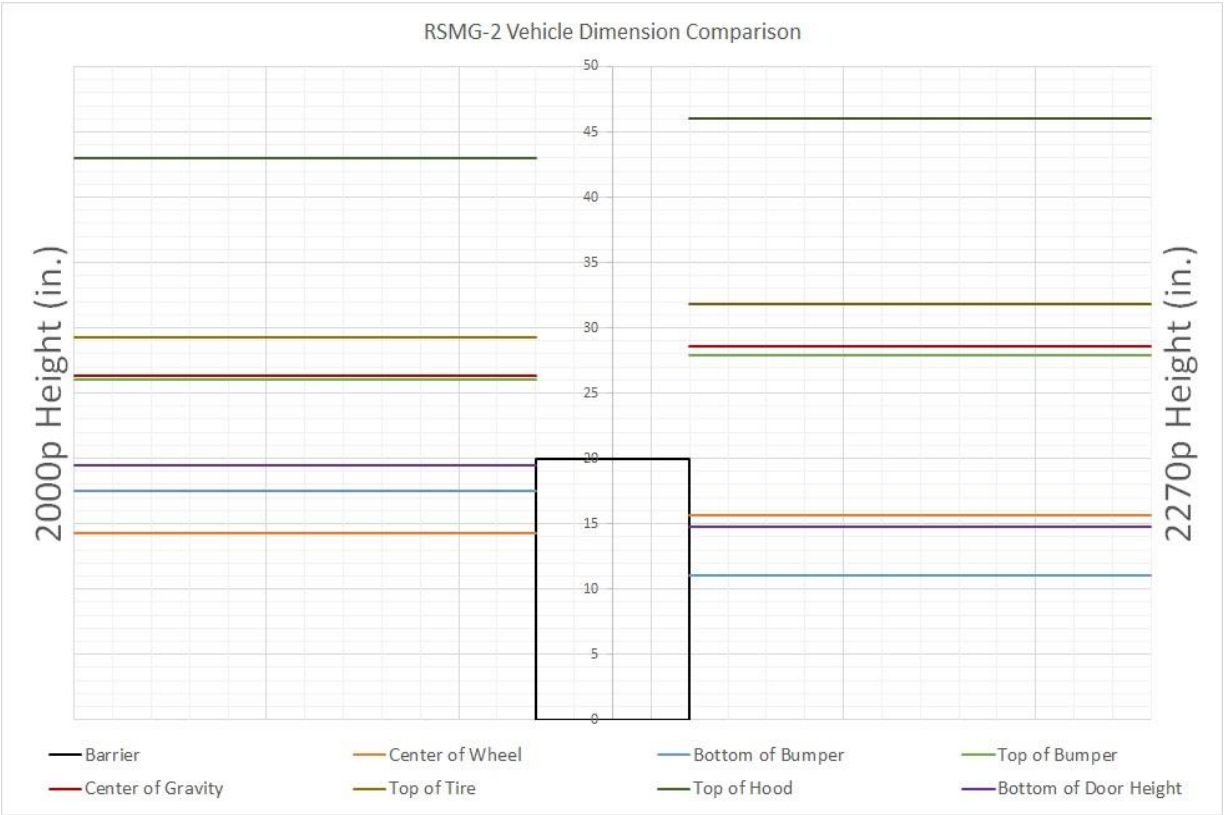


Figure 36. RSMG-2 Vehicle Dimension Comparison

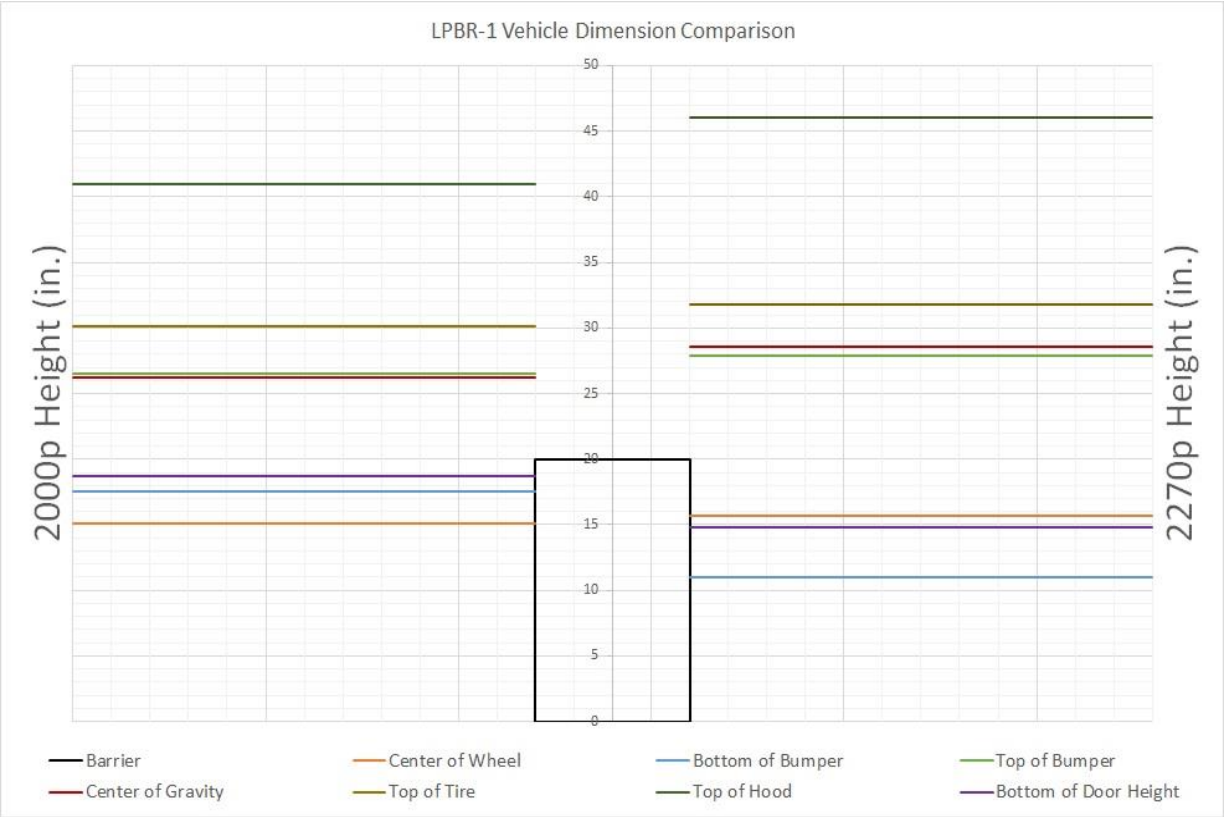


Figure 37. LPBR-1 Vehicle Dimension Comparison

5 INVESTIGATION OF BARRIER HEIGHT

5.1 Simulation Methods

Researchers conducted simulations to investigate rail height effects on vehicle stability during impact. The UNL10xR4 model was modified with different rigid, vertical parapet top rail heights, ranging from 24 to 27 in. (610 to 686 mm). The impact conditions were simulated according to MASH 2016 test designation no. 2-11, consisting of a 5,000-lb (2270-kg) pickup truck impacting the barrier at 44 mph (70 km/h) and at a 25-degree angle. Vehicle roll angle and stability, Zone-of-Intrusion (ZOI) protrusion, and vehicle redirection were evaluated to determine the adequacy of the low-height parapet to redirect the vehicle.

5.2 Simulated Evaluation of Minimum Barrier Height

5.2.1 24-in. (610-mm) Barrier Height Simulation

The first simulation involved a 24-in. (610-mm) barrier height. During simulation, the vehicle impacted the barrier and was redirected without overriding the barrier or rolling over, as shown in Figure 38. The lateral extents of protrusion and associated vertical coordinates of the bumper, fender, and box are shown in Table 11. The maximum lateral extent occurred at the tail end of the box, and was equal to 14.8 in. (376 mm) at a height of 44.8 in. (1,138 mm) above the ground line during tail slap. The ZOI envelope for the 24-in. (610-mm) barrier height simulation is shown in Figure 39.

Table 11. ZOI Values for MASH 2-11 Simulation: 24-in. (610-mm) Tall, Rigid Vertical Parapet

Vehicle Component	Maximum Lateral Protrusion ⁽¹⁾	Height of Protruding Element ⁽¹⁾
Bumper	13.6 in. (345 mm)	33.3 in. (846 mm)
Fender & Headlight	14.6 in. (371 mm)	43.9 in. (1,115 mm)
Rear Corner of Box	14.8 in. (376 mm)	44.8 in. (1,138 mm)

(1) Datum reference for ZOI measurement corresponds to the leading edge of the barrier at roadway height.

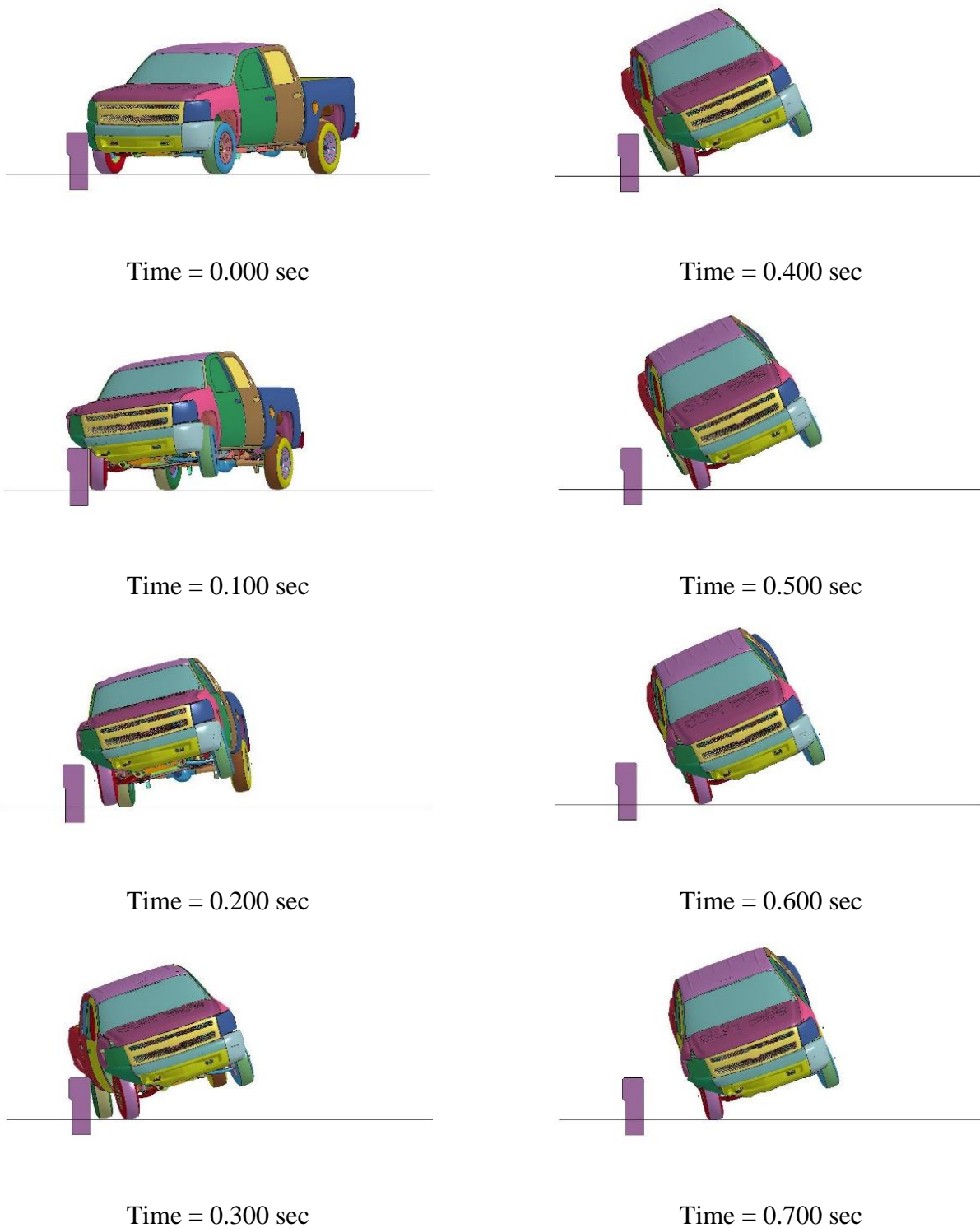


Figure 38. Downstream Sequential View, 24-in. (610-mm) Tall Barrier Simulation

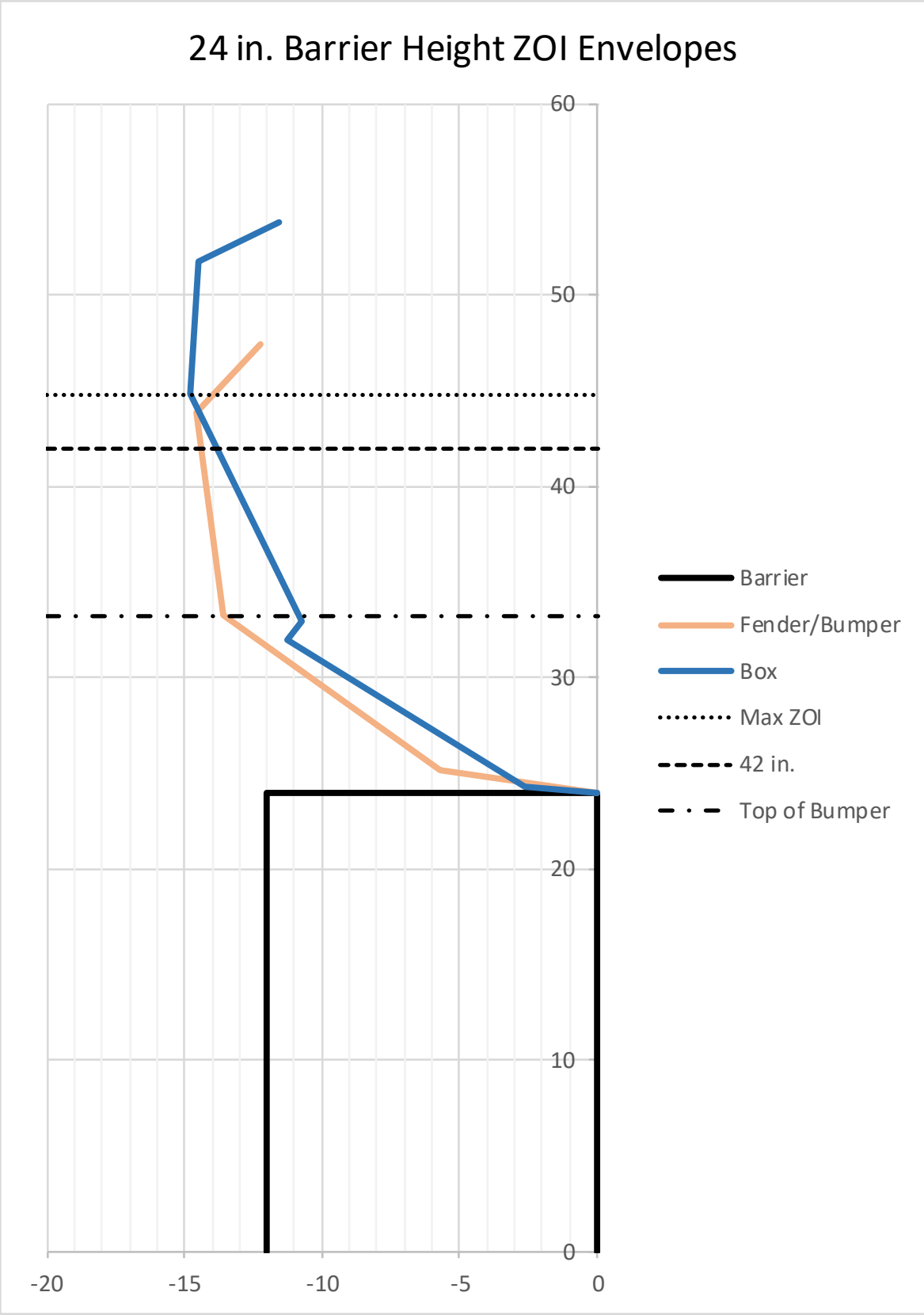


Figure 39. 24-in. (610-mm) Barrier Height Simulation ZOI Envelope

5.2.2 25-in. (635 mm) Barrier Height Simulation

The next simulation used a barrier with total overall height of 25 in. (635 mm). Similar to the 24-in. (610-mm) barrier height simulation, the Silverado model impacted the barrier and was redirected, as shown in Figure 40. No override or excessive vehicle roll, pitch, or yaw were observed during simulation. When using a 25-in. (635-mm) barrier height, the front bumper reached a maximum ZOI of 10.3 in. (262 mm) at a height of 32.2 in. (818 mm) over the ground line. The maximum ZOI of the vehicle over the rail occurred at the box, and was equal to 14.1 in. (358 mm) at a height of 50.4 in. (1,279 mm) above the ground line. The lateral extents of protrusion and associated vertical coordinates of the bumper, fender, and box are shown in Table 12. The ZOI envelope for the front end of the vehicle as well as the box during the 25-in. (635-mm) barrier height simulation is shown in Figure 41.

Table 12. ZOI Values for MASH 2-11 Simulation: 25-in. (635-mm) Tall, Rigid Vertical Parapet

Vehicle Component	Maximum Lateral Protrusion ⁽¹⁾	Height of Protruding Element ⁽¹⁾
Bumper	10.3 in. (262 mm)	32.2 in. (818 mm)
Fender	13.1 in. (333 mm)	44.0 in. (1,118 mm)
Rear Corner of Box	14.1 in. (358 mm)	50.4 in. (1,279 mm)

(1) Datum reference for ZOI measurement corresponds to the leading edge of the barrier at roadway height.

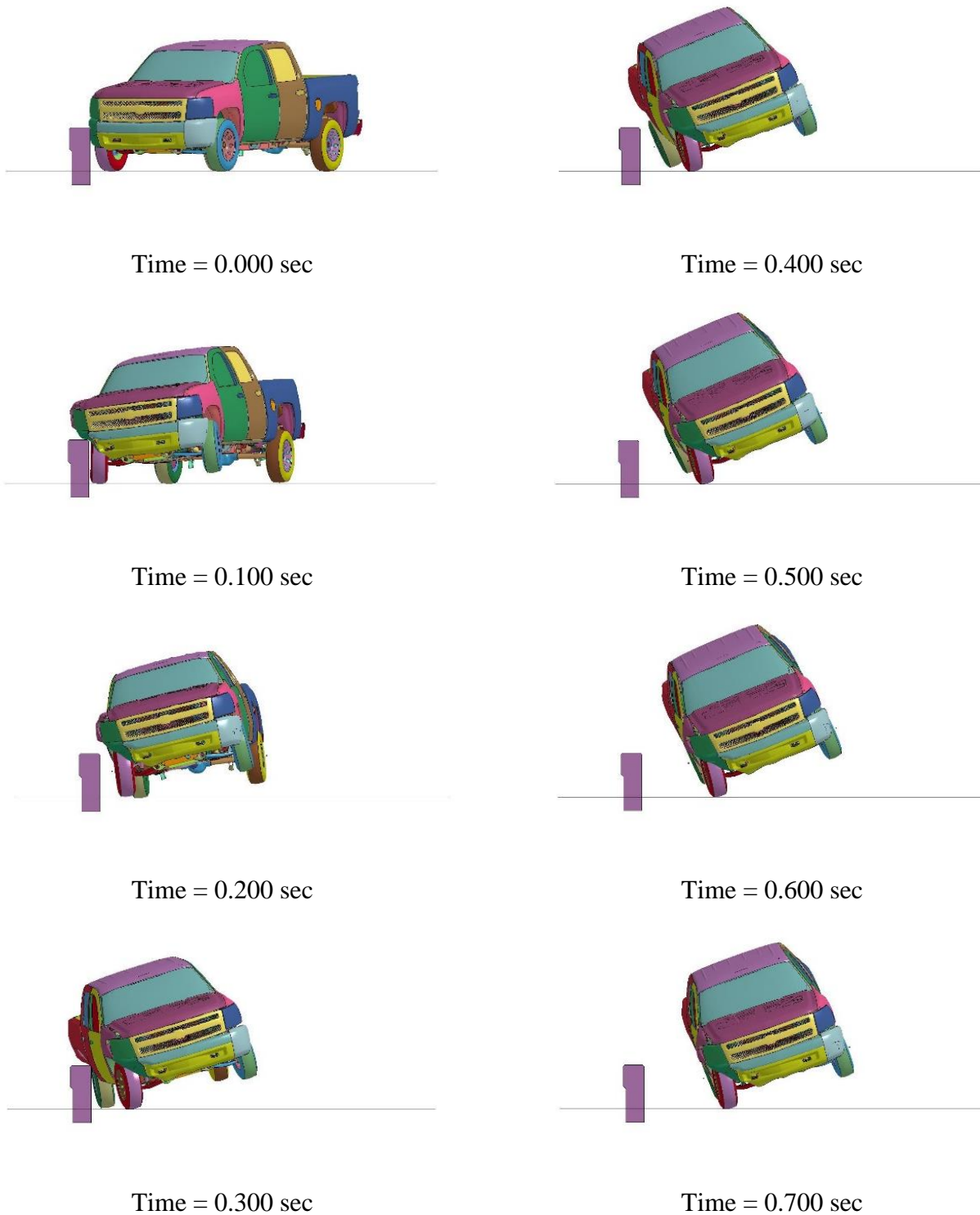


Figure 40. Downstream Sequential View, 25-in. (635 mm) Tall Barrier Simulation

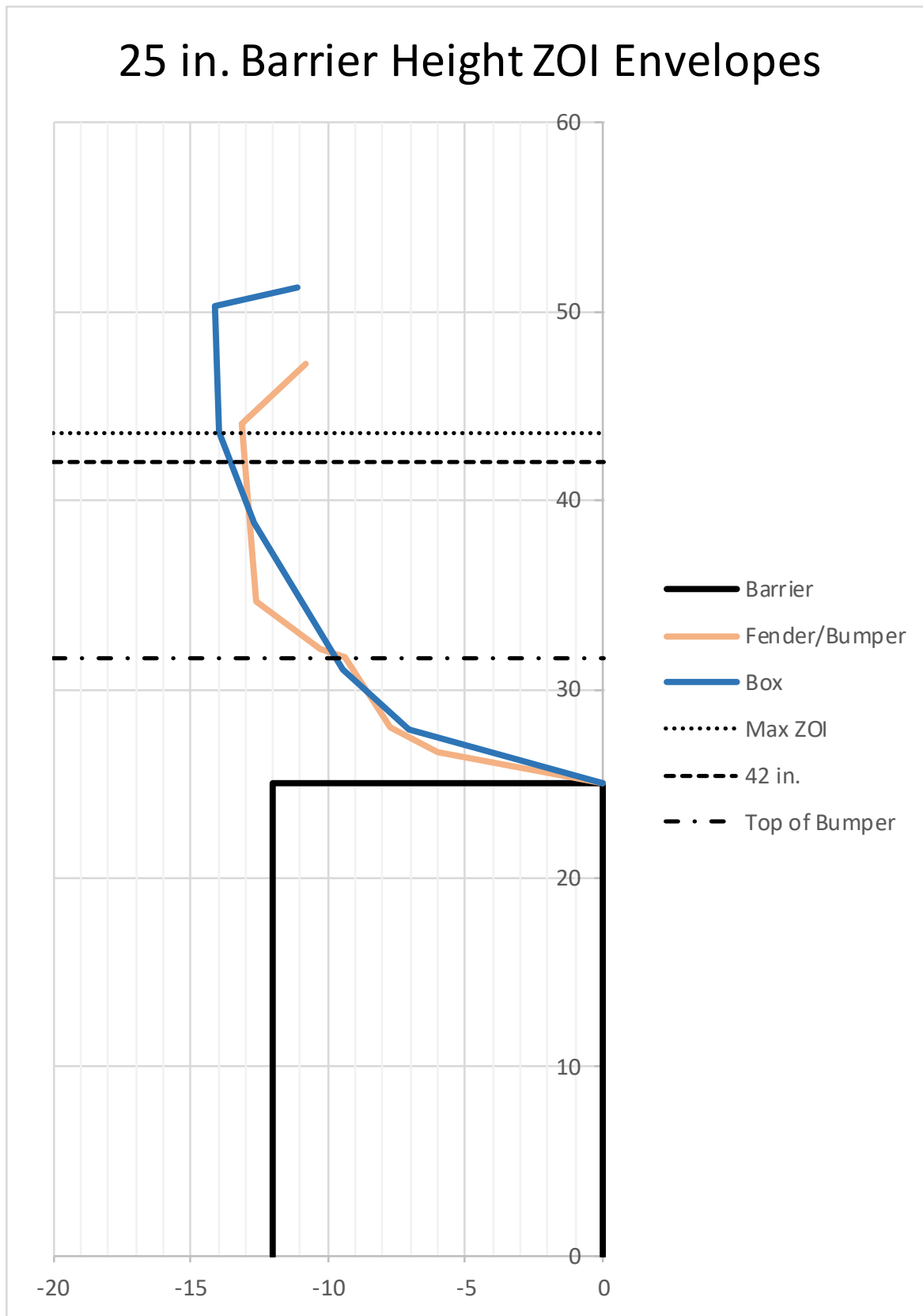


Figure 41. 25-in. (635 mm) Barrier Height Simulation ZOI Envelope

5.2.3 26-in. (660-mm) Barrier Height Simulation

Next, a 26-in. (660-mm) tall barrier was simulated. The vehicle impacted the barrier and was successfully redirected, as shown in Figure 40. Dynamics of the vehicle were determined to be acceptable as the vehicle did not override the barrier or roll over. As with the 24-in. and 25-in. (610-mm and 635-mm) simulations, the maximum ZOI occurred at the trailing end of the box during tail slap, and was equal to 14.2 in. (361 mm) laterally at a height of 50.7 in. (1,288 mm). The lateral extents of protrusion and associated vertical coordinates of the bumper, fender, and box are shown in Table 13. The ZOI envelope for the 26-in. (660-mm) barrier height is shown in Figure 43.

Table 13. ZOI Values for MASH 2-11 Simulation: 26-in. (660-mm) Tall, Rigid Vertical Parapet

Vehicle Component	Maximum Lateral Protrusion ⁽¹⁾	Height of Protruding Element ⁽¹⁾
Bumper	6.7 in. (170 mm)	30.0 in. (762 mm)
Fender	10.7 in. (272 mm)	34.1 in. (866 mm)
Rear Corner of Box	14.2 in. (361 mm)	50.7 in. (1,288 mm)

(1) Datum reference for ZOI measurement corresponds to the leading edge of the barrier at roadway height.

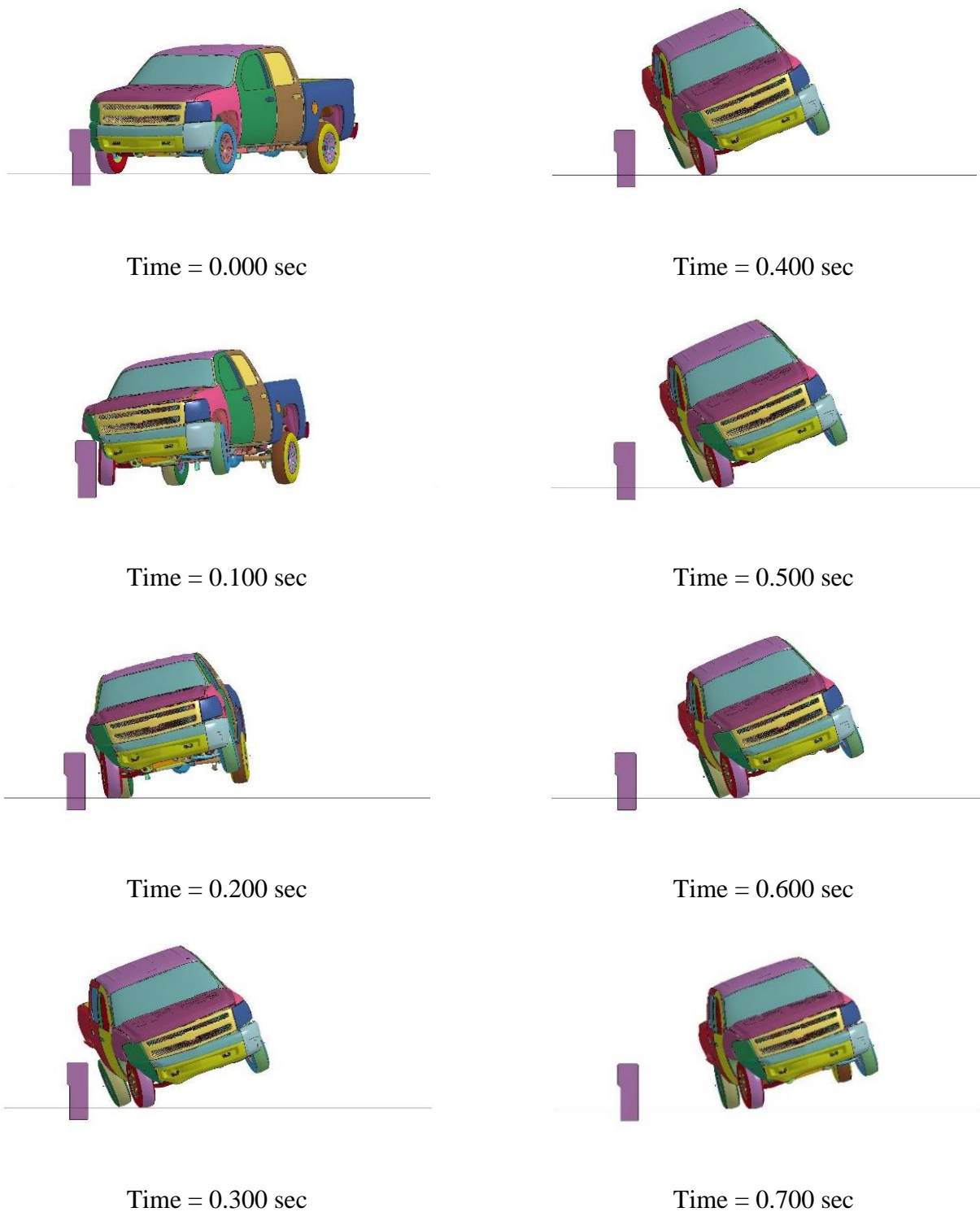


Figure 42. Downstream Sequential View, 26-in. (660-mm) Tall Barrier Simulation

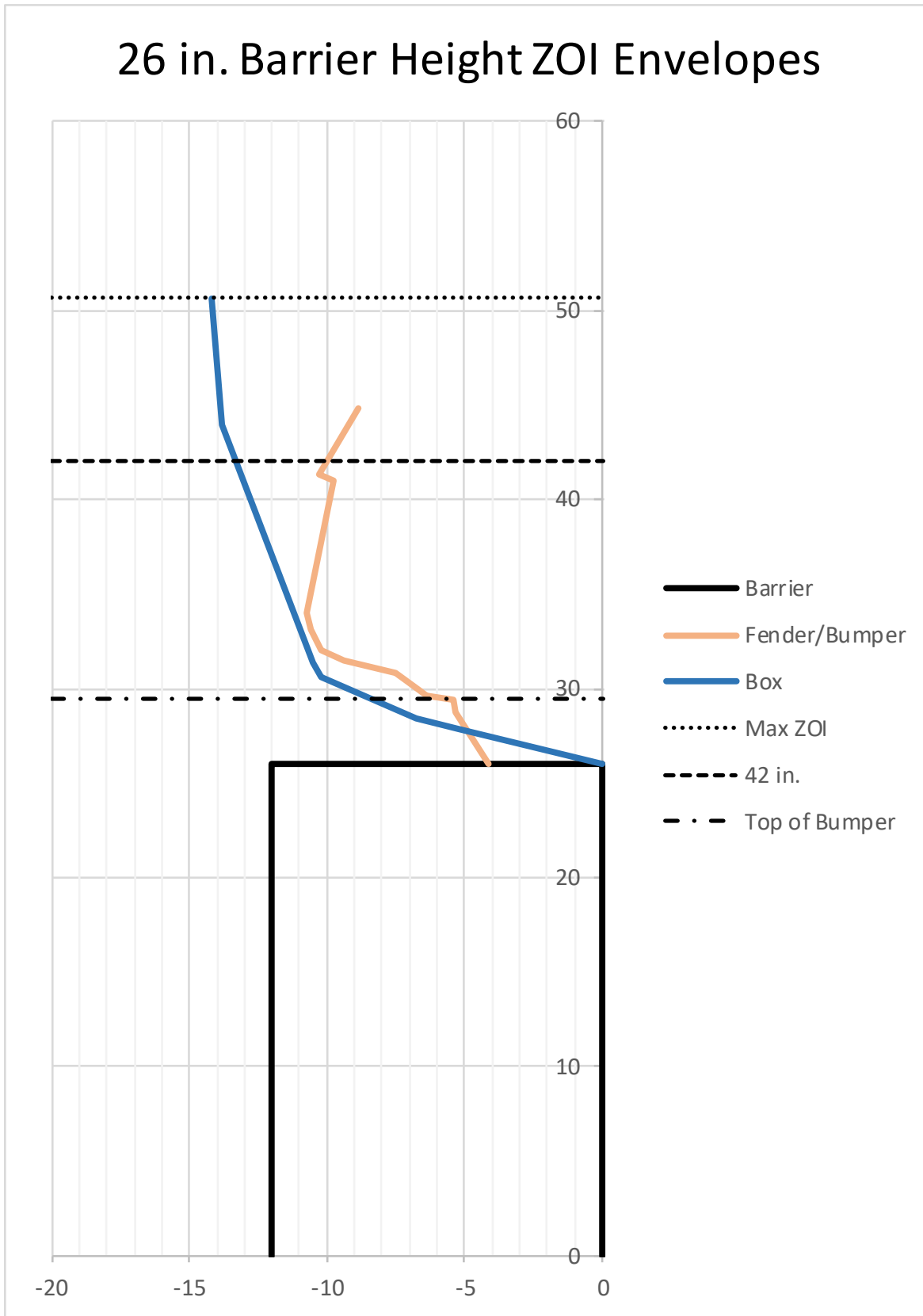


Figure 43. 26-in. (660-mm) Barrier Height Simulation ZOI Envelope

5.2.4 27-in. (686-mm) Barrier Height Simulation

Finally, a barrier height of 27 in. (686 mm) was simulated. When impacted by the Silverado truck model, the 27-in. (686 mm) barrier captured and redirected the vehicle, as shown in Figure 44. The vehicle was redirected without excessive roll, pitch, and yaw. The lateral extents of protrusion and associated vertical coordinates of the bumper, fender, and box are shown in Table 14. Once again, the maximum lateral protrusion of the vehicle past the front face of the barrier occurred at the trailing corner of the box, and was equal to 14.0 in. (356 mm) at a height of 50.9 in. (1,293 mm) above the ground line. The ZOI envelope for the 27-in. (686 mm) barrier height is shown in Figure 45.

Table 14. ZOI Values for MASH 2-11 Simulation: 26-in. (660-mm) Tall, Rigid Vertical Parapet

Vehicle Component	Maximum Lateral Protrusion⁽¹⁾	Height of Protruding Element⁽¹⁾
Bumper	5.0 in. (172 mm)	29.7 in. (754 mm)
Fender	11.7 in. (297 mm)	42.1 in. (1,069 mm)
Rear Corner of Box	14.0 in. (356 mm)	50.9 in. (1,293 mm)

(1) Datum reference for ZOI measurement corresponds to the leading edge of the barrier at roadway height.

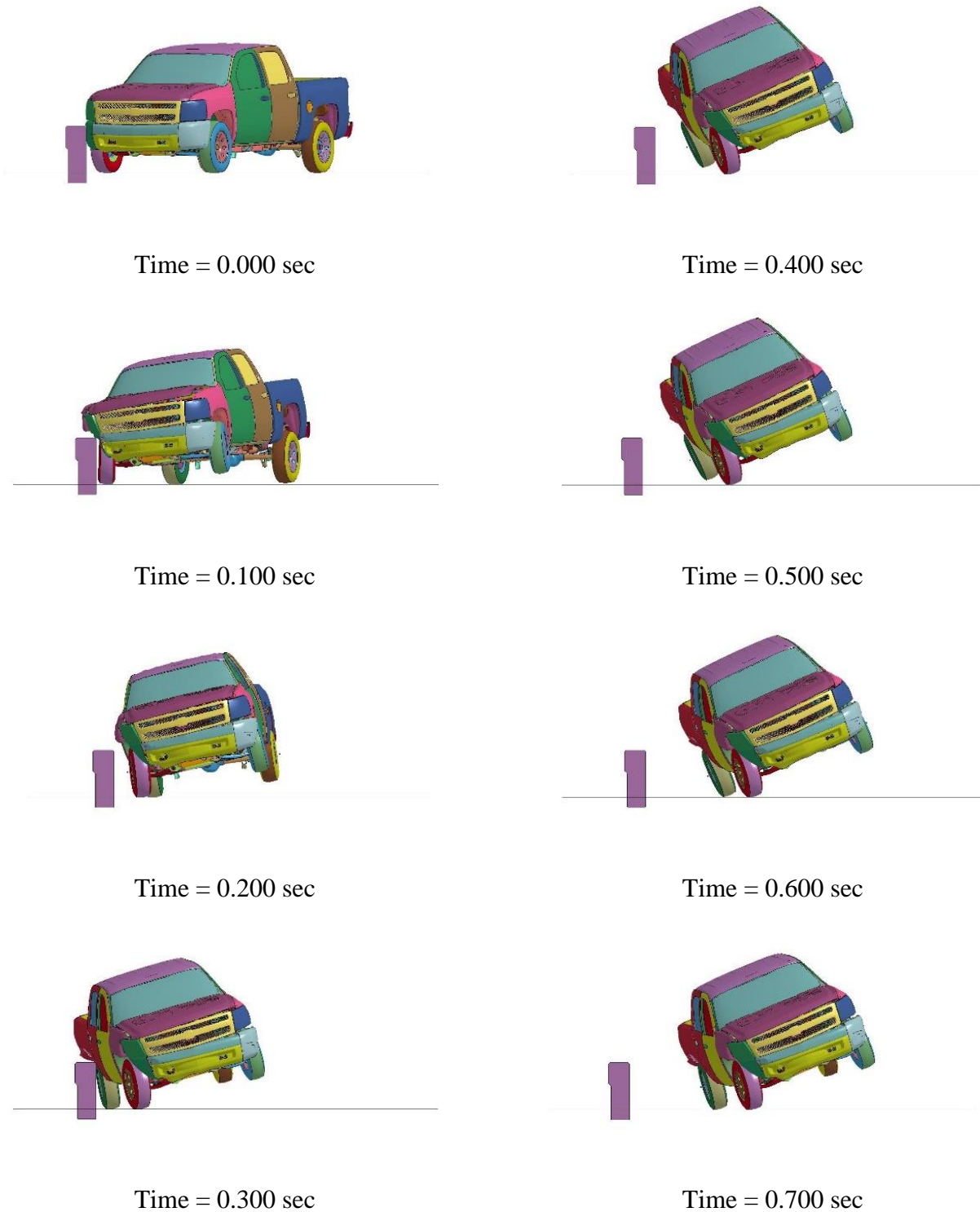


Figure 44. Downstream Sequential View, 27-in. (686 mm) Tall Barrier Simulation

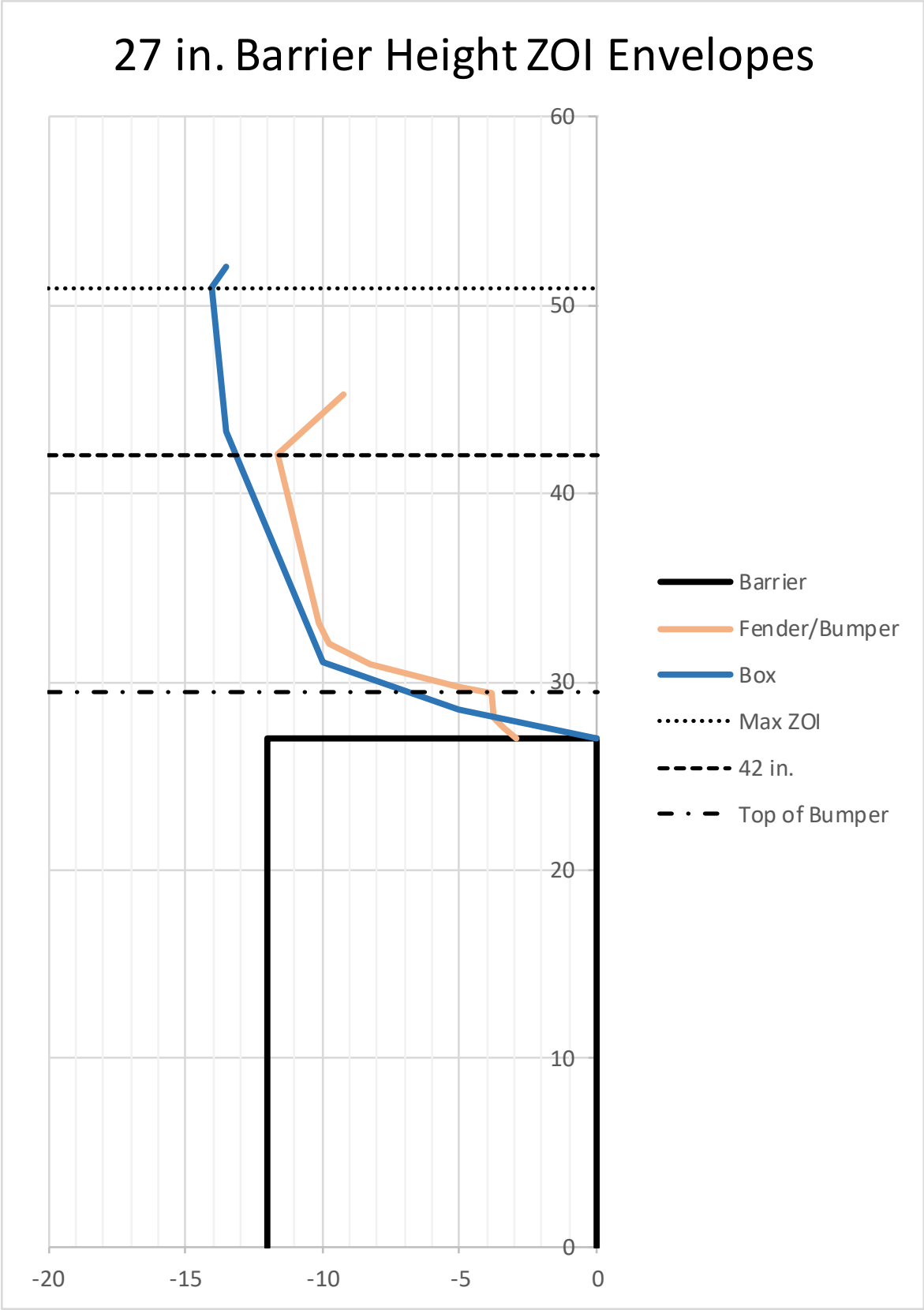


Figure 45. 27-in. (686 mm) Barrier Height Simulation ZOI Envelope

5.3 Height Simulations Comparison

Analysis of the four height simulations showed that each simulated barrier height was able to successfully capture and redirect the vehicle. A comparison of the vehicle dynamics, as shown in Figure 46, shows very little variance as the height of the barrier increased. In general, as the barrier height increased, the roll of the vehicle toward the barrier decreased. However, the 26-in (660-mm) barrier height showed less vehicle roll than the 27-in (686 mm) tall barrier after 400 ms into the simulation, but produced virtually identical roll prior to that point. Overall, the 26-in (660-mm) barrier height produced the most desirable vehicle roll, but variance between the simulations was minor. Similar to roll, the pitch of the vehicle was reduced as the barrier height increased. Once again, the 26-in. (660-mm) and 27-in. (686-mm) barrier heights produced almost identical results. All barriers provided reasonable vehicle pitch characteristics, with the 27-in. (686-mm) barrier providing the lowest overall. All simulations provided the same general trend with respect to yaw. As the barrier height of the vehicle was increased, an increase in yaw toward the barrier was decreased. While differences in yaw were observed between the simulations, the differences were determined negligible as all models provided acceptable results, and yaw of the vehicle was considered less critical than roll and pitch.

Analysis of the ZOI for each of the simulated heights showed a general decrease in maximum ZOI for the front end of the vehicle as barrier height increased, as shown in Figure 47. The decrease in ZOI was caused by increased engagement of the bumper, which produced less bumper and fender override of the barrier as barrier height increased. However, when observing the ZOI produced by the box of the Silverado model during tail slap, the values for each height were all within 1 in. (25 mm) of each other. The ZOI values generated with respect to the rear end of the vehicle for the 24-in. (610-mm), 25-in. (635-mm), 26-in. (660-mm) and 27-in. (686-mm) barriers were 14.8 in. (376 mm), 14.1 in. (358 mm), 14.2 in. (361 mm), and 14.0 in. (356 mm), respectively.

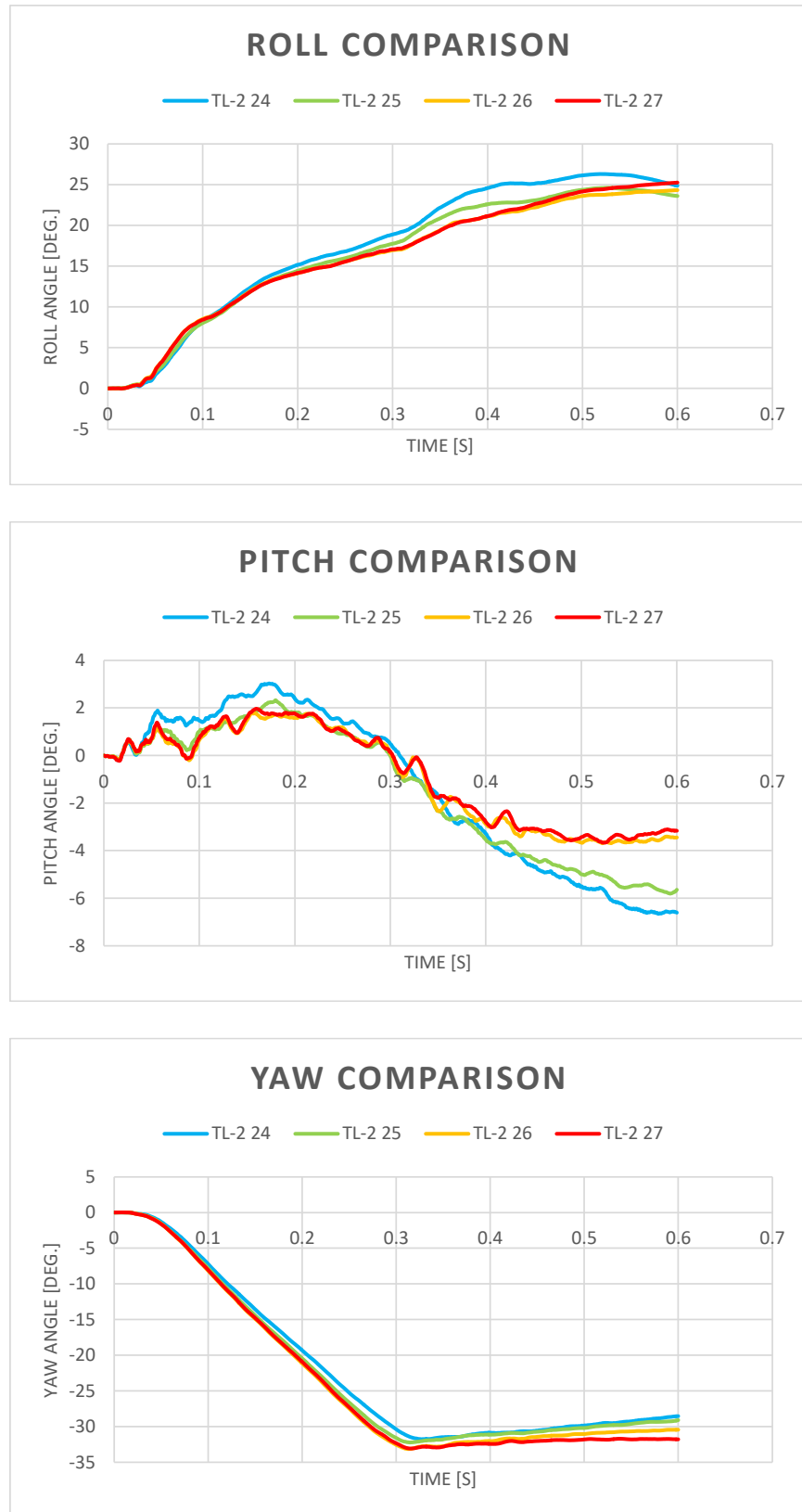


Figure 46. Height Simulation Vehicle Dynamics Comparison

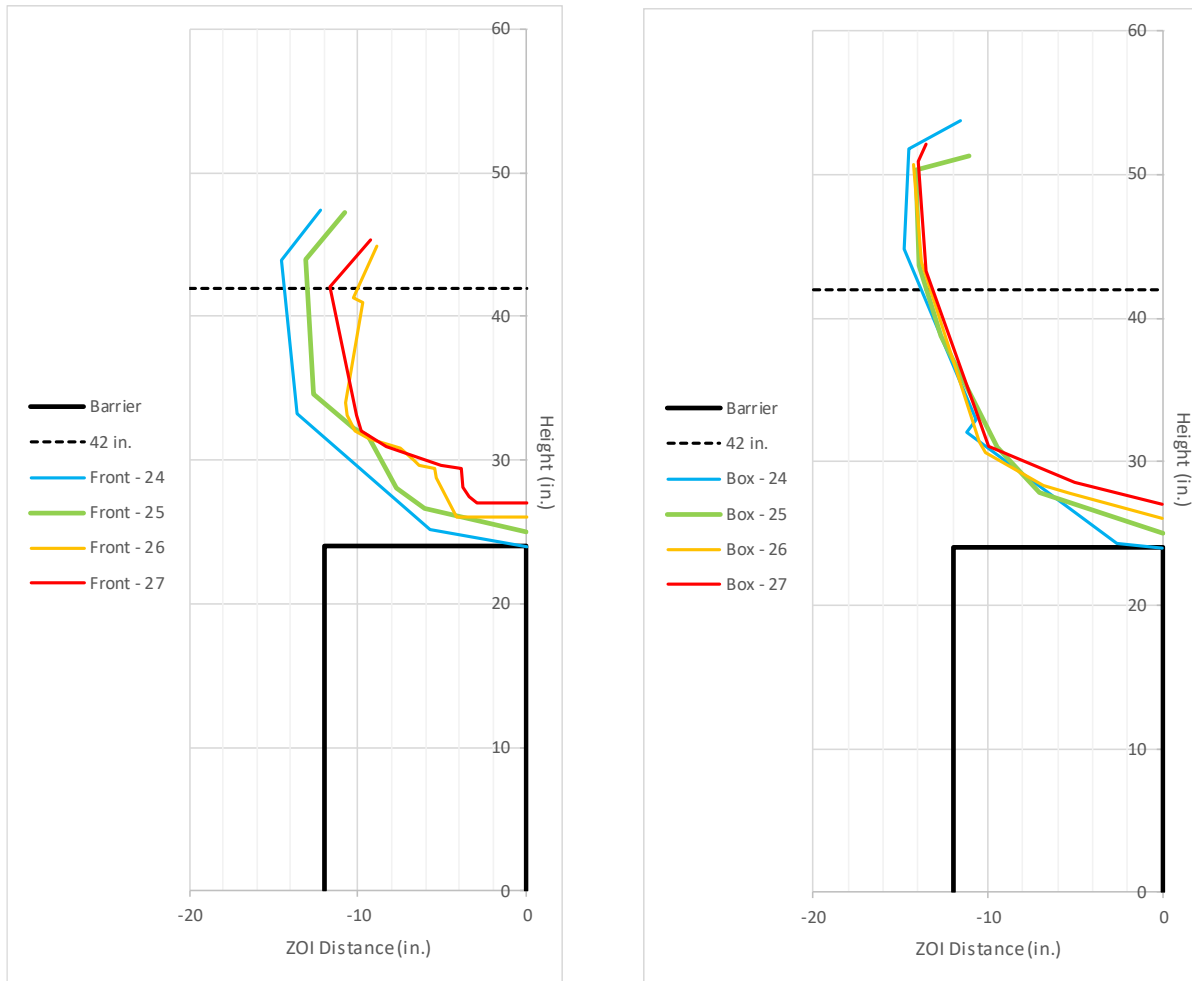


Figure 47. ZOI Comparison for Height Study Simulations, Front (Left) and Rear of Vehicle (Right)

5.4 Conclusion

All simulations performed during the height study showed the ability to capture and redirect the vehicle regardless of barrier height. The vehicle model remained stable and did not show any tendency to override the barrier system. The ZOI measurements at the front of the vehicle were reduced as barrier height increased at the same impact speed and angle, but there was virtually no change in the ZOI measurement of the trailing box corner. Because ZOI was controlled by the upper corner of the pickup box, and because none of the parapet heights resulted in instability or excessive roll, pitch, yaw, or vehicle accelerations, the 24-in. (610-mm) tall, rigid vertical parapet was determined to be the optimal shape for the bicycle rail. The previous geometry analysis of the 2000P and 2270P pickup truck as compared to low-height parapets further reinforced the used of the 24-in. (610-mm) tall parapet.

It is possible that a parapet lower than 24-in. (610-mm) tall could satisfactorily redirect a vehicle at MASH 2-11 impact conditions. However, Iowa DOT requires that the minimum parapet height be 24 in. (610 mm); thus lower barrier heights were not considered.

6 PEDESTRIAN/BICYCLE RAIL DESIGN

6.1 Iowa DOT Requirements

Iowa DOT provided several preferences regarding the design of the vehicle-bicycle-pedestrian rail. First and foremost, the pedestrian/bicycle railing was to be designed to withstand the loadings stated for pedestrian/bicycle railings within *AASHTO LRFD Bridge Design Specifications* [1]. Additionally, Iowa DOT preferred that the pedestrian/bicycle railing be mounted on top of the concrete parapet. Mounting the rail on top would eliminate the need for a backside curb on the bike path in order to comply with American with Disabilities Act (ADA) [45] requirements for railings mounted to the back of the parapet. Iowa DOT also stated the design should maximize visibility by using widely-spaced, small section elements, and minimize horizontal elements used (i.e., use one horizontal rail rather than two). It was desired that the rail design consider the need for increased lateral setback to mitigate negative vehicle interaction with the rail, head ejection concerns, and the potential for the combination rail to interfere with snow plows. Iowa DOT originally preferred to have two configurations, one used when no raised sidewalk was present and one to be used when a 6-in. (152-mm) tall raised sidewalk was present. With respect to the parapet, Iowa DOT stated that the rail design must be compatible with a 10-in. (254-mm) wide concrete parapet utilizing no. 4 steel reinforcement.

6.2 LRFD Pedestrian/Bicycle Railing Design Loading

Chapter 13 of *AASHTO LRFD Bridge Design Specifications* [1] lays out the design requirements for railings. Specifically, sections 13.8 through 13.10 describe the design requirements for pedestrian, bicycle, and combination rails. With respect to geometry of the system, the railing was required to have an overall height of at least 42 in. (1,067 mm) above the top of the walkway or bicycle path, e.g., a 24-in. (610-mm) tall parapet must have an added 24-in. (610-mm) tall pedestrian/bicycle rail attached to achieve a 42 in. (1,067 mm) overall height when installed adjacent to a 6-in. (152-mm) tall raised pathway.

The design specifications also defined the maximum clear opening space for the railing. Clear space is defined as the space between horizontal and/or vertical elements. For the lower 27 in. (686 mm) of the railing, any clear space must be small enough to prevent a 6-in. (152-mm) diameter sphere from passing through. For any part of the railing above 27 in. (686 mm), the clear space must prevent pass-through of an 8-in. (203-mm) diameter sphere. However, the opening size recommendations for pedestrian/bicycle railings are only specified for railings on the outer edge of a bikeway when highway traffic is separated from the pathway by a traffic railing. Iowa DOT was concerned with the pedestrian/bicycle railing on the separator barrier only. Thus, the combination pedestrian/bicycle railing was not subject to the pass-through specifications, but still needed to meet the 42-in. (1,067-mm) height relative to the surface of the sidewalk or bikeway and the structural loading requirement.

With respect to the structural capacity of the railing, design specifications required that the railing withstand specified design loads. The design live load for pedestrian/bicycle railings was specified as 50 lb/ft (730 N/m) acting transversely and vertically, simultaneously, as shown in Figure 48, as well as a 200-lb (889-N) concentrated load acting simultaneously with the previous loads at any point and in any direction at the top of the longitudinal element. Pedestrian/bicycle

railing posts should be designed for a concentrated design live load applied transversely at the CG of the upper longitudinal element. The value of the concentrated design live load for posts is calculated using Equation 1.

$$P_{LL} = 200 + 50L \quad (1)$$

Where: P_{LL} = Post live load

L = Post spacing

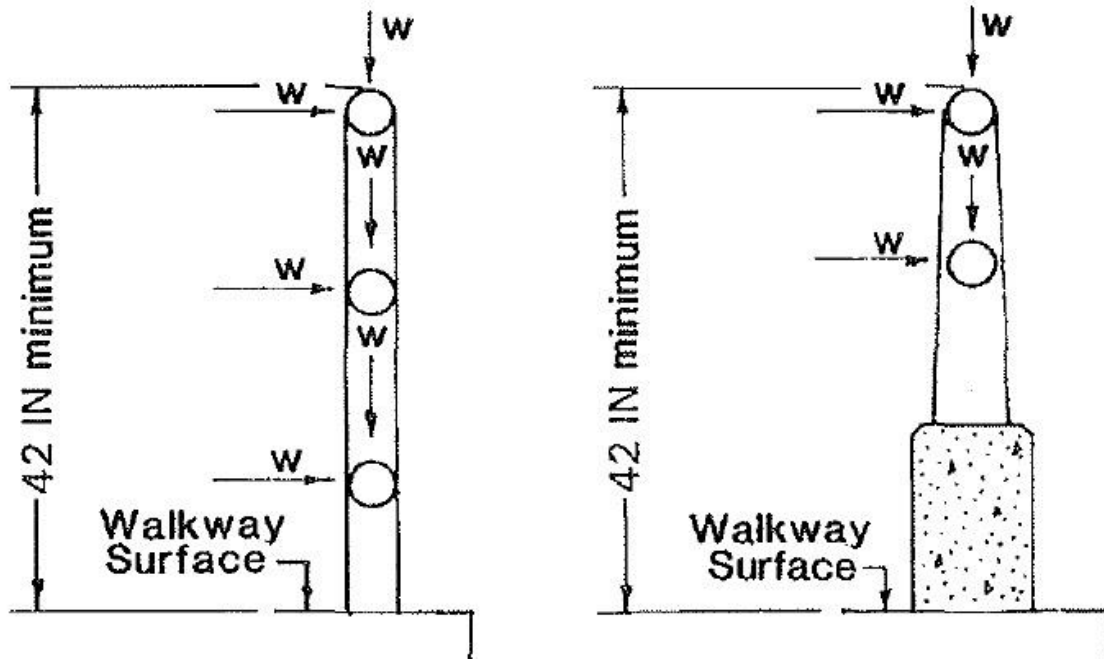


Figure 48. AASHTO LRFD Pedestrian/Bicycle Rail Loading [1]

6.3 Rail and Post Design Concepts

In attempt to meet Iowa DOT's preferences, multiple design concepts were generated. Sketches of the proposed concepts are shown in Figure 49. First, in order to keep the design simple and to maximize visibility, all design concepts utilized one rail element placed atop a 24-in. (610-mm) tall parapet. Concept (a) used a vertical post with the rail placed within the post span, concept (b) used a vertical post with the rail placed on the front side of the posts, and concepts (c) and (d) both placed the rail on top of the posts. However, concept (d) set the posts farther back on the baseplates to allow for the vehicle to intrude farther past the front face of the barrier without interaction with the posts and/or rails. Placement of the rail could be centered or shifted to either side of the post to create different rail offsets.

The last four concepts were designed in such a way as to increase rail setback as well as provide a more aesthetically-pleasing system. Concept (e) used a horizontal steel tube welded to a vertical tube, creating a 90-degree angle, while concepts (f) and (g) both angled toward the pedestrian/bicycle traffic side, to different degrees, in order to increase rail set back. Concept (h)

used a 90-degree radius bend so only one element needed to be used. The rail could be placed in multiple orientations for these concepts, similar to concepts (a) through (d). For all concepts, square, rectangular, or round sections could be used.

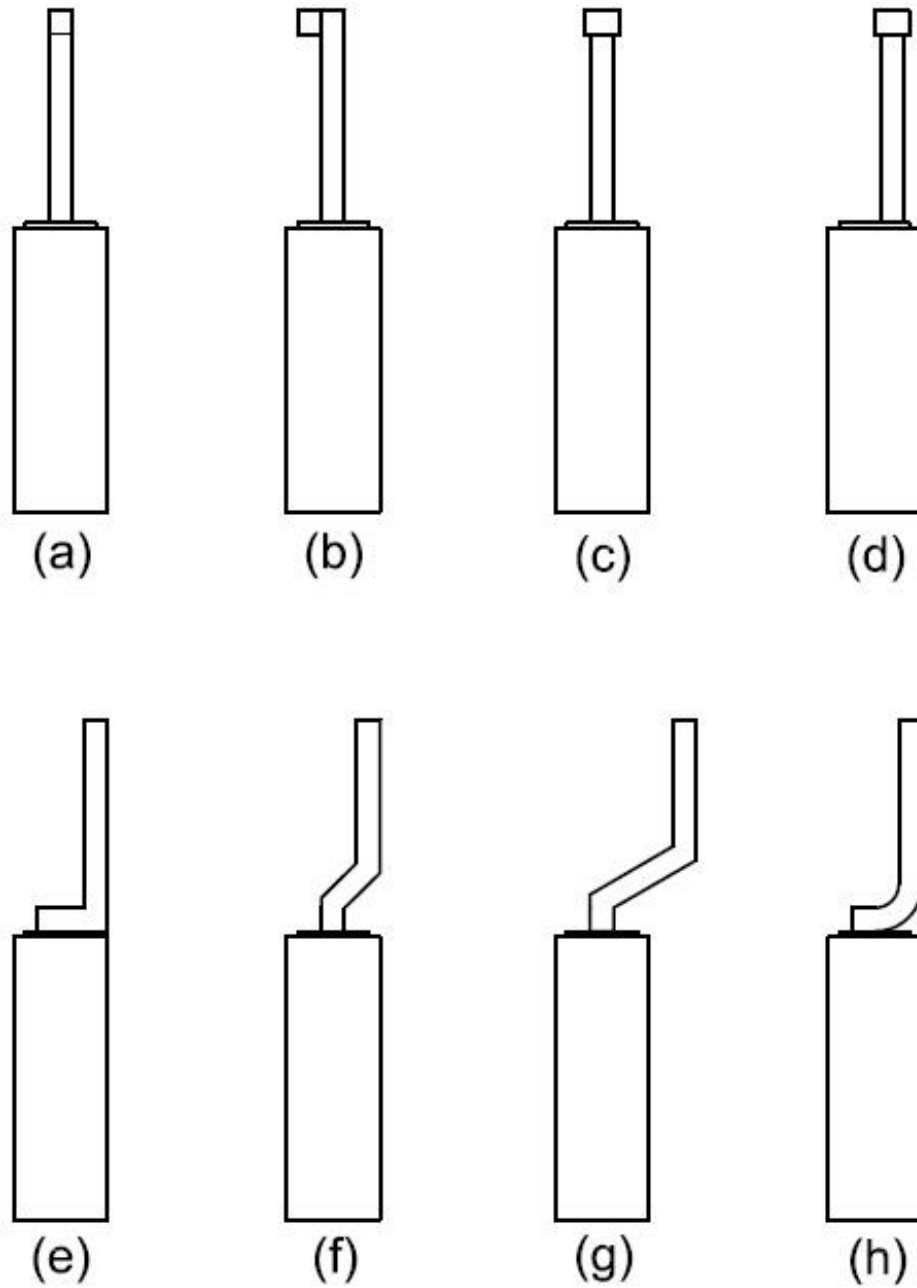


Figure 49. Rail Design Concepts

6.4 Rail and Post Connection Concepts

Three main concepts were created to attach the rail to the post section as well as connect the post to the baseplate. The first connection concept attached the rail to the post using steel angle brackets and either bolts or welds, as shown in Figure 50. The second concept considered fully welding the rail to the post and the post to the baseplate, as shown in Figure 51. The third concept used a combination of welding angle brackets to either the post or the rail and using bolts for the other connections, as shown in Figure 52.

The fully-bolted concept was believed to have the most predictable, consistent behavior during impact. Installation and repair were also considered to be simpler for the fully-bolted concept, as only simple hand tools would be needed. Galvanization of bolt-assembled hardware was also believed to be more reliable and consistent, compared to welded components. Bolt hardware is standardized and readily available, and relatively inexpensive, and could be cheaper than labor costs associated with individual welded rail assemblies. However, assemblies were less clean and aesthetic, and additional tooling was required to assemble the components. In addition, multiple components were needed to assemble the structure. As a result, it was not the preferred concept by Iowa DOT.

The fully-welded concept provided a cleaner appearance than the bolted or combination concepts due to a reduced number of parts and removal of protruding elements, such as bolts, washers, and nuts. Iowa DOT indicated that these sections would be prefabricated by welding in a shop, sent for galvanization, and shipped to the installation site. Although some concerns were raised about the quality, capability, and labor required to weld sections on an installation site (field welding) as well as apply galvanization, Iowa DOT did not believe field welding would be the preferred method of rail assembly. Nonetheless, galvanization of closed, welded sections requires careful design to allow proper galvanization flow to prevent “floating” in the tank or incomplete surface protection, and those changes could structurally weaken the rail. In addition, damaged rail sections must be completely replaced by wholly new fabricated sections, as field repairs consisting of component replacement would be nearly impossible.

The final option consisted of a mix of welded and bolted connections. The upper two bracket-to-rail attachments would be welded to the post, and the welded brackets would be bolted to the rail. This concept ensured better control of galvanizing thickness and flow, allowed for faster repairs of damaged hardware in the field, and easier assembly of post and bracket connections. However, the concept still required additional tooling to connect the rail, was not substantially simpler than the fully-bolted concept (only reduced hardware by one bolt, nut, and washer), and still utilized protruding bolt and nut elements.

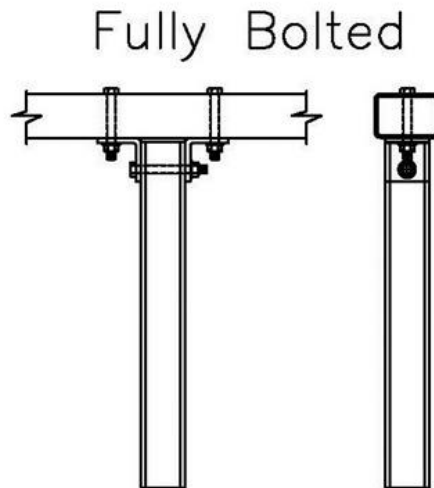


Figure 50. Fully-Bolted Connection Concept

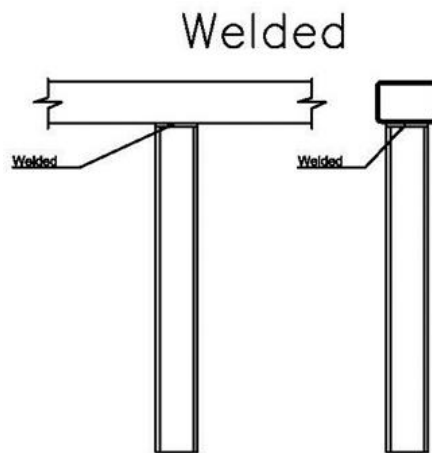


Figure 51. Fully-Welded Connection Concept

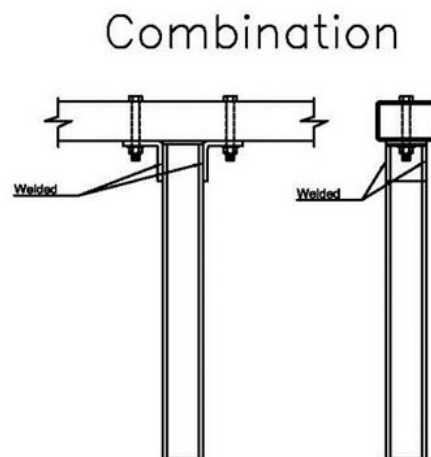


Figure 52. Combination Connection Concept (Iowa DOT-Preferred Concept)

6.5 Concept Selection

After discussion with Iowa DOT, it was decided to move forward with the fully-welded concept. The use of concept (d) would keep the system simple while providing increased rail setback to reduce the severity of negative interaction with the system. Consequently, the system was designed to allow for the sections to be assembled in 20-ft (6-m) sections while utilizing a 10-ft (3-m) post spacing.

Early concepts for the combination TL-2 parapet and bicycle rail utilized two different designs: one for use with a raised pedestrian sidewalk, and one without a raised pedestrian sidewalk. Iowa DOT selected to proceed with only one configuration consisting of a 24-in. (610-mm) tall parapet and a 24-in. (610-mm) tall pedestrian/bicycle rail, giving the system an overall height of 48 in. (1,219 mm). By designing the system with a 48-in. (1,219-mm) overall height, the pedestrian/bicycle rail would be 48 in. (1,219 mm) above the pedestrian/bicycle path when the raised sidewalk was not present and 42 in. (1,067 mm) above the pedestrian/bicycle path when the standard 6-in. (152-mm) raised sidewalk was present, satisfying all geometrical criteria with a single configuration and reducing the likelihood of construction error.

6.6 Post and Rail Calculations

The calculations described herein were used to design an anchored, straight, pedestrian/bicycle rail that was configured with uniform post spacing and mounted on top of a 24-in. (610-mm) tall concrete parapet. The applied loads were defined by the requirements published in *AASHTO LRFD Bridge Design Specifications* [1] for a pedestrian/bicycle rail. These loads corresponded to the critical loading that was applied to the pedestrian/bicycle rail, which generated the critical forces. Section sizes and their capacities were located within the American Institute of Steel Construction's (AISC) *Steel Construction Manual* [46]. Calculations for the final railing design can be found in Appendix A. No additional factors were applied to the pedestrian/bicycle rail live loads, as Iowa DOT considered the live loading presented in *AASHTO LRFD Bridge Design Specifications* [1] for a pedestrian/bicycle rail to already be factored. Appropriate reduction factors were applied to the section capacity equations for the different loading cases.

6.6.1 Longitudinal Rail Element

The longitudinal rail element was designed to withstand two types of live loads: (a) a uniformly distributed load of 50 lb/ft (730 N/m) applied both transversely (y-axis) and vertically (z-axis), and (b) a concentrated load of 200 lb (889 N) applied at any point and in any direction. An example of the design loading conditions with a concentrated load acting vertically downward in the center of the top longitudinal beam is shown in Figure 53.

To determine the rail section size to resist the bending produced by the applied live loading, the rail was treated as a simply supported beam, as shown in Figure 54. The concentrated load was applied directly in the center to maximize the bending moment produced. The bending moment of the rail in the y-direction was calculated using superposition of the concentrated and distributed loads, as shown in Equation 2. The same process was used to calculate the bending moment in the z-direction. However, no concentrated load was present as it was already applied to the y-direction calculation, creating Equation 3. The same process was repeated for the case when the concentrated

load was applied vertically and the bending moment along both axes was calculated using Equations 4 and 5.

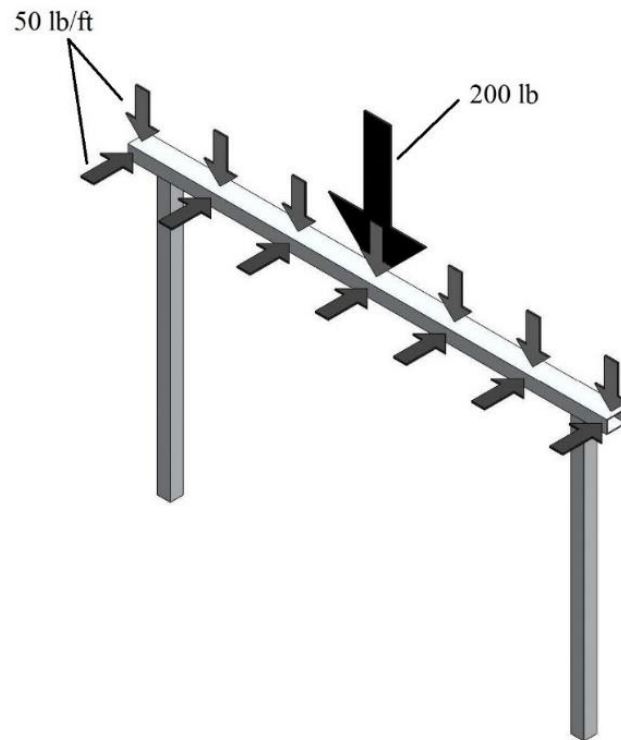


Figure 53. Example of Pedestrian/Bicycle Rail with Vertical Concentrated Load

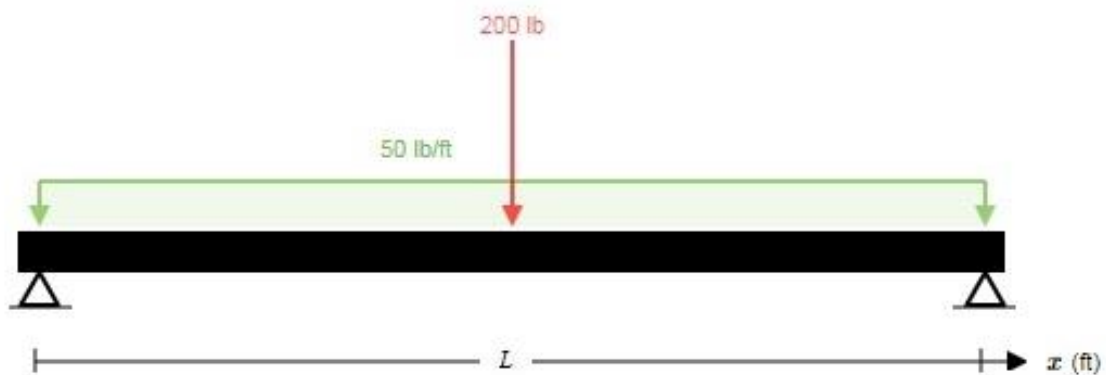


Figure 54. Rail Force Diagram to Maximize Bending

Case 1

$$M_{rail,y-y} = \frac{PL}{4} + \frac{wL^2}{8} \quad (2)$$

$$M_{rail,z-z} = \frac{wL^2}{8} \quad (3)$$

Case 2

$$M_{rail,z-z} = \frac{PL}{4} + \frac{wL^2}{8} \quad (4)$$

$$M_{rail,y-y} = \frac{wL^2}{8} \quad (5)$$

Where: $M_{rail,y-y}$ = Bending moment in rail about rail y-y axis

$M_{rail,z-z}$ = Bending moment in rail about rail z-z axis

P = Concentrated load

w = Distributed load

L = Post spacing

Using a similar configuration, the shear force in the rail section was calculated. However, to maximize shear in the rail, the concentrated load was placed near the end of the rail, as shown in Figure 55. The shear force due to the live loading in this configuration was then calculated in the vertical direction using Equation 6. The same process was applied to the transverse direction, as shown in Equation 7. The concentrated load was omitted as it was already being applied in the vertical direction. The concentrated load was then applied in the transverse direction and the loading on the section was evaluated using Equations 8 and 9.

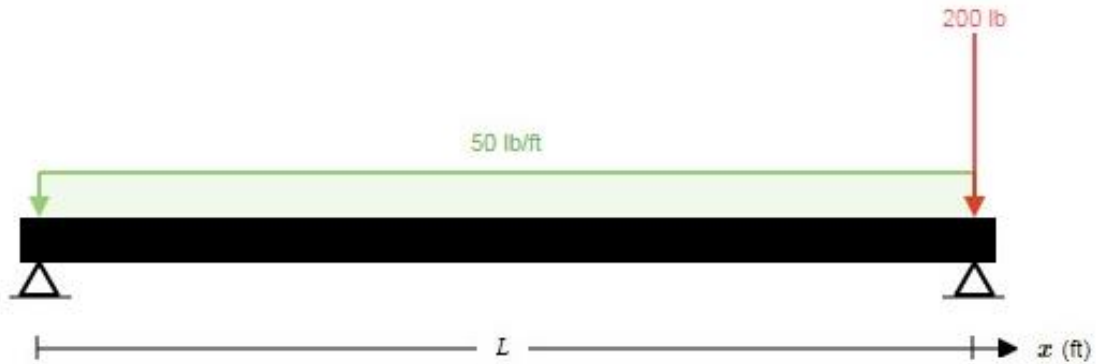


Figure 55. Rail Force Diagram to Maximize Shear

Case 1

$$V_{rail,z-z} = P + \frac{wL}{2} \quad (6)$$

$$V_{rail,y-y} = \frac{wL}{2} \quad (7)$$

Case 2

$$V_{rail,y-y} = P + \frac{wL}{2} \quad (8)$$

$$V_{rail,z-z} = \frac{wL}{2} \quad (9)$$

Where: $V_{rail,z-z}$ = Shear force in rail along z-z axis
 $V_{rail,y-y}$ = Shear force in rail along y-y axis
 P = Concentrated load
 w = Distributed load

Once the live-load bending moment produced by the live loading was found, the proper section needed to be selected to resist the loading. Using the *AISC Steel Construction Manual* [46], section sizes and their flexural capacities were found. Specifically, section F7.1 was used to determine the flexural capacity. Equation F7-1 located within the *AISC Steel Construction Manual* calculates the nominal flexural strength of a section using the plastic section modulus and specified minimum yield stress of the material, as shown in Equation 10. However, it was desired that no plastic deformation should occur from the applied loading, so the elastic section modulus was used in place of the plastic section modulus, as shown in Equation 11. Using the elastic section modulus would limit all deformation to the elastic region of the material's stress-strain curve, thus resulting in no permanent deformation.

$$\phi M_n = \phi F_y Z \quad (10)$$

$$\phi M_{ns} = \phi F_y S \quad (11)$$

Where: ϕM_n = Nominal flexural strength
 ϕM_{ns} = Nominal elastic flexural strength
 F_y = Specified minimum yield stress
 Z = Plastic section modulus
 S = Elastic section modulus
 $\phi = 0.9$

Since the load was applied in two directions, the bending moments in each direction were normalized and summed following the process discussed in section H1 of *AISC Steel Construction Manual*. Specifically, Equation H1-1b sums the moments in the two directions and compares the

result to unity, as shown in Equation 12. If the sum exceeds one, the section is likely to fail plastically. This process was performed for both orientations of the concentrated load.

$$\frac{M_{rail,y-y}}{\phi M_{nsy}} + \frac{M_{rail,z-z}}{\phi M_{nsz}} \leq 1 \quad (12)$$

Where: $M_{rail,y-y}$ = Bending moment in rail about rail y-y axis
 $M_{rail,z-z}$ = Bending moment in rail about rail z-z axis
 $\phi M_{ns,y-y}$ = Nominal elastic flexural strength about y-y axis
 $\phi M_{ns,z-z}$ = Nominal elastic flexural strength about z-z axis

With respect to shear, Chapter G of the AISC *Steel Construction Manual* discusses the determination of shear capacity of various members. Specifically, section G4 was used to find the shear resistance of the rail by following Equation G4-1, as shown in Equations 13 through 16.

$$\phi V_n = \phi 0.6 F_y A_w C_{v2} \quad (13)$$

$$A_w = 2ht \quad (14)$$

$$h = b - 3t \quad (15)$$

$$C_{v2} = 1.0 \quad (16)$$

Where: ϕV_n = Nominal flexural strength
 F_y = Specified minimum yield stress
 A_w = Area of webs
 C_{v2} = Web shear buckling strength coefficient
 h = Width resisting shear force
 t = Design wall thickness
 b = Outside dimension of element
 $\phi = 0.75$

Since the rail was introduced to both flexure and shear, the rail needed to be analyzed with respect to the combined loading section of the AISC *Steel Construction Manual*, Section H3.2. Specifically, the process applies to HSS sections subjected to combined torsion, shear, flexure, and axial force. Due to the loading scenario, only shear and flexure were present. The capacity of the rail was then found using Equation 17. This process was performed for both loading cases and for each major axis of the rail.

$$\frac{M_{rail}}{\phi M_{nsrail}} + \left(\frac{V_{rail}}{\phi V_{nrail}} \right)^2 \leq 1 \quad (17)$$

Where: M_{rail} = Bending moment in rail

ϕM_{nsrail} = Rail's nominal elastic flexural strength

V_{post} = Shear in rail

ϕV_{nrail} = Rail's nominal shear strength

6.6.2 Vertical Post Element

The posts were subjected to a concentrated live load, P_{LL} , as defined in Equation 1. The concentrated live load was applied transversely at the CG of the upper horizontal element. The post was assumed to act as a single cantilever beam, as shown in Figure 56. The bending moment and shear force in the post were calculated using Equations 18 and 19, respectively.

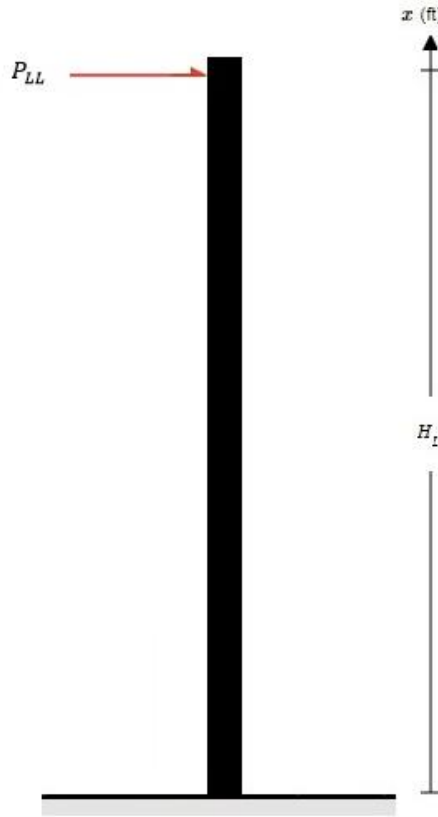


Figure 56. Post Force Diagram

$$M_{Post} = P_{LL}H_L \quad (18)$$

$$V_{post} = P_{LL} \quad (19)$$

Where: M_{post} = Bending moment in post due to force P_{LL}

P_{LL} = Post live load

H_L = Height at which load is applied

V_{post} = Shear in post

The resistance of the post to both flexure and shear were found using the same process used for the rail element. However, loading was only in one direction, removing the need to analyze the moment in two directions. Since the post was introduced to both flexure and shear, a similar process as used for the combined loading applied to the rail was performed using Equation 20.

$$\frac{M_{post}}{M_{nspost}} + \left(\frac{V_{post}}{V_{npost}} \right)^2 \leq 1 \quad (20)$$

Where: M_{post} = Bending moment in post due to force P_{LL}

M_{nspost} = Post's nominal elastic flexural strength

V_{post} = Shear in post

V_{npost} = Post's nominal shear strength

Using this process, a 3-in. x 2-in. x 1/8-in. (76-mm x 51-mm x 3-mm) HSS ASTM A500 Grade C steel tube was selected for the rail, while a 2-in. x 2-in. x 1/8-in. (51-mm x 51-mm x 3-mm) HSS ASTM A500 Grade C steel tube was selected for the post. The selected post section was the smallest square HSS section size listed within the *AISC Steel Construction Manual*, allowing for maximum visibility. For the rail, the section size was chosen to allow for good visibility while providing some post protection and ease within the installation process. By making the rail wider than the post, more surface area was present for connecting the post to the rail. The wider rail also allows the front and rear faces of the post to extend out from the front and rear faces of the rail. This offset of the post from the faces of the rail provided some post snag reduction if a pedestrian/bicyclist were to fall into the system. A post spacing of 120 in. (3,048 mm) was chosen. This post spacing was the largest used on previously reviewed systems. This wide post spacing also would contribute to improved visibility for motorists attempting to observe any hazards beyond the system.

6.7 Baseplate Calculations

The baseplate was designed to allow for mounting the pedestrian/bicycle rail on top of the parapet while providing enough strength to resist the loading conditions. The dimensions of the parapet only allowed for the use of two anchor rods per baseplate, as the reinforcement of the barrier limited the amount of space to place more anchor rods, and the overall width of the parapet provided limited space to effectively use more anchors. Additional anchors could be used, but at the cost of using baseplate dimensions that would be unreasonably large or a reduction in the

anchorage connection capacity. The anchorage connection capacity would be reduced due to the spacing of the anchor rods as the areas of influence would overlap each other to a greater extent, as discussed in the following anchor rod calculations. Thus, the baseplate was designed to have a single row of anchor rod holes aligned along the longitudinal axis of the parapet.

6.7.1 Loading

The baseplate and connections were designed to resist the elastic moment capacity of the post, instead of only resisting the pedestrian/bicycle loading. This design approach provided sufficient baseplate and connection strength to keep the system intact if impacted by a vehicle. Excessively weak baseplates and connections could cause the components of the system to become dislodged and become debris hazards as a result of overloading. With a more robust design approach, the system would be more likely to remain whole, thus making it less of a hazard when impacted under vehicle loading.

6.7.2 Required Thickness

To find the required baseplate thickness, Chapter 1 of AISC's *Steel Design Guide 1* [47] was used. Specifically, the guide discusses the design process to determine the required thickness of the baseplate subjected to an axial load and bending moment on the attached post, as shown in Figure 57. This process assumes the loading on the post creates a stress distribution on the plate and tension within the anchors. From this distribution, the thickness of the baseplate to resist the loading can be found. The first step of the process requires an estimation or selection of desired baseplate dimensions, width and length, and knowledge of loading on the post. Once the desired dimensions were chosen, Equations 21 and 22 were used to determine if the baseplate needed to be designed for small or large eccentricities.

$$e = \frac{M}{P} \quad (21)$$

$$e \leq \frac{N}{6} \quad (22)$$

Where: e = Eccentricity

M = Post bending moment

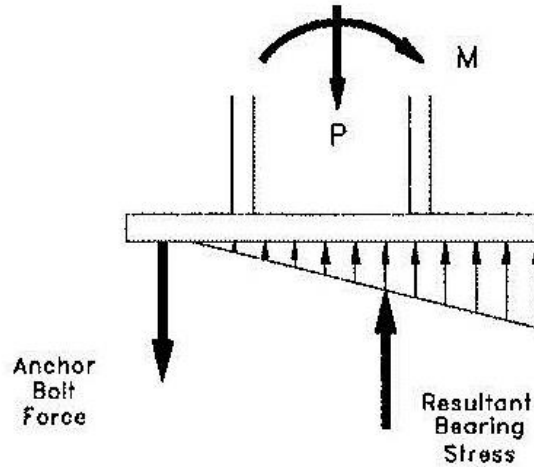
P = Post axial load

N = Depth of baseplate

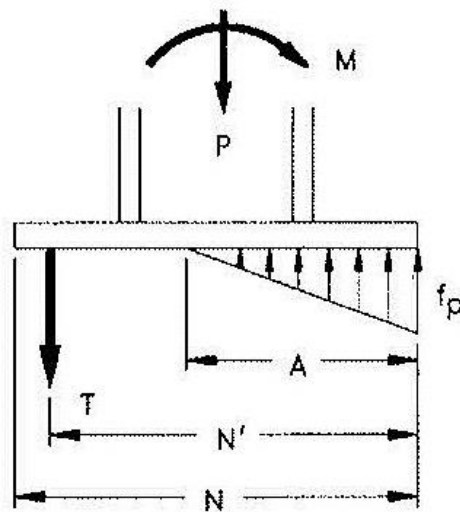
If Equation 22 is satisfied, then the baseplate design needs to follow the process for small eccentricities, otherwise the design process for large eccentricities needs to be followed. For the pedestrian/bicycle rail, it was found that the baseplate needed to be designed for large eccentricity, as the bending moment in the post was much higher than that of the axial load. The process laid out in the design guide for large eccentricities was then followed to determine the required

thickness. From this process it was determined that a ½-in. (13-mm) thick, ASTM A572 Grade 50 steel baseplate would provide adequate strength.

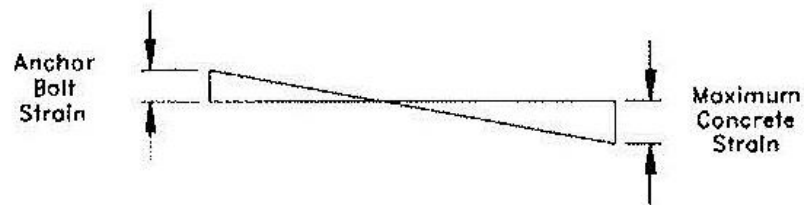
The required thickness of the plate was also checked through the use of simple static beam analysis in order to confirm that the results of design guide process were acceptable. The baseplate was treated like a beam with an applied tension force acting downward due to the anchor rods, a force acting upward due to the contact of the concrete parapet with the baseplate, and a moment acting on the plate from the attached post, as shown in Figure 58. The first case assumed an impact of the system from the traffic side similar to a vehicle impact. The moment for this case was assumed to be the moment capacity of the post. The baseplate was then designed to resist the elastic flexural capacity of the post. The second case applied the pedestrian/bicycle loading on the non-traffic side, creating a bending moment in the opposite direction. For the traffic-side loading case, the plate was assumed to be stiffened by the post, so the back end of the plate acted as a cantilever with a force applied at the end. For the pedestrian/bicycle loading case, it was assumed that the tension force from the anchor rods created a cantilever experiencing a bending moment due to the pedestrian/bicycle load applied on the attached post. The thickness of the baseplate could then be solved using Equations 23 through 25 for both cases.



(a) Resultant Compressive Bearing Stress Under Column Flange



(b) General Case



(c) Strain Distribution

Figure 57. AISC *Steel Design Guide 1* Column Baseplate Loading General Case [47]



Figure 58. Baseplate Simplified Traffic Impact (Top) and Pedestrian/Bicycle Loading (Bottom)

$$\sigma_b = \frac{M}{S} \quad (23)$$

$$S = \frac{bt^2}{6} \quad (24)$$

$$t = \sqrt{\frac{6F_r L}{b\sigma_{allowed}}} = \sqrt{\frac{6M_{P_{LL}}}{b\sigma_{allowed}}} \quad (25)$$

Where: σ_b = Bending stress
 M = Bending moment
 S = Section modulus of baseplate
 b = Width of baseplate cross-section
 t = Thickness of baseplate
 F_R = Force between baseplate and parapet due to rotation
 L = Distance from back of post to rear edge of baseplate
 M_{PLL} = Bending moment from post loading

From this process, it was determined that a $\frac{3}{8}$ -in. (10-mm) thick baseplate was needed to resist the vehicle impact loading case, and a $\frac{5}{8}$ -in. (16-mm) thick baseplate was needed to resist the pedestrian/bicycle loading. To provide adequate strength, a $\frac{5}{8}$ -in. (16-mm) thick, ASTM A572 Grade 50 steel baseplate was selected.

6.7.3 Post Offset

To reduce the amount of vehicle interaction with the pedestrian/bicycle rail, the post was set back, and the baseplate dimensions were defined to accommodate this offset. With the parapet being 10-in. (254-mm) wide with standard $\frac{3}{4}$ -in. (19-mm) chamfers on the front and rear edges of the parapet, the rear edge of the baseplate was placed 1 in. (25 mm) forward from the rear face of the parapet, or the pedestrian/bicycle traffic face. The post was then placed 1 in. (25 mm) forward from the rear edge of the baseplate, thus creating a post offset of 6 in. (152 mm) from the front, or traffic-side, face of the parapet.

While the previous simulation height study suggested that the vehicle could intrude up to 14.8 in. (376 mm), design constraints could not allow for a post offset that would completely eliminate the possibility for vehicle-post interaction. Because of this fact, the post offset was maximized for the parapet and baseplate dimensions to reduce interaction as much as possible.

6.8 Post-Rail and Post-Baseplate Connection Calculations

6.8.1 Post-Baseplate Loading

The post-baseplate connection was analyzed using both the pedestrian/bicycle and vehicle impact loading. However, the vehicle impact loading was considered to be a more extreme case, as it provided higher bending moment and shear force in the post. Designing the post-baseplate welds to resist the vehicle impact loading provided a more conservative approach. Designing for vehicle impact load also would reduce the chance that system would become a debris hazard when impacted by a vehicle by allowing the posts to deform first rather than immediately detach due to low connection strength.

For the vehicle impact loading, it was assumed that the loading would apply enough force to exceed the flexural capacity of the post. Once the post met its flexural capacity, no more force could be applied to the post. It was then assumed that the weld would need to resist the moment capacity of the post as well as the shear force to develop that moment. The shear force was assumed to be created by a concentrated force applied 10 in. (254 mm) above the base of the post, as shown in Figure 59. This height was based on vehicle structure intrusion in the previous barrier height simulations. The height corresponded to a location at which the vehicle would impact the post if the post were present during that simulation effort, and that height was confirmed in the full-system simulation effort. Using the assumed impact height along with the flexural capacity of the post, the force applied from the impact loading was found using Equation 26. This force was then used as the shear force for designing the weld.

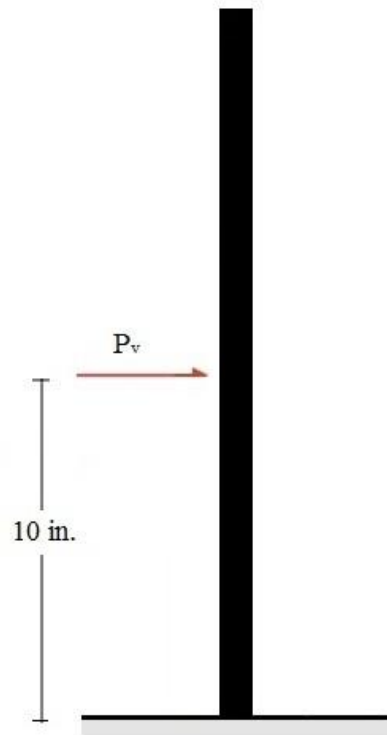


Figure 59. Post Vehicle Impact Loading

$$P_v = \frac{M_{NP}}{10} \quad (26)$$

Where: P_v = Assumed vehicle impact load

M_{NP} = Post nominal flexural capacity

The bending moment that corresponded to the flexural strength of the post was assumed to create an upward tension force on the weld attaching the front flange of the post to the baseplate, as shown in Figure 60. The post was assumed to rotate about the base of the rear flange when the

moment was applied to it. This rotation of the post would cause the front flange of the post to displace vertically and when welded, would experience a tension force. The tension force was then found using Equation 27.

$$T_w = \frac{M_P}{n} \quad (27)$$

Where: T_w = Tension in weld
 M_P = Bending moment in post
 n = Depth of post

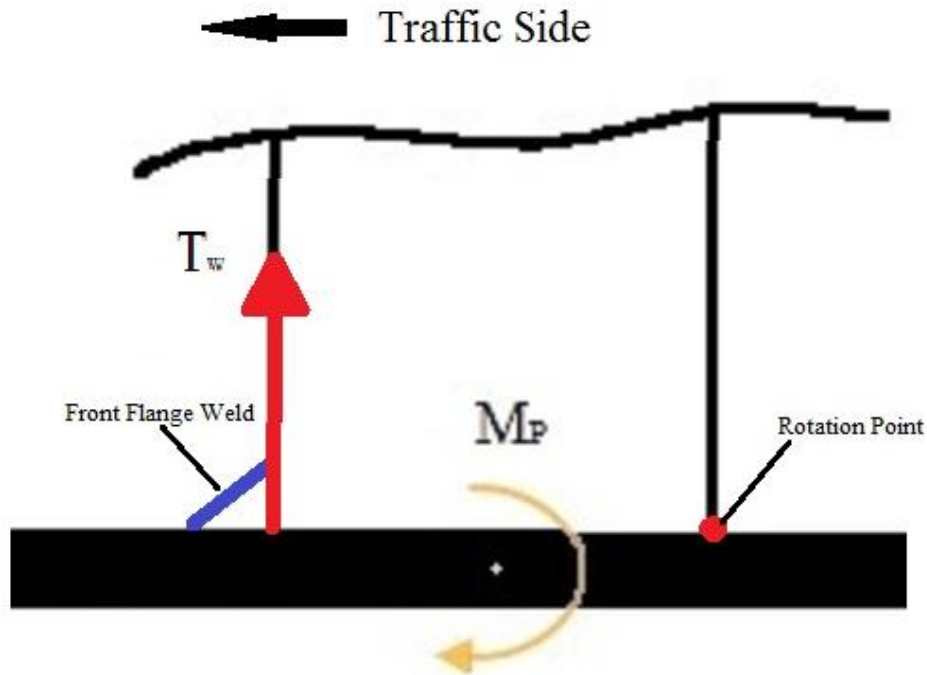


Figure 60. Post-Baseplate Front-Flange Weld Tension Diagram

The rail-post connection was designed to resist the previously-stated pedestrian/bicycle impact loading. The same type of rotation used for the post analysis was applied to the rail-post connection. Since the load was applied laterally at the center of the front flange of the rail, a moment would be produced at the connection. It was assumed that the rail would rotate about the point where the rear flange of the post met the rail, thus creating a tension force like the post-baseplate connection, as shown in Figure 61. The tension force was found in a similar manner to the post-baseplate connection using Equation 28.

$$T_w = \frac{P_P h}{2n} \quad (28)$$

Where: T_w = Tension in weld
 P_p = Pedestrian/Bicycle load
 h = Height of rail
 n = Depth of post

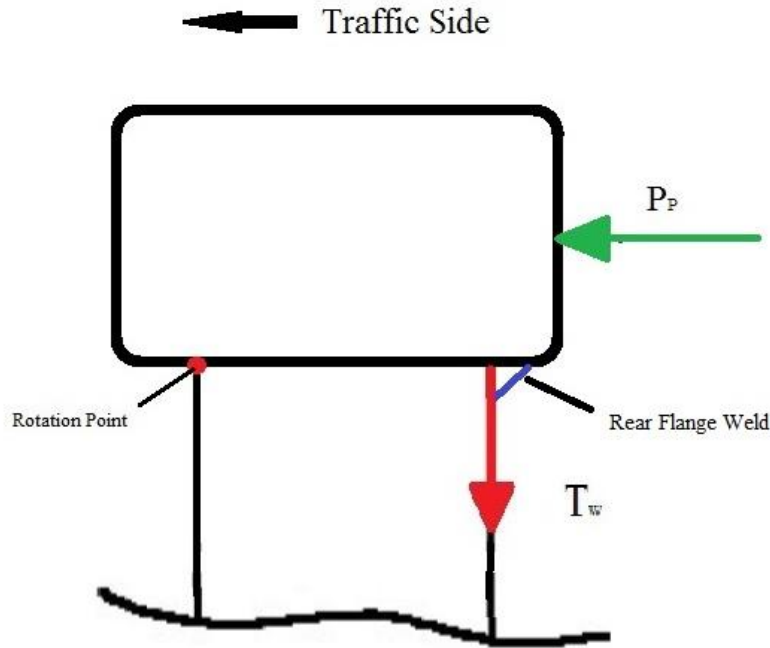


Figure 61. Rail-Post Rear-Flange Weld Tension

6.8.2 Weld Calculations

To attach the rail to the post and the post to the baseplate, fillet welds were used and analyzed using Section J2 of the AISC *Steel Construction Manual* [46]. The welds were assumed to be applied fully along all faces of the post for both the rail-post and post-baseplate connections. The strength of the welds was analyzed using Equation J2-5, as shown in Equation 29.

$$\phi R_n = \phi 0.60 F_{EXX} (1.0 + 0.50 \sin^{1.5} \theta) A_{we} \quad (29)$$

Where: ϕR_n = Weld resistance
 F_{EXX} = Filler metal classification strength
 A_{we} = Effective area of the weld
 θ = Angle between the line of action of the required force and the weld longitudinal axis
 $\phi=0.75$

The shear force was assumed to be resisted by the welds placed parallel to the load applied for both the rail-post and post-baseplate connections. The tension force created by the moment in the rail and post was assumed to be resisted by the weld along the front-flange. Also, the weld size was determined based on the size limitations for fillet welds within Chapter J of the AISC *Steel Construction Manual* [46]. Specifically, Table J2.4 specifies that when the thinnest joining material is $\frac{1}{4}$ in. (6 mm) or less, the minimum weld size that can be used is $\frac{1}{8}$ in. (3 mm). Additionally, it is stated that the maximum weld size along edges of material less than $\frac{1}{4}$ in. (6 mm) thick cannot exceed the thickness of the material. Since the thickness of the post and rails were chosen to be $\frac{1}{8}$ in. (3 mm) and the baseplate to be $\frac{5}{8}$ in. (16 mm), the weld size selected was $\frac{1}{8}$ in. (3 mm).

Using this process, it was found that $\frac{1}{8}$ -in. (3-mm) fillet welds using E70 filler metal would provide enough resistance to prevent failure when the pedestrian/bicycle loading was applied to the system for both connections. When analyzing the weld resistance of the post-baseplate connection under vehicle impact load, it was found that the front-flange weld did not provide enough strength when considered to act alone. However, this analysis was considered conservative as the front weld would not be the only weld resisting the tension force. The welds placed on the webs of the post would also provide tension resistance. Additionally, Table J2.5 within AISC *Steel Construction Manual* [46] states that tensions applied to fillet welds for parallel parts can be neglected for the design process. For shear, it was found that the weld resistance greatly exceeded the required strength needed to prevent failure under vehicle impact loading.

6.9 Anchor Rod Calculations

The design of epoxy adhesive anchorages for the railing-to-parapet connection was developed using ACI 318-14 procedures for concrete breakout, steel fracture, and bond strength [48]. The design calculations considered steel fracture, concrete breakout, and adhesive bond failure in tension. Shear calculations considered steel fracture, concrete breakout, and concrete pryout. The calculations also accounted for reduction in anchor capacity due to the distance to the edge of the parapet and anchor spacing based on the area of influence for the concrete and bond failures, as well as reduction factors for steel and concrete breakout for the loadings both in shear and tension. Anchorage area of influence defines a region of the concrete where the anchorage forces are distributed in order to develop load for both concrete breakout and bond strength. If these areas exceed the edge of the parapet or overlap the area of influence of other anchors, then the capacity of the anchor is reduced by the ratio of the unavailable area divided by the original assumed influence area. A simple example of area of influence for two anchors that exceed the concrete edge and interfere with adjacent anchors is shown in Figure 62. The purple area denotes where the area of influence extends beyond the parapet edges. The orange area indicates where the area of influence for anchors “A” and “B” overlap. In this area, only half of the overlapping area can be utilized by each anchor, so the anchor capacity must be reduced accordingly [49].

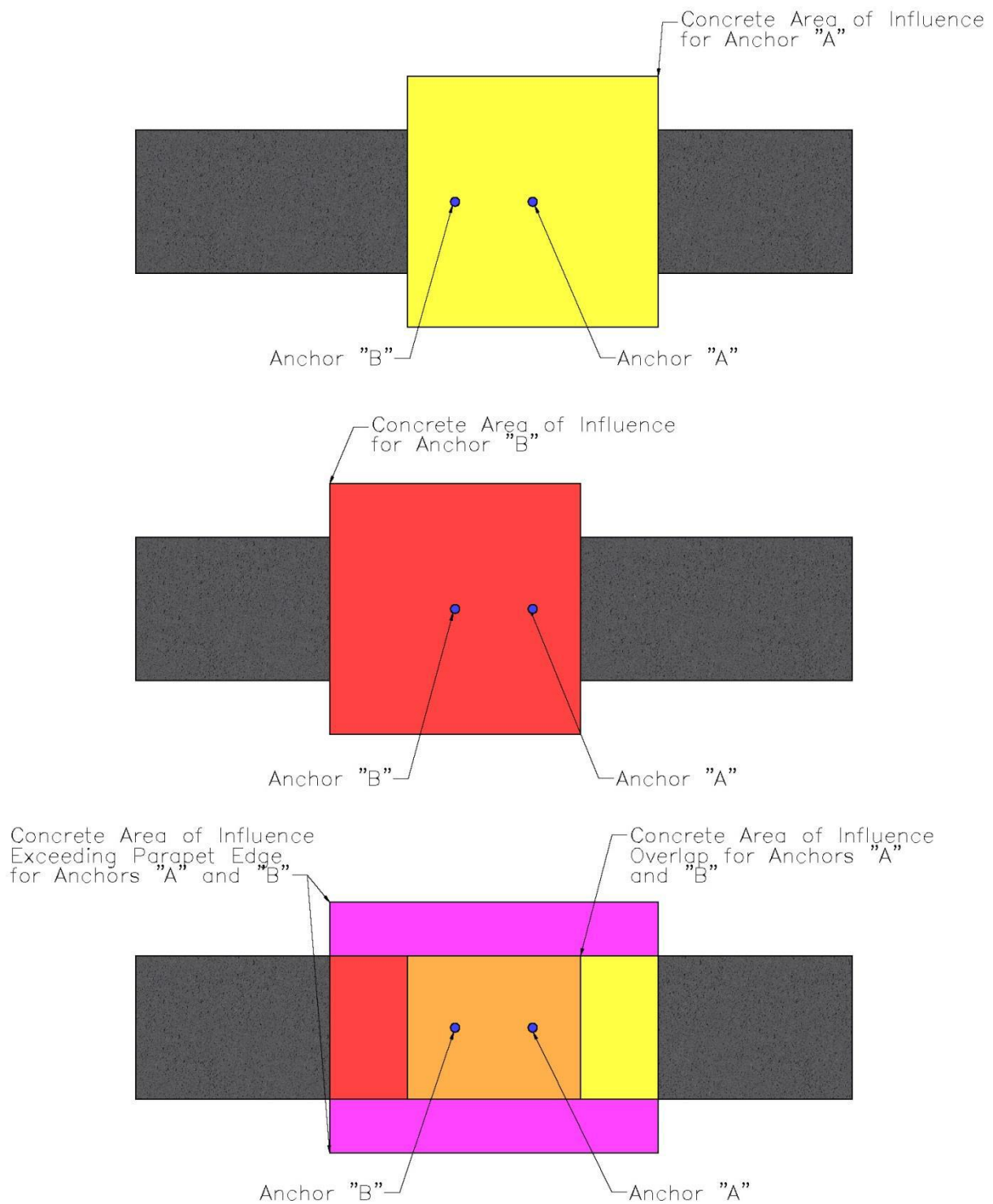


Figure 62. Concrete Area of Influence for Two Adjacent Anchors on Concrete Parapet [49]

A final note should be made regarding an additional modification that was made to the ACI 318-14 calculations for this project. Originally, the anchorage capacity was calculated just as ACI 318-14 entailed. However, anchor rod forces from the full-system simulation, discussed in later chapters, greatly exceeded the initial calculated values. Because of this finding, the anchorage capacity calculations were revisited in order to ensure the anchor rods would provide enough capacity to resist the forces observed in the simulation effort. Calculations for tensile concrete breakout capacity indicated that extremely large embedment depths would be required to provide the desired anchorage capacity. These calculations assume a concrete cone failure of the parapet that extends diagonally from the base of the anchor to the edges of the area of influence. While this assumption may be true for large-area, unreinforced slabs, it was not believed to be accurate for the reinforced concrete parapet in this research. A more reasonable form of the failure mode was believed to be a hybrid concrete cone and adhesive bond failure, as shown in Figure 63. In this type of failure mode, the concrete cone failure is prevented from extending to the base of the anchor by the longitudinal rebar. The hybrid failure assumption was extended to the ACI 318-14 calculations by assuming that the upper portion of the anchor embedment contributed to the concrete breakout and the lower portion of the embedment contributed to a bond failure. Thus, the calculations for the concrete breakout and bond strength were performed with different anchor embedment depths and then summed to determine the tensile anchor capacity [49].

This process was used in a previous MwRSF project, which involved redesigning the BR27C systems to use epoxy adhesive anchorage connections rather than the original cast-in-place anchor method used [49]. During bogie testing, it was found that the described method provided adequate capacity in tension for the two anchor rod case, bogie test no. IBP-3. Results from testing showed that anchor rod tension forces could have reached approximately 36.2 kips (161.0 kN), while calculations using the hybrid epoxy anchorage method calculated a capacity of 35.5 kips (157.9 kN). Results of the test when compared to initial calculations indicated that the hybrid epoxy method was reasonably accurate, so the process was considered to be acceptable for use in this design.

Originally, the tension force in the anchor rods was taken as the value calculated during the baseplate thickness determination process. However, once the system was simulated, which will be discussed in a following section, it was found that the tension forces were much higher than expected. The calculations were then performed once again using these higher tension values to ensure that the anchorage connection provided enough strength to prevent failure.

Using the stated methods, proper epoxy anchorage parameters were found. An embedment depth of 12 in. (305 mm) was chosen, with the first 5.5 in. (140 mm) resisting concrete breakout and the bottom 6.5 in. (165 mm) resisting bond failure. These values corresponded to the point at which the concrete breakout cone came into contact with the longitudinal reinforcement of the parapet. The anchor rod was chosen to be a ¾-in. (19-mm) diameter, ASTM F1554 Grade 105 threaded rod. Upon modification to the anchorage connection, the baseplate designed was revaluated to accommodate the increased anchor rod diameter and spacing.

All calculations for anchorages were performed using Hilti RE-500 epoxy adhesive, which has a bond strength of 1,560 psi (10.8 MPa). The concrete compressive strength for the design calculations was assumed to be 4,000 psi (27.6 MPa).

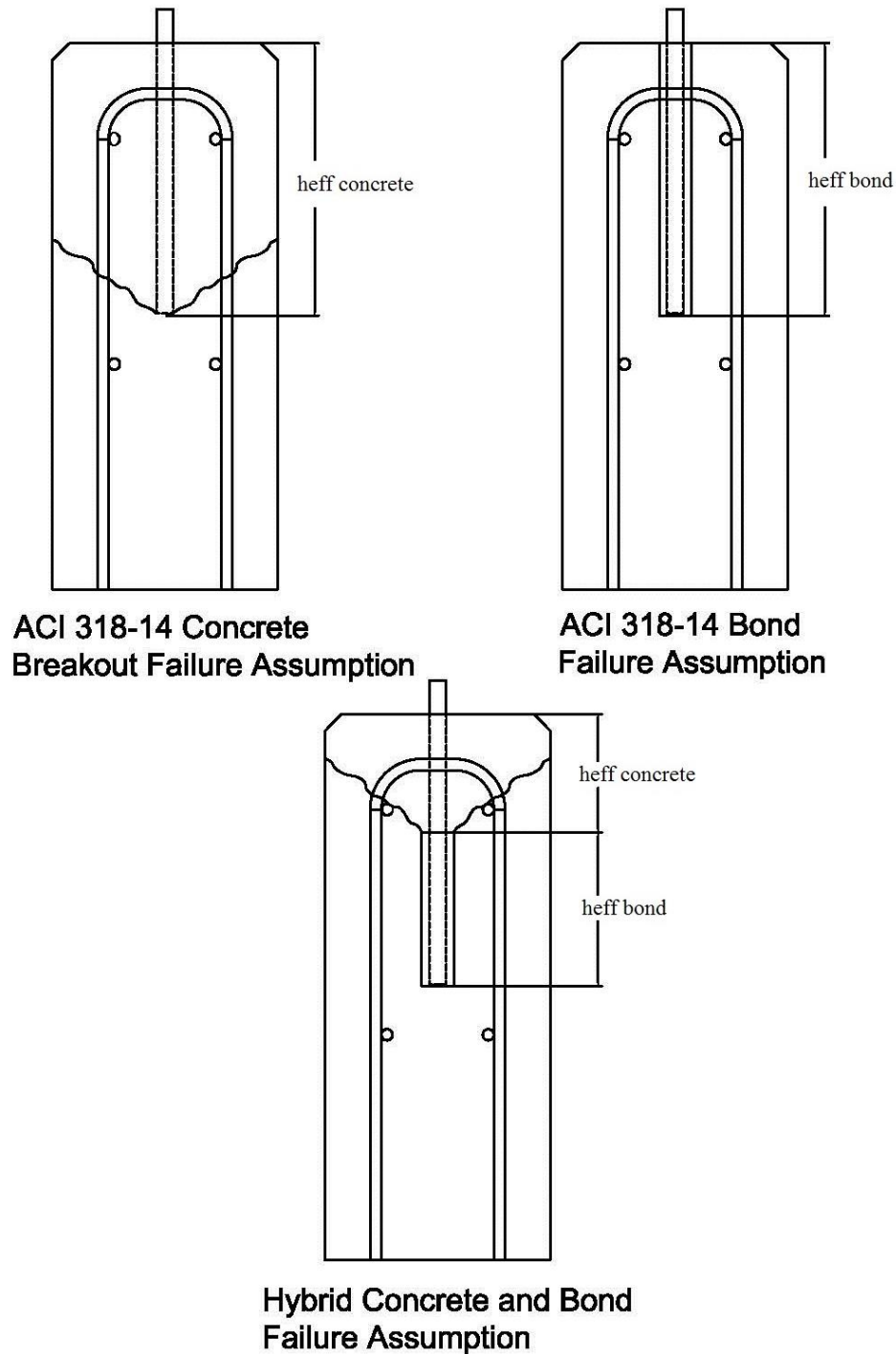


Figure 63. Comparison of ACI 318-14 Concrete Breakout and Hybrid Failure Assumptions [49]

6.10 Splice Tube

To ease installation and repair of the system, splice tubes were used to connect rail sections. Splice tubes allow sections of rails to be more easily connected and disconnected than their welded counterparts. Splice tubes simply slide into the ends of adjacent rail sections and allow the

connection of those rail sections through the use of hex bolts, in this case, that extend from the top of the rail sections through the splice tube and out the bottom side of rail sections. An example of the standard splice tube configuration is shown in Figure 64.

Since splice tubes join rail sections, they also experience the same loading as the rail sections. This requires that splice tube sections have equal or higher resistance to bending than the rail sections they connect. Designing the splice tube in this way ensures that failure will not occur at the splice as this could expose the ends of the rail section and create a spearing hazard.

The bending strength of any cross section is dependent upon the section modulus. The chosen rail section, which was 3 in. x 2 in. x $\frac{1}{8}$ in. (76 mm x 51 mm x 3 mm), had a section modulus of 0.867 in.³ (14,208 mm³) about the x-axis and 0.692 in.³ (11,340 mm³) about the y-axis. The splice tube would need to have a higher section modulus in both axes to be considered stronger. Since the splice tube needed to slide into the rail section, the proper splice tube dimensions needed to be selected to provide adequate clearance. It was determined that the splice tube should allow for a minimum clearance of $\frac{1}{8}$ in. (3 mm) on all sides when inserted into the rail. This selection would allow for the tube to be easily inserted into the rail and prevent binding in case of minor splice tube or rail warpage. Thus, the splice tube outside dimensions needed to be 2½ in. x 1½ in. (64 mm x 25 mm) at most. However, no standard section size listed within the *AISC Steel Construction Manual* [46] provided adequate stiffness and clearance.

Typical Splice Tube Detail

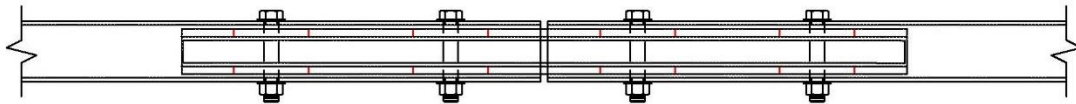


Figure 64. Typical Splice Tube Detail

Since no standard section sizes provided the correct strength and clearance, a built-up section design was pursued. Built-up sections are the joining of plate steel, usually by fillet welds, to create a non-standard section. An example of the cross section of a built-up section is shown in Figure 65. Using this method allows the designer to select all the parameters of the section to meet design needs.

To solve for section modulus, the built-up section was analyzed as separate sections then summed to find the total section modulus about both major axes. First, the two plates parallel to the axis of bending were analyzed, creating a configuration similar to Figure 66. The section modulus for this case was then solved using Equation 30. The plates perpendicular to the axis of bending were treated simply as rectangles, as shown in Figure 67, and the appropriate section modulus was calculated using Equation 31. The section moduli from both cases were then summed in order to find the total section modulus. The same process was repeated about the other major axis.

$$S_1 = \frac{b(d^3 - d_1^3)}{6d} = \frac{b((2t_1 + d_1)^3 - d_1^3)}{6(2t_1 + d_1)} \quad (30)$$

Where: S_1 = Section Modulus of Parallel Plates

b = Width of horizontal plates

d = Outside distance between plates

d_1 = Inside distance between plates

t_1 = Thickness of horizontal plates

$$S_2 = \frac{2b_1d_2^2}{6} = \frac{2t_2d_2^2}{6} \quad (31)$$

Where: S_2 = Section Modulus of Perpendicular Plates

d_2 = Height of vertical plates

b = Width of vertical plates

t_1 = Thickness of horizontal plates

t_2 = Thickness of vertical plates

Using this process, a 2½-in. x 1½-in. x 5/16-in. (64-mm x 38-mm x 8-mm) built-up section, utilizing 3/16-in. (5-mm) fillet welds provided the appropriate strength and clearance. The section modulus of the designed built-up section was calculated to be 1.044 in.³ (17,108 mm³) about the strong axis and 0.695 in.³ (11,389 mm³) about the weak axis, providing a built-up section with higher bending capacity along both major axes. The section also provided the necessary clearance of 1/8 in. (3 mm) on all sides.

The rail sections were designed to be spliced at 20-ft (6.1-m) intervals, and each rail was connected to the next rail with a splice tube assembly using a ½-in. (13-mm) gap between each rail end. The splices in the rail were placed 30 in. (762 mm) away from the end of the post. The splice was placed at this location (quarter-span) rather than at the mid-span of the rail because maximum bending would occur in the center of the span. Placing the splice at quarter-span was used to reduce the loading to the splice tube assembly.

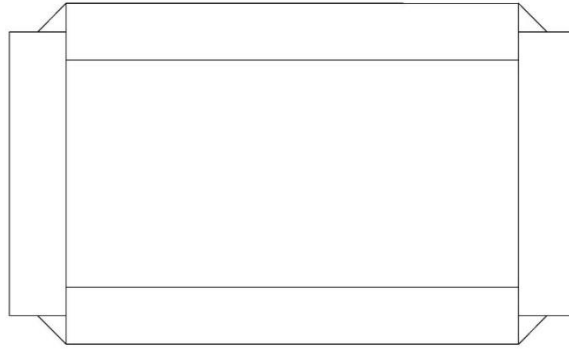


Figure 65. Standard Built-up Section Cross Section

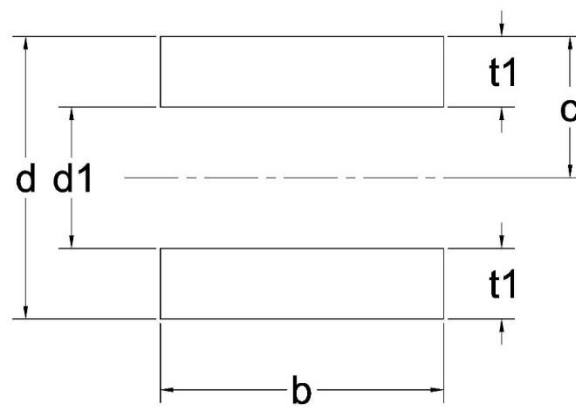


Figure 66. Splice Tube Parallel Plates Configuration for Section Modulus Calculation

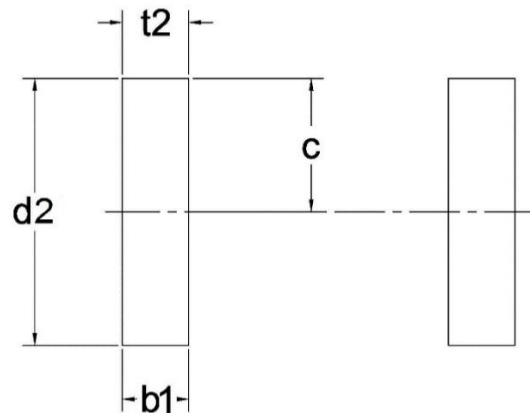


Figure 67. Splice Tube Perpendicular Plates Configuration for Section Modulus Calculation

6.11 Parapet Details

The general parapet dimensions desired by Iowa DOT was 24 in. (610 mm) tall by 10 in. (254 mm) wide. The compressive strength of the concrete was specified to be 4,000 psi (27.6 MPa). The reinforcement for the parapet was determined by MwRSF engineers to resist an estimated TL-2 vehicle impact loading of 35 kips (156 kN) using yield-line theory. Iowa DOT had

stated that the design should employ no greater than no. 4 steel reinforcing bars using 2-in. (51-mm) concrete clear cover.

Since MASH TL-2 impacts into rigid barriers had not yet been conducted, the required design strength for the parapet was scaled from known impact loads of MASH TL-3 impacts into rigid parapets, which have typically been around 70 kips. This 70 kip load was scaled down according to the difference in Impact Severity (IS) between MASH TL-2 and TL-3. The IS for a TL-2 impact is approximately 50 percent of the IS for a TL-3 impact. Thus, the required TL-2 barrier strength was established as half that of a TL-3 system, or 35 kips. Note, AASHTO's LFRD Bridge Design Specifications currently list the TL-2 and TL-3 impact loads, which haven't yet been updated to reflect MASH standards, as 27 kips and 54 kips respectively. The MASH TL-3 impact load of 70 kips represents a 30 percent increase over the previous NCHRP Report 350 TL-3 impact load of 54 kips. When the same 30 percent increase is applied to the old TL-2 load of 27 kips, the resulting MASH TL-2 load would be estimated as 35 kips.

The barrier geometry was selected by the Iowa DOT and Yield Line Analysis was utilized to design a reinforcement configuration that would ensure a strength above the 35 kip required strength. The final barrier configuration had a design strength over 40 kips only because the Iowa DOT did not want to utilize rebar smaller than #4 bars.

6.12 Preliminary Design Details for Full System Simulation Effort

The design that was modeled for the final simulation effort utilized the parapet details selected by Iowa DOT, which was a 24-in. (610-mm) tall by 10-in. (254-mm) wide concrete parapet. For the posts, HSS 3-in. x 2-in. x $\frac{1}{8}$ in. (76-mm x 51-mm x 3-mm) ASTM A500 Grade C steel tube sections were selected. For the rails, HSS 2-in. x 2-in. x $\frac{1}{8}$ in. (51-mm x 51-mm x 3-mm) ASTM A500 Grade C steel sections were chosen. The baseplate dimensions were 6 in. (152 mm) deep by 7 in. (178 mm) wide by $\frac{3}{8}$ in. (10 mm) thick and the material selected was ASTM A572 Grade 50 steel. The post was placed on the baseplate such that it allowed for the front flange of the post to have a 5-in. (127-mm) offset from the front face of the parapet.

The baseplate design allowed for the use of two anchor rods spaced 5 in. (127 mm) apart along the longitudinal axis of the barrier. These anchor rods were centered between the front and rear faces of the parapet. The anchor rods selected were $\frac{5}{8}$ -in. (16-mm) diameter, ASTM F1554 Grade 55 threaded rods utilizing an embedment depth of 6 in. (152 mm) and epoxy to attach them to the parapet. The post-to-baseplate and rail-to-post connections used $\frac{1}{8}$ -in. (3-mm) fillet welds.

The attached bicycle rail was designed to be installed using 20-ft (6-m) pre-assembled sections with a post spacing of 10 ft (3 m). For future full-scale crash testing, the design was assembled with five sections, creating an overall system length of 100 ft (30.5 m). Adjacent rail sections were connected through the use of splices tubes and ASTM A325 bolts. Originally, HSS 2½-in. x 1½-in. x $\frac{1}{8}$ in. (64-mm x 38-mm x 3-mm) ASTM A500 Grade C steel sections and $\frac{1}{8}$ -in. (3 mm) thick ASTM A572 thick shims were selected. However, during the simulation process, the splice tube assemblies were changed to the same built-up splice tube sections that were employed in the final system design.

7 MASH 2270P PICKUP TRUCK SIMULATION OF FULL SYSTEM

7.1 Introduction

After the system was preliminarily designed, the next step involved simulation of the system to predict its crash performance during testing. This process was performed to confirm that design choices were appropriate and to determine the location of the Critical Impact Point (CIP), which is the location that creates the worst-case impact scenario. The model simulated the test conditions of MASH 2016 test designation no. 2-11, in which a 2270P pickup truck model impacts the system at 44 mph (70 km/h) at a 25-degree impact angle. The ability of the system to capture and redirect the vehicle, the severity of snag between the vehicle and the attached steel railing, and component forces were all observed to evaluate the performance of the preliminary design.

7.2 System Model

The main components, such as the parapet, rails, posts, splice tubes, baseplates, and connection hardware were initially modeled within Solidworks, meshed using Hypermesh, and the impact was simulated using LS-DYNA. The concrete parapet had dimensions of 24 in. (610 mm) tall by 10 in. (254 mm) wide by 100 ft (30.5 m) long, used a vehicle-to-barrier friction of 0.4, and was modeled as rigid and fixed.

The vehicle used in the simulations was the same UNL10x model that was determined to be the most accurate during the validation effort. The impact conditions of the simulation were defined to replicate the conditions of MASH 2016 test designation no. 2-11, which are the test conditions that will be used to evaluate the system's performance in full-scale crash testing. Both full-scale testing and simulation were believed to be more critical with the pickup truck test (MASH test no. 2-11) than the small car test (MASH test no. 2-10), therefore initial simulations focused on evaluation with the Chevrolet Silverado 2270P vehicle model.

The mid-planes of the posts, rails, and splice tubes were modeled using shell elements. The shell elements were then given appropriate contact thickness in order to properly model the sections. The material properties were defined using data from previous static testing of ASTM A500 grade B steel using *MAT_PIECEWISE_LINEAR_PLASTICITY. The testing showed that the strength of ASTM A500 Grade B steel exceeded the nominal values stated for ASTM A500 Grade C steel assumed for the combination rail tubing. Thus, it was determined to be acceptable to use the ASTM A500 Grade B steel material model as it was already defined.

To model the welds between the post and the rails, the nodes between the posts and rails were merged. Current simulations of weld tearing and material failure require extensive investigation to weld release and material failure parameters based on weld thickness, base material strength, discontinuities or differences in as-produced weld geometries, and accurate failure prediction of the base material. Due to time and funding limitations on this project, weld failure was not considered. Because weld failure will cause the post-to-rail and post-to-parapet connection to fail, weld failure would likely reduce (not increase) snagging. Therefore, by not modeling weld failure, simulations which predict successful behavior according to MASH would give more confidence in the adequacy of the recommended system design during testing.

The baseplates were modeled similarly to the posts and rails, but with different material properties. The mid-planes were meshed using shell elements and the material properties were defined using *MAT_PIECEWISE_LINEAR_PLASTICITY. It was desired that the material properties matched ASTM A572 Grade 50 steel. Previous work performed at MwRSF stated that ASTM A572 Grade 50 steel was similar to AASHTO M180 steel used in guardrail systems [50]. The stress-strain curve was taken from that work and modified to better match the nominal properties of ASTM A572 Grade 50 steel. Originally, the material model had a defined yield strength of 65 ksi (450 MPa). This value was reduced to 50 ksi (350 MPa), and the stress-strain curve was modified to match expected yield and ultimate stresses. The modified stress-strain curve, along with the original, is shown in Figure 68. The connection of the post to the baseplate was treated in the same manner as the post-rail connection.

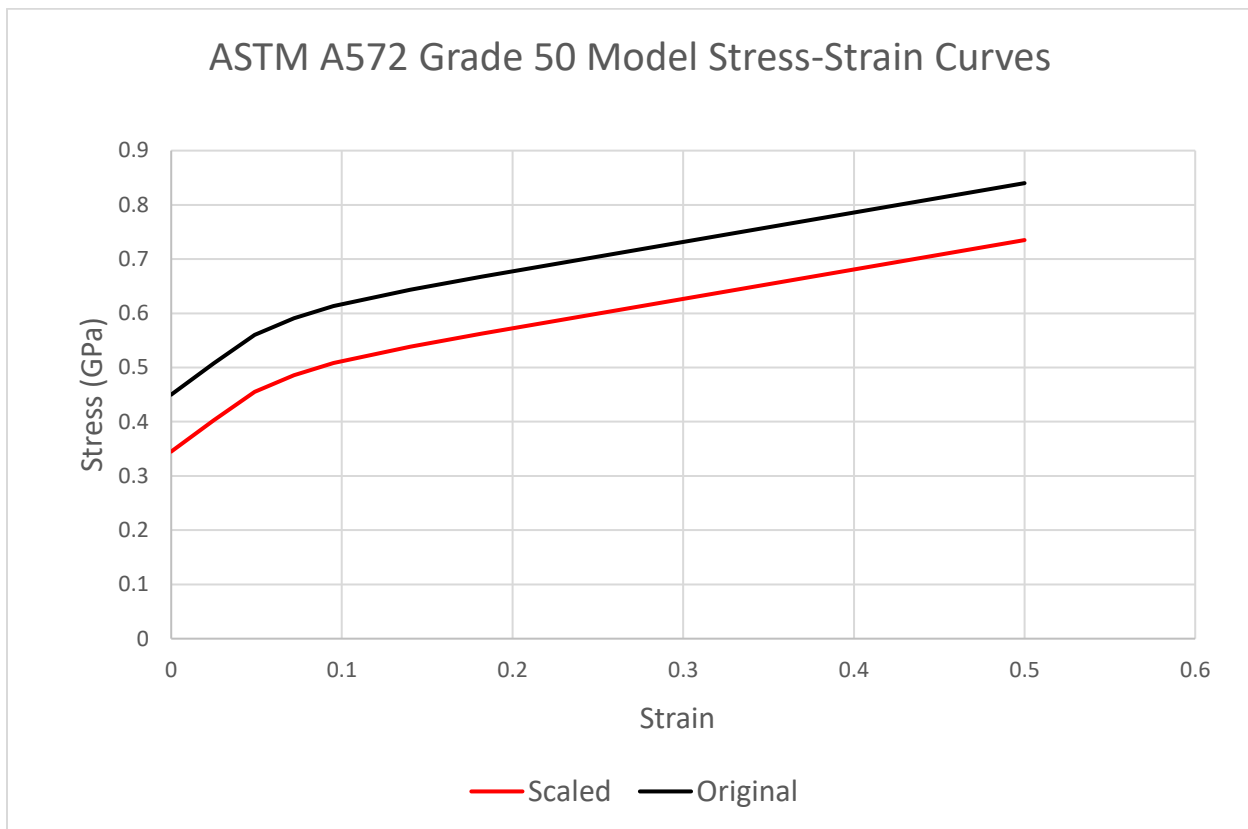


Figure 68. ASTM A572 Model Stress-Strain Curve Comparison

The anchor rod shafts were modeled as hexagonal cylinders rather than trying to mesh the threads. Meshing threads was determined unnecessary as that amount of detail would take many elements and drastically increase computing cost for little gain. To make up for the absence of threads, the nodes of the nut were merged to the shaft, thus creating a rigid bond between the shaft and nut. To connect the anchor rod to the parapet, the nodes of the anchor rod shaft were merged with the nodes on the top surface of the parapet. There was no need to model the anchor rods exactly as they would appear in the actual system, as no concrete deformation would occur in the simulation due to the parapet's rigid material properties.

These anchor rods were meshed using solid elements defined with *MAT_PIECEWISE_LINEAR_PLASTICITY for the material properties. A similar process to define the stress-strain curve as used previously was applied to the anchor rods using a stress-strain curve generated from testing of ASTM A325 bolts. However, the anchor rods needed to be scaled up, as the ASTM A325 model had a defined yield strength of 92 ksi (634 MPa) and the ASTM F1554 Grade 105 anchor rods assumed for the combination rail design had a yield strength of 105 ksi (724 MPa). The baseplate, post, and anchor rod mesh is shown in Figure 69.

The geometry of the splice tube connection hardware was similar to that of the anchor rods. The bolt head and nut were modeled as hexagonal cylinders on the ends of the splice tube bolt shaft, as shown in Figure 70. The nodes of the nut and bolt model were merged to the shaft to create a rigid connection. Once again, solid elements were used with material properties defined by *MAT_PIECEWISE_LINEAR_PLASTICITY. The material properties were selected to match the unmodified ASTM A325 bolt model mentioned previously.

For both the anchor rods and splice tube bolts, *INITIAL_STRESS_SECTION was used to generate preload. This method compresses the element that the section is defined on until that element reaches a defined stress value and holds that value for a defined amount of time. An example of the stressed and unstressed state is shown in Figure 71.

The final full-system model is shown in Figures 72 through 75. The system was modeled with five rail sections, thus creating an overall length of 100 ft (30.5 m). Additional cross sections were created to monitor forces at the base of the impacted post, anchor rods at that same post, and the splice tube bolts at the splice nearest the impact. The modeling techniques only allowed for deformation modes of the railing, and no failure of the connection could occur. Since the connections could not fail, the loads into the components would be expected to reach values higher than what would occur in full-scale crash testing.

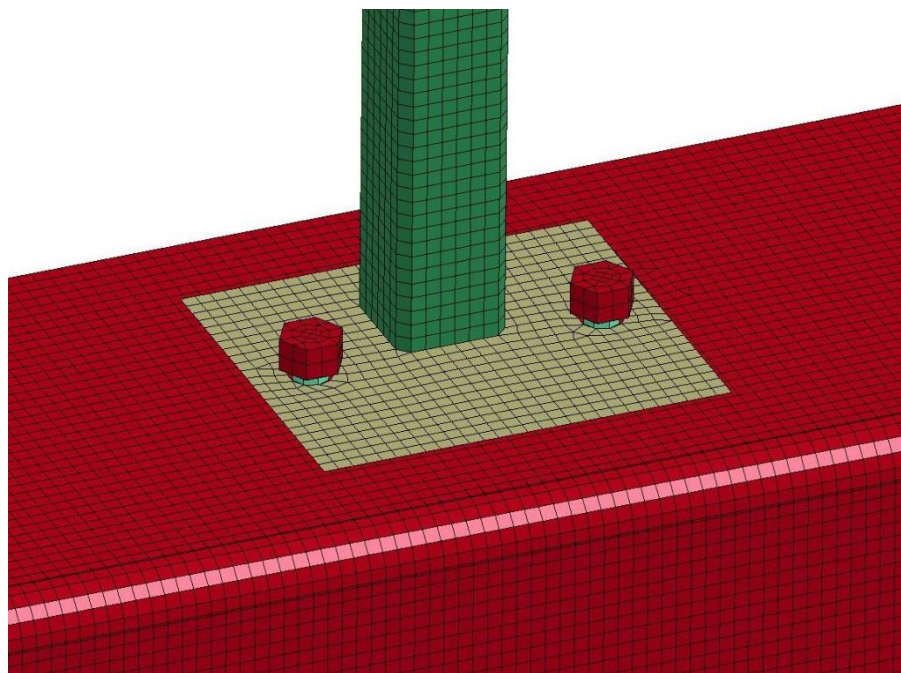


Figure 69. Post-Baseplate and Anchor Rod Connection

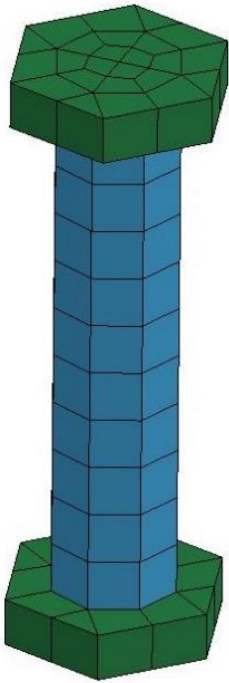


Figure 70. Splice Tube Bolt Model

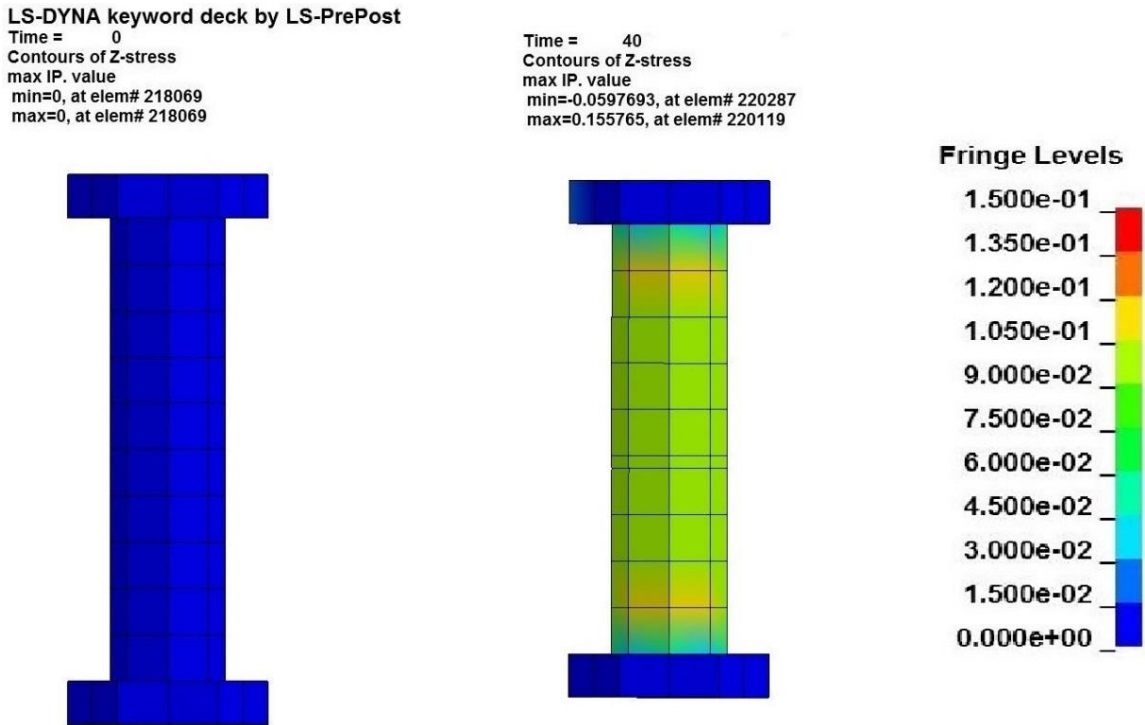


Figure 71. Splice Tube Bolt Assembly with No Preload (Left) and with Preload (Right)

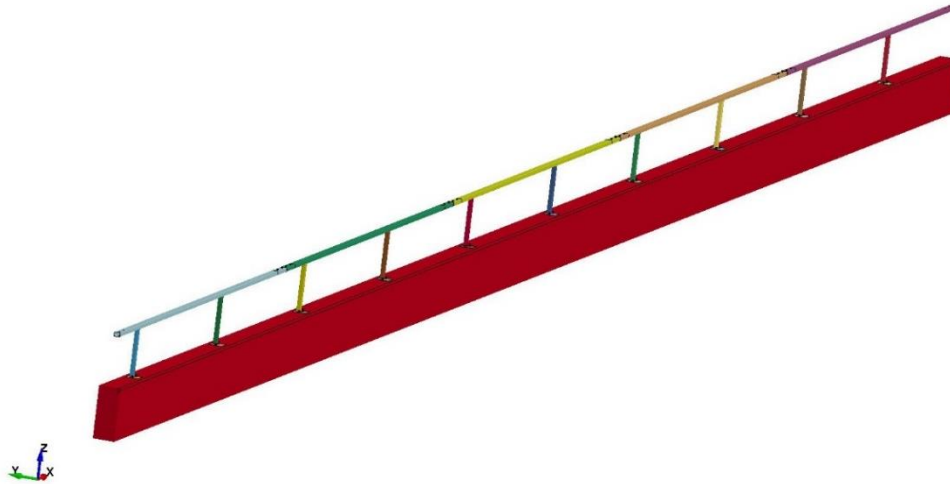


Figure 72. Combination Rail Model

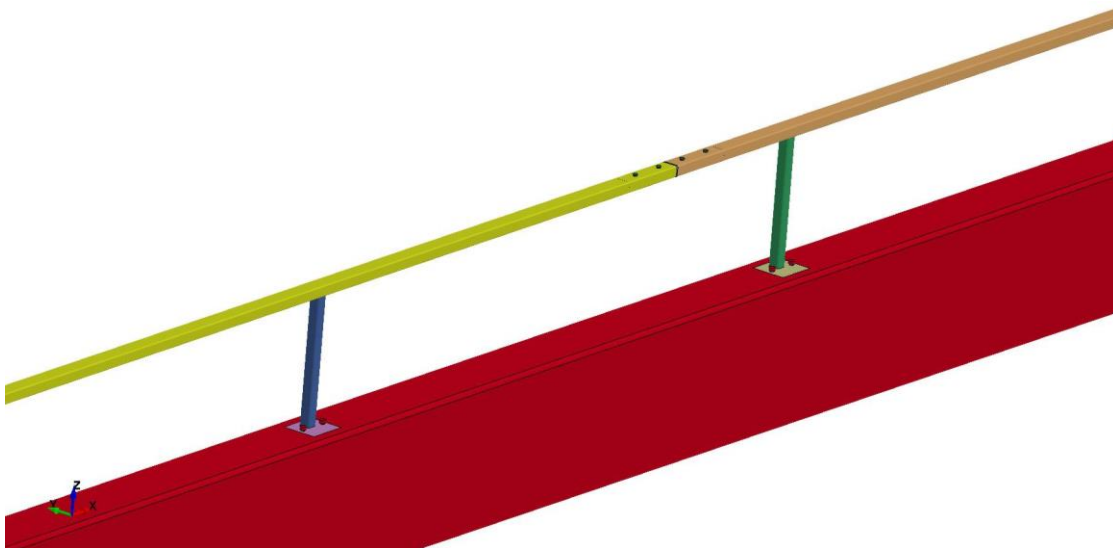


Figure 73. Combination Rail Close-Up

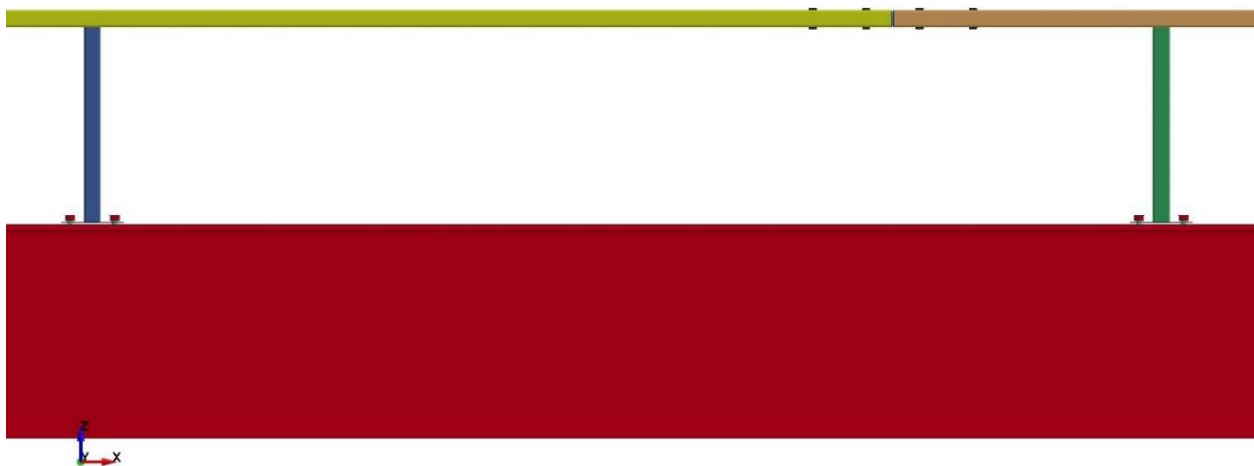


Figure 74. Combination Rail Front-View



Figure 75. Full Impact Model Top-View

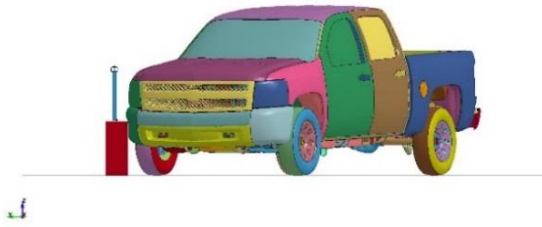
7.3 Simulation Results

Multiple impact locations were simulated to analyze the barrier performance and determine the CIP. Specifically, seven different impact locations were chosen to try to select the worst-case impact scenario. During this process, vehicle change in velocity, anchor rod/splice tube bolt forces, post/rail deformations, and vehicle intrusion were monitored to help select the CIP for full-scale crash testing, as well as to make necessary design changes based on the performance. Overall, snag severity was considered to be the most important factor when determining the CIP for this system.

The first simulated impact location involved the vehicle model impacting 4.3 ft (1.3 m) upstream (US) from Post No. 7. This location was chosen to try to maximize vehicle snag on the post. Graphical results of the simulation are shown in Figure 76. The vehicle impacted the post, which caused the post to deflect backward and eventually buckle. The front bumper and headlight assembly came into contact with the post, followed by significant snagging of the right-front fender on Post No. 7, as shown in Figure 77. The vehicle continued forward and was safely redirected by the system.

The next simulated case involved the vehicle impacting 3.3 ft (1 m) US from Post No. 7. Graphical results of the simulation are shown in Figure 78. The vehicle impacted the post, causing the post to buckle at the point where the front bumper made contact as well as just above the baseplate. The front bumper and the headlight assembly came into contact with the post, followed by significant snagging of the right-front fender on Post No. 7, as shown in Figure 79. The vehicle continued forward and was safely redirected by the system.

LS-DYNA keyword deck by LS-PrePost
Time = 0.000



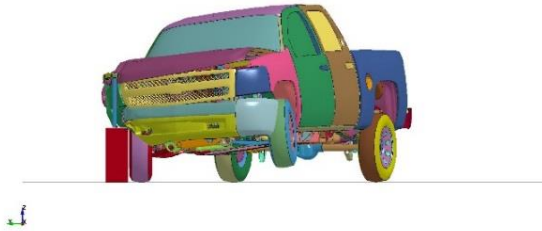
Time = 0.000 sec

LS-DYNA keyword deck by LS-PrePost
Time = 0.400



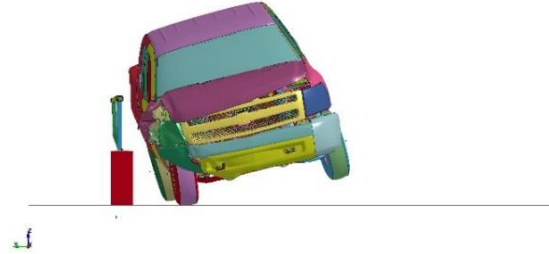
Time = 0.400 sec

LS-DYNA keyword deck by LS-PrePost
Time = 0.100



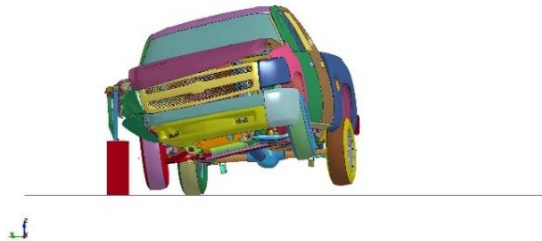
Time = 0.100 sec

LS-DYNA keyword deck by LS-PrePost
Time = 0.500



Time = 0.500 sec

LS-DYNA keyword deck by LS-PrePost
Time = 0.200



Time = 0.200 sec

LS-DYNA keyword deck by LS-PrePost
Time = 0.600



Time = 0.600 sec

LS-DYNA keyword deck by LS-PrePost
Time = 0.300



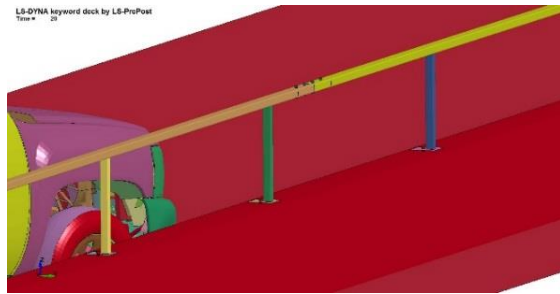
Time = 0.300 sec

LS-DYNA keyword deck by LS-PrePost
Time = 0.700

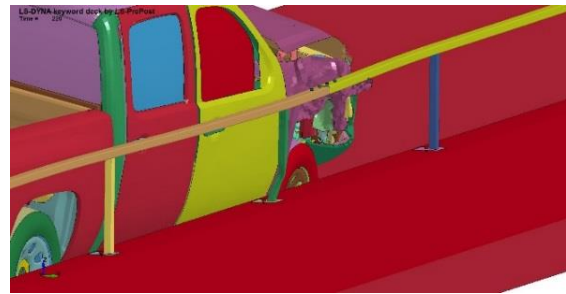


Time = 0.700 sec

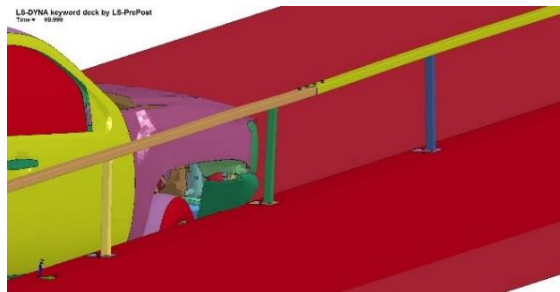
Figure 76. Downstream Sequential Views, Impact 4.3 ft (1.3 m) US from Post No. 7 Simulation



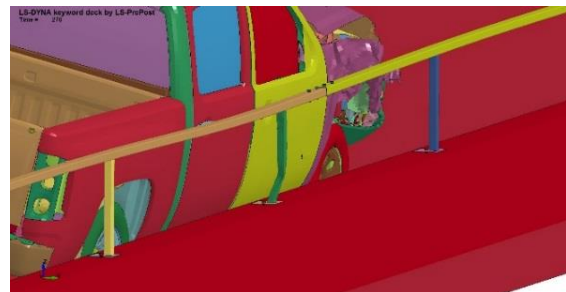
Time = 0.000 sec



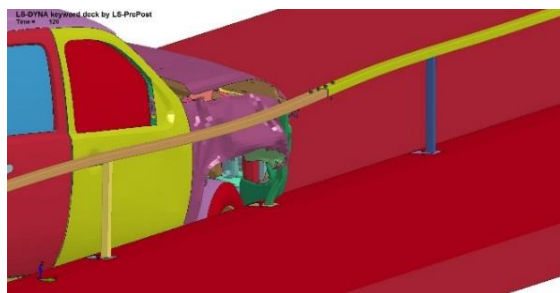
Time = 0.200 sec



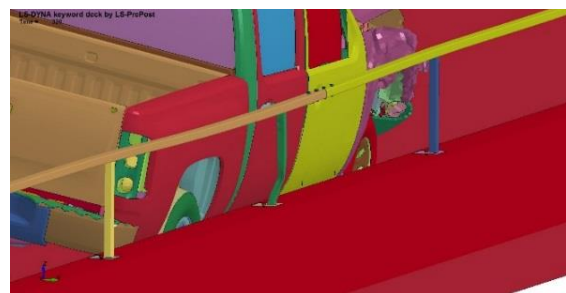
Time = 0.050 sec



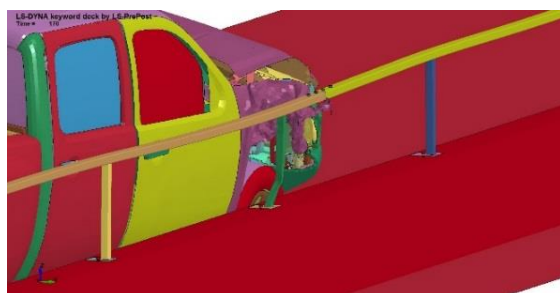
Time = 0.250 sec



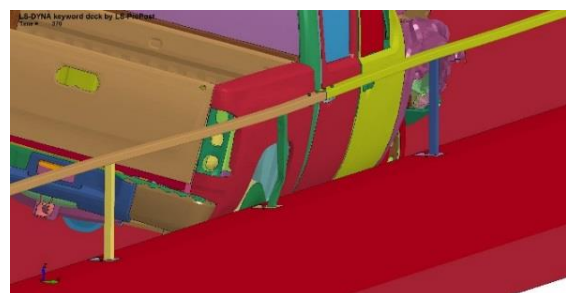
Time = 0.100 sec



Time = 0.300 sec



Time = 0.150 sec



Time = 0.350 sec

Figure 77. Post Snag Sequential Views, Impact 4.3 ft (1.3 m) US from Post No. 7 Simulation

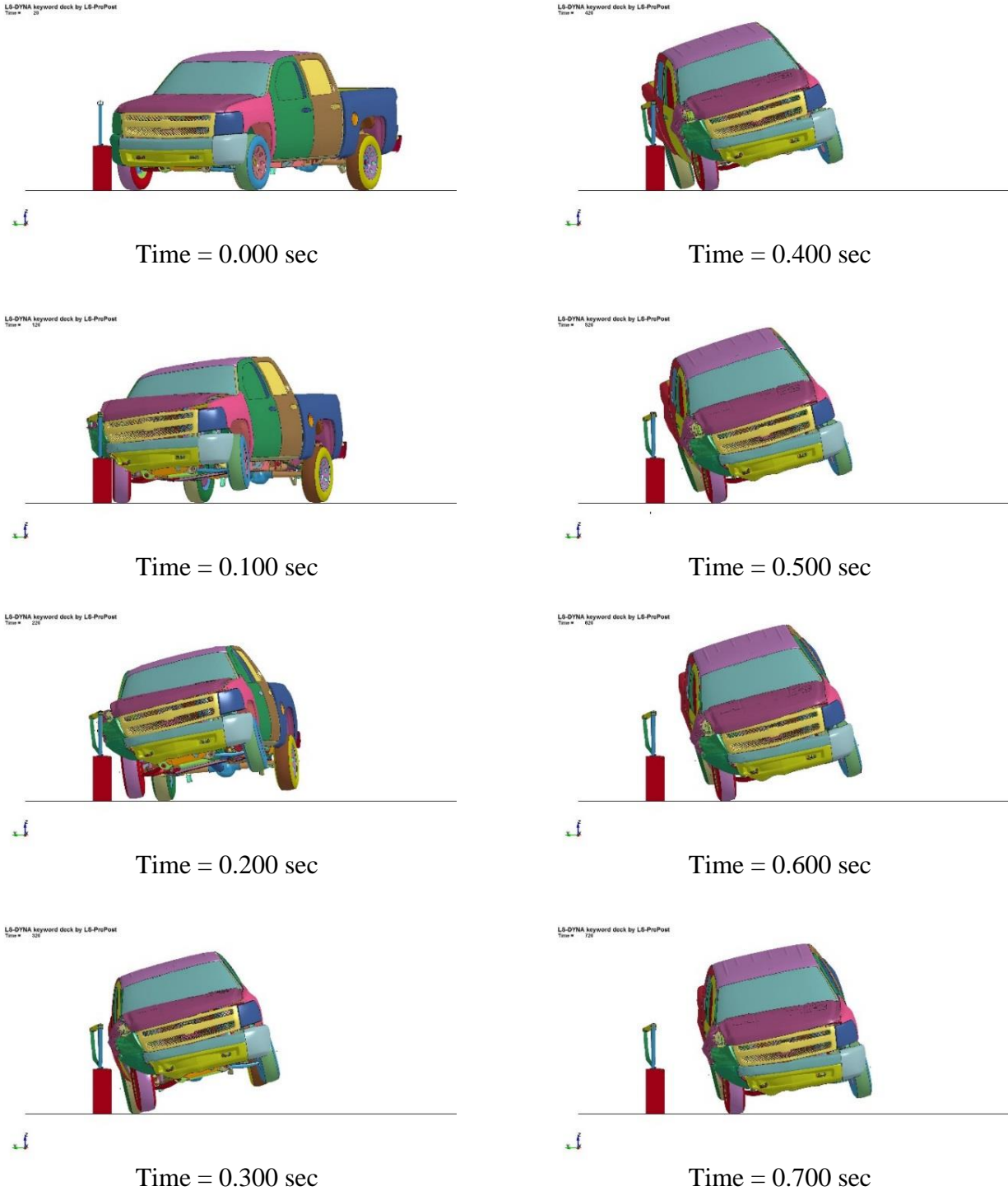
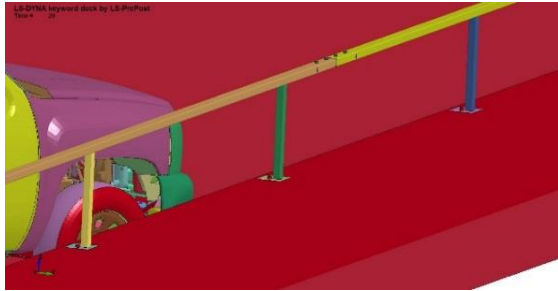
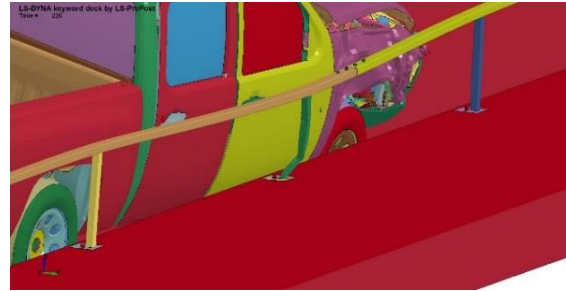


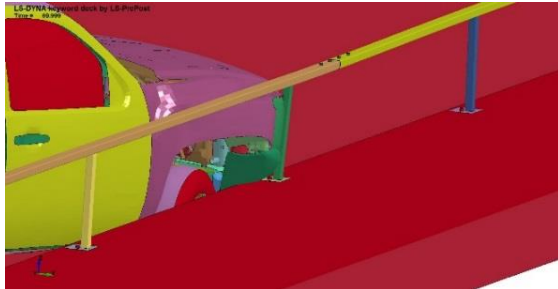
Figure 78. Downstream Sequential Views, Impact 3.3 ft (1 m) US from Post No. 7 Simulation



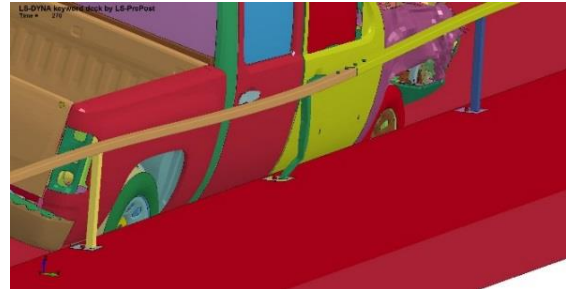
Time = 0.000 sec



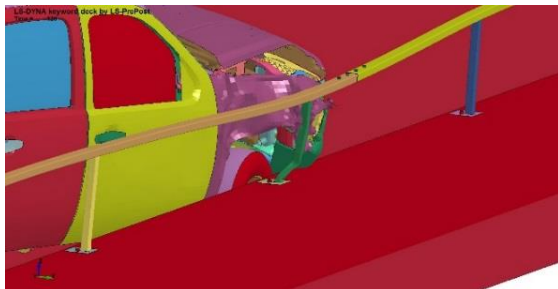
Time = 0.200 sec



Time = 0.050 sec



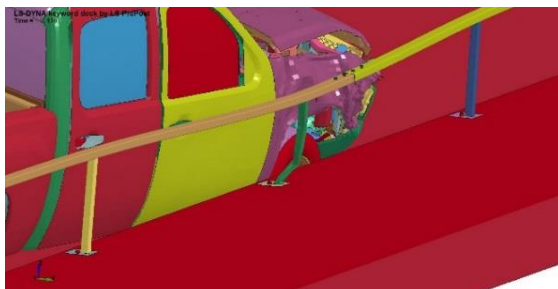
Time = 0.250 sec



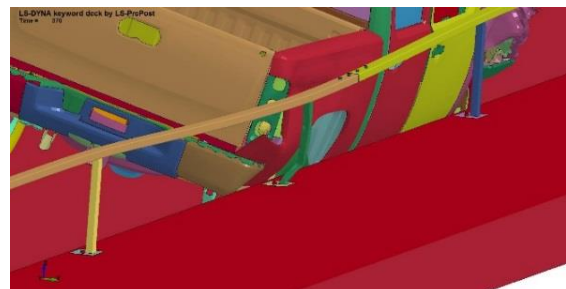
Time = 0.100 sec



Time = 0.300 sec



Time = 0.150 sec



Time = 0.350 sec

Figure 79. Post Snag Sequential Views, Impact 3.3 ft (1 m) US from Post No. 7 Simulation

The next simulated case involved the vehicle impacting 1.7 ft (0.5 m) US from Post No. 7. Graphical results of the simulation are shown in Figure 80. Similarly to the previous simulations, the vehicle impacted the post, causing the post to buckle at the point where the front bumper made contact. The front bumper and headlight assembly came into contact with the post, followed by significant snagging of the right-front fender on Post No. 7, as shown in Figure 81. Following the post buckling, the baseplate experienced significant bending due to post rotation. The vehicle continued forward and was safely redirected by the system.

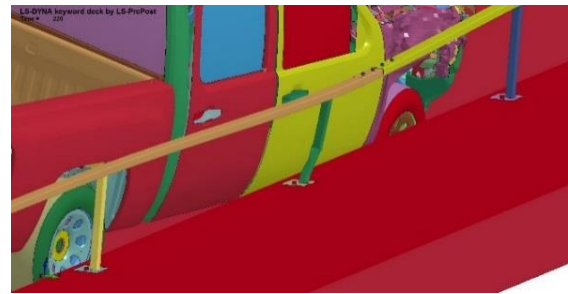
The next simulations were modeled to evaluate loading and snag on the splice and splice hardware. The first simulation involved the vehicle impacting 2.6 ft (0.8 m) US from the splice downstream (DS) from Post No. 7. The second case simulated the same impact point, however, the splice was placed US from Post No. 7 rather than DS in an attempt to snag both the splice and post. Graphical results from both of these simulations are shown in Figures 82 through 84. For both cases, the vehicle impacted the system with minor interaction between the vehicle and the splice section. Slight snagging of the fender and hood on the splice tube bolts was observed. In the reversed case, the fender experienced snagging on the post DS from the impacted splice. As the simulations continued, the vehicle was safely redirected without excessive pitch or roll motions.



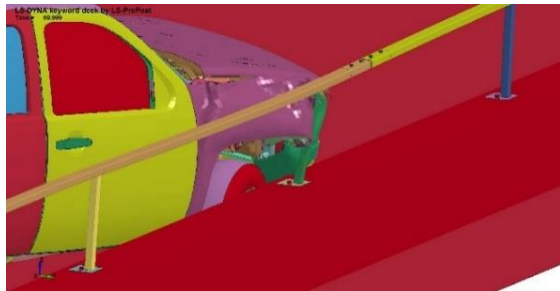
Figure 80. Downstream Sequential Views, Impact 1.7 ft (0.5 m) US from Post No. 7 Simulation



Time = 0.000 sec



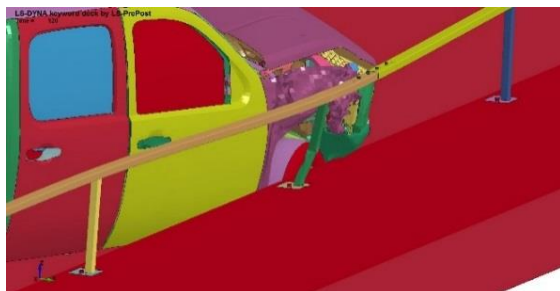
Time = 0.200 sec



Time = 0.050 sec



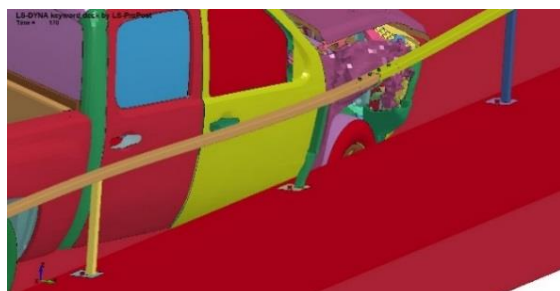
Time = 0.250 sec



Time = 0.100 sec



Time = 0.300 sec



Time = 0.150 sec



Time = 0.350 sec

Figure 81. Post Snag Sequential Views, Impact 1.7 ft (0.5 m) US from Post No. 7 Simulation

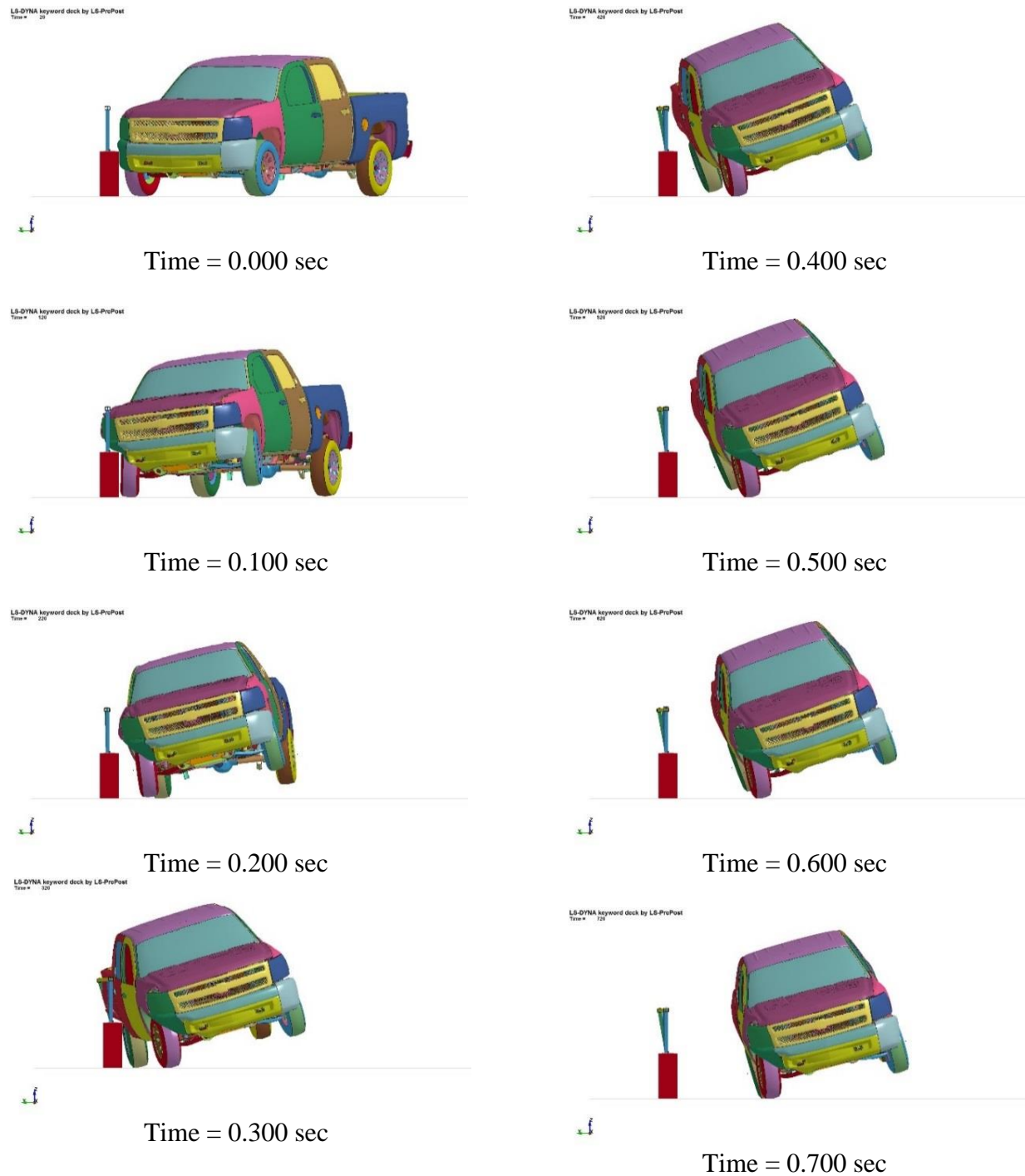
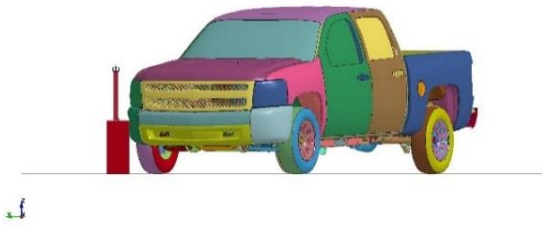


Figure 82. Downstream Sequential Views, Impact 2.6 ft (0.8 m) US from Splice Simulation

LS-DYNA keyword dock by LS-PrePost
Time = 20



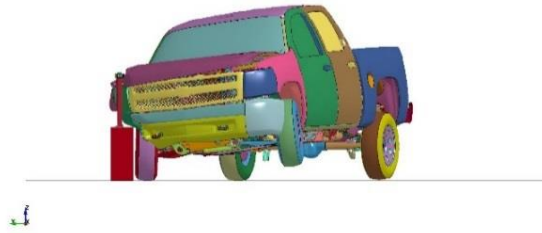
Time = 0.000 sec

LS-DYNA keyword dock by LS-PrePost
Time = 400



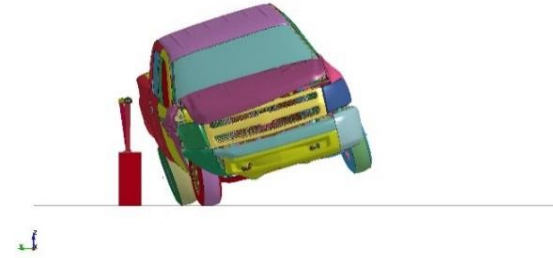
Time = 0.400 sec

LS-DYNA keyword dock by LS-PrePost
Time = 820



Time = 0.100 sec

LS-DYNA keyword dock by LS-PrePost
Time = 820



Time = 0.500 sec

LS-DYNA keyword dock by LS-PrePost
Time = 220



Time = 0.200 sec

LS-DYNA keyword dock by LS-PrePost
Time = 420



Time = 0.600 sec

LS-DYNA keyword dock by LS-PrePost
Time = 320



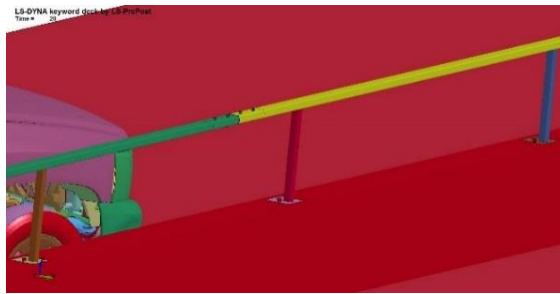
Time = 0.300 sec

LS-DYNA keyword dock by LS-PrePost
Time = 720

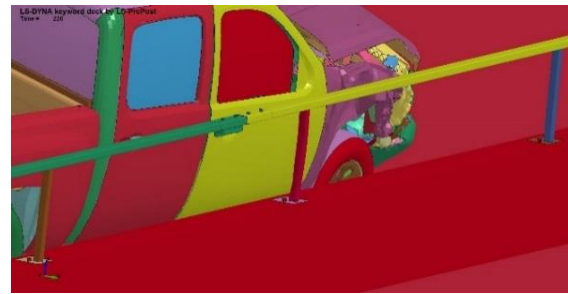


Time = 0.700 sec

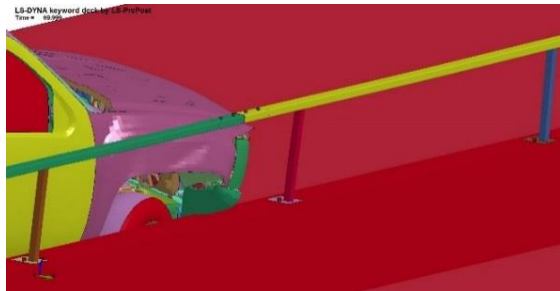
Figure 83. Downstream Sequential Views, Impact 2.6 ft (0.8 m) US from Splice Reversed Simulation



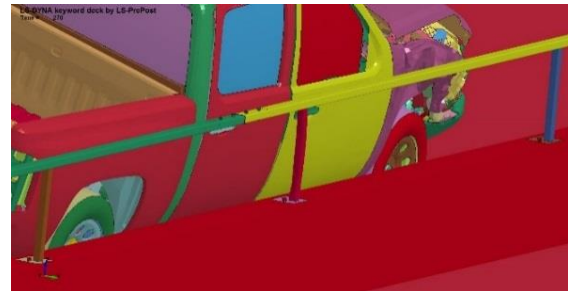
Time = 0.000 sec



Time = 0.200 sec



Time = 0.050 sec



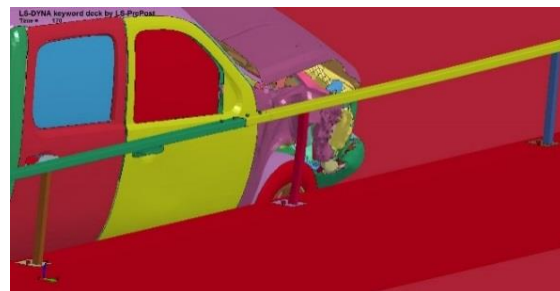
Time = 0.250 sec



Time = 0.100 sec



Time = 0.300 sec



Time = 0.150 sec



Time = 0.350 sec

Figure 84. Post Snag Sequential Views, Impact 2.6 ft (0.8 m) US from Splice Reversed Simulation

After the graphical results were analyzed, two additional simulations were created to gather more data to determine the CIP. The first simulation used an impact 3.8 ft (1.2 m) US from Post No. 7. This impact location was chosen because the impacts at 4.3 ft (1.3 m) and 3.3 ft (1 m) US from Post No. 7 seemed to result in the greatest snag. Thus, it was desired to see if snag could be increased using an impact location between those two points. The second simulation involved a vehicle impact point of 3.3 ft (1 m) US from the Splice section. This point was chosen to confirm that snag and loading on the splice was relatively minor and resulted in a similar outcome as the other splice impact simulation. Thus, post snag was the most severe outcome. Graphical results of these two simulations are shown in Figures 85 and 86.

For the simulation where the vehicle impacted 3.8 ft (1.2 m) US from Post No. 7, similar results to previous post snag simulations were observed. The vehicle impacted the system and was redirected safely. During impact the fender snagged on the post, as shown in Figure 87. Buckling of the post was present at the location where the bumper contacted with the post.

For the simulation where the vehicle impacted 3.3 ft (1 m) US of Splice DS from Post No. 7, the vehicle showed little interaction with the splice. Slight snagging between the vehicle fender and splice bolt assemblies occurred, along with minor snagging of the right-front fender on the post, but nothing severe.

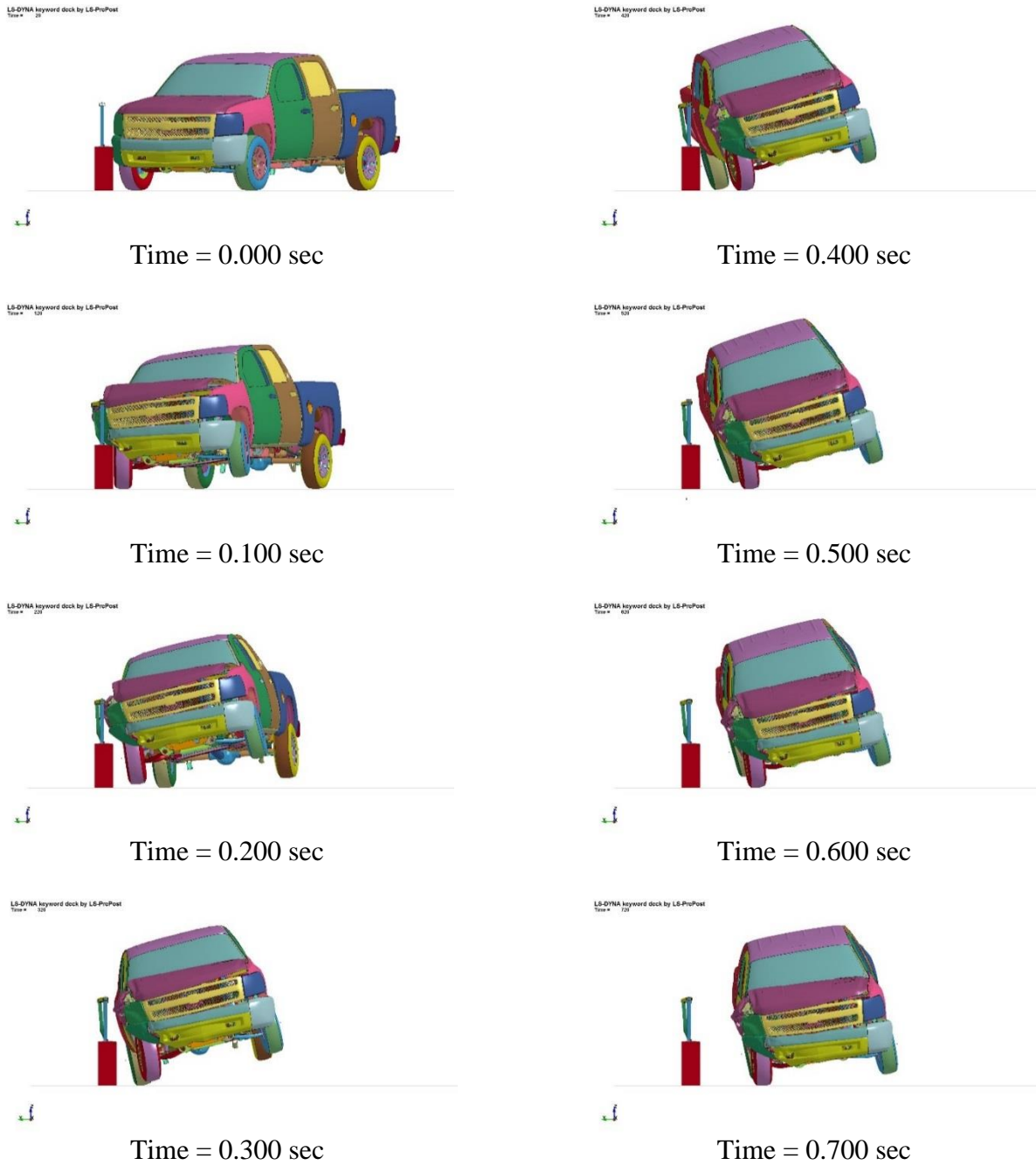


Figure 85. Downstream Sequential Views, Impact 3.8 ft (1.2 m) US from Splice Simulation

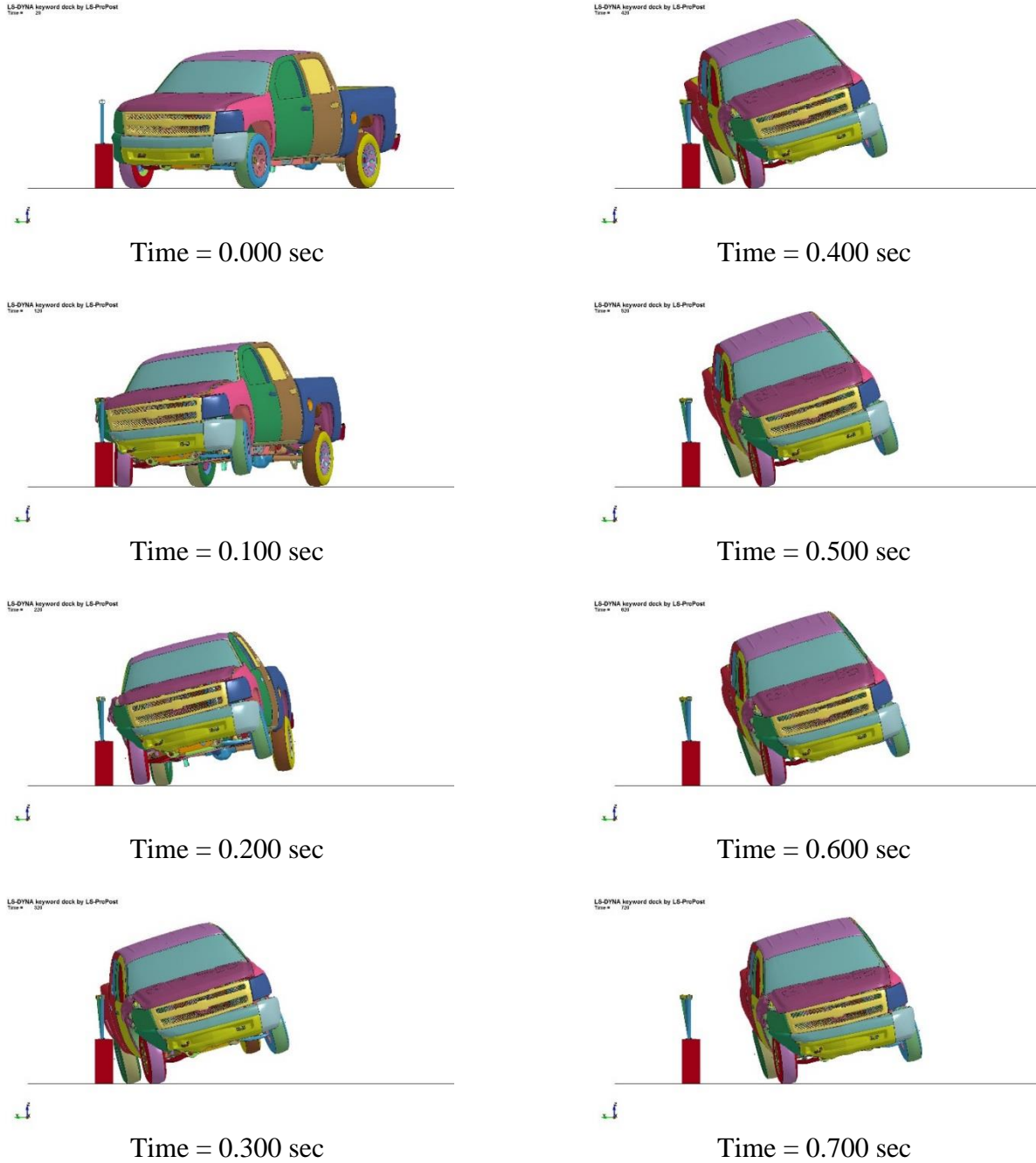
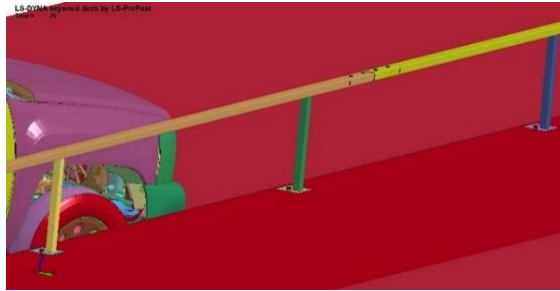


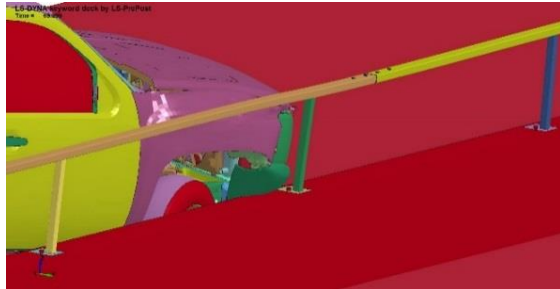
Figure 86. Downstream Sequential Views, Impact 3.3 ft (1 m) US from Splice Simulation



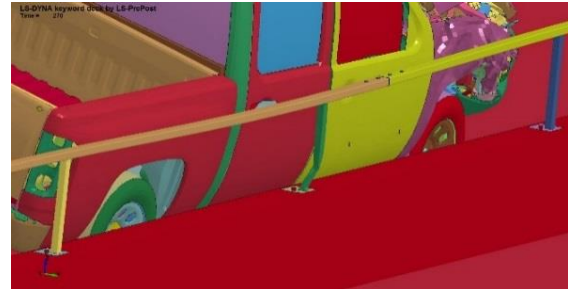
Time = 0.000 sec



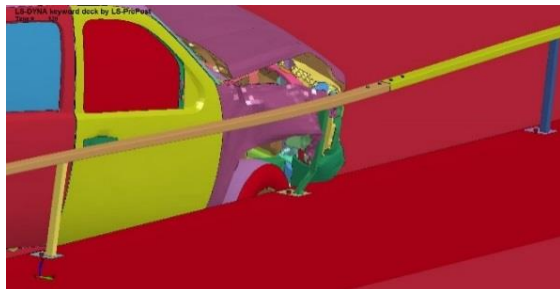
Time = 0.200 sec



Time = 0.050 sec



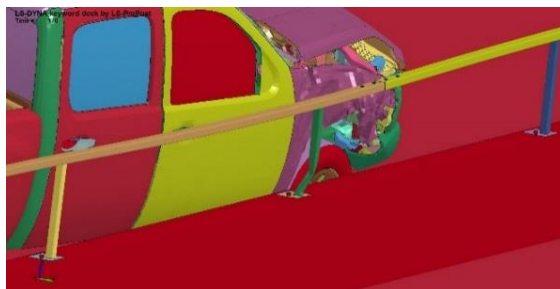
Time = 0.250 sec



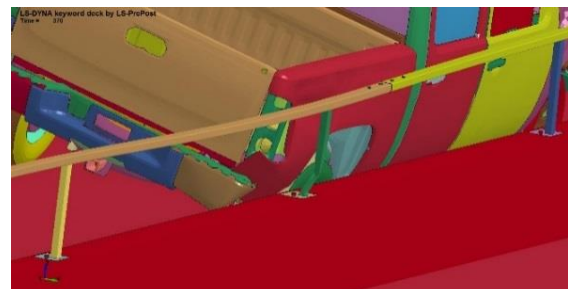
Time = 0.100 sec



Time = 0.300 sec



Time = 0.150 sec



Time = 0.350 sec

Figure 87. Post Snag Sequential Views, Impact 3.8 ft (1.2 m) US from Splice Simulation

7.4 CIP Determination

7.4.1 Post Deformation

To determine the snag severity, multiple aspects of the simulation were reviewed. First, the vehicle model and system were analyzed visually. During the cases where post snag occurred, snag of the vehicle on the post caused a high level of deformation to the right-front fender, as shown in Figures 88 through 93. However, the deformation did not seem realistic and would be expected to cause tearing in full-scale crash testing. Tearing of the fender should decrease the severity of the snag, but to what degree is unknown. For these cases, the 1.7 ft (0.5 m) US from Post No. 7 simulation provided the most fender damage, but all results were deemed similar.

The simulation with an impact located 3.3 ft (1 m) US from post no. 7 case showed the most post deformation and deflection. This finding suggested that interaction of the vehicle with the post was the highest in this case, possibly maximizing snag propensity. However, evaluation of post snag severity based on deformation was difficult to quantify without proper fender failure modes built into the vehicle model, and several other impact locations indicated significant post deformations. Lateral and longitudinal deflections measured at the top of the impacted post for each simulation are listed in Table 15.

While some degree of post deformation resulted from snag, quantifying the severity of the snag on visual deformation and post deflection was difficult and could lead to incorrect selection of the most severe snag case. For the splice snag cases, the height of the rail led to little interaction between the vehicle and the splice section. The lack of interaction caused very little snagging of the vehicle on the splice, and the post snag cases were considered to be more critical. The reversed splice and the 3.3 ft (1 m) US from Splice cases produced some snag of the right-front fender on the post, but not to the same degree as the other simulations.

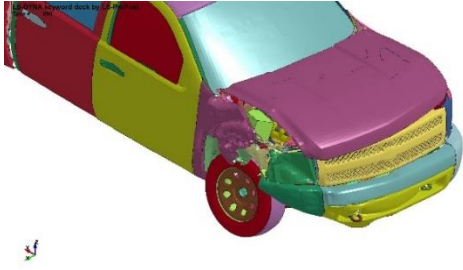


Figure 88. 4.3 ft (1.3 m) US Post No. 7 Fender Damage

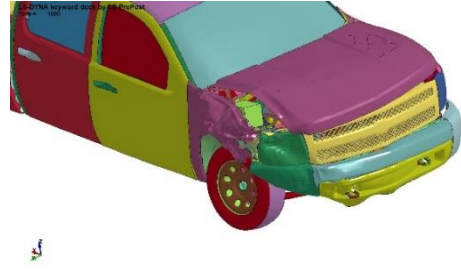


Figure 91. 3.8 ft (1.2 m) US Post No. 7 Fender Damage

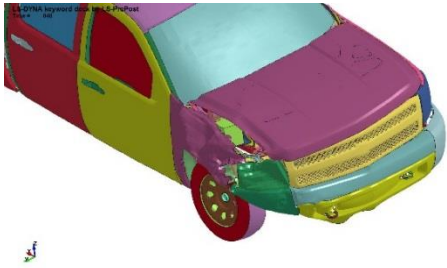


Figure 89. 3.3 ft (1 m) US Post No. 7 Fender Damage

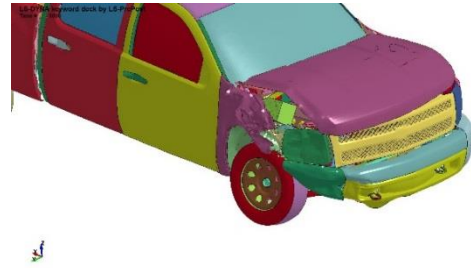


Figure 92. 2.6 ft (0.8 m) US Splice Reversed. Fender Damage

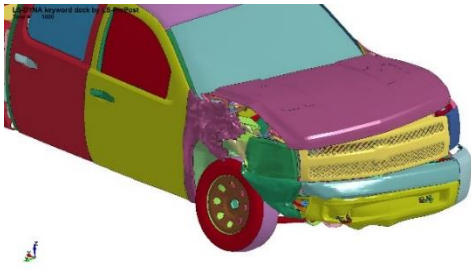


Figure 90. 1.7 ft (0.5 m) US Post No. 7 Fender Damage

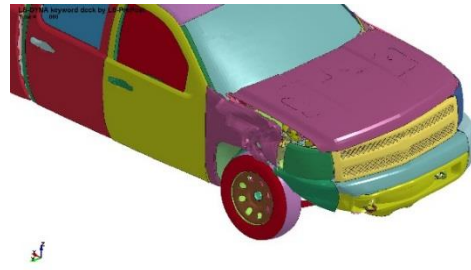


Figure 93. 3.3 ft (1 m) US Splice Fender Damage

Table 15. Post Lateral and Longitudinal Deflections

Simulation Run	Lateral Deflection in. (mm)	Longitudinal Deflection in. (mm)
4.3 ft (1.3 m) US from Post No. 7	3.73 (95)	0.64 (16)
3.3 ft (1 m) US from Post No. 7	6.66 (169)	0.44 (11)
1.7 ft (0.5 m) US from Post No. 7	6.34 (161)	0.65 (17)
2.6 ft (0.8 m) US from Splice	1.12 (29)	0.05 (1)
2.6 ft (0.8 m) US from Splice Reversed	1.07 (27)	0.40 (10)
3.8 ft (1.2 m) US from Post No. 7	4.88 (124)	0.49 (12)
3.3 ft (1 m) US from Splice	3.70 (94)	0.46 (11)

7.4.2 Vehicle Velocity Change

Next, the change in velocity of the vehicle model was analyzed in order to help determine snag severity. Change in velocity of the vehicle is the integration of the acceleration of the vehicle, as measured at the CG of the vehicle. The higher the acceleration experienced by the vehicle, the higher the change in velocity. In general, the more severe the vehicle snag, then the higher the accelerations experienced by the vehicle, which in turn creates a higher change in velocity of that vehicle. A comparison plot of the change in velocity for each simulated case is shown in Figures 94 and 95.

For all simulations, change in velocity of the CG of the vehicle was determined in the longitudinal and lateral directions, as well as the resultant of the two directions. For these three scenarios, all simulations showed minimal differences. For the simulations performed, the 1.7 ft (0.5 m) US from Post No.7 impact provided the highest peak changes in velocity, while the 2.6 ft (0.8 m) US from Splice impact showed the lowest change in velocity, as shown in Figures 94 and 95. The initial peak resultant change in velocities were all within 3 ft/s (0.9 m/s). With the difference in magnitudes between each simulation being relatively small and the simulations all following the same general trend, the CIP selection was not deemed to be strongly related to vehicle change in speed.

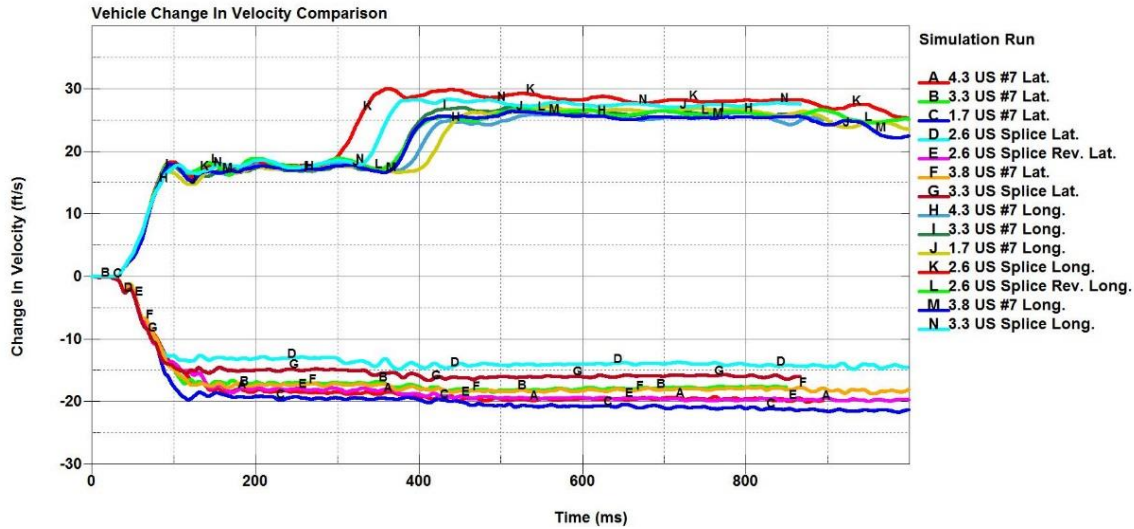


Figure 94. Longitudinal and Lateral Vehicle Change in Velocity Comparison

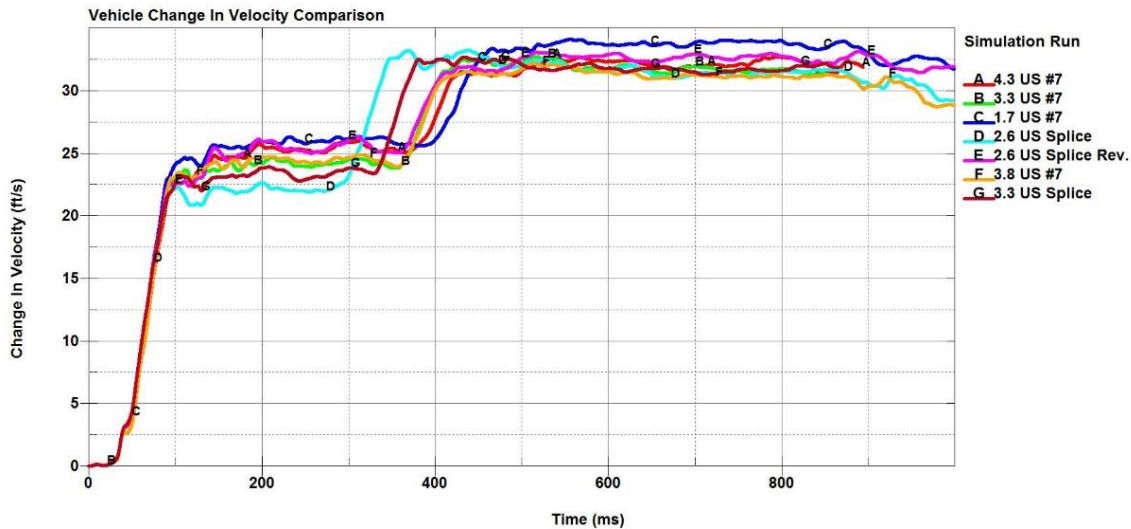


Figure 95. Longitudinal and Lateral Resultant Vehicle Change in Velocity Comparison

7.4.3 Lateral Vehicle Overlap

The final step taken to help determine CIP was to analyze the lateral vehicle overlap beyond the impacted post. Overlap was defined as the vehicle extent laterally behind the front face of the post. Overlap was considered pertinent as the vehicle intrusion behind the front face of the post indicates whether a vehicle will interact with that post as the impact event continues. A high overlap was assumed to create more snag risk, while a low overlap was considered to create less snag risk.

The measured overlap of the vehicle just before impacting the post and the maximum overall value during post impact for each simulation is shown in Table 16. For vehicle overlap at impact and the maximum value, the 3.8 ft (1.2 m) US from Post No. 7 simulation provided the

highest measured values. The 1.7 ft (0.5 m) US from Post No. 7 produced the lowest overlap value at initial post impact, while the 2.6 ft (0.8 m) US from Splice reversed simulation provided the lowest maximum value. The two splice impact simulations did not produce any overlap as the vehicle model impacted just DS from the post. The measured values of overlaps from the simulations suggests that the 3.8 ft (1.2 m) US from Post No. 7 impact point simulation showed the most snag potential due to having the highest overlap values.

Table 16. Vehicle Post Overlap

Simulation Impact Location	At Impact in. (mm)	Maximum in. (mm)
4.3 ft (1.3 m) US from Post No. 7	8.26 (210)	8.31 (211)
3.3 ft (1 m) US from Post No. 7	7.47 (190)	8.39 (213)
1.7 ft (0.5 m) US from Post No. 7	3.67 (93)	7.73 (196)
2.6 ft (0.8 m) US from Splice	N/A	N/A
2.6 ft (0.8 m) US from Splice Reversed	7.25 (184)	7.25 (184)
3.8 ft (1.2 m) US from Post No. 7	8.51 (216)	8.99 (228)
3.3 ft (1 m) US from Splice	N/A	N/A

*N/A = Not Applicable

7.4.4 CIP Determination Conclusion

From the analysis of the simulations, it was determined that the 3.8 ft (1.2 m) US from Post No. 7 simulation provided the highest snag severity. Overlap of the vehicle was considered to be the most critical factor to determine an impact point that would provide highest snag severity. Overlap was used in lieu of post deformation because the combination rail was modeled without component failure and snag severity was difficult to quantify through the deformation of system components due to the unquantified relationship between post deflection and snag severity. Since snag severity was considered to be the main factor in CIP selection, the 3.8 ft (1.2 m) US from Post No. 7 was chosen as the CIP. It was chosen because it provided the highest combination of overlap and a change in velocity as compared to the other simulations.

7.5 Additional Simulation Analysis

Along with the analysis to determine CIP, additional analyses were performed in order to determine if the design would perform acceptably. Based on the results of this investigation, certain design aspects were altered in order to create a better performing system.

7.5.1 Anchor Rod Forces

Using the cross sections placed in the model, the forces imparted to the anchor rods were analyzed. Specifically, the anchor rod tension and shear forces were analyzed. The peak tension and shear forces experienced by both the US and DS anchor rod on the impacted post are shown in Table 17. Originally, the baseplate calculations indicated that the anchor rods would experience 3.87 kips (17.21 kN) from the specified post loading. However, the loading calculations only took into consideration loading along one axis and not the complex 3D loading the vehicle would apply to the post. The simulation results showed approximately a six times increase over the calculated tension forces.

Upon viewing the forces imparted to the anchor rods, it was decided that reevaluation of the anchorage design was necessary. This reevaluation led to increasing the anchor rod diameter to ¾ in. (19 mm), the use of the hybrid epoxy anchorage design process, and increasing the anchor rod grade from Grade 55 to 105, as stated in Chapter 6. The anchorage capacity was increased to withstand the observed tension forces experienced in the simulations, except for the highest case of 23.24 kips (103.4 kN). This value was deemed an outlier, and may not occur if weld, bearing, or part failure occurred during at test. Thus, the ¾-in. (19-mm) diameter anchor was believed to be adequate.

Table 17. US and DS Anchor Rod Forces

Simulation Run	Tension kips (kN)		X Shear kips (kN)		Y Shear kips (kN)		Resultant Shear kips (kN)	
	US	DS	US	DS	US	DS	US	DS
4.3 ft (1.3 m) US from Post No. 7	15.79 (70.26)	14.82 (65.91)	-3.96 (-17.60)	-1.59 (-7.05)	1.91 (8.49)	1.49 (6.62)	4.41 (19.64)	2.09 (9.30)
3.3 ft (1 m) US from Post No. 7	16.33 (72.64)	14.45 (64.29)	-2.28 (-10.18)	-1.84 (-8.18)	2.44 (10.86)	1.73 (7.71)	2.91 (12.93)	2.04 (9.06)
1.7 ft (0.5 m) US from Post No. 7	23.24 (103.36)	14.99 (66.69)	-3.68 (-16.36)	1.84 (8.18)	-1.96 (-8.71)	-1.01 (-4.48)	3.68 (16.35)	1.93 (8.59)
2.6 ft (0.8 m) US from Splice	15.62 (69.48)	15.38 (68.43)	-1.35 (-6.01)	1.39 (6.19)	0.45 (2.00)	0.82 (3.65)	1.38 (6.13)	1.39 (6.19)
2.6 ft (0.8 m) US from Splice Reversed	12.98 (57.75)	12.02 (53.47)	-1.41 (-6.29)	0.43 (1.91)	-0.56 (-2.50)	0.83 (3.68)	1.52 (6.75)	1.04 (4.63)
3.8 ft (1.2 m) US from Post No. 7	16.78 (74.66)	14.50 (64.50)	-4.27 (-18.99)	1.43 (6.37)	2.10 (9.34)	1.97 (8.77)	4.38 (19.50)	2.04 (9.07)
3.3 ft (1 m) US from Splice	15.77 (70.15)	15.24 (67.77)	-2.27 (-10.10)	0.99 (4.39)	1.11 (4.93)	0.96 (4.27)	2.46 (10.94)	1.05 (4.65)

7.5.2 Splice Tube Capacity

During initial simulations, it was observed that the splice tube was not performing as expected. Vehicle impact caused the system to oscillate heavily near the ends of the rail sections where the splice tubes were located. Deformation of the impacted splice tube in bending was also observed, indicating the section did not provide adequate bending strength. This observation led to the reevaluation of the preliminary design, which utilized HSS sections and shims, and eventually to the use of the built-up section splice tube, as discussed in the previous chapter. Clearances between the splice tube and rail as well as the splice tube section properties were modified to improve the observed behavior.

7.5.3 Splice Tube Bolt Forces

The shear forces imparted to the splice tube bolts for the chosen CIP simulation were also monitored and then used to determine splice tube dimensions that would provide adequate capacity to resist the forces. The shear forces measured at the top and bottom of each splice tube bolt are shown in Table 18. The Center Downstream (CDS) splice tube bolt experienced the highest lateral and longitudinal shear forces, while the US splice tube bolt experienced the highest resultant shear force. The longitudinal shear force was used to determine if the section of both the splice tube and rail provided enough capacity to resist bearing failure and tear out, while the maximum resultant shear was used in to determine if the bolts themselves provided enough shear capacity. The magnitudes of the shear forces were rather low compared to the capacity of the rail, splice tube, and splice tube bolts, so it was determined that the choice of splice tube bolts provided adequate capacity to resist the forces experienced in the simulations.

Table 18. 3.8 ft (1.2 m) US from Post No. 7, Splice Bolt Shear Forces

Load Parameter	Location	US	CUS	CDS	DS
X Shear kips (kN)	Top	0.0247 (0.11)	-0.0328 (-0.146)	0.0436 (0.194)	0.04 (0.178)
	Bottom	0.0254 (0.113)	-0.0369 (-0.164)	0.0423 (0.188)	0.0375 (0.167)
Y Shear kips (kN)	Top	0.127 (0.563)	0.1086 (0.483)	0.135 (0.6)	-0.112 (-0.498)
	Bottom	0.132 (0.585)	0.105 (0.465)	0.124 (0.551)	-0.105 (-0.465)
Resultant Shear kips (kN)	Top	0.219 (0.974)	0.206 (0.917)	0.137 (0.607)	0.124 (0.55)
	Bottom	0.229 (1.018)	0.197 (0.878)	0.128 (0.57)	0.118 (0.523)

7.6 Conclusions

The CIP was determined to be 3.8 ft. (1.2 m) US from a post through the simulation of multiple impact locations. This location was chosen as it provided the most vehicle overlap, suggesting that it would create the highest snag severity of the simulated locations. Forces in the anchor rods and splice tube bolts were monitored and used to evaluate whether they provided adequate capacity to resist the loads. It was found that the capacity of the anchor rods needed to be increased, while the chosen splice tube bolts were determined to provide enough strength. While the model may not have provided the failure modes of an actual system with complete accuracy, it was believed that the results from the simulation were sufficient to identify the critical impact point and provide conservative guidance on the system loading.

Next, researchers evaluated the system with an 1100C model to determine the predicted severity during a small car impact. Further modifications to the system, if any, would be reviewed to determine if additional adjustments of the model for the 2270P vehicle model simulations were required.

8 MASH 1100C SMALL CAR SIMULATION OF FULL SYSTEM

8.1 1100C Simulation

Originally, the 2270P vehicle used in MASH 2016 test designation no. 2-11 was considered to be the more severe impact case due to vehicle behavior. The dimensions of the 2270P vehicle make it more likely to experience vehicle instability and/or override with respect to low-height systems, and provided an increased ZOI envelope, creating a higher snag probability when compared to the 1100C vehicle. However, the height of the parapet that was selected suggested that interaction between the bicycle rail and the 1100C small car could occur. Consequently, simulations involving the 1100C small car were performed to observe the likelihood and/or severity of vehicle contact with the attached bicycle rail. More specifically, it was desired to see if the interaction of the 1100C vehicle with the bicycle rail would induce contact with the passenger window and the potential for subsequent window fracture, which would be cause for failure according to MASH 2016 test designation no. 2-10 criteria. While this interaction was not expected, the simulation effort was performed to confirm this expectation and investigate the potential snag of the 1100C vehicle on the combination rail. Graphical results of the simulation were analyzed to determine the severity of the vehicle-to-rail interaction.

8.1.1 Simulation Details

The simulation effort modeled the 1100C vehicle impacting the combination rail model used in the previous simulation effort. The impact conditions followed MASH 2016 test designation no. 2-10, which involves the 1100C small car impacting the system at 44 mph (70 km/h) and at a 25-degree impact angle. The impact point was selected such that the vehicle would provide the highest post overlap to maximize snag probability, as well as to increase probability of the vehicle's side passenger windows contacting the attached bicycle rail.

8.1.2 Results

During simulation of the impact event, the 1100C vehicle impacted the system 2.3 ft (0.7 m) US from post no. 4. As the impact continued, the vehicle's front bumper, right fender, and right headlight assembly extended past the front face of the barrier, leading to the headlight assembly contacting post no. 4. The vehicle's contact with the attached bicycle railing caused damage to both the headlight assembly and the right fender. As the vehicle continued, the top of the vehicle rolled toward the barrier, then rolled away from the system, and the vehicle was successfully redirected. Graphical results from the simulation are shown in Figure 96.

8.1.3 Vehicle-To-Rail Interaction

The simulation showed that the 1100C vehicle could contact the system. However, the interaction between the vehicle and the attached bicycle rail was relatively minor. While the vehicle's front-right headlight assembly did come into contact with post no. 4, no permanent deformation of the post occurred, suggesting a minor snag event, as shown in Figure 97. Further, no contact between the side passenger windows and the attached bicycle rail was observed during simulation.

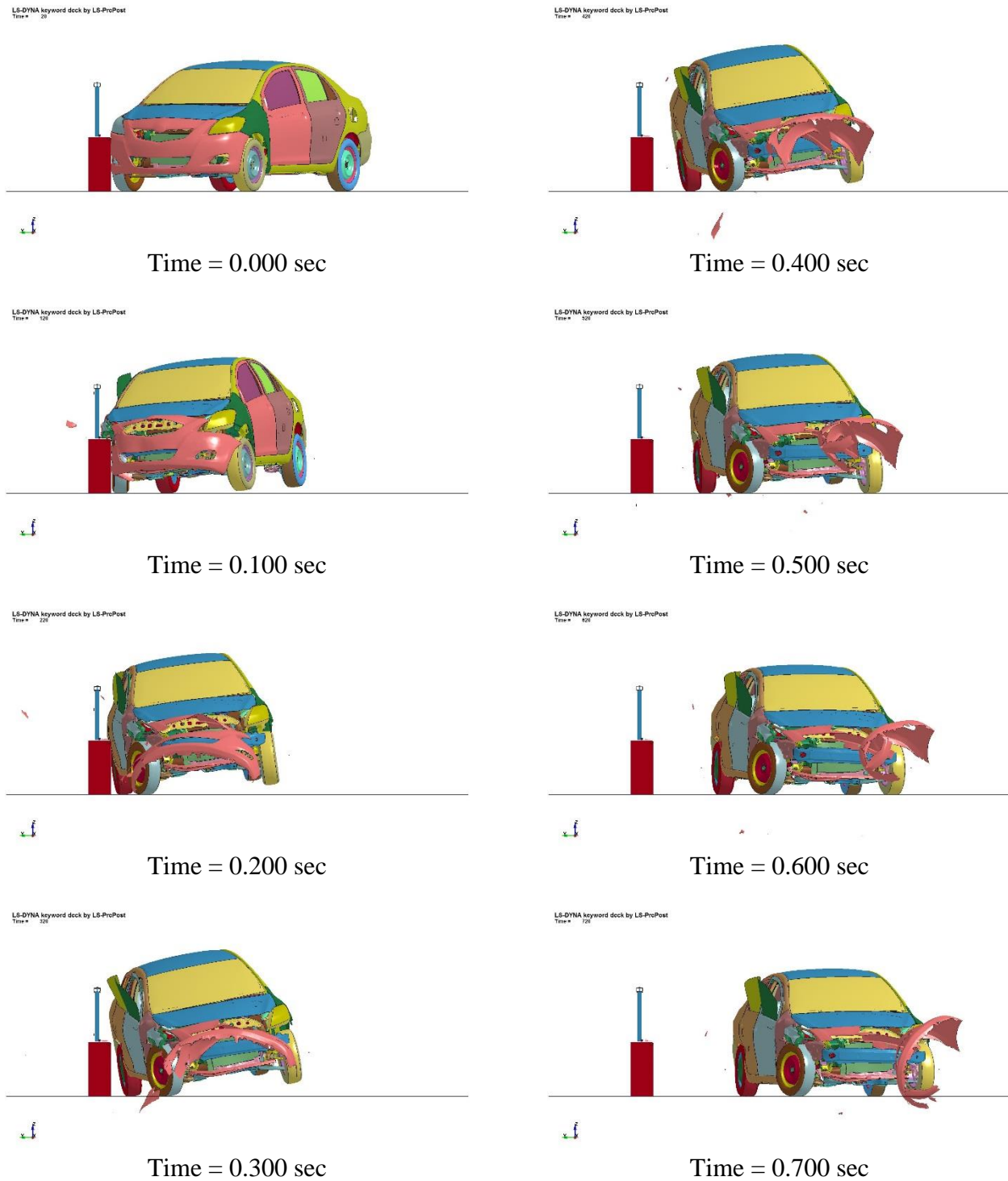
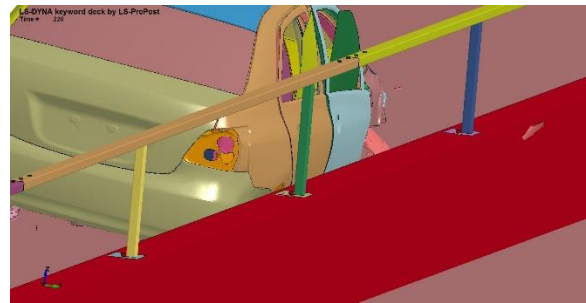


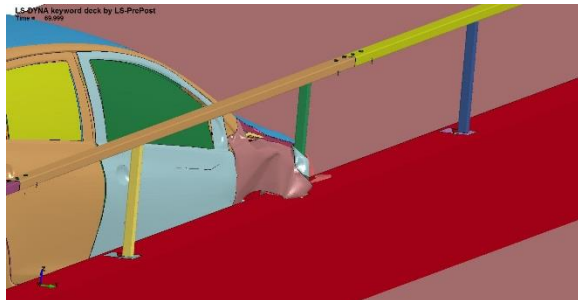
Figure 96. Downstream Sequential Views, 1100C Simulation



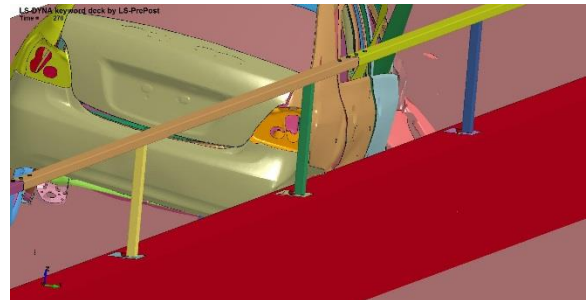
Time = 0.000 sec



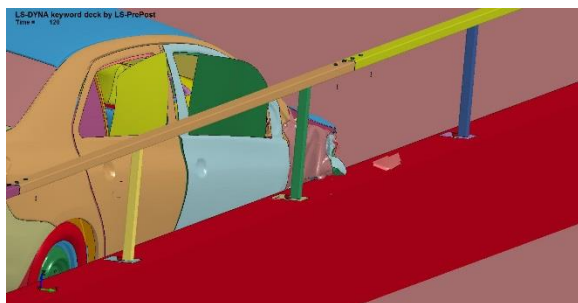
Time = 0.200 sec



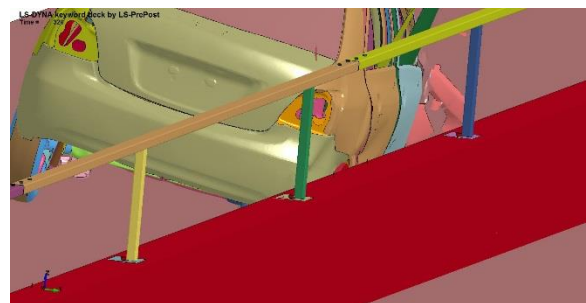
Time = 0.050 sec



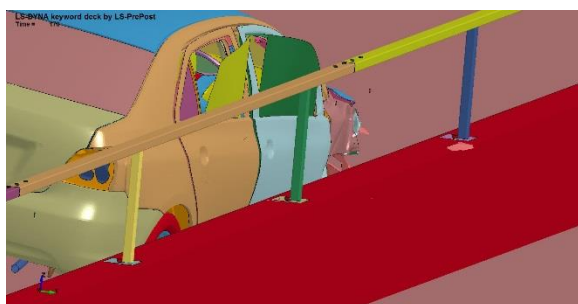
Time = 0.250 sec



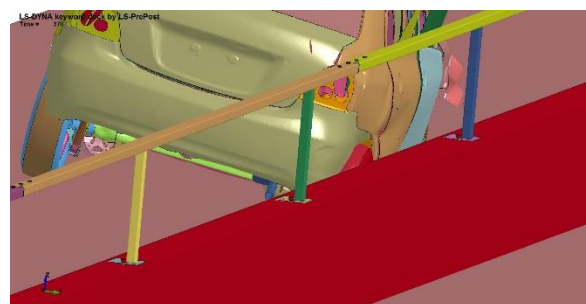
Time = 0.100 sec



Time = 0.300 sec



Time = 0.150 sec



Time = 0.350 sec

Figure 97. Post Snag Sequential Views, 1100C Simulation

8.1.1 1100C Simulation Conclusion

Simulation results showed that the 1100C model contacted the attached bicycle railing and created a minor snag event. No contact of the vehicle passenger side windows with the system occurred, which provided confidence that shattering of the side window due to interaction with the bicycle rail would not occur in real world conditions. Overall, the simulation effort confirmed that MASH 2016 test designation no. 2-11 would provide a more severe impact scenario than MASH 2016 test designation no. 2-10, as expected for the nature of this system.

8.2 Conclusion

The simulation results indicated that the system was able to contain and safely redirect the 1100 C vehicle. MASH 2016 test designation no. 2-11 was confirmed to be the more critical impact condition due to the nature of the system well the results of the small car simulation effort.

9 COMBINATION TRAFFIC/BICYCLE RAIL DESIGN DETAILS

The proposed barrier system is configured to be 100 ft – 4½ in. (30.6 m) long and consist of a bicycle rail mounted on top of a vertical-faced concrete parapet, as shown in Figures 98 through 111.

The longitudinal rail of the upper bicycle rail is to be fabricated with 3-in. x 2-in. x ⅛-in. (76-mm x 51-mm x 3-mm) ASTM A500 Grade C structural steel tubing. The longitudinal rail consists of 20 ft (6.1 m) long sections spliced at the quarter-span between two posts. The rails are to be attached to the top of the posts using ⅛-in. (3-mm) fillet welds around the entire post section.

The expansion/splice tubes for the rail ends are to be fabricated with two 28-in. (718-mm) long by 2-in. (51-mm) wide by ¼-in. (6-mm) thick ASTM A572 Gr. 50 steel plates welded to two 28¼-in. (718-mm) long by 1¼-in. (32-mm) wide by ⅝-in. (8-mm) thick ASTM A572 Gr. 50 steel plates using ⅜-in. (5-mm) fillet welds. The combination of plates will create outside dimensions of 2½ in. x 1½ in. (64 mm x 38 mm). The expansion/splice tubes would be inserted into the longitudinal rail ends and held in place with four ½-in. (13-mm) diameter, 3¼-in. (83-mm) long ASTM F3125 bolts placed vertically, two in the US tube section and two in the DS tube section.

The US and DS end sections will not utilize an anchored termination to the parapet for the suggested full-scale crash testing. Termination design configurations will be suggested upon successful completion of full-scale crash testing of the proposed system.

The 21⅜-in. (543-mm) tall steel posts shall be fabricated with 2-in. x 2-in. x ⅛-in. (51-mm x 51-mm x 3-mm) ASTM A500 Grade C structural steel tubing. A 9¼-in. x 7-in. x ⅝-in. (235-mm x 178-mm x 16-mm) ASTM A572 Grade 50 steel plate shall be welded to the base of each post in order to attach it to the top of the barrier with two ¾-in. (19-mm) diameter, 14-in. (356-mm) long ASTM F1554 Grade 105 anchor rods. The posts are to be attached to the barrier with the anchor rods placed in a line along the longitudinal axis of the barrier spaced 5 in. (127 mm) apart using epoxy adhesive with a minimum bond strength of 1,560 psi (10.8 MPa). All connection hardware shall be dip coated using the appropriate ASTM galvanization process and specification as stated in the Bill of Materials, shown in Figure 111. The posts were designed to be spaced 10 ft (3 m) on center. The overall height of the system is to be 48 in. (1,219 mm) above the ground line.

The parapet shall consist of NE mix 47BD concrete or similar concrete mix with a minimum concrete compressive strength of 4,000 psi (27.6 MPa). The reinforcement shall consist of ASTM A615 Grade 60 #4 rebar steel coated with ASTM A775 or ASTM A934 epoxy. The stirrups are to be placed at 24-in. (610-mm) spacing and 12 in. (305 mm) at the end sections. A total of four longitudinal bars shall be utilized with a vertical spacing of 10¼ in. (260 mm) between the two lower and two upper longitudinal bars.

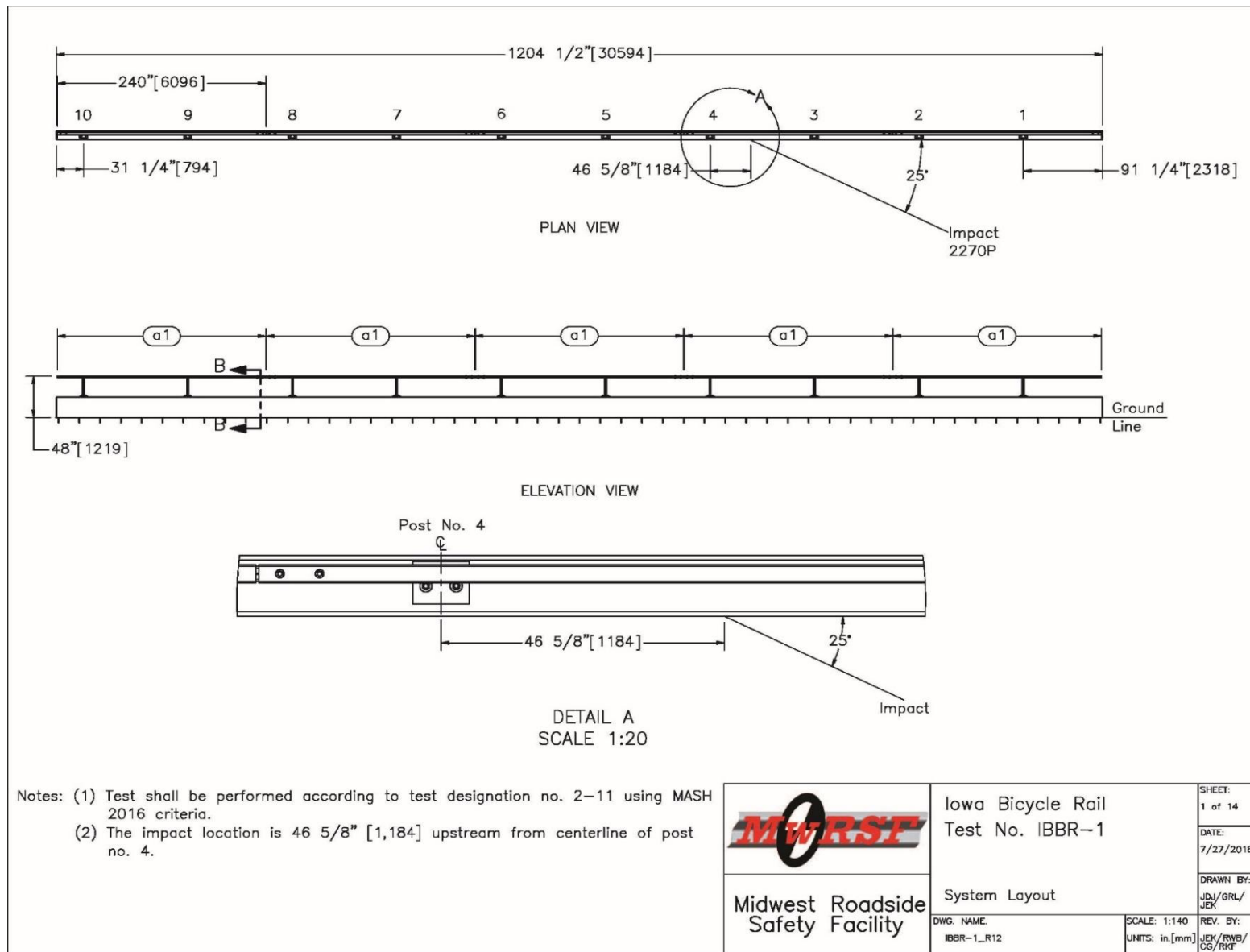


Figure 98. Iowa Bicycle Rail – System Layout

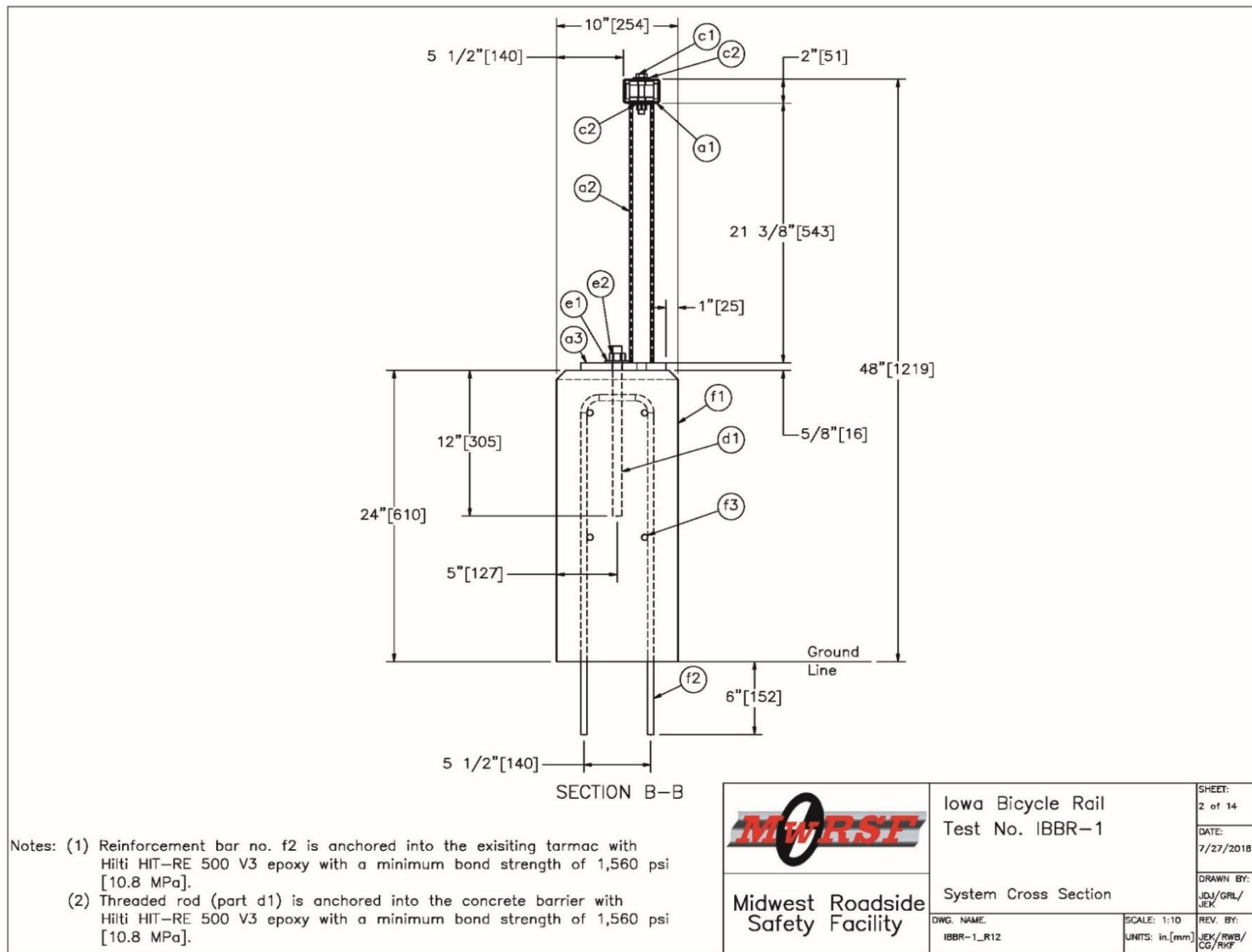


Figure 99. Iowa Bicycle Rail – System Cross Section

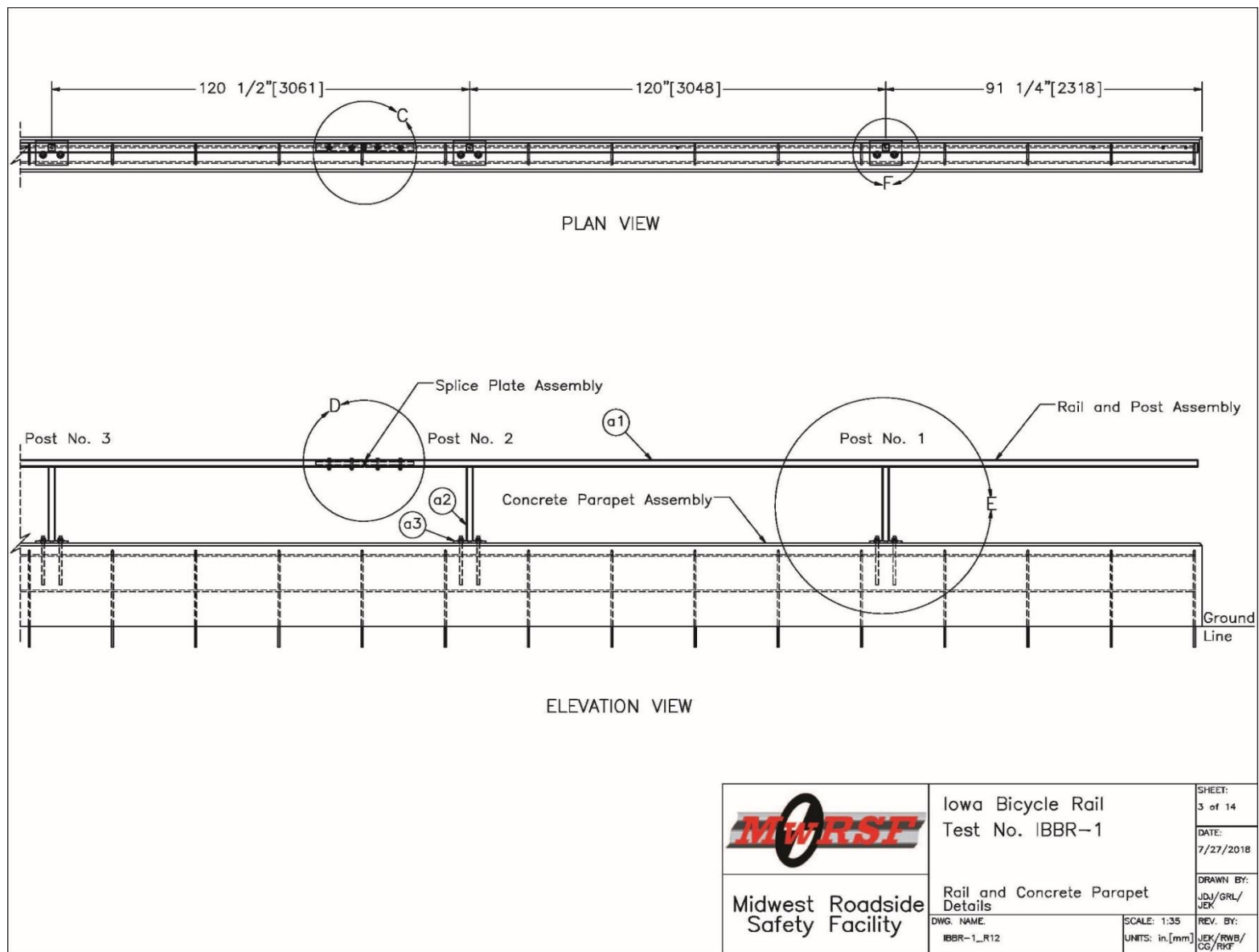


Figure 100. Iowa Bicycle Rail – Rail and Concrete Parapet Details

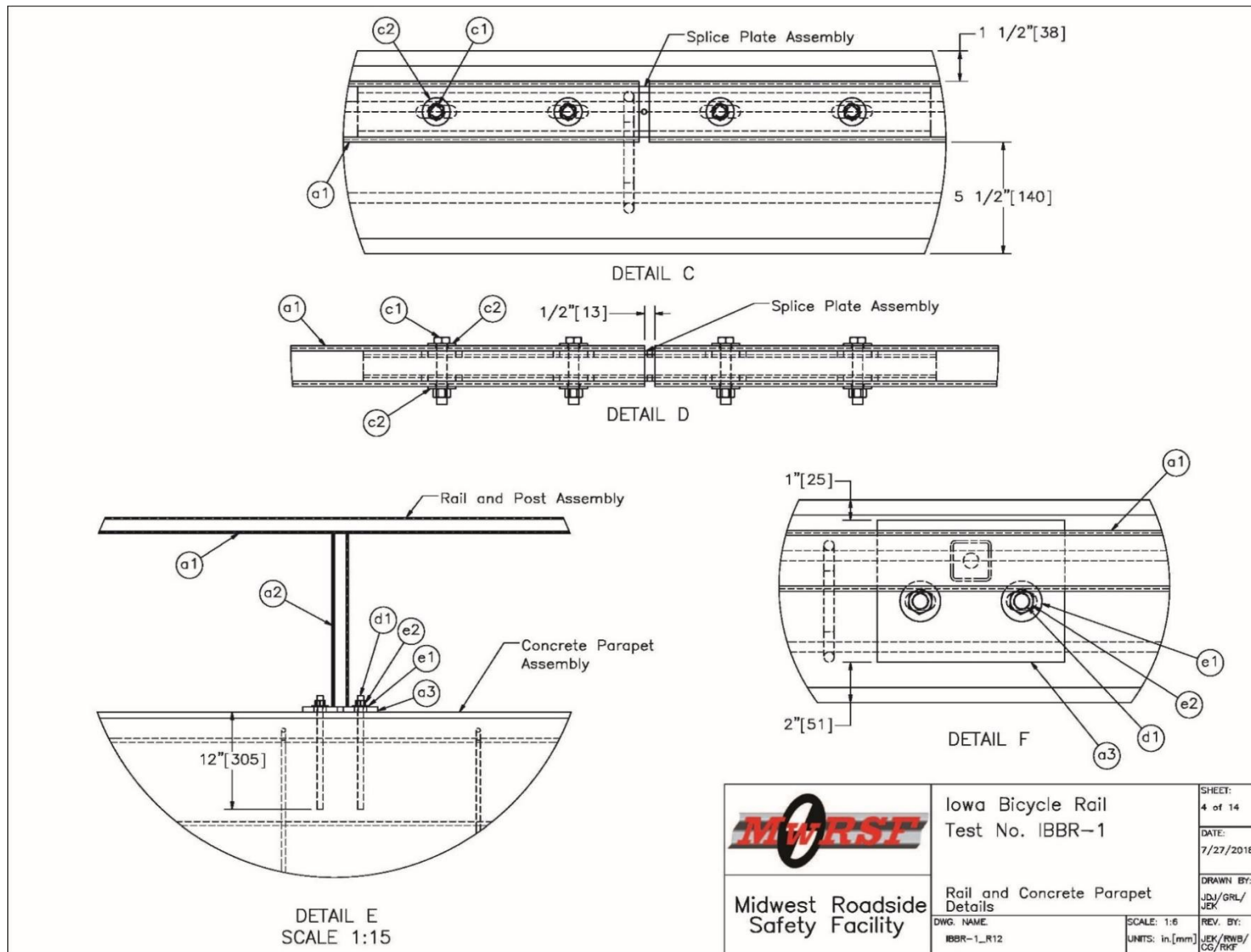


Figure 101. Iowa Bicycle Rail – Rail and Concrete Parapet Details

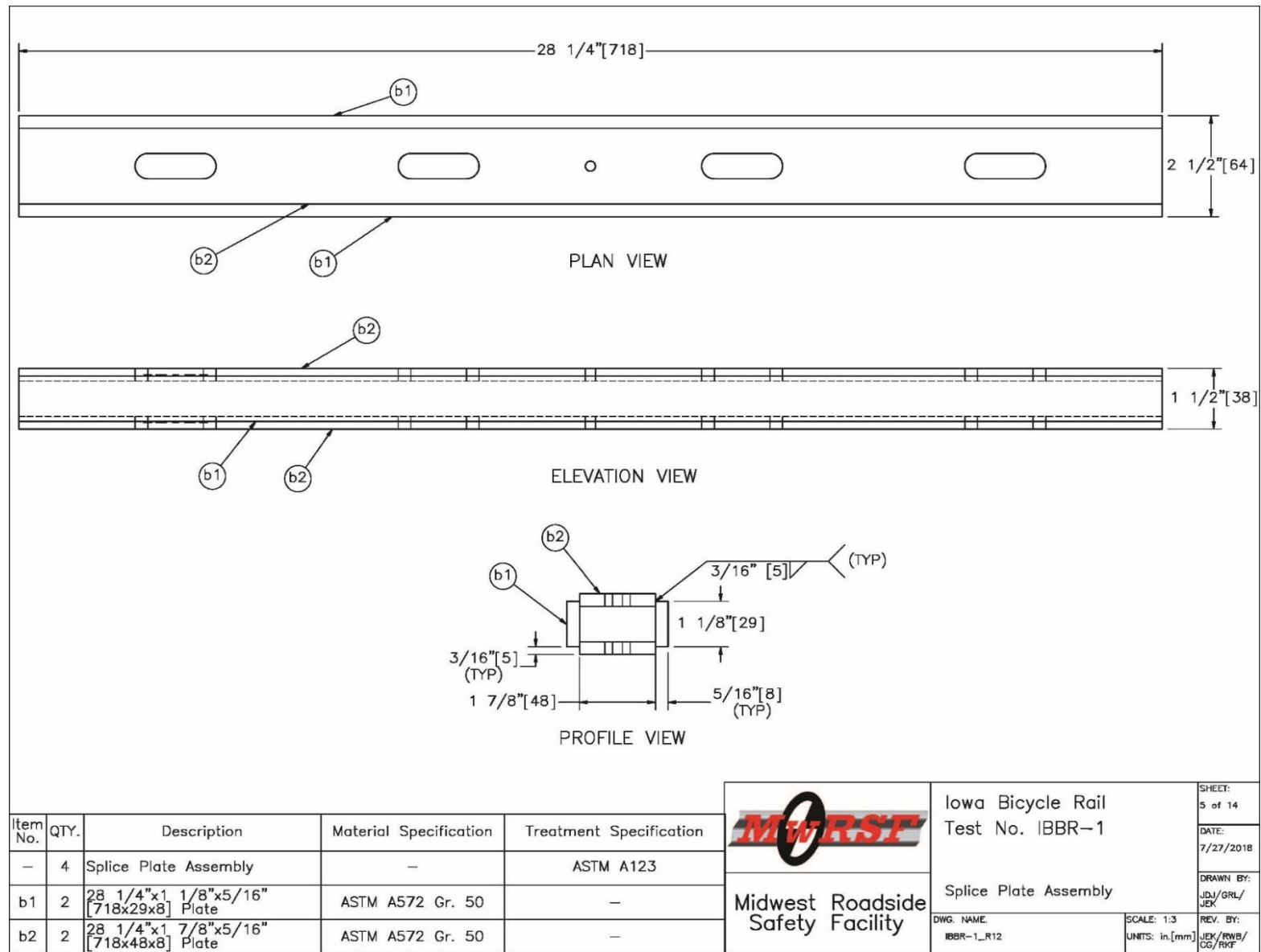


Figure 102. Iowa Bicycle Rail – Splice Plate Assembly

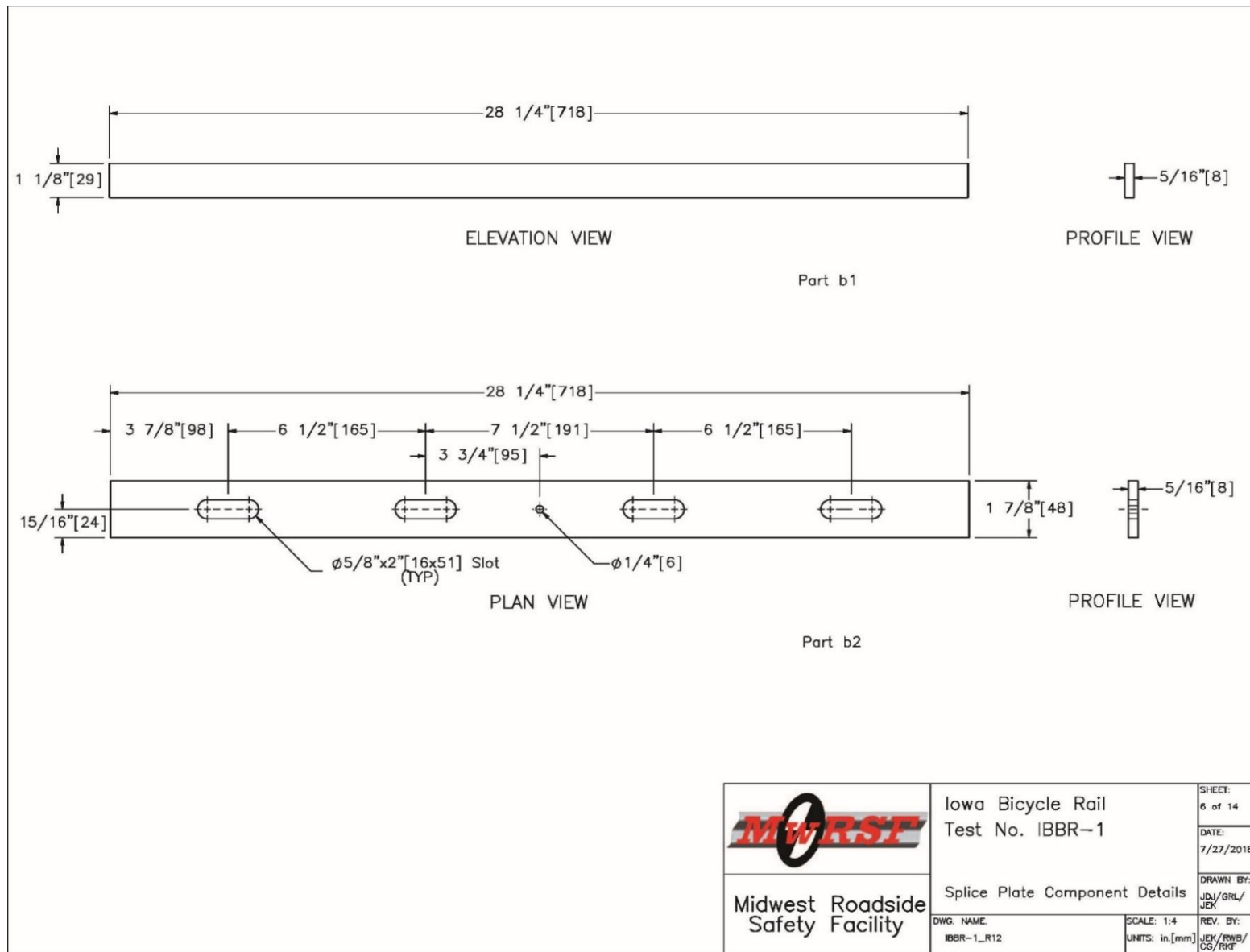


Figure 103. Iowa Bicycle Rail – Splice Plate Component Details

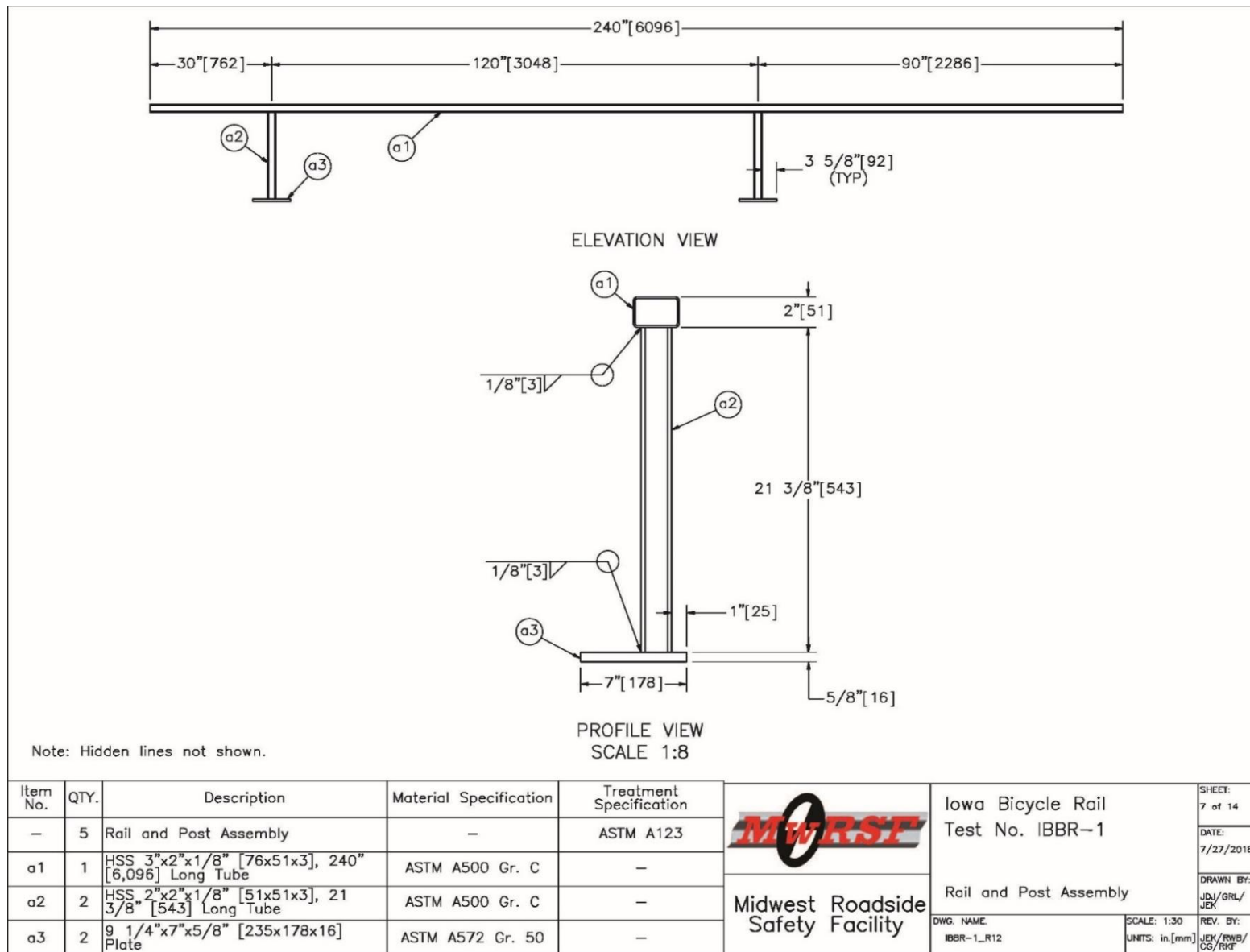


Figure 104. Iowa Bicycle Rail – Rail and Post Assembly

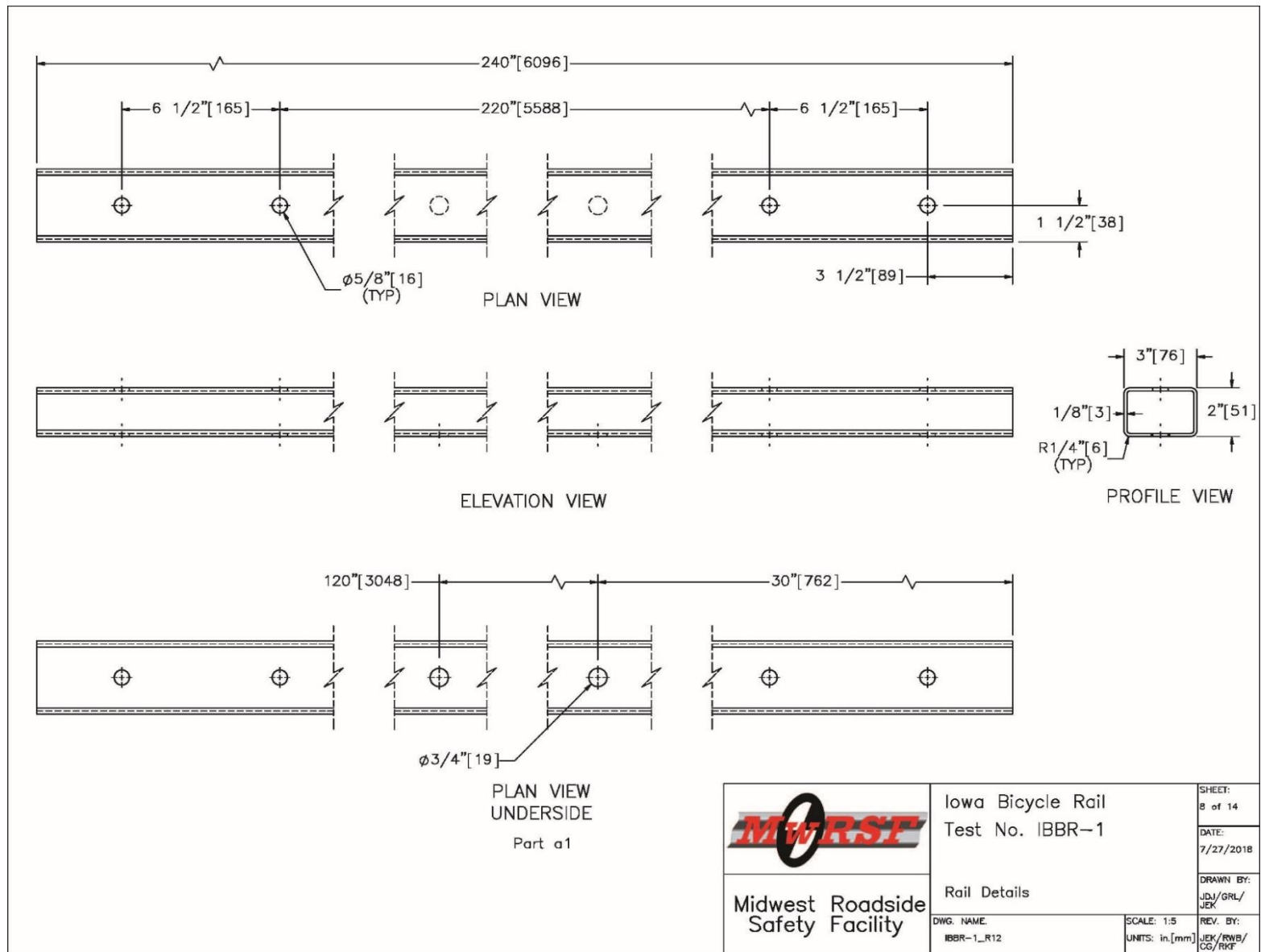


Figure 105. Iowa Bicycle Rail – Rail Details

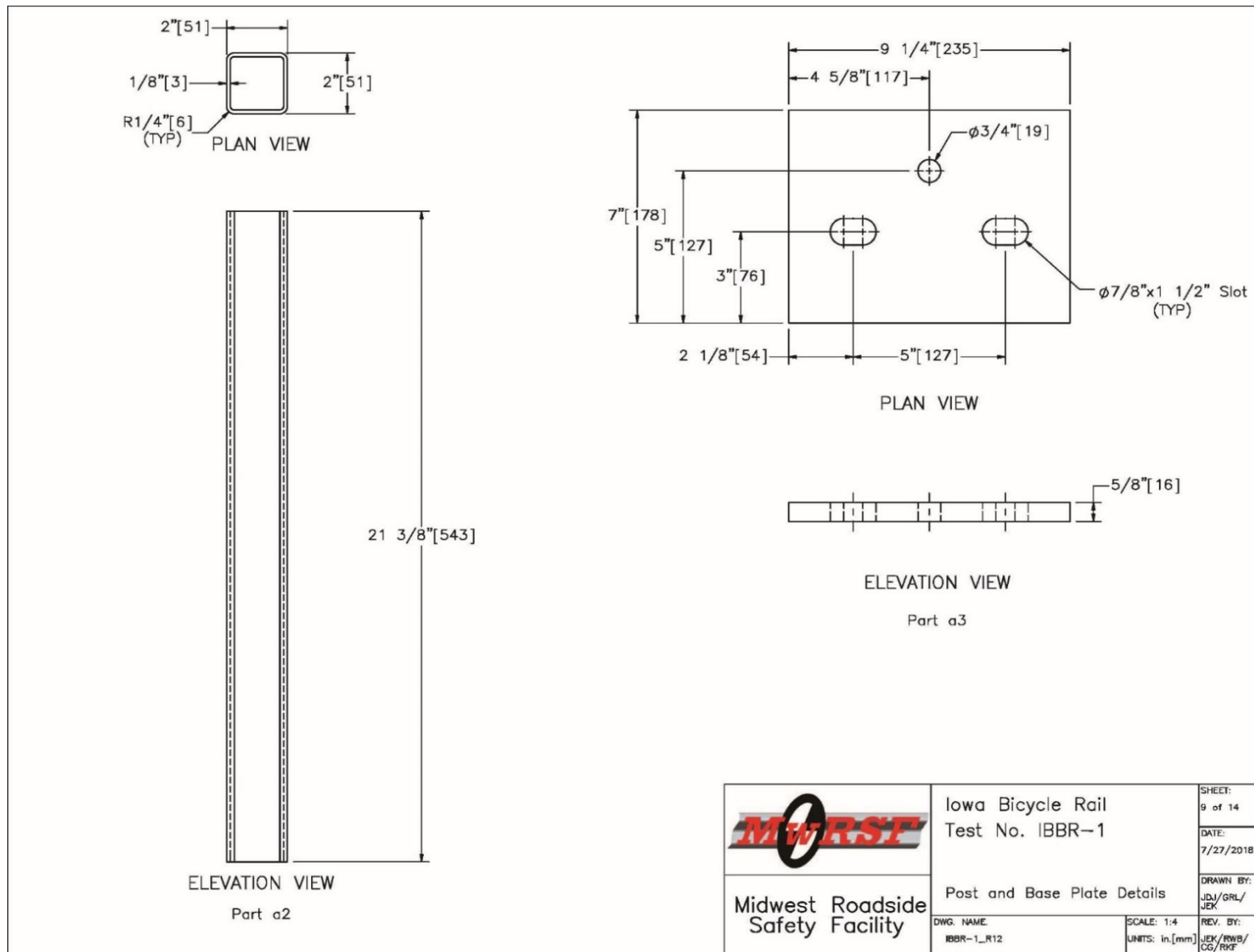


Figure 106. Iowa Bicycle Rail – System Post and Base Plate Details

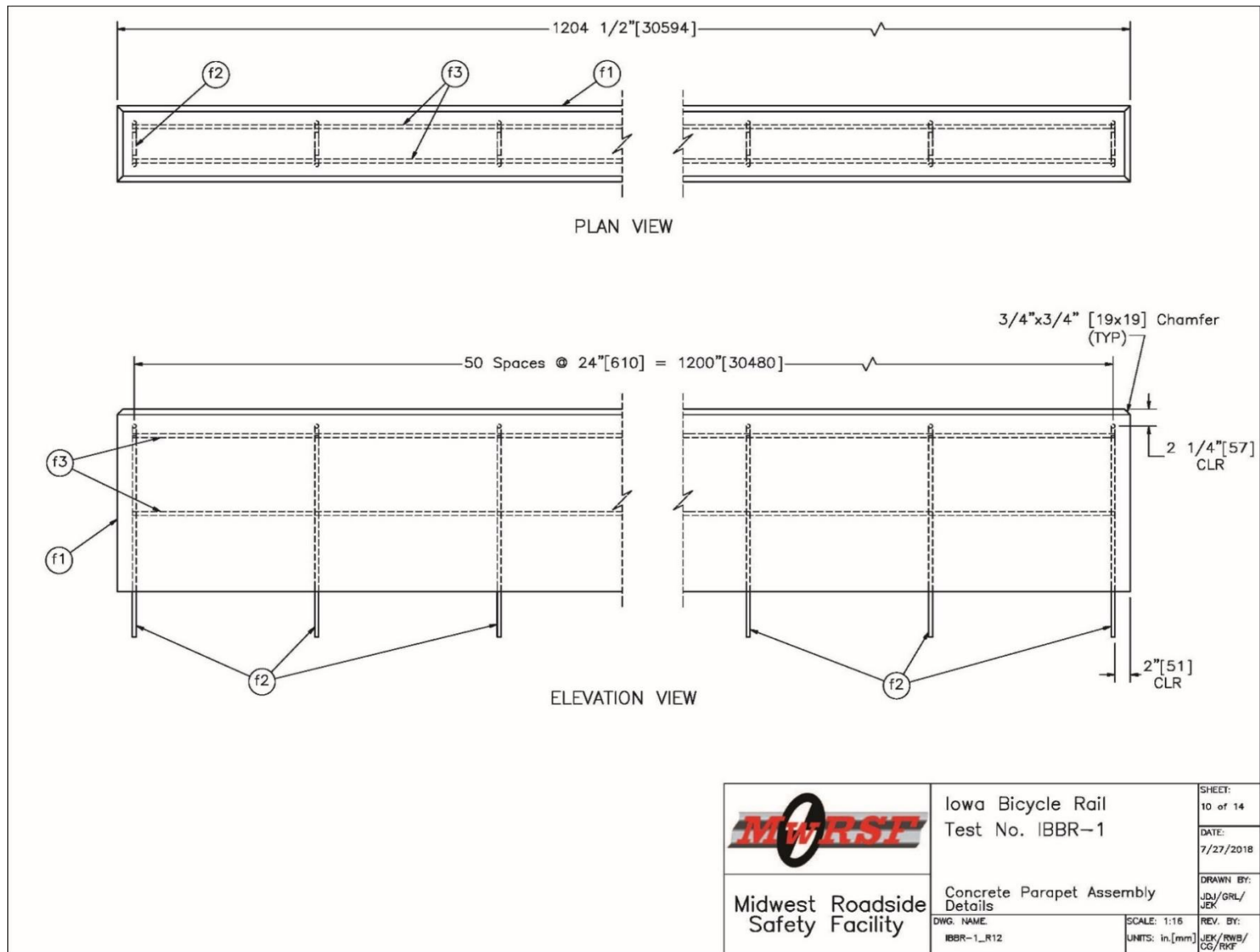


Figure 107. Iowa Bicycle Rail – Concrete Parapet Assembly Details

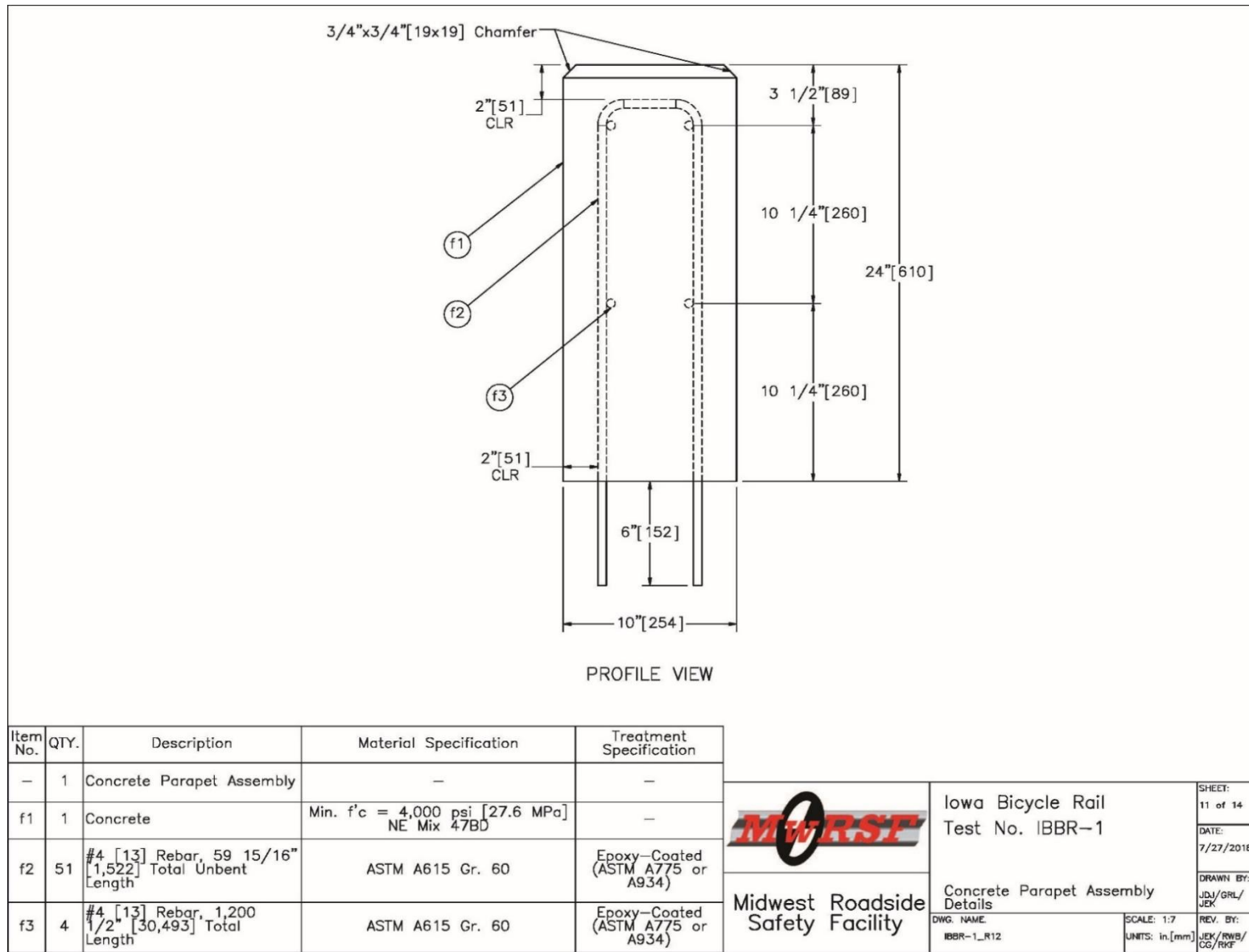


Figure 108. Iowa Bicycle Rail – Concrete Parapet Assembly Details

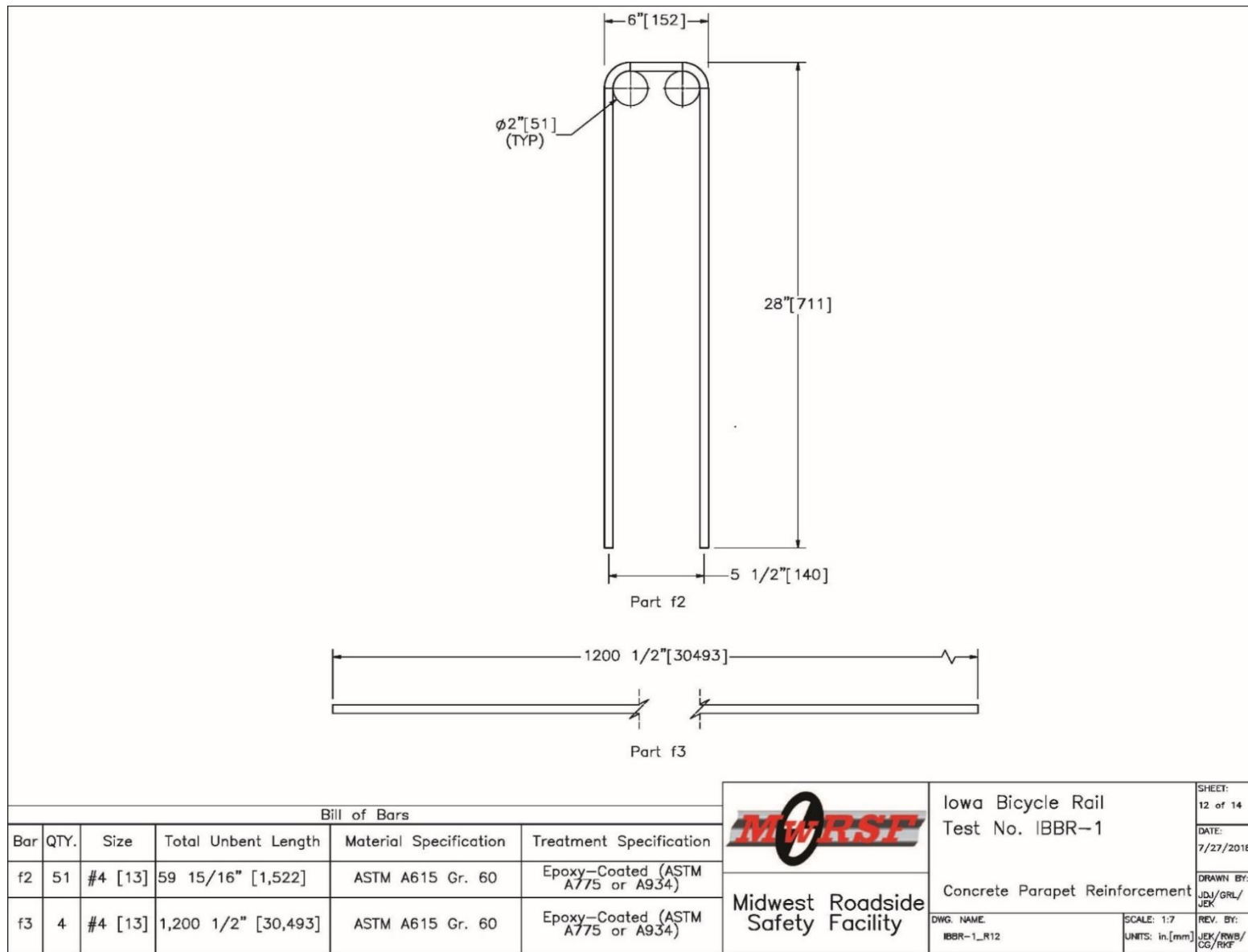


Figure 109. Iowa Bicycle Rail – Concrete Parapet Reinforcement

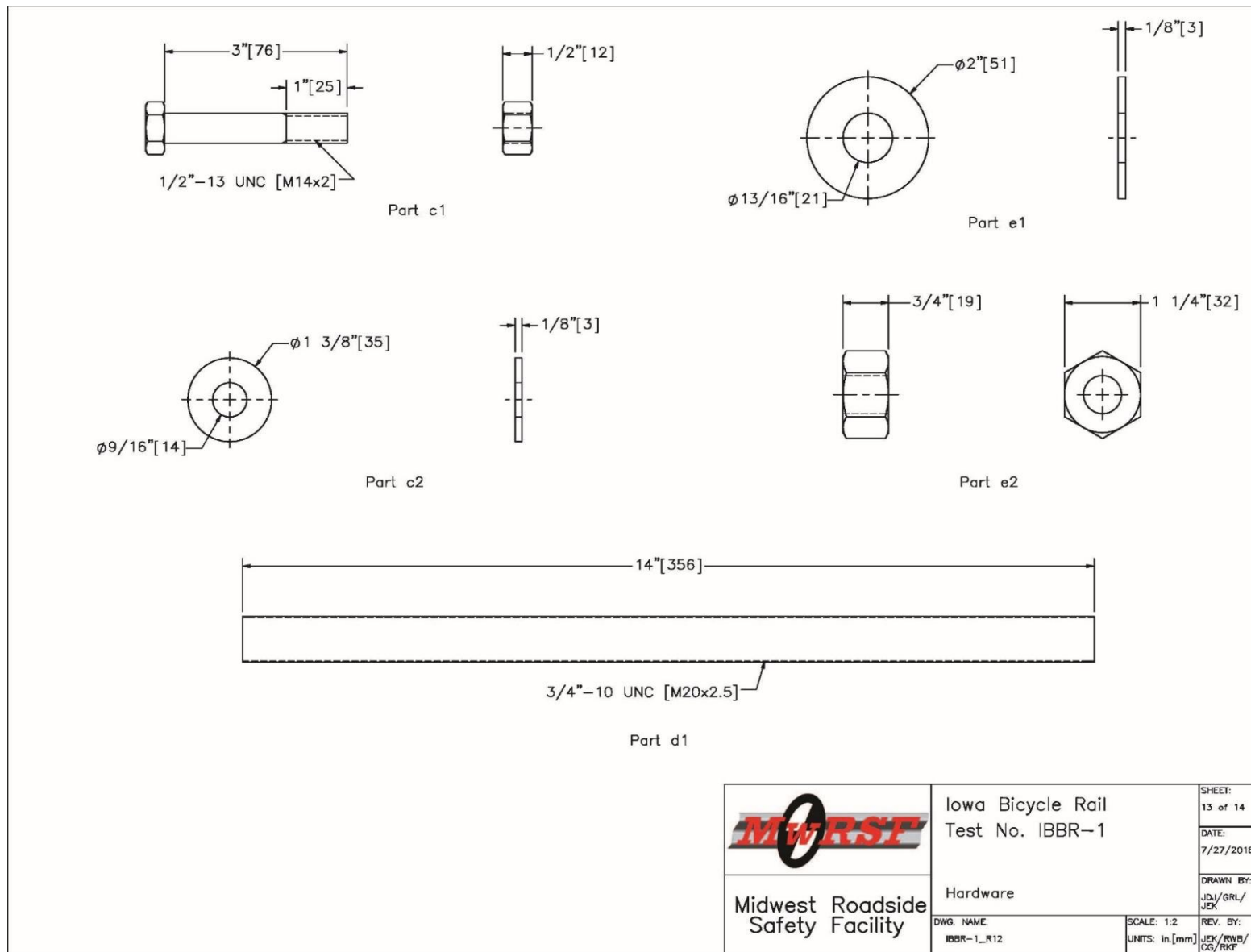



Figure 110. Iowa Bicycle Rail – Hardware

Item No.	QTY.	Description	Material Specification	Treatment Specification	Hardware Guide
a1	5	HSS 3"x2"x1/8" [76x51x3], 240" [6,096] Long Tube	ASTM A500 Gr. C	—	—
a2	10	HSS 2"x2"x1/8" [51x51x3], 21 3/8" [543] Long Tube	ASTM A500 Gr. C	—	—
a3	10	9 1/4"x7"x5/8" [235x178x16] Plate	ASTM A572 Gr. 50	—	—
b1	8	28 1/4"x1 1/8"x5/16" [718x29x8] Plate	ASTM A572 Gr. 50	—	—
b2	8	28 1/4"x1 7/8"x5/16" [718x48x8] Plate	ASTM A572 Gr. 50	—	—
c1	16	1/2"—13 UNC [M14x2], 3" [76] Long Heavy Hex Head Bolt and Nut	Bolt— ASTM F3125 Gr. A325 Type 1 or equivalent Nut — ASTM A563DH or equivalent	ASTM A153 or B695 Class 55 or F1136 Gr.3 or F2329 or F2833 Gr. 1	FBX14b
c2	32	1/2" [13] Dia. Plain Round Washer	ASTM F844	ASTM A123 or A153 or F2329	FWC14a
d1	20	3/4"—10 UNC [M20x2.5], 14" [356] Long Fully Threaded Rod	ASTM F1554 Gr. 105	ASTM A123 or B695 Class 55 or F2329	FRR20b
e1	20	3/4" [19] Dia. Plain Round Washer	ASTM F844	ASTM A123 or A153 or F2329	FWC20a
e2	20	3/4"—10 UNC [M20x2.5] Heavy Hex Nut	ASTM A563DH	ASTM A153 or B695 Class 55 or F2329	FBX20a
f1	1	Concrete	Min. f'c = 4,000 psi [27.6 MPa] NE Mix 47BD	—	—
f2	51	#4 [13] Rebar, 59 15/16" [1,522] Total Unbent Length	ASTM A615 Gr. 60	Epoxy-Coated (ASTM A775 or A934)	—
f3	4	#4 [13] Rebar, 1,200 1/2" [30,493] Total Length	ASTM A615 Gr. 60	Epoxy-Coated (ASTM A775 or A934)	—
—	1	Epoxy	Min. bond strength = 1,560 psi [10.8 MPa] (Hilti HIT-RE 500 V3)	—	—



Midwest Roadside
Safety Facility

Iowa Bicycle Rail
Test No. IBBR-1

Bill of Materials

DWG. NAME:
IBBR-1_R12

SCALE: None
UNITS: in./mm

REV. BY:
JEK/RWB/
CG/RRF

SHEET:
14 of 14

DATE:
7/27/2018

DRAWN BY:
JDI/GRL/
JEK

Figure 111. Iowa Bicycle Rail – Bill of Materials

10 SUMMARY AND RECOMMENDATIONS

10.1 Summary

The objective of this study was to develop a TL-2 combination bridge separation barrier with an upper bicycle railing for Iowa DOT. The new system could be used when sidewalks or trails are present on vehicular bridges. Existing combination barrier systems utilized by Iowa DOT were not previously crash tested to any impact safety standards. Thus, it was desired to have the new barrier system meet AASHTO MASH 2016 TL-2 standards.

First, a literature search was conducted to review existing combination rails, low-height parapets, vertical parapets, as well as ZOI studies pertaining to these systems, which can be found in Chapter 2. The reviewed systems and studies were used to provide guidance on the system design, such as rail configuration and placement as well as parapet height. During this process, it was found that a limited number of crashworthy combination rails existed. Specifically, no MASH 2016 TL-2 combination rails or low-height, vertical-face parapets were identified, and limited research results existed on ZOI envelopes for these systems. Thus, the data gathered provided general guidance, but could not be directly applied to the design.

Chapter 3 discussed the initial simulation effort that was performed. This process began with the validation of the vehicle model using previous full-scale crash testing. Three initial models of MASH 2016 test designation no. 3-11 were simulated using the 2270P Silverado truck model to impact the T222 barrier. The results from those simulations were compared to results obtained in full-scale crash test no. 490024-2-1. From these initial simulations, the vehicle model that performed most like the test vehicle in the actual crash test was selected and refined to create a more accurate model. Friction parameters, tire models, barrier modeling techniques, and steering damping were all studied during the validation process in attempt to create better agreement between the simulation model and full-scale crash test data.

Once the vehicle model was validated, the parapet height study was conducted using the validated model parameters. The parapet height study resulted in the selection of a 24-in. (610-mm) tall concrete barrier as simulation suggested that it would perform adequately while providing Iowa DOT with the lowest-height parapet. During the simulation of the impact event, the vehicle was captured and redirected with no vehicle override of the barrier system. From this effort, the ZOI of the vehicle at this height was analyzed to help determine the probability of vehicle-to-rail interaction and with placement of the rail to reduce the snag severity. The observed ZOI values produced suggested that vehicle interaction with a future bicycle railing was unavoidable, so the system needed to be designed while anticipating this interaction.

Vehicle and system dimensions from previous full-scale crash tests were reviewed to provide additional guidance on parapet height, as discussed in Chapter 4. The results from this review suggested that a 24-in. (610-mm) tall parapet would provide adequate height to capture and redirect the 2270P truck. This review also showed that systems lower than 24 in. (610 mm) safely captured and redirected impacting vehicles under NCHRP 350 TL-2 conditions. However, these systems were tested to older crash test standards that used the smaller 2000P truck rather than the 2270P truck, so results of the previous tests could not be directly applied to the system at hand.

After selecting the parapet height, the bicycle railing design process began, which was initially discussed in Chapter 6. Multiple bicycle rail concepts were produced and presented to Iowa DOT to receive input and feedback. Iowa DOT selected the top mounted, offset-post configuration using welded connections as the preferred design. An overall height of 48 in. (1,219 mm) was chosen along with the rail-to-rail connection method using splice tubes. The loading conditions from *AASHTO LRFD Bridge Design Specifications* [1] were used to determine the section sizes.

Capacities of the rail and post sections, baseplates, and welded connections were calculated using methods and procedures provided in AISC's *Steel Construction Manual* [46]. This analysis led to the selection of a 3-in. x 2-in. x $\frac{1}{8}$ -in. (76-mm x 51-mm x 3-mm) rail section, a 2-in. x 2-in. x $\frac{1}{8}$ -in. (51-mm x 51-mm x 3-mm) post section, and a 9 $\frac{1}{4}$ -in. x 7-in. x $\frac{5}{8}$ -in. (235-mm x 178-mm x 16-mm) baseplate, all connected with $\frac{1}{8}$ -in. (3-mm) fillet welds. The splice tube design process led to the selection of a built-up section using four $\frac{5}{16}$ -in. (8-mm) thick steel plates connected through the use of $\frac{1}{8}$ -in. (3-mm) fillet welds at the outer corners.

To attach the bicycle rail to the concrete parapet, epoxy adhesive and threaded anchor rods were employed as per Iowa DOT's request. Originally, the connection was designed exactly as described in the ACI 318-14 concrete code. The capacity of the anchorage connection in shear and tension was found with the methods described by ACI 318-14 and compared with the expected/calculated system forces. Due to the width of the parapet, the process needed to be modified to consider the reduced available concrete area. The required embedment depth suggested a concrete area of influence that was larger than the width would allow. The capacity of the connection was then reduced by the ratio of the unavailable area divided by the original assumed influence area, thus decreasing the capacity of the anchorage connection as embedment depth increased. This method suggested that a 6-in. (152-mm) embedment depth would provide the necessary capacity when the anchor rods were placed in the center of the parapet along the parapet's longitudinal axis. However, simulation of the system model showed much higher anchor rod tension forces than originally calculated. The anchorage connection was then redesigned using a hybrid method that took into consideration the reinforcement of the parapet using the higher tension values observed during simulation. This process led to the selection of a 12-in. (305-mm) anchor rod embedment depth as well as an increase in anchor rod grade and diameter.

Using the preliminary design details developed during the design process, a system model was created to study the performance of the system as well as determine the CIP for future full-scale crash testing, as discussed in Chapter 7. The vehicle model and model parameters found during the validation effort were used for the simulation effort to examine system behavior. The parapet was modeled as rigid shells with overall parapet dimensions of 24 in. (610 mm) tall by 10 in. (254 mm) wide by 100 ft (30.5 m) long. The rail sections, post sections, baseplates, and splice tube inserts were modeled as shells and used steel properties. The properties for each of the components were scaled or modified to better match the specific material properties that would be used during full-scale crash testing of the system. The connections between the post and baseplates, as well as the connections between the post and the rails, were modeled by simply merging the nodes at the intersection of the components. The splice tube bolts and anchor rods were modeled using solid elements with the appropriate steel properties. Nodes of the anchor rods that intersected with the parapet model were merged to the parapet, creating an infinitely-strong bond between them.

The vehicle model was given an initial velocity of 44 mph (70 km/h) and an angle relative to the system of 25 degrees to simulate MASH 2016 TL-2 testing conditions. During this process, the simulation was observed to ensure that the overall performance of the system was acceptable and used to determine if redesign of any component was necessary. Overall, the system captured and redirected the vehicle successfully without the occurrence of unacceptable vehicle snag. Additionally, the CIP for future full-scale crash testing was determined through the simulation of the vehicle impacting the barrier system model at multiple impact points. Due to the nature of the system, snag severity was considered to be the most important factor in determining the CIP. Several other parameters, such as vehicle damage, system damage, vehicle accelerations and velocities, and vehicle overlap of the system were observed and measured. From this process, it was concluded that an impact 3.8 ft (1.2 m) US from a post would provide the highest probability of snag and the highest snag severity for all of the impact points simulated based on observed overlap. Thus, this impact point was chosen as the CIP to be used in full-scale crash testing.

After the simulation effort was conducted, the barrier design details were confirmed and finalized for use in the full-scale crash testing program. The suggested final design system details are presented in Chapter 9.

10.2 Recommendations

It is recommended that the proposed system undergo full-scale crash testing to evaluate system performance using MASH 2016 test designation no. 2-11, which involves the 2270P truck impacting the system with a velocity of 44 mph (70 km/h) at an angle of 25 degrees to evaluate the performance of the system. This test designation was selected due the 2270P vehicle providing the highest vehicle instability, potential for vehicle-to-rail interaction, and system loading. Test designation no. 2-10, which involves the 1100C vehicle, was not considered to be as critical due to simulation analysis with the 1100C vehicle demonstrating reduced vehicle snag on the combination rail, increased vehicle stability, reduced propensity for vehicle override, and no indication of side window contact with the barrier as compare to the 2270P. The critical impact point is 45 $\frac{5}{8}$ in. (1158 mm) US from Post No. 4, as shown in Figure 98 within Chapter 9. Once the test is conducted, results should be analyzed in order to determine if the system meets the requirements associated with MASH 2016 test designation no. 2-11.

11 REFERENCES

1. *AASHTO LRFD Bridge Design Specifications*, Seventh Edition, American Association of State Highway and Transportation Officials (AASHTO), Washington, D.C., 2014. *Manual for Assessing Safety Hardware (MASH)*, Second Edition, American Association of State Highway and Transportation Officials (AASHTO), Washington, D.C., 2016.
2. Ross, H.E., Sicking, D.L., Zimmer, R.A., and Michie, J.D., *Recommended Procedures for the Safety Performance Evaluation of Highway Features*, National Cooperative Highway Research Program (NCHRP) Report No. 350, Transportation Research Board, Washington, D.C., 1993.
3. *Manual for Assessing Safety Hardware (MASH)*, American Association of State Highway and Transportation Officials (AASHTO), Washington, D.C., 2009.
4. *Manual for Assessing Safety Hardware (MASH) – Second Edition*, American Association of State Highway and Transportation Officials (AASHTO), Washington, D.C., 2016.
5. Hirsch, T.J., Buth, C.E., and Campise, W., *Aesthetically Pleasing Concrete Combination Pedestrian-Traffic Bridge Rail – Texas Type C411*, Research Report 1185-3F, Texas Transportation Institute, Texas A&M University, College Station, Texas, October 1990.
6. Hirsch, T.J. and Buth, C.E., *Aesthetically Pleasing Concrete Combination Pedestrian-Traffic Bridge Rail*, Transportation Research Record No. 1367. Transportation Research Board. National Research Council, Washington D.C., December 1992, pages 23-35.
7. *AASHTO Guide Specifications for Bridge Railings*, American Association of State Highway and Transportation Officials (AASHTO), Washington, D.C., 1989.
8. Buth, C.E., Hirsch, T.J., and Menges, W.L., *Testing Of New Bridge Rail and Transition Designs Volume III: Appendix B BR27D Bridge Railing*, Report No. FHWA-RD-93-060, Texas Transportation Institute, Texas A&M University, College Station, Texas, June 1997.
9. Bullard, D.L., Jr., Menges, W.L., and Buth, C.E., *Development of Combination Pedestrian Traffic Bridge Railings*. Transportation Research Record No. 1468, Transportation Research Board, National Research Council, Washington D.C., December 1994, pages 41-53.
10. Alberson, D.C., Menges, L.W., Buth, C.E., *Performance Level 1 Bridge Railings*, Transportation Research Record No. 1500, Transportation Research Board, National Research Council, Washington D.C., December 1995, pages 80-91.
11. Buth, C.E., Hirsch, T.J., and Menges, W.L., *Testing Of New Bridge Rail and Transition Designs Volume III: Appendix G BR27C Bridge Railing*, Report No. FHWA-RD-93-065, Texas Transportation Institute, Texas A&M University, College Station, Texas, June 1997.

12. Buth, C.E. and Menges, W.L., *Testing and Evaluation of Retrofit Bridge Railings and Transition*. Report No. FHWA-RD-96-032, Submitted to the Office of Safety and Traffic Operations R&D. Federal Highway Administration, Performed by Texas Transportation Institute, Texas A&M University, College Station, Texas, January 1997.
13. Meline, R., Jewell, J., and Peter, R., *Vehicle Crash Tests of the Aesthetic, See-Through Concrete Bridge Rail With Sidewalk, Type 80 SW*, Report No. 59-680600, Materials Engineering and Testing Services, California Department of Transportation, Sacramento, California, August 1999.
14. Polivka, K.A., Faller, R.K., Keller, E.A., Sicking, D.L., Rohde, J.R., and Holloway, J.C., *Design and Evaluation of the TL-4 Minnesota Combination Traffic/Bicycle Bridge Rail*, Research Report No. TRP-03-74-98, Project No. SPR-3(17), Midwest Roadside Safety Facility, University of Nebraska-Lincoln, Lincoln, Nebraska, November 1998.
15. Hascall, J.A., Polivka, K.A., Rohde, J.R., Faller, R.K., Sicking, D.L., and Holloway, J.C., *Design and Evaluation of an Open Traffic/Bicycle Bridge Railing System*, Research Report No. TRP-03-162-07, Project No. SPR-3(17), Midwest Roadside Safety Facility, University of Nebraska-Lincoln, Lincoln, Nebraska, February 9, 2007.
16. Whitesel D., Jewell, J., and Meline, R., *Compliance Crash Testing of the Type 732SW Bridge Rail*, Report No. FHWA/CA15-2181, Roadside Safety Research Group, California Department of Transportation, Sacramento, California, May 9, 2016.
17. Hirsch, T.J., Buth, C.E., Campise W.L., and Kaderka, D., *Crash Test of Texas T202*, Report No. FHWA/TX-88/1179-2F, Texas Transportation Institute, Texas A&M University, College Station, Texas, May 1989.
18. Buth, C.E., Williams, W.F., Bligh, R.P., Menges, W.L., and Butler, B.G., *Tests 4, 5, & 6: NCHRP Report 350 Testing Of The Texas Type T202 Bridge Rail*, Report No. FHWA/TX-99/1804-3, Texas Transportation Institute, Texas A&M University, College Station, Texas, December 1998.
19. Buth, C.E., Williams, W.F., Bligh, R.P., Menges, W.L., and Haug, R.R., *Performance Of The TxDOT T202 (MOD) Bridge Rail Reinforced With Fiber Reinforced Polymer Bars*, Report No. FHWA/TX-03/0-4138-3, Texas Transportation Institute, Texas A&M University, College Station, Texas, December 1998.
20. Stout, D., Hinch, J., and Sawyer, D., *Guardrail Testing Program: Final Report*, Final Report to the Eastern Federal Lands Highway Division, Federal Highway Administration, FHWA Report No. FHWA-RD-90-087, ENSCO Report No. FHWA-89-07, ENSCO, Inc., Springfield, Virginia, June 1990.
21. Hancock, K.L., Hansen, A.G., and Mayer, J.B., *Aesthetic Bridge Rails, Transitions, and Terminals For Park Roads and Parkways*, Report No. FHWA-RD-90-052, Submitted to the Office of Safety and Traffic Operations R&D, Federal Highway Administration, Performed by The Science Corporation Engineering Systems Division, Northwest Washington, D.C., May 1990.

22. Post, E.R., Faller, R.K., Pfeifer, B.G., and Holloway, J.C., *Full-Scale Vehicle Crash Test on the Iowa Steel Temporary Barrier Rail*, Research Report No. TRP-03-20-89, Midwest Roadside Safety Facility, University of Nebraska-Lincoln, Lincoln, Nebraska, December 1989.
23. Faller, R.K., Holloway, J.C., Pfeifer, B.G., and Rosson, B.T., *Performance Level 1 Tests on the Nebraska Open Concrete Bridge Rail*, Research Report No. TRP-03-28-91, Midwest Roadside Safety Facility, University of Nebraska-Lincoln, Lincoln, Nebraska, February 1992.
24. Holloway, J.C., Faller, R.K., Wolford, D.F., Dye, D.L., Sicking, D.L., *Performance Level 2 Tests on a 29-in. Open Concrete Bridge Rail*, Research Report No. TRP-03-51-95, Midwest Roadside Safety Facility, University of Nebraska-Lincoln, Lincoln, Nebraska, June 1996.
25. Polivka, K.A., Faller, R.K., Rohde, J.R., Reid, J.D., Sicking, D.L., and Holloway, J.C., *Safety Performance Evaluation of the Nebraska Open Bridge Rail on an Inverted Tee Bridge Deck*, Research Report No. TRP-03-133-04, Midwest Roadside Safety Facility, University of Nebraska-Lincoln, Lincoln, Nebraska, January 21, 2004.
26. Guidry, T.R., and Beason, W.L., *Development of a Low-Profile Portable Concrete Barrier*, Report No. TX-92/990-4F, Texas Transportation Institute, Texas A&M University, College Station, Texas, November 1991.
27. Bligh, R.P., Mak, K.K., and Hirsch, T.J., *Evaluation of Tennessee Bridge Rail Designs*, Report No. RF 7199-1, Texas Transportation Institute, Texas A&M University, College Station, Texas, May 1994.
28. Polivka, K.A., Faller, R.K., Sicking, D.L., Rohde, J.R., Reid, J.D., and Holloway, J.C., *Development of a Low-Profile Bridge Rail for Test Level 2 Applications*, Research Report No. TRP-03-109-02, Midwest Roadside Safety Facility, University of Nebraska-Lincoln, Lincoln, Nebraska, August 20, 2002.
29. Consolazio, G., Gurley, K., Ellis, R., Wilkes, J., and Shriner, J., *Temporary Low Profile Barrier Roadside Safety: Phase II*, Report No. BC976, Department of Civil & Coastal Engineering, University of Florida, Gainesville, Florida, January 2003.
30. Johnson, E.A., Faller, R.K., Reid, J.D., Sicking, D.L., Bielenberg, R.W., Lechtenberg, K.A., and Rosenbaugh, S.K., *Analysis, Design, and Dynamic Evaluation of a TL-2 Rough Stone Masonry Guardwall*. Research Report No. TRP-03-217-09, Midwest Roadside Safety Facility, University of Nebraska-Lincoln, Lincoln, Nebraska, May 6, 2009.
31. Reid, J.D., Faller, R.K., *A New TL-2 Rough Stone Masonry Guardwall*, Transportation Research Record: Journal of the Transportation Research Board, Washington, D.C., 2010.
32. Keller E.A., Sicking, D.L., Faller, R.K., Polivka, K.A., and Rohde, J.R., *Guidelines for Attachments to Bridge Rails and Median Barriers*, Research Report No. TRP-03-98-03, Project No. SPR-3(17), Midwest Roadside Safety Facility, University of Nebraska-Lincoln, Lincoln, Nebraska, February 26, 2003.

33. Halquist, L.O., *LS-DYNA Keyword User's Manual*, Version 970, Livermore Software Technology Corporation, Livermore, California, 2003.
34. Williams, F.W., Bligh, R.P. and Menges. W.L., *MASH Test 3-11 of the TxDOT T222 Bridge Rail*. Report No. FHWA/TX-14/9-1002-12-13, Submitted to the Office of Safety and Traffic Operations R&D, Federal Highway Administration, Performed by Texas Transportation Institute, Texas A&M University, College Station, Texas, July 2016.
35. Reid, J.D., Bosch, D.A., and Bielenberg, R.W., "Detailed Tire Model for Crash Applications", *International Journal of Crashworthiness*, Vol 12 Issue 5, pp. 521-529.
36. Stolle, C.S., Rilett, L.R., Faller, R.K., Reid, J.D., Jones, E.G., and Holloway, J.C., *Simulation of Pickup Truck-to-Curb Impacts Using LS-DYNA*, Final Report to SDDCTEA, Midwest Report No. TRP-03-306-14, Midwest Roadside Safety Facility, University of Nebraska-Lincoln, October 2014.
37. Stolle, C.J., Reid, J.D., and Faller, R.K., *Zone of Intrusion for Permanent 9.1-Degree Single-Slope Concrete Barriers*, Research Report No. TRP-03-292-13, Midwest Roadside Safety Facility, University of Nebraska-Lincoln, Lincoln, Nebraska, March 14, 2014.
38. Reid, J.D. and Sicking, D.L., *Zone of Intrusion Study*, Research Report No. TRP-03-242-10, Midwest Roadside Safety Facility, University of Nebraska-Lincoln, Lincoln, Nebraska, October 15, 2010.
39. *Expert Autostats*, 4N6XPRT Systems, La Mesa, California, 2012.
40. Mohan, P., Ritter, M., Marzougui, D., Brown, D., Kan, C., and Opiela, K., *Modeling, Testing, and Validation of the 2007 Chevy Silverado Finite Element Model*, Working Paper No. NCAC 2009-W-005, National Crash Analysis Center, George Washington University, October 2009.
41. Asadollahi Pajouh, M., Bielenberg, R.W., Schmidt, J.D., Lingenfelter, J., Faller, R.K., and Reid, J.D., *Placement of Breakaway Light Poles Located Directly Behind Midwest Guardrail System (MGS)*, Research Report No. TRP-03-361-17, Midwest Roadside Safety Facility, University of Nebraska-Lincoln, Lincoln, Nebraska, June 29, 2017.
42. Meyer, D.T., Reid, J.D., Lechtenberg, K.A., Bielenberg, R.W., and Faller, R.K., *Increased Span Length for the MGS Long-Span Guardrail System Part II: Full-Scale Crash Testing*, Research Report No. TRP-03-339-17, Midwest Roadside Safety Facility, University of Nebraska-Lincoln, Lincoln, Nebraska, April 7, 2017.
43. Rosenbaugh, S.K., Fallet, W.G., Faller, R.K., Bielenberg, R.W., Reid, J.D., *34-in. Tall Thrie Beam AGT to Concrete Buttress*, Draft Report, Research Report No. TRP-03-389-18, Midwest Roadside Safety Facility, University of Nebraska-Lincoln, July 11, 2017.
44. *Mash Testing of Bullnose with Break Away Steel Posts (Test Nos. MSPBN-1-3)*, Draft Report, Research Report No. TRP-03-367-17, Midwest Roadside Safety Facility, University of Nebraska-Lincoln, Lincoln, Nebraska, June 8, 2018.

45. *2010 ADA Standards for Accessible Design*, United States Department of Justice, September 2010.
46. *Steel Construction Manual*, Fifteenth Edition, First Printing, American Institute of Steel Design (AISC), 2017.
47. *Steel Design Guide 1*, 2nd Edition, First Printing, American Institute of Steel Design (AISC), May 2006.
48. ACI Committee 318, *Building Code Requirements for Structural Concrete (ACI 318-14) and Commentary*, Farmington Hills, Michigan, American Concrete Institute, August 2014
49. Bielenberg, R.W., Reid, J.D., Rosenbaugh, S.K., Haase, A.J., and Faller, R.K., *Attachment of Combination Rails to Concrete Parapets Utilizing Epoxy Adhesive Anchors*, Research Report No. TRP-03-325-15, Midwest Roadside Safety Facility, University of Nebraska-Lincoln, Lincoln, Nebraska, November 3, 2015.
50. Humphrey, B.M., Faller, R.K., Bielenberg, R.W., Reid, J.D, and Negahban, M., *Improved Methodologies in Modeling and Predicting Failure in AASHTO M-180 Guardrail Steel Using Finite Element Analysis – Phase I*, Research Report No. TRP-03-333-16, Midwest Roadside Safety Facility, University of Nebraska-Lincoln, Lincoln, Nebraska, August 23, 2016.

12 APPENDICES

Appendix A. Rail Design Calculations

Using the pedestrian/bicycle loading stated in *AASHTO LRFD Bridge Design Specifications* [1] and the rail/post section configurations/equations discussed in Chapter 6, both shear loading and bending moments were calculated, as shown in Table A-1.

Table A-1. Rail and Post - Shear and bending Moment Values

Post Spacing (Rectangular)		Distributed Load w	
10 ft		50 lb/ft	
120 in.		4.17 lb/in.	
		Point Load P	
		200 lb	
Railing Height			
1.875 ft			
22.5 in.	XX		
23 in.	YY		
	<u>Rail</u>		
	Shear		
	Horizontal	450 lb	
	Vertical	250 lb	
	Moment		
	Horizontal	13500 lb-in.	
	Vertical	7500 lb-in.	
	<u>Post</u>		
	Shear		
		700 lb	
	Moment		
	XX	15750 lb-in.	
	YY	16100 lb-in.	

The section properties for various rectangular and square HSS ASTM A500 Grade C sections were all gathered from the *AISC Steel Construction Manual* [46] and compiled into a Microsoft Excel spreadsheet. The section properties were then referenced in order to calculate their capacities, using Microsoft Excel's formula functions, due to the loading conditions. Both the rail and post section properties that were selected for the final design are shown in Tables A-2 and A-3.

Table A-2. Rail Section Details

Property	Value	Units
Rail section	3 x 2 x 0.125	in.
Rail height	24	in.
Nominal depth	3	in.
Nominal width	2	in.
Wall thickness, t	0.116	in.
h	2.652	in.
b	1.652	in.
b/t	22.86	
h/t	14.24	
S_{x-x}	0.867	in. ³
S_{y-y}	0.692	in. ³

Table A-3. Post Section Details

Property	Value	Units
Post section	2 x 2 x 0.125	in.
Post spacing	120	in.
Nominal depth	2	in.
Nominal width	2	in.
Wall thickness, t	0.116	in.
h	1.652	in.
b	1.652	in.
b/t	14.24	
h/t	14.24	
S_{x-x}	0.486	in. ³
S_{y-y}	0.486	in. ³

With the loads and capacities known, a comparison between the capacities and loads was performed to select the appropriate section. The comparison between capacity and load for the final selected sections is shown in Table A-4.

Table A-4. Rail and Post - Load vs. Resistance Comparisons

Rail	Nominal Capacity		Required Design Load
XX Shear	8623.4 lb	>	250 lb
YY Shear	13843.4 lb	>	450 lb
XX Shear	8623.4 lb	>	450 lb
YY Shear	13843.4 lb	>	250 lb
Horizontal Moment	39015.0 lb-in	>	13500 lb-in.
Vertical Moment	31140.0 lb-in	>	7500 lb-in.
Normalized	0.587	<	1
Horizontal Moment	31140.0 lb-in	>	13500 lb-in.
Vertical Moment	39015.0 lb-in	>	7500 lb-in.
Normalized	0.626	<	1
Normalized	0.436	<	1
Post	Nominal Capacity		Required Design Load
XX Shear	8623.4 lb	>	700 lb
YY Shear	8623.4 lb	>	700 lb
XX Moment	21870.0 lb-in	>	15750 lb-in
YY Moment	21870.0 lb-in	>	16100 lb-in

Table A-5 displays the calculations performed for the process above using the equations discussed in Chapter 6. The calculations performed in Table A-5 were the same as used to populate the cells in both the Capacity and Required Design Load columns in Table A-4.

Table A-5. Rail and Post - Load and Capacity Calculations

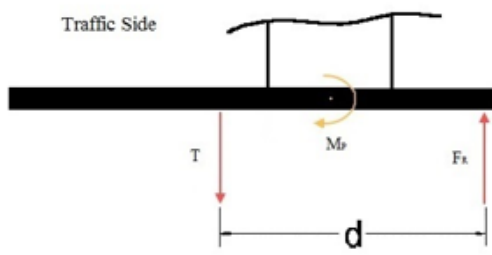
Load Calculations					
Variables	Case	Equation	Calculation	Load	
Rail - 3" x 2" x 1/8"					
P = 200 lb	Moment y-y, Case 1	Equation 2	$M_{(rail,y-y)} = PL/4 + (wL^2)/8$	$= (200 \cdot 120/4) + ((4.1667 \cdot 120^2)/8)$	= 13500 lb-in.
L = 120 in.	Moment z-z, Case 1	Equation 3	$M_{(rail,z-z)} = (wL^2)/8$	$= ((4.1667 \cdot 120^2)/8)$	= 7500 lb-in.
w = 4.1667 lb/in.	Moment z-z, Case 2	Equation 4	$M_{(rail,z-z)} = PL/4 + (wL^2)/8$	$= (200 \cdot 120/4) + ((4.1667 \cdot 120^2)/8)$	= 13500 lb-in.
	Moment y-y, Case 2	Equation 5	$M_{(rail,y-y)} = (wL^2)/8$	$= ((4.1667 \cdot 120^2)/8)$	= 7500 lb-in.
	Shear z-z, Case 1	Equation 6	$V_{(rail,z-z)} = P + wL/2$	$= 200 + (4.1667 \cdot 120/2)$	= 450 lb
	Shear y-y, Case 1	Equation 7	$V_{(rail,y-y)} = wL/2$	$= (4.1667 \cdot 120/2)$	= 250 lb
	Shear y-y, Case 2	Equation 8	$V_{(rail,y-y)} = P + wL/2$	$= 200 + (4.1667 \cdot 120/2)$	= 450 lb
	Shear z-z, Case 2	Equation 9	$V_{(rail,z-z)} = wL/2$	$= (4.1667 \cdot 120/2)$	= 250 lb
Post - 2" x 2" x 1/8"					
H_L = 23 in.	Moment	Equation 18	$M_{Post} = P_{LL} \cdot H_L = (200 + 4.1667 \cdot L) \cdot H_L$	$= (200 + 4.1667 \cdot 120) \cdot 23$	= 16100 lb-in.
	Shear	Equation 19	$V_{post} = P_{LL} = 200 + 4.1667 \cdot L$	$= 200 + 4.1667 \cdot 120$	= 700 lb
Capacity Equations					
Variables	Case	Equation	Calculation	Load	
Rail - 3" x 2" x 1/8"					
$\phi_b = 0.9$	Moment y-y	Equation 11	$\phi_b \cdot M_n = \phi_b \cdot F_y \cdot S_{y-y}$	$= 0.9 \cdot 50000 \cdot 0.867$	= 39015 lb-in.
$S_{y-y} = 0.867 \text{ in.}^3$	Moment z-z	Equation 11	$\phi_b \cdot M_n = \phi_b \cdot F_y \cdot S_{z-z}$	$= 0.9 \cdot 50000 \cdot 0.692$	= 31140 lb-in.
$S_{z-z} = 0.692 \text{ in.}^3$	Combined Moment, Case 1	Equation 12	$M_{(rail,y-y)}/\phi M_{nsy} + M_{(rail,z-z)}/\phi M_{nsz}$	$= (13500/39015) + (7500/31140)$	= 0.587 < 1
$\phi_v = 0.75$	Combined Moment, Case 2	Equation 12	$M_{(rail,y-y)}/\phi M_{nsy} + M_{(rail,z-z)}/\phi M_{nsz}$	$= (7500/39015) + (13500/31140)$	= 0.626 < 1
$A_w = 2ht$	Shear z-z,	Equation 13	$\phi_v \cdot V_n = \phi_v \cdot 0.6 F_y \cdot A_w \cdot C_{v2}$	$= 0.75 \cdot 0.6 \cdot 50000 \cdot 2 \cdot 1.652 \cdot 0.116$	= 8623.4 lb
$h = b - 3t$	Shear y-y,	Equation 13	$\phi_v \cdot V_n = \phi_v \cdot 0.6 F_y \cdot A_w \cdot C_{v2}$	$= 0.75 \cdot 0.6 \cdot 50000 \cdot 2 \cdot 2.652 \cdot 0.116$	= 13843.4 lb
$C_{v2} = 1.0$	Combined Shear/Moment	Equation 17	$M_{rail}/\phi M_{nsrail} + (V_{rail}/\phi V_{nrail})^2$	$= (13500/31140) + (450/8623.4)^2$	= 0.436 < 1
	Combined Shear/Moment	Equation 17	$M_{rail}/\phi M_{nsrail} + (V_{rail}/\phi V_{nrail})^2$	$= (7500/39015) + (250/13843.4)^2$	= 0.193 < 1
Post - 2" x 2" x 1/8"					
$S = 0.486 \text{ in.}^3$	Moment	Equation 18	$\phi_b \cdot M_n = \phi_b \cdot F_y \cdot S$	$= 0.9 \cdot 50000 \cdot 0.486$	= 21870 lb-in.
	Shear	Equation 19	$\phi_v \cdot V_n = \phi_v \cdot 0.6 F_y \cdot A_w \cdot C_{v2}$	$= 0.75 \cdot 0.6 \cdot 50000 \cdot 2 \cdot 1.652 \cdot 0.116$	= 8623.4 lb
	Combined Shear/Moment	Equation 17	$M_{rail}/\phi M_{nsrail} + (V_{rail}/\phi V_{nrail})^2$	$= (16100/21870) + (700/8623.4)^2$	= 0.743 < 1

Table A-6 displays the process followed and the equations used to determine the required baseplate thickness using the *AISC Steel Design Guide 1* [47] for column baseplates. This process assumed an applied moment and axial load to the post from the pedestrian/bicycle loading. ASTM A572 Grade 50 steel properties were used to design the baseplate.

Table A-6. AISC Baseplate Design Guide Calculations

Variable	Input	Units	Calculation	Description
B	9.25	in.		Width of BP
N	7	in.		Depth of BP
Pu	0.45	kips		Axial Load on BP
M	24.3	kip-in.		Max Moment at Base of Post
Fp1	2.75	ksi	$\phi * 0.85 * F_c' * \text{SQRT}(A_1/A_2)$	Allowable Bearing Stress
Fp2	4.42	ksi	$\phi * 1.7 * F_c'$	Allowable Bearing Stress
Fp	2.75	ksi		Allowable Bearing Stress
e	54.0	in.		Eccentricity
f'	33.64	kips	M/P_u	
A	7.13	in. ²	$(f' + \sqrt{(f')^2 - 4 * (F_p * B/6) * (P_u * A' + M)}) / (F_p * B/3)$	length of bear stress block along N
A	0.82	in. ²	$(f' - \sqrt{(f')^2 - 4 * (F_p * B/6) * (P_u * A' + M)}) / (F_p * B/3)$	length of bear stress block along N
T	9.97	kips	$(F_p * A * B/2) - P_u$	Tension in Anchors
T/2	4.99		$T/2$	Tension in each Anchor
T	9970.2	lb		Tension in Anchors
T/2	4985.1	lb		Tension in each Anchor
Critical Section	2.55	in.	$(N - 0.95d)/2$	Critical Section
m	2.55	in.	$(N - 0.95d)/2$	location of critcal section along N
n	3.675	in.	$(B - 0.95d)/2$	location of critical section along B
fpu(m)	-5.79	ksi	$F_p * (A - m)/A$	Pressure at critical bending plane
Mupl	-0.32	kip-in./in.	$(F_p * m^2/2) + ((F_p - f_{pu}(m)) * m^2/3)$	Required moment strength
Mupl	2.49	kip-in./in.	$T * (m - 3) / (2 * (m - 3))$	Required moment strength
t	0.47	in.	$\sqrt{4 * M_{pl} / (\phi * F_y)}$	required thickness

The additional required thickness and anchor rod tension calculation process is shown in Figure A-1. This procedure is explained in the baseplate section of Chapter 6. Case 1 studied the condition where the pedestrian/bicycle loading was placed on the non-traffic side. Case 2 studied a loading applied on the traffic side that would exceed the post's moment capacity.



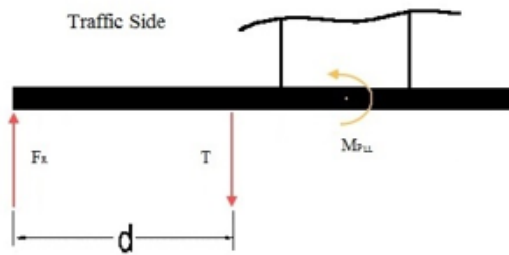
$$M_{NP} = 24300 \text{ lb} - \text{in.} = 24.3 \text{ kip} - \text{in.}$$

$$F = T = \frac{M_{NP}}{d} = \frac{24.3}{4} = 6.075 \text{ kip}$$

$$\sigma_b = \frac{M}{S} \quad S = \frac{bt^2}{6}$$

$$t = \sqrt{\frac{6F_r L}{b\sigma_{\text{allowed}}}} = \sqrt{\frac{6M_{PLL}}{b\sigma_{\text{allowed}}}} = \sqrt{\frac{6(6.075)}{(9.25 - 3)(50)}} = 0.342 \text{ in}$$

required thickness = 3/8 in.



$$M_{NP} = 16100 \text{ lb} - \text{in.} = 16.1 \text{ kip} - \text{in.}$$

$$F = T = \frac{M_{NP}}{d} = \frac{16.1}{3} = 5.367 \text{ kip}$$

$$\sigma_b = \frac{M}{S} \quad S = \frac{bt^2}{6}$$

$$t = \sqrt{\frac{6F_r L}{b\sigma_{\text{allowed}}}} = \sqrt{\frac{6M_{PLL}}{b\sigma_{\text{allowed}}}} = \sqrt{\frac{6 * 16.1}{(9.25 - 3)(50)}} = 0.556 \text{ in}$$

required thickness = 5/8 in.

Figure A-1. Baseplate Additional Calculations

The process followed and equations used to calculate the load and capacities of the fillet welds used in the final design are shown in Table A-7. The calculations used in Table A-7 were the same used to populate the cells in Table A-8. The loads and capacities were compared to evaluate the section of interest's ability to resist the design loads.

Table A-7. Weld - Load and Capacity Calculations

Load Equations				
Variables	Case	Equation	Calculation	Load
Post-to-Baseplate				
d_post = 2 in.	Shear , Ped. Loading	$V_{post} = P_{LL} = 200 + 4.1667 * L$	$= 200 + 4.1667 * 120$	$= 700 \text{ lb}$
M_NP = 24300 lb-in.	Front Flange Tension, Ped Loading	$T_{ff} = M_{post} / d_{post}$	$= 16100 / 2$	$= 8050 \text{ lb}$
b_post = 2 in.	Shear, Veh. Loading	$V_{post,veh} = M_{NP} / 10$	$= 24300 / 10$	$= 2430 \text{ lb}$
	Front Flange Tension, Veh. Loading	$T_{ff,veh} = M_{NP} / b_{post}$	$= 24300 / 2$	$= 12150 \text{ lb}$
Rail-to-Post				
d_rail = 2 in.	Shear , Ped. Loading	$V_{rail} = P_{LL} = 200 + 4.1667 * L$	$= 200 + 4.1667 * 120$	$= 700 \text{ lb}$
	Front Flange Tension, Ped Loading	$T_{ff} = P_{LL} * d_{rail} / (2 * d_{post})$	$= 700 * 2 / (2 * 2)$	$= 350 \text{ lb}$
Capacity Equations				
Variables	Case	Equation	Calculation	Load
Post-to-Baseplate				
$\phi_w = 0.75$	Shear	$\phi_w * R_n = 2 * \phi_w * 0.60 F_{EXX} (1.0 + 0.50 \sin^{1.5} \theta) A_{we}$	$= 2 * 0.75 * 0.6 * 70000 * 1 * 0.088375 * 2$	$= 11135.25 \text{ lb}$
F_EXX = 70 ksi	Front Flange Tensions	$\phi_w * R_n = 2 * \phi_w * 0.60 F_{EXX} (1.0 + 0.50 \sin^{1.5} \theta) A_{we}$	$= 0.75 * 0.6 * 70000 * 1.5 * 0.088375 * 2$	$= 8351.44 \text{ lb}$
A_w = t*d				
t = 0.707*a = 0.707*0.125				

Table A-8. Weld Connection Load vs. Resistance Comparisons

Post-Base Weld	Nominal Capacity		Required Design Load
Front Weld Tension	8351.4 lb	>	8050.0 lb
Shear	11135.3 lb	>	700.0 lb
Front Weld Tension	8351.4 lb	>	8050.0 lb
Shear	22270.5 lb	>	700.0 lb
Shear vs. Impact Shear	11135.3 lb	>	2430.0 lb
Impact Tension	8351.4 lb	<	12150.0 lb
	19486.7 lb	>	12150.0 lb
Rail-Post Weld	Nominal Capacity		Required Design Load
XX Shear Strength	11135.3 lb	>	700.0 lb
YY Shear Strength	11135.3 lb	>	700.0 lb
Combined	22270.5 lb	>	700.0 lb
Front Weld Tension	8351.4 lb	>	350.0 lb

Figures A-2 and A-3 both display the outputs from the hybrid epoxy anchorage design process. The process was performed using a modified Microsoft Excel spreadsheet that was designed to calculate the epoxy anchorage capacities according to ACI concrete code. The outputs shown were then compared to the anchor rod tensions and shear force values observed during simulation to ensure the connection provided adequate capacity.

TENSION ANCHORS (FRONT FACE)			
Embedment Depth, h_{ef} :	5.5	in.	
Embedment Depth, h_{ef} :	6.5	in.	
Total	12	in.	
Steel Bar Diameter, d_a :	0.75	in.	
Area of Steel, A_s :	0.334	in. ²	
Front (Tension) Anchor Spacing, s :	5	in.	
Front (Tension) Anchor to deck edge, $c_{a,min}$:	5	in.	
Bond Strength, τ_{cr} :	1440	psi	
Steel Ultimate Strength, f_{uta} :	105	ksi	
Concrete Strength, f'_c :	4000	psi	
Deck Reinforced? (y/n):	y		
Steel DIF, ψ_{sd} :	1		
Concrete DIF, ψ_{cd} :	1		
Adhesive/Bond DIF, ψ_{bd} :	1		
		Tension	Shear
ACI Steel Strength Reduction Factor, ϕ_s :	0.75	0.65	
ACI Concrete Strength Reduction Factor, ϕ_c :	0.65	0.75	
ACI Adhesive Strength Reduction Factor, ϕ_a :	0.65	NA	
TENSION CAPACITY			
Steel Fracture: $\phi N_s = A_s N_s f_{uta} \psi_{sd}$			
	$\phi N_s =$	26.30	kips
Concrete Breakout: $\phi N_{cb} = A_{Nc}/A_{Nco} * \psi_{ed,N} \psi_{c,N} \psi_{cp,N} \psi_{cd} * N_b$			
	$N_b = k_c * h_{ef}^{1.5} \sqrt{f'_c}$		
	k_c :	17	(24 for cast in place, 17 for post installed)
	$\psi_{c,N}$:	1.4	(1.25 for cast in anchors, 1.4 for post installed)
	$N_b =$	13.87	kips
	C_{ac} :	11	
	$\psi_{cp,N}$:	1	
	$\psi_{ed,N}$:	0.881818	
	$A_{Nco} = 9 * h_{ef}^2$:	272.25	in. ²
	A_{Nc} :	103.75	in. ²
	A_{Nc}/A_{Nco} :	0.381084	
	$\phi N_{cb} =$	4.24	kips
Adhesive / Bond Failure: $\phi N_a = A_{Na}/A_{Na0} * \psi_{ed,Na} \psi_{cp,Na} \psi_{bd} * N_{ba}$			
	$N_{ba} = \tau_{cr} \pi d_a h_{ef}$		
	$N_{ba} =$	22.05	kips
	$A_{Na0} = (2 * C_{Na})^2$		
	$C_{Na} = 10 * d_a * \sqrt{\tau_{cr}/1100}$		
	$C_{Na} =$	8.58	in.
	$A_{Na0} =$	294.55	in. ²
	$A_{Na} =$	85.81163	in. ²
	A_{Na}/A_{Na0} :	1	134.9403
	$\psi_{cp,Na}$:	1	(should be the same as $\psi_{cp,N}$)
	$\psi_{ed,Na}$:	0.874801	
	$\phi N_a =$	12.54	kips

Figure A-2. Tensile Adhesive Anchorage Calculations

SHEAR ANCHORS (BACK FACE)													
Number of	9												
Embedment Depth, h_{ef} :	12 in.												
Steel Bar Diameter, d_b :	0.75 in.												
Area of Steel, A_s :	0.334 in. ²												
Anchor Spacing, s :	5 in.												
Anchor to Deck Edge Distance, c_{a1} :	5 in.												
Steel Ultimate Strength, f_{uta} :	105 ksi												
Concrete Strength, f'_c :	4000 psi												
Deck Thickness, h_d :	24 in.												
Deck Reinforced? (y/n):	y												
Bond Strength, τ_{cr} :	1440 psi												
<table border="1"> <thead> <tr> <th colspan="2">Shear Strengths</th> </tr> <tr> <th>Failure Mode</th> <th>Load (kips)</th> </tr> </thead> <tbody> <tr> <td>Steel Fracture:</td> <td>22.80</td> </tr> <tr> <td>Concrete Breakout:</td> <td>2.23</td> </tr> <tr> <td>Concrete Pryout:</td> <td>10.21</td> </tr> </tbody> </table>				Shear Strengths		Failure Mode	Load (kips)	Steel Fracture:	22.80	Concrete Breakout:	2.23	Concrete Pryout:	10.21
Shear Strengths													
Failure Mode	Load (kips)												
Steel Fracture:	22.80												
Concrete Breakout:	2.23												
Concrete Pryout:	10.21												
Total Anchor Shear for Barrier													
LCR:	1 ft												
$\phi V_{barrier}$:	5.35 kips												
SHEAR CAPACITY													
Steel Fracture: $\phi V_{sa} = A_s N f_{uta} \psi_{ed}$ deleted 0.6 factor													
ϕV_{sa} :	22.80 kips												
Concrete Breakout: $\phi V_{cb} = A_{vc} / A_{vc0} * \psi_{ed,N} \psi_{c,N} \psi_{cp,N} \psi_{cd} * N_b$													
$V_{b1} = 7 * (l_e / d_b)^{0.2} * \sqrt{d_b} * \sqrt{f'_c} * C_{a1}^{1.5}$													
l_e : 6.00													
V_{b1} : 6.50 kips													
$V_{b2} = 9 * C_{a1}^{1.5} * \sqrt{f'_c}$													
6.36 kips													
$V_b = \min(V_{b1}, V_{b2})$: 6.36 kips													
$\psi_{ed,N}$: 1 (only reduced for anchor adjacent to deck discontinuity)													
$\psi_{c,N}$: 1.4 (1.4 for uncracked deck, 1.2 for cracked reinforced)													
$\psi_{h,N}$: 1.00													
$A_{vc0} = 4.5 * (c_{a1})^2$: 112.5 in. ²													
A_{vc} : 37.5 in. ²													
A_{vc0} / A_{vc} : 0.333333													
ϕV_{cb} : 2.23 kips													
Concrete Pryout Strength: $\phi V_{cp} = k_{cp} N_p$													
k_{cp} : 2													
$N_{cp} = \min(N_{cb}, N_a)$													
$N_{cb} = A_{Nc} / A_{Nco} * \psi_{ed,N} \psi_{c,N} \psi_{cp,N} \psi_{cd} * N_b$													
$N_b = k_c * h_{ef}^{1.5} * \sqrt{f'_c}$													
k_c : 17													
$\psi_{c,N}$: 1.4													
N_b : 44.69 kips													
c_{ac} : 24													
$\psi_{cp,N}$: 1													
$\psi_{ed,N}$: 0.783333													
$A_{Nco} = 9 * h_{ef}^2$: 1296 in. ²													
A_{Nc} : 180 in. ²													
A_{Nc} / A_{Nco} : 0.138889													
N_{cb} : 6.81													
N_{cp} : 6.81													
ϕV_{cp} : 10.21 kips													
$N_a = A_{Na} / A_{Nao} * \psi_{ed,Na} \psi_{cp,Na} \psi_{bd} * N_{ba}$													
$N_{ba} = \tau_{cr} \pi d_b h_{ef}$													
N_{ba} : 40.72 kips													
$A_{Nao} = (2 * C_{Na})^2$													
$C_{Na} = 10 * d_b * \sqrt{(\tau_{cr} / 1100)}$													
C_{Na} : 8.58													
$A_{Nao} = 294.55$ in. ²													
$A_{Na} = 85.81163$ in. ²													
A_{Na} / A_{Nao} : 0.291336													
$\psi_{cp,Na}$: 1 (should be the same as $\psi_{cp,N}$)													
$\psi_{ed,Na}$: 0.874801													
N_a : 10.38													

Figure A-3. Shear Adhesive Anchorage Calculations

The section modulus calculations for the final built-up splice tube section are shown in Figure A-4. The results from the calculation were compared with the section properties of the selected rail section in Table A-2 to ensure the section provided more bending resistance than the rail sections it would be connecting.

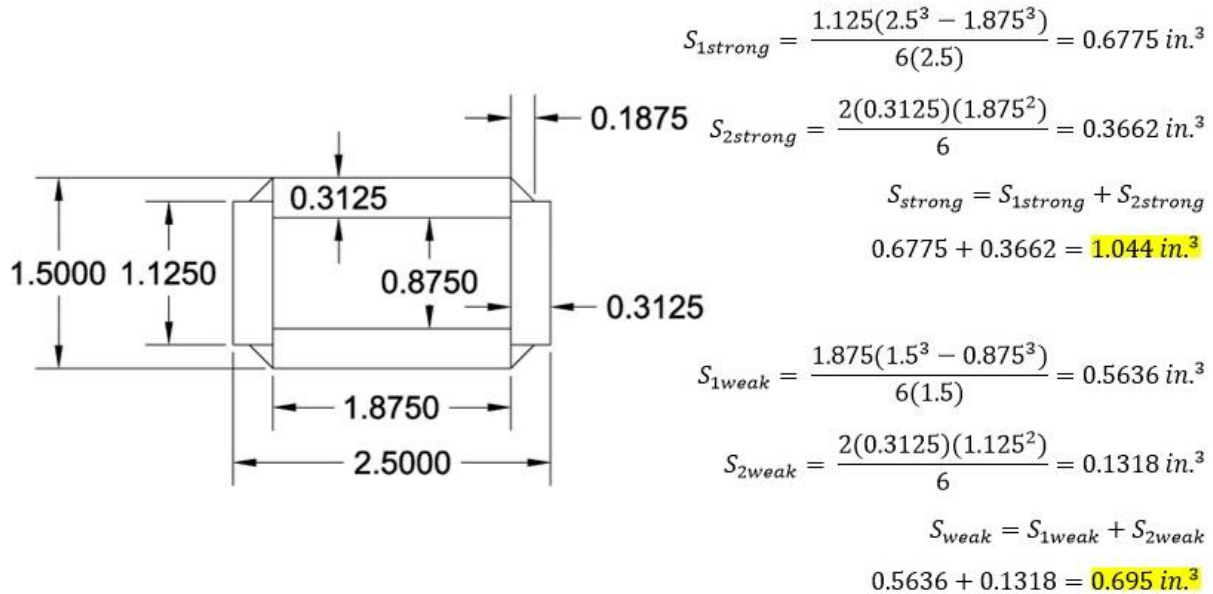


Figure A-4. Built-Up Splice Tube Section Moduli Calculations

END OF DOCUMENT